This is to certify that the
dissertation entitled

Analysis of Ribose Dynamics in RNA Molecules Utilizing ^{13}C NMR Spin Relaxation Techniques Determined with Novel Specific Isotope Labeling Scheme

presented by

James Edward Johnson, Jr.

has been accepted towards fulfillment
of the requirements for the

Ph.D. degree in Biochemistry & Molecular Biology

Charles L. Hoogstraten
Major Professor's Signature

Nov. 12, 2008
Date

Analysis of Ribose Dynamics in RNA Molecules Utilizing ^{13}C NMR Spin Relaxation Techniques Determined with Novel Specific Isotope Labeling Scheme

By

James Edward Johnson, Jr.

A DISSERTATION

Submitted to
Michigan State University
In partial fulfillment of the requirements
For the degree of

DOCTOR OF PHILOSOPHY

Biochemistry and Molecular Biology

2008

ABSTRACT

Analysis of Ribose Dynamics in RNA Molecules Utilizing ^{13}C NMR Spin Relaxation Techniques Determined with Specific Isotope Labeling Scheme

By

James Edward Johnson, Jr.

With the increased recognition of the varied roles that RNA molecules can perform in biology, there has come a larger interest in the study of RNA structure and function. In many cases, the function of structured RNA molecules such as ribozymes depends to a great extent on conformational dynamics on various time scales. While conformational exchange on the μs-ms timescale has been studied in nucleic acid side-chain bases using sophisticated ^{13}C NMR spin relaxation experiments, the ribose ring of RNA is poorly suited for these experiments due to magnetic interference arising from ^{13}C–^{13}C interactions in uniform ^{13}C labeled samples. To alleviate these errors, a novel alternate-site ^{13}C labeling scheme was developed to isolate ^{1}H-^{13}C spin systems within the ribose ring suitable for ^{13}C NMR studies.

Using *Escherichia coli* strains deficient in the oxidative portion of the pentose phosphate pathway, 2′ and 4′ ^{1}H-^{13}C spin systems have been isolated rendering these ribose sugars suitable for ^{13}C NMR studies. Using ^{13}C spin relaxation measurements for rAMP solvated in D_8-glycerol samples to simulate various correlation times, it was demonstrated that magnetic interactions from

adjacent ^{13}C nuclei can be a source of error in R_1 measurements for molecules with long correlation times and in $R_{1\rho}$ measurements where coupled ^{13}C nuclei have similar effective fields. The alternate-site labeling scheme is a practical approach to removing these errors. Comprehensive analysis of ribose carbons for the tetraloop region of the GCAA RNA hairpin has been determined via the incorporation of ribonucleotides using the alternate-site labeling scheme. From the combined analysis of CPMG and $R_{1\rho}$ data measurements, timescales of ribose pucker transitions were observed for the dynamic tetraloop region. Exchange lifetimes for ribose carbons within the tetraloop were observed to be similar within error, indicative of concerted motions for multiple residues. Also, temperature dependent studies, activation energies for ribose pucker transitions were determined.

With the validation of the alternate site labeling scheme, preliminary studies have been performed for more biologically relevant RNA ribozymes, particularly the hairpin ribozyme. The methods reported in herein will open a new window into the analysis of conformational dynamics in RNA molecules and advance efforts to understand the correlation between dynamics and function in ribozymes and other RNA systems.

To my mother and father for many years of sacrifice so that I could have the opportunities I do now.

To my wife for her love and support so I could be the man I am today.

ACKNOWLEDGMENTS

I've never been eloquent with words, so the words here are insufficient to express my deep gratitude to so many people who have helped me get here. I want to thank Dr. Charles Hoogstraten for letting me join his lab and mentoring me all these years, even though I had no experience in the fields of NMR or RNA. His guidance has helped shape me into a budding scientist. I'm thankful for him seeing potential in me, even when I couldn't see it myself. I would like to thank my committee members Drs. John Wang, Bob Hausinger, Honggao Yan, and David Weliky for their critical analyses of my work so I could become a better scientist.

I would like to thank all past and present members of the Hoogstraten lab for a friendly and wonderful environment in which to work. I appreciate Mina trying to teach me kinetic principles while I tried to teach her NMR methods. I want to thank Kristy for not only being a fellow co-worker but a wonderful friend. I want to thank all of the friends I've made since joining the biochemistry department.

I want to thank my wife and family for all their love and support as I pursued my dreams, especially Prof., Papa, and Mother who passed on before they could see me accomplish this milestone.

TABLE OF CONTENTS

Images in this thesis are presented in color

LIST OF TABLES

LIST OF FIGURES

ABBREVIAITONS

4WJ	four-way junction
8BrG	8-bromo-guanosine
BPTI	basic pancreatic trypsin inhibitor
COSY	correlated spectroscopy
CPMG	Carr-Purcell-Meiboom-Gill
CSA	chemical shift anisotropy
DSS	sodium 2,2 dimethyl-2-silapentane-5-sulfonate
E. coli	*Escherichia coli*
FRET	fluorescence resonance energy transfer
hNOE	heteronuclear nuclear Overhauser enhancement
HSQC	heteronuclear single quantum coherence
LB	Luria-Bertani
LNA	locked nucleic acid
NMR	nuclear magnetic resonance
NOE	nuclear Overhauser enhancement
NOESY	nuclear Overhasuer enhancement spectroscopy
PPP	pentose phosphate pathway
R_1	longitudinal relaxation rate
$R_{1\rho}$	rotating-frame transverse relaxation rate
R_2	transverse relaxation rate

R5P	ribose-5-phosphate
rAMP	adenosine monophasphate
rcCPMG	relaxation compensated Carr-Purcell-Meiboom-Gill
RF	radio frequency
RNA	ribonucleic acid
rNMPs	ribonucleotide monophosphates
rNTPs	ribonucleotide triphosphates
S/N	signal to noise
sshNOE	steady-state heteronuclear nuclear Overhauser enhancement
T_1	longitudinal relaxation time
T_2	transverse relaxation time
TOCSY	total correlated spectroscopy

Chapter 1

Introduction

Discovery of Ribozymes. RNA molecules take part in essential roles in many cellular processes. Previously, RNA was thought to have a secondary role in the cell: a genetic translator in the form of messenger RNA, an amino acid chaperone in the form of transfer RNA, and a structural support for macromolecular complexes in the form of ribosomal RNA (1). However, the scientific community was forever changed in the early 1980s when the labs of Drs. Thomas Cech and Sydney Altman discovered the existence of catalytic RNAs, or ribozymes. Both labs were able to demonstrate that RNA alone performs chemistry without the aid of amino acid side chains from proteins (2,3). These findings have changed the way RNA is viewed in the cell and have sparked a revolution of RNA discoveries and uses. Different RNA systems have since been discovered to control gene expression including RNA riboswitches, microRNAs, and RNA interference in addition to ribozymes (4-7), demonstrating the diversity of RNA functions in the cell.

General Mechanism of Catalysis. Ribozymes have been found in various cellular functions such as viral replication, splicing of intronic genes, maturation of tRNA molecules (8), and there is evidence that the ribosome is a ribozyme (9). Examples of naturally occurring ribozymes are the hammerhead (10), hairpin (11), Hepatitis Delta virus (12), *Neurospora* Varkud satellite (13), group I (2) and II intron (14), and the RNA subunit of ribonuclease P (3). Most ribozymes catalyze phosphotransferase reactions along the phosphate backbone with mechanisms similar to ribonucleases (15,16) (Fig. 1.1). The active site architecture of ribozymes are positioned to deprotonate the nucleophile, stabilize

the charge build-up of the transition state, and protonate the leaving group. Metal ions have been implicated to participate in the catalytic mechanism similar to the amino acid side chain imidazoles in ribonuclease A (9). This is similar for ribozymes where metal ions have been implicated in assisting the catalytic mechanism in most cases. In special cases, such as the hairpin ribozyme, metal ions are not observed in the active site leading to the theory that the nucleobases take part as the primary role in catalysis (17,18). This theory is further supported from the crystal structure of the full-length hammerhead ribozyme where no metals were observed in the active site (19).

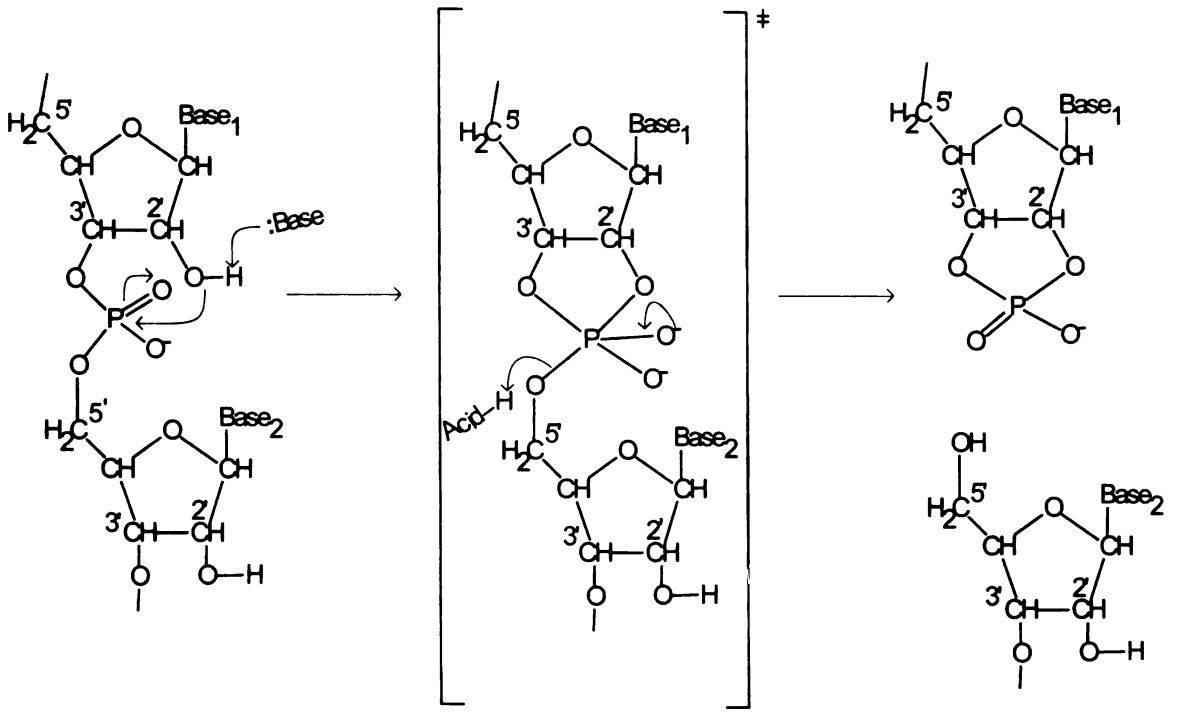

Figure 1.1: Proposed mechanisms for RNA strand scission catalyzed by ribozymes.

Evidence of Dynamics in RNA Systems. Conformational dynamics are well known to play an important role in the function of enzymes. Similarly, there is increasing evidence that conformational changes are crucial to ribozyme function. For example, active site architecture has been studied in minimal sequence hammerhead ribozyme through several crystal structures. Pley *et al.* (20) crystallized the hammerhead using a DNA inhibitor strand, while Scott *et al.* (21) crystallized the hammerhead using a 2′-O-methyl group in place of the reactive 2′-OH. The reactive 2′ oxygen was not observed in either structure within proper distance of the scissile phosphate for in-line nucleophilic attack. However, Klug and coworkers (22) crystallized unmodified hammerhead molecules with and without metal ions, using flash-freezing to capture the intermediate structure. Also, Dunham *et al.* (23) crystallized a hammerhead sequence with a phosphodiester linkage between stems I and II to mimic the pre-catalytic state. In this structure, the nucleophile was positioned very close to proper orientation; it was theorized that a sugar pucker transition could complete the alignment necessary for in-line nucleophilic attack. Comparison of all of the crystal structures suggests a model where the hammerhead undergoes a conformational change to position the reactive groups congruent with in-line nucleophilic attack. Recently, the crystal structure of the full length 63 nucleotide hammerhead ribozyme solved by Martick and Scott (19) with a 2′-O-methyl group revealed tertiary interactions that induce structural changes aligning the reactive ribose ring very close to the proper geometry for in-line nucleophilic attack.

Taken together, these results suggest that investigation of dynamics within the active site of ribozymes can be crucial to understand the catalytic mechanism.

Another ribozyme system where conformational change has been shown to contribute greatly to the catalytic mechanism is the hairpin ribozyme. The hairpin ribozyme is a RNA four-way helix junction (4WJ) where two helices A and B must interact for catalysis. While metal ions have been shown to facilitate proper RNA folding, they have not been directly linked to the catalytic mechanism. Ferre-D'Amare and co-workers (18) have crystallized several 4WJ hairpin constructs to investigate the catalytic site of the hairpin ribozyme. Using a 2'-O-methyl group in place of the reactive 2'-OH for A_{-1}, extensive conformational changes were observed, including the formation of a cross-stem Watson-Crick base pair for G_{+1} and C_{25}. The formation of this base pair constrains A_{-1} and G_{+1} into C2'-endo conformation aligning the proposed nucleophile and leaving group. The significance of sugar pucker was further elucidated in the comparison of transition state mimic hairpin crystals as well as wild type crystals (24). Superposition of the precursor, transition state mimic, and product constructs revealed a rigid active site were motion was confined to the scissile phosphate and ribose ring of A_{-1}, where a change in the sugar pucker was observed. Salter *et al.* (25) crystallized multiple analogs for G_8 using a 2'-O-methyl group in place of the reactive 2'-OH for A_{-1}. Removal of functional groups for G_8 was shown, in some cases, to alter the sugar pucker of A_{-1}. Along

with the hammerhead ribozyme, conformational changes appear to be critical to the reaction mechanism.

Experimental Methods to Probe Dynamics. Several methods have been used to study conformational changes of ribozymes. Turner and coworkers (26) used fluorescence detected stopped-flow methods to investigate binding of RNA oligomers to *Tetrahymena thermophila* ribozyme. Also, Burke and coworkers (27) have used fluorescence resonance energy transfer to study conformational changes such as loop-loop interaction for the hairpin ribozyme. One drawback to these methods is that investigation of the fluorophore can be insensitive to localized conformational changes that do not alter the global structure. To focus on more localized motions, incorporation of fluorescent nucleotide analogs can elucidate internal motions in nucleic acids. For example, the use of 2-aminopurine analogs has been used to probe structural changes through base extrusions for trans-activator responsive region hairpin of human immunodeficiency virus type 1 binding to ligands (28).

Nuclear magnetic resonance (NMR) spectroscopy is a powerful method to measure localized conformational changes. Using NMR techniques, each residue can be investigated, which can reveal localized motions throughout the molecule in a site-specific fashion. NMR methods can be used to investigate dynamics across a broad range of timescales. For ribozymes, different timescales may be important for catalysis. A possible model for the reaction mechanism of some ribozymes is presented in figure 1.2, where the ground state (E-S), which is not suitable for catalysis, proceeds to a pre-catalytic state (E-S*)

that more closely resembles the transition state before products (E-P) are formed. NMR spin relaxation studies can measure "fast" dynamics on the picosecond to nanosecond timescale, such as segmental motions. In addition, "slow" dynamics can be measured on the microsecond to millisecond timescale to investigate conformational changes between states. The use of NMR dynamic studies can be useful to help reveal how motions participate in catalysis.

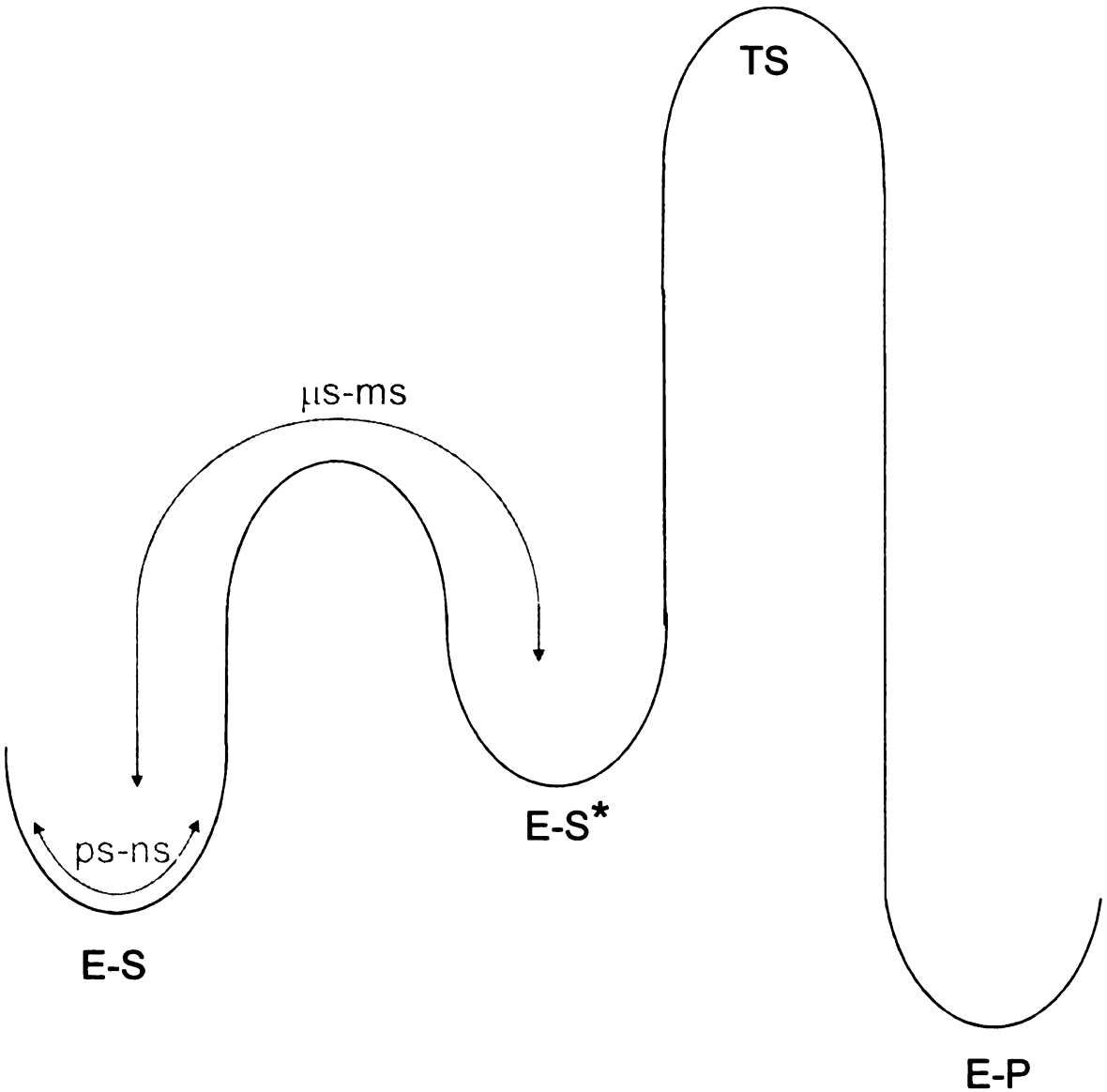

Figure 1.2: Reaction coordinate illustrating motional timescales best suited for NMR spin relaxation studies. E-S represents enzyme-substrate ground state complex, E-S* represent pre-catalytic state, TS represents transition state, and E-P represents enzyme-product complex. Figure was adapted from Hoogstraten and Sumita, "Structure-function relationships in RNA and RNP enzymes: recent advances" published in Biopolymers (2007) (29).

NMR Dynamic Studies. NMR spin relaxation experiments have been used to investigate dynamics of macromolecules, particularly longitudinal (T_1) and transverse (T_2) relaxation as well as heteronuclear nuclear Overhauser enhancement (hNOE) measurements. In an early study, Gurd and co-workers (30) employed natural abundance ^{13}C NMR T_1 measurements to investigate motions within ribonuclease A. Interestingly, multiple dynamics were observed for β- and ε-carbons. Glushko *et al.* (31) further analyzed segmental motions of ribonuclease A through pH studies. Investigating ^{13}C T_1 measurements with a pH range of 6.55 to 1.46, they were able to analyze not only segmental motions, but conformational changes due to protein denaturation. Roberts and coworkers (32) were perhaps one of the first groups to measure rotation correlation times from ^{15}N T_1 and hNOE measurements in not only proteins, but tRNA as well. For amide resonances of lysozyme, determination of motional parameters for amides of lysine groups was in excellent agreement with ^{13}C T_1 measurements of ε-carbons of lysine side chains. These results were significant because they demonstrate that NMR methods can be used to investigate fast internal motions within macromolecules. Also, ^{13}C and ^{15}N dynamic studies can report on similar motional modes. For example, Hawkes *et al.* (33) measured ^{13}C and ^{15}N T_1 measurements for gramicidin S. In short, a method was outlined to study internal dynamics of macromolecules that can differentiate local fluctuations from global

motions. Several groups used this approach to extract dynamic properties using ^{13}C and ^{15}N NMR spin relaxation measurements (34-38).

While early ^{13}C and ^{15}N spin relaxation measurements were valuable for determining local motional modes within macromolecules, these experiments suffered from limitations. All the previously mentioned works were obtained using one-dimensional direct ion detect spectroscopy of natural abundance ^{13}C and/or ^{15}N. ^{13}C has a natural abundance of 1% while ^{15}N has a natural abundance of just 0.4%. To offset this limitation, groups have used substantial sample concentrations, in excess of 20 mM for solution state NMR. This also leads to issues with sample solubility, which can severely limit studies of macromolecules. Another issue that hampered data analysis is spectral overlap. In most cases, one-dimensional ^{13}C and ^{15}N spectra had very few residues that were resolved from other residues. For example, Gurd and co-workers (30,31) measured effective correlation times for α-carbon envelopes as opposed to individual residues. In this case, individual residues with different rotational correlation times can be masked by global motions.

To offset this, heteronuclear two-dimensional spectroscopy experiments were developed (39,40). These pulse sequences are important because they provide enhanced sensitivity to nuclei with low gyromagnetic ratios as well as providing a second dimension of chemical shifts for decreased spectral overlap. Several groups have used these pulse sequences to measure T_1 values in

proteins (41-43). Nirmala and Wagner (43) developed a two-dimensional pulse sequence to measure ^{13}C T_1 values for nearly all α-carbons in basic pancreatic trypsin inhibitor (BPTI) at natural abundance. This result is significant because they were able to measure individual ^{13}C T_1 values for α-carbons as opposed to a bulk T_1 values. Indeed, ^{13}C T_1 measurements in the BPTI showed a high degree of variability. With the advances in spectrometer field strength combined with two-dimensional pulse sequences, the measurement of dynamics in macromolecules became more practical.

Relaxation of ^{13}C and ^{15}N nuclei in solution predominately arises from dipolar interaction from covalently bound protons. T_1, T_2, and hNOE depend on spectral density functions, which are Fourier transformations of the auto-correlation function for molecular motion (44). Richarz *et al.* (34) used ^{13}C T_1 and hNOE values to determine internal dynamics for ^{13}C carbons of BPTI. In this work, internal dynamics were interpreted using the wobbling in a cone model proposed by Kinosita *et al.* (45). From this model, information such as rotation about single bonds and diffusion of a rotation axis inside the cone can be determined. Other models can be used to determine internal dynamics within macromolecules (46,47). Likewise, Lipari and Szabo (48) were able to extract similar internal dynamic parameters for nucleic acid fragments using different models of internal motions. The models corresponded to different physical representations, but yielded the same numerical value of the order parameter.

Model-Free Formalism. Lipari and Szabo (49,50) developed a model-independent formalism to correlate dynamic properties to measured relaxation rates. In this "model-free" approach, fast internal motions can be described by a generalized order parameter, S^2, which is the measure of the degree of spatial restriction of the motion, and an effective correlation time, τ_e, which is a measure of the rate of the motion for a given nucleus. This formalism removes the ambiguity of internal dynamics interpretation. The model-free formalism has been validated over a wide range of motions, including for anisotropic rotations where the overall motion cannot be described by a single correlation time.

Because motional parameters describing fast motion can be determined in an independent fashion, the model free approach has been widely accepted to investigate internal dynamics using NMR. Early use of the model-free approach was done by Bax and co-workers (51), where internal dynamics for amides of ^{15}N uniformly enriched staphylococcal nuclease were investigated at several field strengths using ^{15}N T_1, T_2 and hNOE measurements. Pulse sequences were developed to accurately measure T_1, T_2, and hNOE data. Staphylococcal nuclease exhibited a uniform structure with similar S^2 for nearly all amide resonances measured, an average value of 0.86 for S^2. Some N- and C-terminal residues were shown to have significant disorder as well as effective correlation times. In particular, the C-terminal residue Gly-148 was reported to have a S^2 and τ_e of 0.23 and 120 ps, respectively (51). In addition to interpreting fast

motions, investigations of slow motions were performed. Transverse relaxation measurements are sensitive chemical or conformational exchange on the microsecond to millisecond timescale. In staphylococcal nuclease, Glu-52 and Lys-53 exhibited $1/T_2$ values 2.5 times larger than the average $1/T_2$ values (51), indicative of conformational motions on the μs to ms timescale. This is plausible because these residues are located within a flexible region of the molecule (52). Interestingly, T_1 values measured for these residues are similar to T_1 values measured for nearly all residues. Taken together, these results were significant to the field of NMR spectroscopy because the validity of using NMR spin relaxation studies to probe internal motions across a broad range of timescales were demonstrated.

Torchia and co-workers (53) extended interpretation of internal dynamics to ^{13}C methyl groups of leucine residues. In this approach, internal dynamics were determined from an extension to the Lipari-Szabo formalism by Clore *et al.* (54). The approach by Clore *et al.* was developed to include "slow" motions that are an order of magnitude larger than effective correlation times, yet still faster than the overall isotropic correlation time. Using this extended model free approach, Torchia *et al.* were able to separate order parameters of leucine ^{13}C methyl carbons into flexible and rigid groups (53). The rigid ^{13}C carbons S^2_s (see next paragraph) values were found to be similar to S^2 values for backbone ^{15}N amide resonances using the standard model free approach. This result is

useful because it demonstrates the presence of dynamics of side chains in addition to backbone nuclei.

Previously, exchange contributions were determined from comparisons of R_2 ($1/T_2$) values. Wright and co-workers integrated exchange contributions on the μs to ms timescale that contribute to the overall transverse relaxation mechanism into the model-free analysis using the term R_{ex}, the contribution to the observed transverse relaxation rate due to exchange (55,56). Analysis of internal motions using the extended model-free formalism can be daunting due to the numerous motional parameters. Palmer and co-workers (57) have developed the user-friendly ModelFree computer program that aids in the selection of motional parameters that best represents the data. Using this program, five different conditions of molecular motions were utilized to best fit the experimental data, which includes isotropic and anisotropic conditions. Palmer and co-workers (57) were able to investigate dynamics across a broad range of motional timescales. For example, complex dynamics were discovered within a flexible region of *E. coli* ribonuclease HI where internal motions of nuclei in this region could be described using all conditions possible (57).

Relaxation Dispersion. The analysis of fast dynamics has been well documented using the model-free formalism. However, dynamics on the μs-ms timescale are not well determined using this approach. Many biological processes such as catalysis, protein folding, and allosteric transitions occur on these timescales (58). Using the model-free approach, chemical or conformational changes that affect the measured chemical shift are described

with the term, R_{ex}. A more definitive description of the R_{ex} term can done by investigating the transverse relaxation rate as a function of effective field strength. In early work of this type, Luz and Meiboom previously utilized spin echo delays to determine proton transfer between trimethylammonium ion and trimethylamine in solution using Carr-Purcell-Meiboom-Gill (CPMG) pulse scheme (59). In this work, it was derived that transverse relaxation rates in the presence of chemical or conformational exchange depend on the average lifetime of exchange for a nuclei, pulse repetition rate, fractional populations of exchanging states, and chemical shift difference between states. Similar derivations were made for the rotating frame $R_{1\rho}$ pulse scheme (60,61) where magnetization is spin-locked in the rotating frame by the application of a radio frequency field. Again, transverse $R_{1\rho}$ measurements in the presence of exchange varies as a function of the spin-lock power deposition, lifetime of exchange for the nuclei, fractional population of n sites, and chemical shift difference between sites. Arseniev and co-workers (62) applied a ^{15}N spin-echo modulated CPMG pulse sequence to investigate μs-ms motions for amides in bacterioopsin. In this work, all exchange lifetimes for backbone amides excluding N and C termini were determined to within error of each other, leading to a model where cooperative motion was occurring for the α-helices. It was interpreted that the R_{ex} contribution was due to helix-helix interaction whereby the helices exhibit slight shifting along each other, changing the tilt or bend.

Exchange contributions have also been determined using power-dependent $R_{1\rho}$ experiments. Using spin-echo modulated CPMG and/or power-dependent $R_{1\rho}$ experiments, dynamics on the μs-ms timescale can be probed.

NMR Dynamic Studies of RNA Molecules. Dynamics of proteins have been studied extensively using the model-free formalism (55,56,63-72). By contrast, the investigation of dynamics of nucleic acids using the model free approach has only been done for a few cases (73-81). Spielmann (73) investigated natural abundance aromatic and deoxyribose dynamics in a DNA oligomer and DNA oligomer complexed with a dye. Using the extended model free analysis, extensive dynamics were observed in the un-liganded DNA oligomer including average S^2 values of 0.79 and several residues exhibiting R_{ex} contributions. Upon binding the dye, previously observed dynamics were quenched or reduced indicative of the DNA oligomer becoming more structured. Hall and Tang (75) investigated temperature-dependent dynamics for purine bases in the iron responsive element RNA hairpin also using the model-free approach. At 20 °C, order parameters obtained varied little among resonances throughout the molecule, supporting the NMR structure where loop residues were stacked and structured similar to stem residues. As the temperature increased, a reduction in structure was observed for the loop residues while the stem residues maintained their structure similar to that observed at 20 °C. From these works as well as others, internal dynamics can be investigated in nucleic acids to probe motional modes of nucleic acids.

Spin-echo modulated CPMG (82-91) and power-dependent $R_{1\rho}$ experiments (92-98) have been implemented even less in nucleic acids (76,99-102). Hoogstraten *et al.* (99) investigated ^{13}C aromatic dynamics in the lead-dependent ribozyme. Using power-dependent $R_{1\rho}$ experiments, several exchange lifetimes on the microsecond regime were observed, including exchange lifetimes for C2 and C8 nuclei of A_{25}. The exchange lifetimes determined from $R_{1\rho}$ experiments were very similar to exchange lifetimes for protonation of A_{25} N1 determined by line-shape analysis (103). These results show the usefulness of obtaining motional parameters in RNA molecules. A_{25} is cross-strand from the catalytic residue, C_6 (see chapter 4). It was hypothesized that dynamics observed at this residue was indicative of base flipping for C_6. Blad *et al.* (100) also obtained motional parameters from power-dependent $R_{1\rho}$ experiments for base as well as C1′ sugar atoms in the U6 RNA intramolecular stem–loop (see figure 1.3 for numbering). This work was unique in the measurement of exchange lifetimes for the sugar atom C1′. By obtaining multiple motional parameters for the base and sugar moiety of a residue, correlated motions can be investigated. Indeed, Blad *et al.* (100) were able to fit $R_{1\rho}$ data to a single nucleotide exchange lifetime for C1′ and base atoms of four residues in the RNA oligomer. Interestingly, all exchange lifetimes measured were similar within error. These residues were found throughout the oligomer and not

localized to a particular region. It was hypothesized that these residues were reporting on a single global conformational rearrangement within the U6 RNA by determining motional parameters using a global exchange lifetime of 84 μs (100). Taken together, μs to ms motions can be determined in nucleic acids to probe not only localized motions, but global conformational fluctuations as well.

Limitation of NMR Studies in RNA Molecules. Both ^{13}C and ^{15}N nuclei have been used to analyze motions in proteins. Nucleic acids have relatively few protonated ^{15}N nuclei for analysis similar to proteins (104), since ^{15}N nuclei can only be found in the aromatic bases of nucleic acids. Because of this, ^{15}N dynamic studies are restricted to the aromatic ring in RNA molecules. However, there are protonated carbons located in both the aromatic base and significantly in the ribose ring (Fig. 1.3). Unfortunately, the structure of the ribose ring leads to ^{13}C-^{13}C interactions, which can lead to difficulty in unambiguously understanding relaxation mechanisms in uniformly ^{13}C enriched nucleotides (105). To offset this limitation, groups employed several methods to obtain isolated ^{1}H-^{13}C spin systems for accurate measurements including acquiring relaxation measurements at natural isotopic abundance (73,106) and using low levels of partial ^{13}C fractional enrichment (74,107). While these experiments remove unwanted ^{13}C-^{13}C interaction, they suffer severe sensitivity loss. Other ways to highly enrich ^{13}C sites are the use of chemical synthesis to specifically

prepare the ribose ring of nucleic acids (108-110). However, this approach can be laborious and time consuming. While information about RNA dynamics has been obtained for ^{13}C base resonances (75,111), little information has been obtained for ^{13}C ribose resonances. In cases where ribose dynamics has been obtained, analysis has been limited to C1′ and/or C5′ resonances (76,79,100,108). As seen earlier, measured ^{15}N amide backbone dynamics of BPTI showed a high degree of similarity with several ^{13}C methyl groups while some differed, revealing a case where dynamics are highly localized (53). It is possible that nucleic acids could display a similar trend where significant base dynamics can be observed while little to no dynamics are discerned for the ribose ring, or vice versa. To circumvent these issues, extension of NMR dynamics studies to the ribose ring is needed.

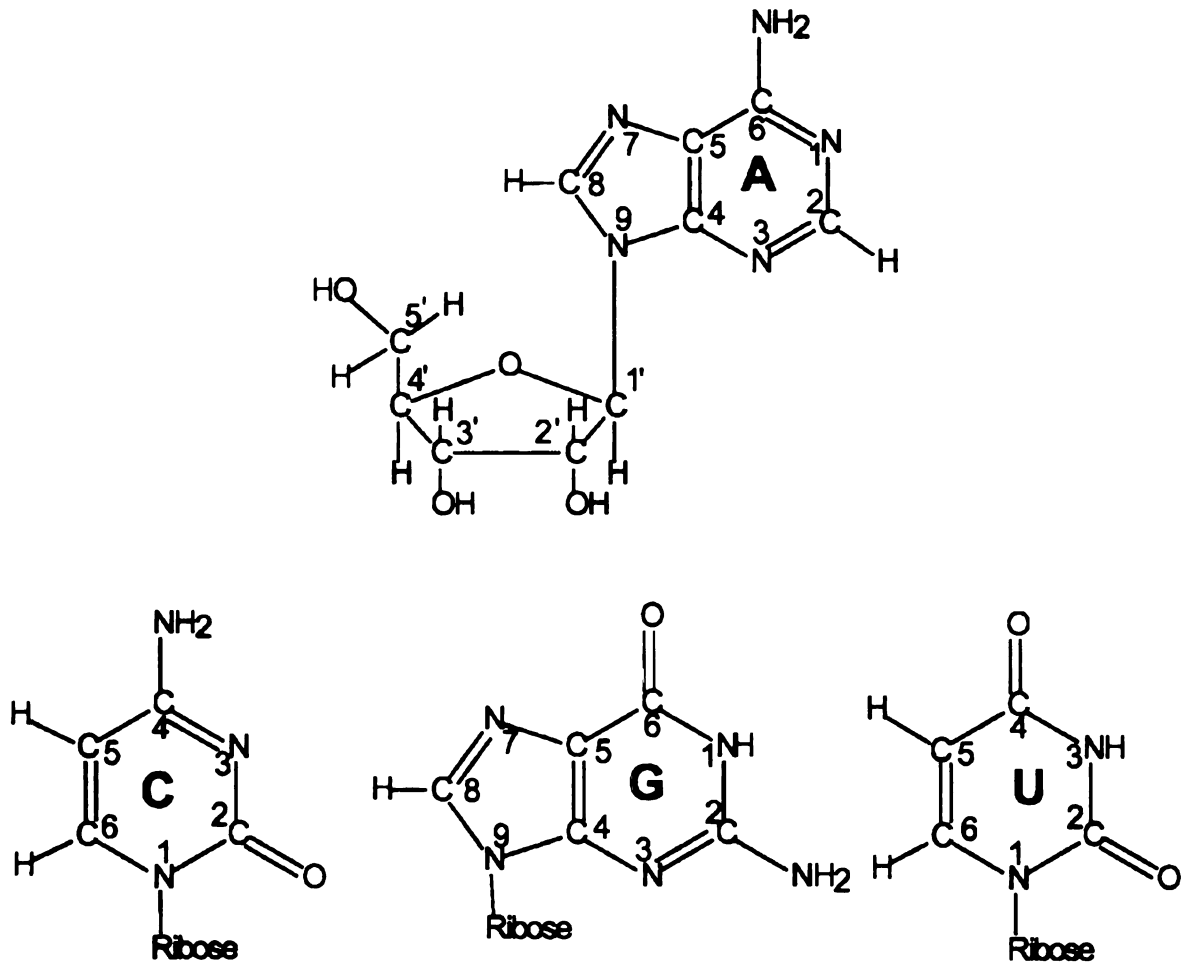

Figure 1.3: Structure of the nucleic acid base and sugar ring for ribonucleosides. **A**denosine, **C**ytidine, **G**uanosine, and **U**ridine ribonucleosides are shown where carbon nuclei accessible to NMR relaxation studies are highlighted in red.

The goal of this thesis is to investigate dynamics in RNA systems using sophisticated ^{13}C NMR spin relaxation experiments. In chapter 2, methods are presented to specifically ^{13}C label the ribose ring of ribonucleotides, including an alternating ^{13}C-^{12}C isotope labeling scheme, rendering the ribose ring suitable for ^{13}C NMR spin relaxation studies. R_1 and $R_{1\rho}$ data acquired for specific labeled ribose is compared to uniformly labeled ribose to investigate the effect of ^{13}C-^{13}C interactions. In chapter 3, extensive analyses of ribose dynamics are presented for the GCAA RNA hairpin using the specific labeling scheme. Analyses of multiple timescales are included through the use of the model-free formalism and combined spin-echo modulated CPMG and $R_{1\rho}$ measurements. In chapter 4, preliminary analysis of ribose dynamics within the active site of the lead-dependent ribozyme is presented with ^{13}C specific labeled cytidine incorporation. In chapter 5, preliminary ^{1}H, ^{13}C, and ^{15}N chemical shift assignments are reported for wild type and mutant domain A of the hairpin ribozyme. In chapter 6, general conclusions are made and possible directions for future research are outlined.

REFERENCES

1. Bloomfield, V.A., Crothers, D.M. and Tinoco, I., Jr. (2000) *Nucleic Acids: Structures, Properties, and Functions*. University Science Books, Sausalito, California, USA.

2. Kruger, K., Grabowski, P.J., Zaug, A.J., Sands, J., Gottschling, D.E. and Cech, T.R. (1982) Self-splicing RNA: autoexcision and autocyclization of the ribosomal RNA intervening sequence of Tetrahymena. *Cell*, **31**, 147-157.

3. Guerrier-Takada, C., Gardiner, K., Marsh, T., Pace, N. and Altman, S. (1983) The RNA moiety of ribonuclease P is the catalytic subunit of the enzyme. *Cell*, **35**, 849-857.

4. Montange, R.K. and Batey, R.T. (2008) Riboswitches: emerging themes in RNA structure and function. *Annu Rev Biophys*, **37**, 117-133.

5. Dykxhoorn, D.M. and Lieberman, J. (2005) The silent revolution: RNA interference as basic biology, research tool, and therapeutic. *Annu Rev Med*, **56**, 401-423.

6. Bushati, N. and Cohen, S.M. (2007) microRNA functions. *Annu Rev Cell Dev Biol*, **23**, 175-205.

7. Khan, A.U. and Lal, S.K. (2003) Ribozymes: a modern tool in medicine. *J Biomed Sci*, **10**, 457-467.

8. Kuimelis, R.G. and McLaughlin, L.W. (1998) Mechanisms of ribozyme-mediated RNA cleavage. *Chem Rev*, **98**, 1027-1044.

9. DeRose, V.J. (2002) Two decades of RNA catalysis. *Chem Biol*, **9**, 961-969.

10. Symons, R.H. (1997) Plant pathogenic RNAs and RNA catalysis. *Nucleic Acids Res*, **25**, 2683-2689.

11. Hampel, A. and Tritz, R. (1989) RNA catalytic properties of the minimum (-)sTRSV sequence. *Biochemistry*, **28**, 4929-4933.

12. Thill, G., Vasseur, M. and Tanner, N.K. (1993) Structural and sequence elements required for the self-cleaving activity of the hepatitis delta virus ribozyme. *Biochemistry*, **32**, 4254-4262.

13. Saville, B.J. and Collins, R.A. (1990) A site-specific self-cleavage reaction performed by a novel RNA in Neurospora mitochondria. *Cell*, **61**, 685-696.

14. Peebles, C.L., Perlman, P.S., Mecklenburg, K.L., Petrillo, M.L., Tabor, J.H., Jarrell, K.A. and Cheng, H.L. (1986) A self-splicing RNA excises an intron lariat. *Cell*, **44**, 213-223.

15. Roberts, G.C., Dennis, E.A., Meadows, D.H., Cohen, J.S. and Jardetzky, O. (1969) The mechanism of action of ribonuclease. *Proc Natl Acad Sci U S A*, **62**, 1151-1158.

16. Doudna, J.A. and Lorsch, J.R. (2005) Ribozyme catalysis: not different, just worse. *Nat Struct Mol Biol*, **12**, 395-402.

17. Donahue, C.P., Yadava, R.S., Nesbitt, S.M. and Fedor, M.J. (2000) The kinetic mechanism of the hairpin ribozyme *in vivo*: influence of RNA helix stability on intracellular cleavage kinetics. *J Mol Biol*, **295**, 693-707.

18. Rupert, P.B. and Ferre-D'Amare, A.R. (2001) Crystal structure of a hairpin ribozyme-inhibitor complex with implications for catalysis. *Nature*, **410**, 780-786.

19. Martick, M. and Scott, W.G. (2006) Tertiary contacts distant from the active site prime a ribozyme for catalysis. *Cell*, **126**, 309-320.

20. Pley, H.W., Flaherty, K.M. and McKay, D.B. (1994) Three-dimensional structure of a hammerhead ribozyme. *Nature*, **372**, 68-74.

21. Scott, W.G., Finch, J.T. and Klug, A. (1995) The crystal structure of an all-RNA hammerhead ribozyme: a proposed mechanism for RNA catalytic cleavage. *Cell*, **81**, 991-1002.

22. Scott, W.G., Murray, J.B., Arnold, J.R., Stoddard, B.L. and Klug, A. (1996) Capturing the structure of a catalytic RNA intermediate: the hammerhead ribozyme. *Science*, **274**, 2065-2069.

23. Dunham, C.M., Murray, J.B. and Scott, W.G. (2003) A helical twist-induced conformational switch activates cleavage in the hammerhead ribozyme. *J Mol Biol*, **332**, 327-336.

24. Rupert, P.B., Massey, A.P., Sigurdsson, S.T. and Ferre-D'Amare, A.R. (2002) Transition state stabilization by a catalytic RNA. *Science*, **298**, 1421-1424.

25. Salter, J., Krucinska, J., Alam, S., Grum-Tokars, V. and Wedekind, J.E. (2006) Water in the active site of an all-RNA hairpin ribozyme and effects of Gua8 base variants on the geometry of phosphoryl transfer. *Biochemistry*, **45**, 686-700.

26. Bevilacqua, P.C., Kierzek, R., Johnson, K.A. and Turner, D.H. (1992) Dynamics of ribozyme binding of substrate revealed by fluorescence-detected stopped-flow methods. *Science*, **258**, 1355-1358.

27. Walter, N.G., Hampel, K.J., Brown, K.M. and Burke, J.M. (1998) Tertiary structure formation in the hairpin ribozyme monitored by fluorescence resonance energy transfer. *EMBO J*, **17**, 2378-2391.

28. Bradrick, T.D. and Marino, J.P. (2004) Ligand-induced changes in 2-aminopurine fluorescence as a probe for small molecule binding to HIV-1 TAR RNA. *RNA*, **10**, 1459-1468.

29. Hoogstraten, C.G. and Sumita, M. (2007) Structure-function relationships in RNA and RNP enzymes: recent advances. *Biopolymers*, **87**, 317-328.

30. Allerhand, A., Doddrell, D., Glushko, V., Cochran, D.W., Wenkert, E., Lawson, P.J. and Gurd, F.R.N. (1971) Conformation and segmental motion of native and denatured ribonuclease A in solution. Application of natural-abundance carbon-13 partially relaxed Fourier transform nuclear magnetic resonance. *J Am Chem Soc*, **93**, 544-546.

31. Glushko, V., Lawson, P.J. and Gurd, F.R. (1972) Conformational states of bovine pancreatic ribonuclease A observed by normal and partially

relaxed carbon 13 nuclear magnetic resonance. *J Biol Chem*, **247**, 3176-3185.

32. Gust, D., Moon, R.B. and Roberts, J.D. (1975) Applications of natural-abundance nitrogen-15 nuclear magnetic resonance to large biochemically important molecules. *Proc Natl Acad Sci U S A*, **72**, 4696-4700.

33. Hawkes, G.E., Randall, E.W. and Bradley, C.H. (1975) Theory and practice for studies for peptides by ^{15}N nuclear magnetic resonance at natural abundance: gramicidin S. *Nature*, **257**, 767-772.

34. Richarz, R., Nagayama, K. and Wuthrich, K. (1980) Carbon-13 nuclear magnetic resonance relaxation studies ofinternal mobility of the polypeptide chain in basic pancreatic trypsininhibitor and a selectively reduced analogue *Biochemistry*, **19**, 5189-5196.

35. Fuson, M.M. and Prestegard, J.H. (1983) Dynamics of an interfacial methylene in dimyristoylphosphatidylcholine vesicles using carbon-13 spin relaxation. *Biochemistry*, **22**, 1311-1316.

36. Henry, G.D., Weiner, J.H. and Sykes, B.D. (1986) Backbone dynamics of a model membrane protein: ^{13}C NMR spectroscopy of alanine methyl groups in detergent-solubilized M13 coat protein. *Biochemistry*, **25**, 590-598.

37. Smith, G.M., Yu, L.P. and Domingues, D.J. (1987) Directly observed 15N NMR spectra of uniformly enriched proteins. *Biochemistry*, **26**, 2202-2207.

38. Dellwo, M.J. and Wand, A.J. (1989) Model-independent and model-dependent analysis of the global and internal dynamics of cyclosporin A. *J Am Chem Soc*, **111**, 4571-4578.

39. Morris, G. and Freeman, R. (1979) Enhancement of nuclear magnetic resonance signals by polarization transfer. *J Am Chem Soc*, **101**, 760-762.

40. Freeman, R., Mareci, T.H. and Morris, G.A. (1981) Weak satellite signals in high-resolution NMR spectra: Separating the wheat from the chaff. *J Magn Reson*, **42**, 341-345.

41. Kay, L.E., Jue, T.L., Bangerter, B. and Demou, P.C. (1987) Sensitivity enhancement of ^{13}C T_1 measurements via polarization transfer. *J Magn Reson*, **73**, 558-564.

42. Sklenar, V., Torchia, D.A. and Bax, A. (1987) Measurement of carbon-13 longitudinal relaxation using ^{1}H detection. *J Magn Reson*, **73**, 375-379.

43. Nirmala, N.R. and Wagner, G. (1988) Measurement of ^{13}C relaxation times in proteins by two-dimensional heteronuclear ^{1}H-^{13}C correlation spectroscopy. *J Am Chem Soc*, **110**, 7557-7558.

44. Abragam, A. (1961) *Principles of Nuclear Magnetism*. Oxford University Press, USA.

45. Kinosita, K., Jr., Kawato, S. and Ikegami, A. (1977) A theory of fluorescence polarization decay in membranes *Biophys. J.*, **20**, 289-305.

46. Wittebort, R.J. and Szabo, A. (1978) Theory of NMR relaxation in macromolecules: Restricted diffusion and jump models for multiple internal rotations in amino acid side chains. *J Chem Phys*, **69**, 1722-1736

47. Woessner, D.E. (1962) Spin relaxation processes in a two-proton system undergoing anisotropic reorientation *J Chem Phys*, **36**, 1-4.

48. Lipari, G. and Szabo, A. (1981) Nuclear magnetic resonance relaxation in nucleic acid fragments: models for internal motion. *Biochemistry*, **20**, 6250-6256.

49. Lipari, G. and Szabo, A. (1982) Model-free approach to the interpretation of nuclear magnetic resonance relaxation in macromolecules. 1. theory and range of validity. *J Am Chem Soc*, **104**, 4546-4559.

50. Lipari, G. and Szabo, A. (1982) Model-free approach to the interpretation of nuclear magnetic resonance relaxation in macromolecules. 2. analysis of experimental results. *J Am Chem Soc*, **104**, 4559-4570.

51. Kay, L.E., Torchia, D.A. and Bax, A. (1989) Backbone dynamics of proteins as studied by ^{15}N inverse detected heteronuclear NMR spectroscopy: application to staphylococcal nuclease. *Biochemistry*, **28**, 8972-8979.

52. Torchia, D.A., Sparks, S.W. and Bax, A. (1989) Staphylococcal nuclease: sequential assignments and solution structure. *Biochemistry*, **28**, 5509-5524.

53. Nicholson, L.K., Kay, L.E., Baldisseri, D.M., Arango, J., Young, P.E., Bax, A. and Torchia, D.A. (1992) Dynamics of methyl groups in proteins as studied by proton-detected ^{13}C NMR spectroscopy. Application to the leucine residues of staphylococcal nuclease. *Biochemistry*, **31**, 5253-5263.

54. Clore, G.M., Szabo, A., Bax, A., Kay, L.E., Driscoll, P.C. and Gronenborn, A.M. (1990) Deviations from the simple two-parameter model-free approach to the interpretation of nitrogen-15 nuclear magnetic relaxation of proteins. *J Am Chem Soc*, **112**.

55. Palmer, A.G., 3rd, Rance, M. and Wright, P.E. (1991) Intramolecular motions of a zinc finger DNA-binding domain from Xfin characterized by proton-detected natural abundance carbon-13 heteronuclear NMR spectroscopy. *J Am Chem Soc*, **113**, 4371-4380.

56. Stone, M.J., Fairbrother, W.J., Palmer, A.G., 3rd, Reizer, J., Saier, M.H., Jr. and Wright, P.E. (1992) Backbone dynamics of the *Bacillus subtilis* glucose permease IIA domain determined from ^{15}N NMR relaxation measurements. *Biochemistry*, **31**, 4394-4406.

57. Mandel, A.M., Akke, M. and Palmer, A.G., 3rd. (1995) Backbone dynamics of *Escherichia coli* ribonuclease HI: correlations with structure and function in an active enzyme. *J Mol Biol*, **246**, 144-163.

58. Palmer, A.G., 3rd, Kroenke, C.D. and Loria, J.P. (2001) Nuclear magnetic resonance methods for quantifying microsecond-to-millisecond motions in biological macromolecules. *Methods Enzymol*, **339**, 204-238.

59. Luz, Z. and Meiboom, S. (1963) Nuclear magnetic resonance study of the protolysis of trimethylammonium ion in aqueous solution - order of the reacton with respect to solvent. *J Chem Phys*, **39**, 366-370.

60. Jones, G.P., Douglass, D.C. and McCall, D.W. (1965) Apparatus for the detection of ultraslow atomic motion by magnetic resonance techniques *Rev Sci Instrum*, **36**, 1460-1465.

61. Douglass, D.C. and Jones, G.P. (1966) Nuclear magnetic relaxation of *n*-alkanes in the rotating frame. *J Chem Phys*, **45**, 956-963

62. Orekhov, V., Pervushin, K.V. and Arseniev, A.S. (1994) Backbone dynamics of (1-71)bacterioopsin studied by two-dimensional ^{1}H-^{15}N NMR spectroscopy. *Eur J Biochem*, **219**, 887-896.

63. Akke, M., Skelton, N.J., Kordel, J., Palmer, A.G., 3rd and Chazin, W.J. (1993) Effects of ion binding on the backbone dynamics of calbindin D9k determined by ^{15}N NMR relaxation. *Biochemistry*, **32**, 9832-9844.

64. Powers, R., Clore, G.M., Stahl, S.J., Wingfield, P.T. and Gronenborn, A. (1992) Analysis of the backbone dynamics of the ribonuclease H domain of the human immunodeficiency virus reverse transcriptase using ^{15}N relaxation measurements. *Biochemistry*, **31**, 9150-9157.

65. Kordel, J., Skelton, N.J., Akke, M., Palmer, A.G., 3rd and Chazin, W.J. (1992) Backbone dynamics of calcium-loaded calbindin D9k studied by two-dimensional proton-detected ^{15}N NMR spectroscopy. *Biochemistry*, **31**, 4856-4866.

66. Palmer, A.G., 3rd, Hochstrasser, R.A., Millar, D.P., Rance, M. and Wright, P.E. (1993) Characterization of amino acid side chain dynamics in a zinc-finger peptide using carbon-13 NMR spectroscopy and time-resolved fluorescence spectroscopy. *J Am Chem Soc*, **115**, 6333-6345.

67. Stone, M.J., Chandrasekhar, K., Holmgren, A., Wright, P.E. and Dyson, H.J. (1993) Comparison of backbone and tryptophan side-chain dynamics of reduced and oxidized *Escherichia coli* thioredoxin using ^{15}N NMR relaxation measurements. *Biochemistry*, **32**, 426-435.

68. Mandel, A.M., Akke, M. and Palmer, A.G., 3rd. (1996) Dynamics of ribonuclease H: temperature dependence of motions on multiple time scales. *Biochemistry*, **35**, 16009-16023.

69. Wikstrom, M., Forsen, S. and Drakenberg, T. (1996) Backbone dynamics of a domain of protein L which binds to immunoglobulin light chains. *Eur J Biochem*, **235**, 543-548.

70. Zhou, H., McEvoy, M.M., Lowry, D.F., Swanson, R.V., Simon, M.I. and Dahlquist, F.W. (1996) Phosphotransfer and CheY-binding domains of the histidine autokinase CheA are joined by a flexible linker. *Biochemistry*, **35**, 433-443.

71. Palmer, A.G., 3rd, Williams, J. and McDermott, A. (1996) Nuclear magnetic resonance studies of biopolymer dynamics. *J Phys Chem*, **100**, 13293-13310.

72. Vugmeyster, L., Trott, O., McKnight, C.J., Raleigh, D.P. and Palmer, A.G., 3rd. (2002) Temperature-dependent dynamics of the villin headpiece helical subdomain, an unusually small thermostable protein. *J Mol Biol*, **320**, 841-854.

73. Spielmann, H.P. (1998) Dynamics of a bis-intercalator DNA complex by ^{1}H-detected natural abundance ^{13}C NMR spectroscopy. *Biochemistry*, **37**, 16863-16876.

74. Kojima, C., Ono, A., Kainosho, M. and James, T.L. (1998) DNA duplex dynamics: NMR relaxation studies of a decamer with uniformly ^{13}C-labeled purine nucleotides. *J Magn Reson*, **135**, 310-333.

75. Hall, K.B. and Tang, C. (1998) ^{13}C relaxation and dynamics of the purine bases in the iron responsive element RNA hairpin. *Biochemistry*, **37**, 9323-9332.

76. Shajani, Z. and Varani, G. (2005) ^{13}C NMR relaxation studies of RNA base and ribose nuclei reveal a complex pattern of motions in the RNA binding site for human U1A protein. *J Mol Biol*, **349**, 699-715.

77. Shajani, Z., Drobny, G. and Varani, G. (2007) Binding of U1A protein changes RNA dynamics as observed by ^{13}C NMR relaxation studies. *Biochemistry*, **46**, 5875-5883.

78. Duchardt, E. and Schwalbe, H. (2005) Residue specific ribose and nucleobase dynamics of the cUUCGg RNA tetraloop motif by NMR ^{13}C relaxation. *J Biomol NMR*, **32**, 295-308.

79. Trantirek, L., Caha, E., Kaderavek, P. and Fiala, R. (2007) NMR ^{13}C-relaxation study of base and sugar dynamics in GCAA RNA hairpin tetraloop. *J Biomol Struct Dyn*, **25**, 243-252.

80. Hansen, A.L. and Al-Hashimi, H.M. (2007) Dynamics of large elongated RNA by NMR carbon relaxation. *J Am Chem Soc*, **129**, 16072-16082.

81. Ferner, J., Villa, A., Duchardt, E., Widjajakusuma, E., Wohnert, J., Stock, G. and Schwalbe, H. (2008) NMR and MD studies of the temperature-dependent dynamics of RNA YNMG-tetraloops. *Nucleic Acids Res*, **36**, 1928-1940.

82. Loria, J.P., Rance, M. and Palmer, A.G. (1999) A relaxation-compensated Carr-Purcell-Meiboom-Gill sequence for characterizing chemical exchange by NMR spectroscopy. *J Am Chem Soc*, **121**, 2331-2332.

83. Millet, O., Loria, J.P., Kroenke, C.D., Pons, M. and Palmer, A.G., 3rd. (2000) The static magnetic field dependence of chemical exchange linebroadening defines the NMR chemical shift time scale. *J Am Chem Soc*, **122**, 2867-2877.

84. Mulder, F.A., Hon, B., Muhandiram, D.R., Dahlquist, F.W. and Kay, L.E. (2000) Flexibility and ligand exchange in a buried cavity mutant of T4 lysozyme studied by multinuclear NMR. *Biochemistry*, **39**, 12614-12622.

85. Mulder, F.A., Mittermaier, A., Hon, B., Dahlquist, F.W. and Kay, L.E. (2001) Studying excited states of proteins by NMR spectroscopy. *Nat Struct Biol*, **8**, 932-935.

86. Tollinger, M., Skrynnikov, N.R., Mulder, F.A., Forman-Kay, J.D. and Kay, L.E. (2001) Slow dynamics in folded and unfolded states of an SH3 domain. *J Am Chem Soc*, **123**, 11341-11352.

87. Cole, R. and Loria, J.P. (2002) Evidence for flexibility in the function of ribonuclease A. *Biochemistry*, **41**, 6072-6081.

88. Kovrigin, E.L., Cole, R. and Loria, J.P. (2003) Temperature dependence of the backbone dynamics of ribonuclease A in the ground state and bound to the inhibitor 5'-phosphothymidine (3'-5')pyrophosphate adenosine 3'-phosphate. *Biochemistry*, **42**, 5279-5291.

89. Korzhnev, D.M., Bezsonova, I., Evanics, F., Taulier, N., Zhou, Z., Bai, Y., Chalikian, T.V., Prosser, R.S. and Kay, L.E. (2006) Probing the transition state ensemble of a protein folding reaction by pressure-dependent NMR relaxation dispersion. *J Am Chem Soc*, **128**, 5262-5269.

90. Korzhnev, D.M., Salvatella, X., Vendruscolo, M., Di Nardo, A.A., Davidson, A.R., Dobson, C.M. and Kay, L.E. (2004) Low-populated folding intermediates of Fyn SH3 characterized by relaxation dispersion NMR. *Nature*, **430**, 586-590.

91. Butterwick, J.A., Patrick Loria, J., Astrof, N.S., Kroenke, C.D., Cole, R., Rance, M. and Palmer, A.G., 3rd. (2004) Multiple time scale backbone dynamics of homologous thermophilic and mesophilic ribonuclease HI enzymes. *J Mol Biol*, **339**, 855-871.

92. Vugmeyster, L., Kroenke, C.D., Picart, F., Palmer, A.G., 3rd and Raleigh, D.P. (2000) ^{15}N $R_{1\rho}$ measurements allow the determination of ultrafast protein folding rates. *J Am Chem Soc*, **122**, 5387-5388.

93. Korzhnev, D.M., Orekhov, V.Y., Dahlquist, F.W. and Kay, L.E. (2003) Off-resonance $R_{1\rho}$ relaxation outside of the fast exchange limit: an experimental study of a cavity mutant of T4 lysozyme. *J Biomol NMR*, **26**, 39-48.

94. Kim, S. and Baum, J. (2004) An on/off resonance rotating frame relaxation experiment to monitor millisecond to microsecond timescale dynamics. *J Biomol NMR*, **30**, 195-204.

95. Massi, F., Johnson, E., Wang, C., Rance, M. and Palmer, A.G., 3rd. (2004) NMR $R_{1\rho}$ rotating-frame relaxation with weak radio frequency fields. *J Am Chem Soc*, **126**, 2247-2256.

96. Massi, F., Grey, M.J. and Palmer, A.G., 3rd. (2005) Microsecond timescale backbone conformational dynamics in ubiquitin studied with NMR R1rho relaxation experiments. *Protein Sci*, **14**, 735-742.

97. Grey, M.J., Tang, Y., Alexov, E., McKnight, C.J., Raleigh, D.P. and Palmer, A.G., 3rd. (2006) Characterizing a partially folded intermediate of the villin headpiece domain under non-denaturing conditions: contribution of His41 to the pH-dependent stability of the N-terminal subdomain. *J Mol Biol*, **355**, 1078-1094.

98. Butterwick, J.A. and Palmer, A.G., 3rd. (2006) An inserted Gly residue fine tunes dynamics between mesophilic and thermophilic ribonucleases H. *Protein Sci*, **15**, 2697-2707.

99. Hoogstraten, C.G., Wank, J.R. and Pardi, A. (2000) Active site dynamics in the lead-dependent ribozyme. *Biochemistry*, **39**, 9951-9958.

100. Blad, H., Reiter, N.J., Abildgaard, F., Markley, J.L. and Butcher, S.E. (2005) Dynamics and metal ion binding in the U6 RNA intramolecular stem-loop as analyzed by NMR. *J Mol Biol*, **353**, 540-555.

101. Shajani, Z. and Varani, G. (2008) ^{13}C relaxation studies of the DNA target sequence for hhai methyltransferase reveal unique motional properties. *Biochemistry*, **47**, 7617-7625.

102. Maltseva, T.V., Földesi, A., Ossipov, D. and Chattopadhyaya, J. (2000) Comparative ^{13}C and ^{2}H relaxation study of microsecond dynamics of the AT tract of selectively $^{13}C/^{2}H$ double-labelled DNA duplexes. *Magn Reson Chem*, **38**, 403-414.

103. Legault, P. and Pardi, A. (1997) Unusual dynamics and pK_a shift at the active site of a lead-dependent ribozyme. *J Am Chem Soc*, **119**, 6621-6628.

104. Akke, M., Fiala, R., Jiang, F., Patel, D. and Palmer, A.G., 3rd. (1997) Base dynamics in a UUCG tetraloop RNA hairpin characterized by ^{15}N spin relaxation: correlations with structure and stability. *RNA*, **3**, 702-709.

105. Batey, R.T., Battiste, J.L. and Williamson, J.R. (1995) Preparation of isotopically enriched RNAs for heteronuclear NMR. *Methods Enzymol*, **261**, 300-322.

106. Borer, P.N., LaPlante, S.R., Kumar, A., Zanatta, N., Martin, A., Hakkinen, A. and Levy, G.C. (1994) ^{13}C-NMR relaxation in three DNA oligonucleotide duplexes: model-free analysis of internal and overall motion. *Biochemistry*, **33**, 2441-2450.

107. Boisbouvier, J., Brutscher, B., Simorre, J.P. and Marion, D. (1999) ^{13}C spin relaxation measurements in RNA: Sensitivity and resolution improvement using spin-state selective correlation experiments. *J Biomol NMR*, **14**, 241-252.

108. Gaudin, F., Chanteloup, L., Thuong, N.T. and Lancelot, G. (1997) Selectively ^{13}C-enriched DNA: dynamics of the C1'H1' and C5'H5' or C5'H5" vectors in d(CGCAAATTTGCG)2. *Magn Reson Chem*, **35**, 561-565.

109. Kline, P.C. and Serianni, A.S. (1990) ^{13}C-enriched ribonucleosides: synthesis and application of ^{13}C-^{1}H and ^{13}C-^{13}C spin-coupling constants to assess furanose and N-glycoside bond conformations. *J Am Chem Soc*, **112**, 7373-7381.

110. SantaLucia, J., Jr., Shen, L.X., Cai, Z., Lewis, H. and Tinoco, I., Jr. (1995) Synthesis and NMR of RNA with selective isotopic enrichment in the bases. *Nucleic Acids Res*, **23**, 4913-4921.

111. Dayie, K.T., Brodsky, A.S. and Williamson, J.R. (2002) Base flexibility in HIV-2 TAR RNA mapped by solution ^{15}N, ^{13}C NMR relaxation. *J Mol Biol*, **317**, 263-278.

Chapter 2

The Development and Characterization of a Novel Alternating Isotope ^{13}C Labeling Scheme for ^{13}C NMR Dynamic Studies in RNA

Portions of this chapter were derived from "Alternate-site isotopic labeling of ribonucleotides for NMR studies of ribose conformational dynamics in RNA" published in the Journal of Biomolecular NMR (2006), written by Dr. Charles G. Hoogstraten and myself.

INTRODUCTION

Heteronuclear NMR spin relaxation is an effective experimental technique to investigate conformational dynamics in biological molecules. Studies have been conducted on timescales that cover the picosecond to millisecond regime (1-5). These studies were made possible by the model-free formalism developed by Lipari and Szabo (6,7) that examine picosecond to nanosecond timescales, and relaxation dispersion curves (8) that probe microsecond to millisecond timescales. Using these approaches, motional parameters can be determined.

NMR relaxation is the process by which the magnetization returns to equilibrium. There are two types of NMR relaxation: longitudinal (z-axis) and transverse (x-y plane). Longitudinal relaxation is the process by which the bulk magnetization reappears along the z-axis, or static field, according to its Boltzmann distribution. Transverse relaxation is the process by which magnetization perpendicular to the static field disappears due to coherence loss. Nuclear spins within a molecule are sensitive to other spins within their environment leading to unique local fields for each nuclear spin. Dipolar coupling is the interaction of nuclear spins through space, which depends on the nuclear spin's orientation to the static magnetic field. Chemical shift anisotropy (CSA) is the orientation dependence of the nuclei with the induced field of the electrons surrounding the nuclei. As a molecule tumbles in solution, the orientation of the nuclei changes and the dipolar coupling and CSA change the localized field at the nucleus which determines the relaxation. The overall molecular tumbling is defined as the overall correlation time τ_C, which is the time it takes for the

molecule to rotate by one radian. Measurements of longitudinal, R_1, and/or transverse, R_2 ($R_{1\rho}$), relaxation rates can yield valuable information.

Another experiment that can affect longitudinal magnetization is steady state heteronuclear Overhauser effect (sshNOE). During this process, application of a weak radio frequency (RF) field at the frequency of one spin for a sufficiently long time can affect non-irradiated spins, enhancing the longitudinal magnetization for the non-irradiated spin. The NOE enhancement depends on the correlation time, and thus can be used to probe internal motions in macromolecules.

As mentioned in chapter one, the model-free approach uses spectral density functions for R_1, R_2 and sshNOE in order to probe motions of nuclei within a molecule to determine motional parameters: an order parameter, S^2 which is a measure of spatial restriction, an effective correlation time, τ_e which is the timescale of internal motion, and R_{ex}, which is the contribution to the observed transverse relaxation rate due to exchange on the μs to ms timescale. It should be noted that CSA relaxation can be neglected at lower to medium field strengths for liquids; however, at higher field strengths, CSA contributions can equal dipole-dipole contributions (4).

The application of the model-free formalism was pioneered by Kay *et al.* (9) where motions for amide ^{15}N nuclei of staphylococcal nuclease were investigated. From R_1, R_2, and hNOE data, Kay *et al.* (9) were able to obtain an

average value for the order parameter, S^2, of 0.86 for all measured amide ^{15}N nuclei of the protein excluding three residues which were located in the termini. These techniques have been applied to other proteins (10-15) as well as nucleic acids (16-21). To interpret R_{ex} contributions more definitively, the use of relaxation dispersive curves have been used to determine chemical shift perturbations for an atom through chemical or conformational changes. In this approach, spin-echo modulated Carr-Purcell-Meiboom-Gill (CPMG) and/or power-dependent spin-locked rotating frame ($R_{1\rho}$) relaxation rates are measured as a function of effective field strength. Millet *et al.* (22) measured exchange contributions for ^{15}N amide resonances in basic pancreatic trypsin inhibitor. In this approach, exchange contributions were observed for several residues near the region of the Cys14-Cys38 disulfide bond where isomerization occurs. Determination of motional timescales for backbone ^{15}N amides as well as ^{13}C sidechain atoms using relaxation dispersion curves in proteins have been utilized (23-32) while applications to ^{13}C atoms in nucleic acids have been sparsely done (18,33-36).

NMR spin relaxation experiments have been aided greatly by the use of isotopic enriched media to incorporate magnetically active nuclei into molecules of interest. Prior to use of isotope labeling, large amounts of sample had to be prepared to compensate for weak signal due to small gyromagnetic ratios for ^{13}C and ^{15}N. In addition, early NMR relaxation experiments were limited to one-

dimensional direct detection (37-39), for which relaxation rates were limited to an ensemble of resonances or isolated resonances. The use of two-dimensional correlated spectroscopy has eliminated this limitation by reducing spectral overlap, thereby greatly aiding dynamic studies within macromolecules.

In nucleic acids, ^{13}C relaxation experiments have been limited primarily to the purine and pyrimidines bases (5). Complete ^{13}C labeling of carbons of the ribose ring using standard uniform enrichment complicates data analysis due to ^{13}C-^{13}C scalar coupling which can cause spectral overlap and/or inaccurate data measurement, as well as dipolar coupling which leads to additional relaxation contributions that can complicate the analysis of spin relaxation experiments. To overcome this limitation, ^{13}C relaxation experiments have been carried out on RNA molecules with natural abundance of ^{13}C isotope (20,40-42) or partial ^{13}C labeling (43,44). Both of these experimental setups are still limited by signal to noise, which can be offset with significant NMR acquisition times and/or the use of a cryogenic-chilled probe. Another way to overcome ^{13}C-^{13}C magnetic interference is the use of specific labeling of ^{13}C resonances. This has been previously done using chemical synthesis (21,45,46), which entails multiple steps not commonly found outside of a synthetic chemistry lab.

Another method to specifically label RNA can be done using bacterial metabolic pathways. Previously, LeMaster and Cronan (47) engineered bacterial strains to specifically ^{13}C label the side chains of amino acids. By deleting

certain enzymes of the citric acid cycle, glycolytic and citric acid cycle intermediates do not interchange carbons. Because of this, labeled precursors can be introduced that give rise to predictable, desirable patterns. LeMaster and Kushlan (48) used one of these *Escherichia coli* strains, DL323, to investigate side chain motions for *E. coli* thioredoxin. From this analysis, the authors were able to observe decreased stability for side chain atoms when compared to backbone atoms of the same residue. It was theorized that this metabolic labeling scheme could be utilized for the ribose of nucleic acids.

Conformational dynamics have been shown to play a critical role in the function of ribozymes, where the ribose ring is often central to the catalytic mechanism. In this chapter, a description of ^{13}C isotopic patterns of ribonucleotides obtained from various *E. coli* harvests is presented. Comparison of R_1 and $R_{1\rho}$ values obtained from alternate-site and uniformly labeled samples is made to examine the effects of ^{13}C-^{13}C magnetic interactions for the ribose ring. With the removal of ^{13}C interactions, accurate motional parameters can be obtained through the use of NMR spin relaxation experiments.

MATERIALS and METHODS

Resuscitation and Storage of* E. coli *strains. *E. coli* strains DL323, K10-15-16, and DF2001 were obtained from the *E. coli* Genetic Stock Center. Samples arrived as lyophylisates on circular pieces of cellulose. The cellulose slips were deposited in a culture tube with 5 mL of enriched Luria-Bertani (LB) media. After

the cellulose was dissolved with mild shaking, 1 mL of each solution was transferred to a culture tube containing 3 mL of enriched LB media, which was incubated overnight at 37 °C. After overnight growth, 1 mL was transferred to 99 mL of LB media. The 100 mL sample was incubated at 37 °C and growth was monitored by measuring the absorbance, A_{600}, to follow the growth curve. When the growth curve indicated stationary growth phase, *E. coli* cell culture was prepared for long-term storage. 500 µL aliquots of *E. coli* cell culture were prepared by making a 1:1 ratio of sample:60% glycerol. The aliquots were frozen in a dry ice and ethanol solution for five mins. The aliquots were then labeled and stored at -80 °C.

Harvest of rNMPs from* E. coli *cells. To obtain ^{13}C labeled ribonucleotide monophosphates (rNMPs) for NMR analysis, frozen *E. coli* cells were resuscitated from long term storage. After minor thawing, a sterile toothpick was used to transfer *E. coli* cells to a culture tube containing 5 mL of LB media and incubated overnight at 37 °C. The overnight growth was then transferred to a flask containing 995 mL of sterile M9 minimal media and 20% ^{13}C specifically labeled glycerol (Cambridge Isotope Laboratories, Inc.) as the sole carbon source. The liter growth of *E. coli* cells was incubated at 37 °C until cell growth reached an A_{600} of 1. Cells were then harvested, lysed, and total nucleic acids were collected, which were subsequently hydrolyzed (49). ^{13}C rAMP was separated from other ribonucleotides using an Akta Basic FPLC (GE Healthcare) using a POROS PI/20 column (20 µm, 4.6 mm × 100 mm) with a linear gradient

from 50 mM NH_4COOH, pH 3.0 to 500 mM NH_4COOH, pH 2.5 over 3.5 mins with a flow rate of 5 mL/min collecting 10 mL fractions. rNMP elution was monitored by UV absorbance, and fractions were pooled and stored at -20 °C.

NMR Spectroscopy. To analyze samples by NMR spectroscopy, all rNMPs were concentrated to 1 to 2 mM in 600 µL with a buffer concentration of 10 mM NaH_2PO_4, pH 7.5, and 60 µL of 10 mM sodium 2,2 dimethyl-2-silapentane-5-sulfonate for reference. H_2O was exchanged with 99.9% D_2O with repeated lyophilization. The final resuspension was done with 99.96% D_2O. For ^{13}C relaxation rates, specifically and uniformly labeled rAMP were prepared to 1 and 0.8 mM concentrations, respectively, as mentioned above and solvated to a final volume of 600 µL in D_8-glycerol. To achieve spectral lock, a special capillary insert filled with D_2O was placed inside the NMR tube.

All spectra were obtained on a 600 MHz Varian UnityInova spectrometer. rNMP mixtures were characterized using one-dimensional ^{13}C decoupled and non-decoupled spectra and two-dimensional ^{1}H-^{13}C heteronuclear single quantum correlation (HSQC) spectra. Relaxation rates were determined using slightly modified, nonconstant-time versions of published sequences as described previously (13). Due to the limited number of resonances and good resolution in the ^{1}H dimension, relaxation spectra were obtained without incrementing t_1. R_1 experiments at 15 °C, 20 °C, 25 °C, and 30 °C with were

acquired with delay times ranging from 100 ms to 3000 ms. $R_{1\rho}$ experiments for the 2′ ^{13}C were also acquired at 15 °C, 20 °C, 25 °C, and 30 °C, while $R_{1\rho}$ experiments for the 4′ ^{13}C was acquired at 20 °C, 25 °C, and 30 °C at approximately 3 kHz spin lock field strength. Data for the 4′ ^{13}C was not collected at 15 °C due to spectral overlap with glycerol satellite peaks. For $R_{1\rho}$, data for ^{13}C C2′ and C4′ were collected separately with the ^{13}C carrier placed on resonance, respectively, at 1550 and 2980 Hz spin-lock fields. Delay periods ranged from 4 to 76 ms.

Data Analysis. All NMR data were processed using FELIX 2002 (Felix NMR, Inc.). Prior to Fourier transformation in the t_2 dimension, a 20% DC offset was applied, data were zero filled, and a 3 Hz exponential line broadening function was applied. For two-dimensional experiments, a cosine-squared apodization function was applied prior to Fourier transformation of the t_1 dimension. To achieve near uniform baseline, the baseline of all one-dimensional spectra were corrected using a baseline correction algorithm. Peak intensities were exported to Igor Pro 4.0 (WaveMetrics). Error bars on intensity measurements were determined by repeating a single delay time three times. ^{13}C relaxation rate constants were determined by nonlinear fitting of the intensity data to a single exponential using Igor Pro 4.0. Errors in rates are those derived from the covariation matrix as reported by the nonlinear fitting routine.

Using the ratio of T_1 to $T_{1\rho}$ for 2′ ^{13}C of the specifically labeled rAMP, it was estimated that the four temperatures of 15, 20, 25, and 30 °C corresponded to rotational correlation times of 16.9, 11.8, 7.8, and 5.4 ns, respectively (50). Assuming a linear scaling of correlation time with molecular weight and taking 6.0–6.4 ns as the correlation time for a 30-nucleotide RNA stem loop in D_2O at 25 °C (33), the 2′ ^{13}C resonances in our samples exhibit relaxation behavior roughly characteristic of RNA oligomers of 82, 57, 38, and 26 nucleotides, respectively, at the four temperatures used.

RESULTS

Labeling scheme. A goal of this work was to develop a biosynthetic isotope labeling pattern that eliminates ^{13}C-^{13}C interaction within the ribose ring. In *E. coli*, ribose-5-phosphate (R5P) used for rNMPs is made via the oxidative and non-oxidative portions of the pentose phosphate pathways (PPP) (Fig 2.1). If glycerol is used as a sole carbon source for bacterial cell cultures, it can enter the metabolic flux of *E. coli* cells via phosphorylation by glycerol kinase. The phosphorylated glycerol-3-phosphate is converted to dihydroxyacetone-3-phosphate by glycerol phosphate dehydrogenase. Isomerization is carried out by triosephosphate isomerase to interconvert dihydroxyacetone-3-phosphate and glyceraldehyde-3-phosphate. Glyceraldehyde-3-phosphate can enter PPP where shown or be converted to other metabolites that enter PPP through gluconeogenisis enzymes.

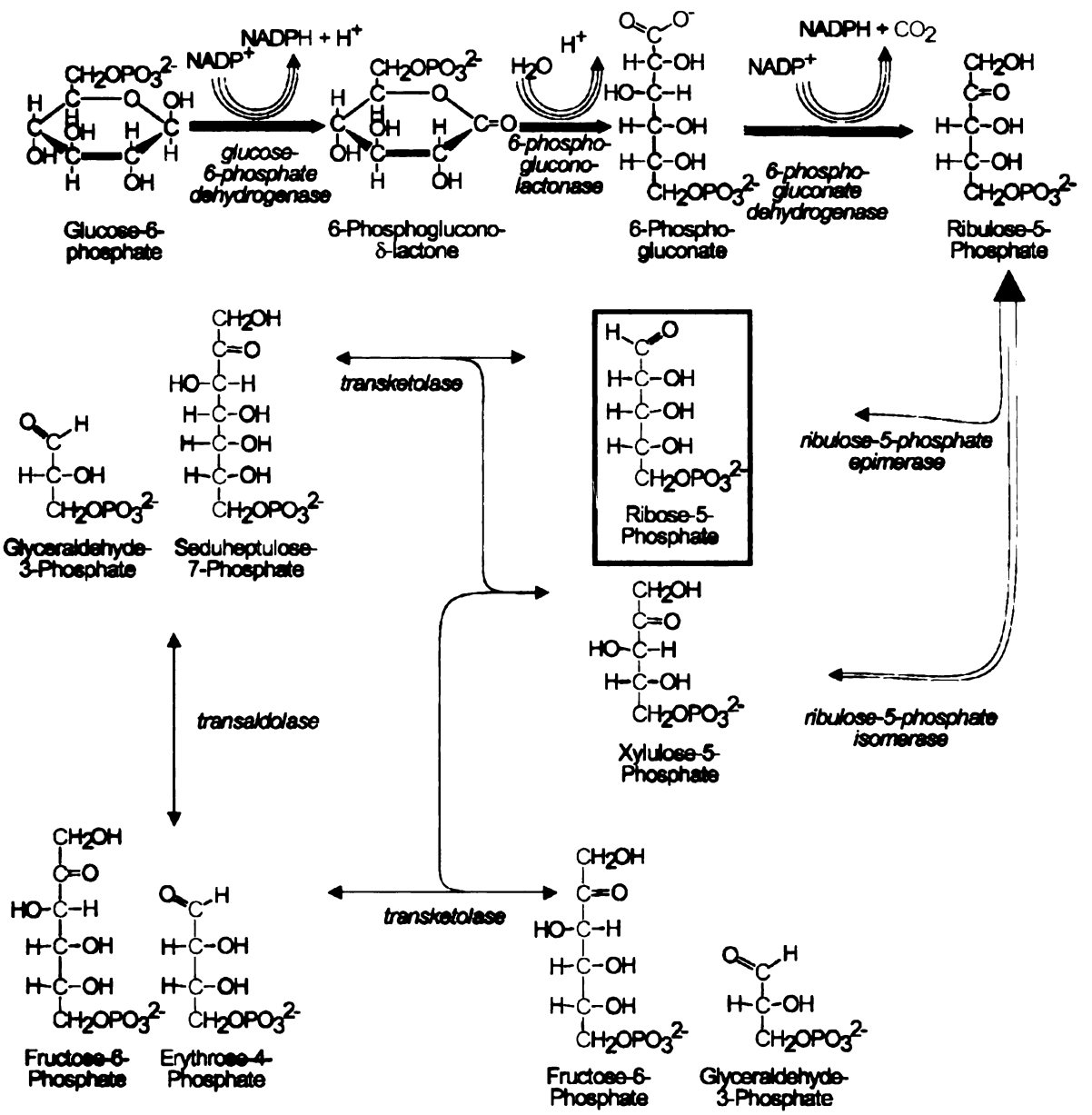

Figure 2.1: Schematic representation of the PPP. The number of arrows represents the number of times the reaction occurs. Atoms are highlighted in color to help illustrate the transfer of atoms and enzymes are italicized. The desired metabolite, R5P, is emphasized. Figure was adapted from Voet, Voet, and Pratt (51).

For the oxidative portion of the PPP, glucose-6-phosphate is the initial metabolite. If glycerol were ^{13}C labeled at the 1′ and 3′ carbon positions, then the glucose-6-phosphate made via gluconeogenesis would be labeled at the 1′, 3′, 4′, and 6′ carbon positions. Alternatively, if the glycerol is labeled only at the 2′ carbon position, then the glucose-6-phosphate molecules would be labeled at the 2′ and 5′ carbon positions. In order to make R5P using the oxidative portion of the PPP, glucose-6-phosphate molecule would yield a ribulose-5-phosphate molecule that was labeled at the 2′, 3′, and 5′ carbon positions for 1,3-$^{13}C_2$ glycerol and 1′ and 4′ carbon positions for 2-^{13}C glycerol, which can be converted to R5P with similar patterns (Fig. 2.2A).

When the cell needs ribose for nucleotide synthesis, the non-oxidative portion of the PPP is utilized. In this pathway, the enzyme transketolase transfers the first two carbons from fructose-6-phosphate to glyceraldehyde-3-phophate to make xylulose-5-phosphate and erythrose-4-phosphate. In the next step, transaldolase transfers the first three carbons from another fructose-6-phosphate molecule to erythrose-4-phosphate yielding glyceraldehyde-3-phosphate and sedohepulose-7-phosphate. Transketolase then transfers the first two carbons from sedohepulose-7-phosphate onto glyceraldehyde-3-phosphate to make xylulose-5-phosphate. Using 1,3-$^{13}C_2$ glycerol as the sole carbon source, xylulose-5-phosphate would be obtained with a labeling pattern of 1′, 3′, 5′ at the carbon positions while ribose-5-phosphate is made with a labeling isotope at the 1′, 2′, 3′, and 5′ carbon positions for the non-oxidative portion of the

PPP (Fig. 2.3). Using 2-^{13}C glycerol as the sole carbon source, xylulose-5-phosphate would be obtained with a labeling pattern of 2′, 4′ at the carbon positions while R5P is made with a labeling isotope at the 4′ carbon position for the non-oxidative portion of the PPP (Fig. 2.4). For purposes of ribonucleotide synthesis, xylulose-5-phosphate can be isomerized to R5P (Fig. 2.2B).

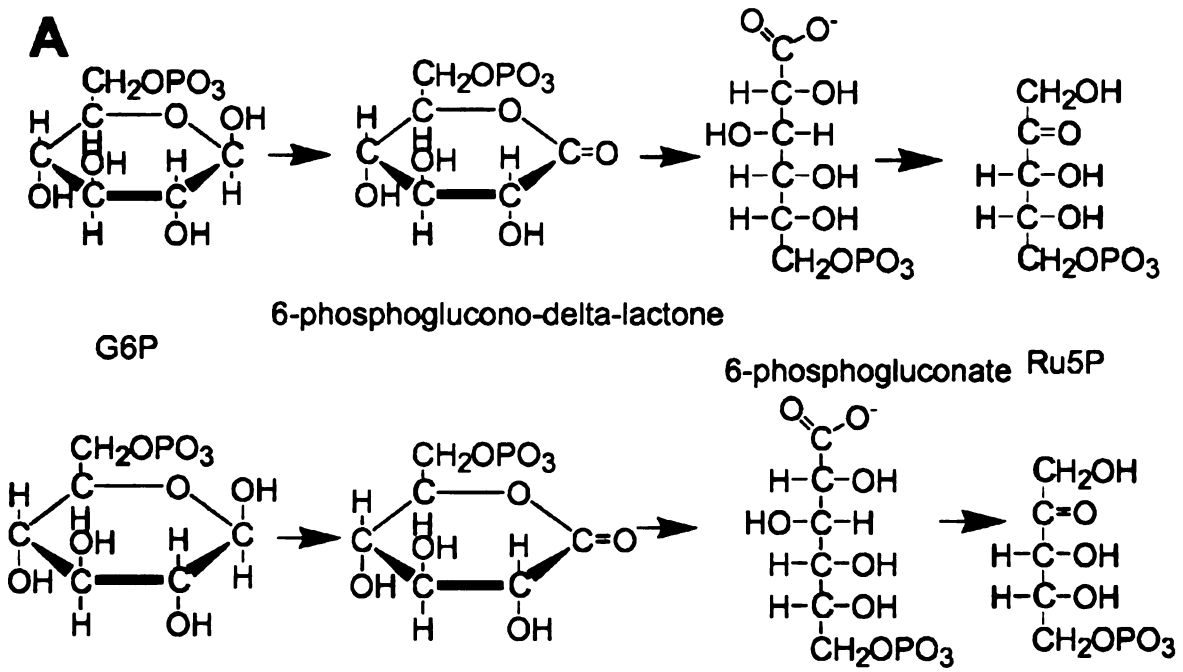

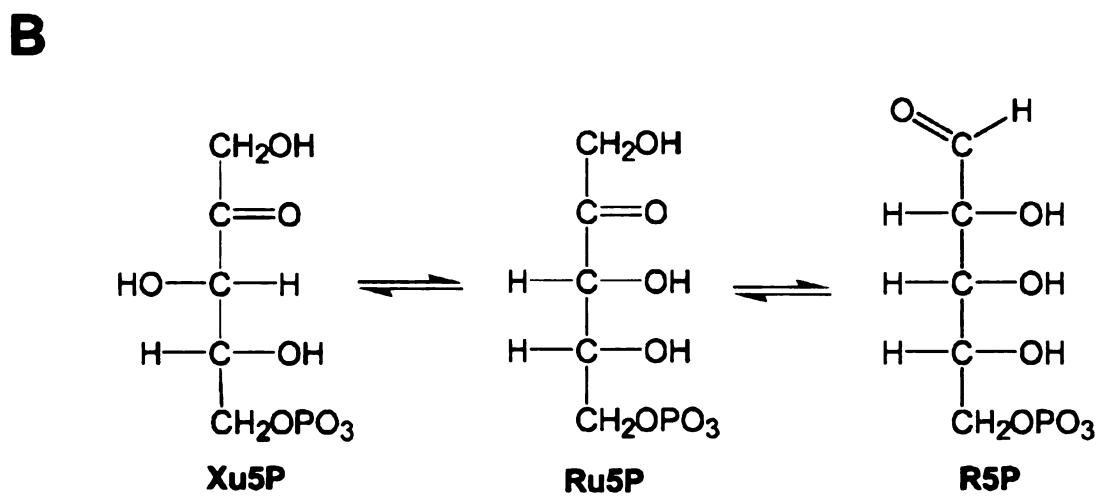

Figure 2.2: (A) Theoretical labeling pattern for the oxidative portion of the PPP. The metabolites would be derived using (top) 1,3-$^{13}C_2$ glycerol and (bottom) 2-^{13}C glycerol as the sole carbon source. Carbons expected to be ^{13}C are labeled red. (B) Interconversion of xylulose-5-phosphate to R5P via ribulose-5-phosphate.

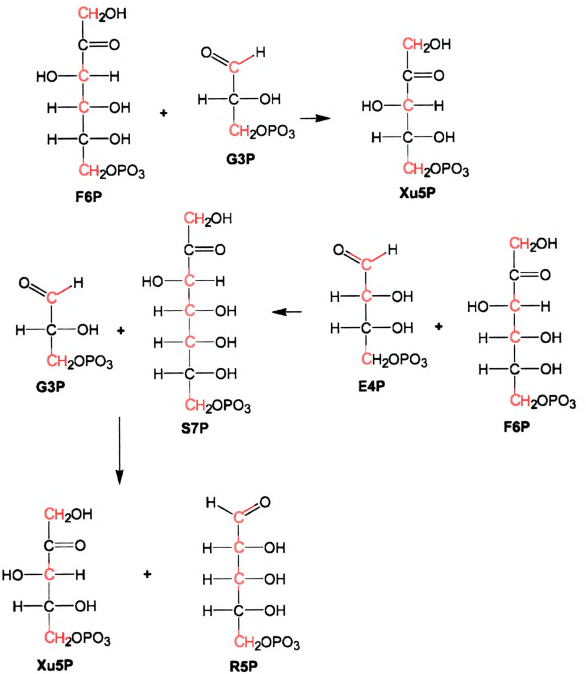

Figure 2.3: Theoretical labeling pattern of carbons for the non-oxidative portion of the PPP using 1,3-$^{13}C_2$ glycerol as the sole carbon source. Expected ^{13}C carbons are labeled in red.

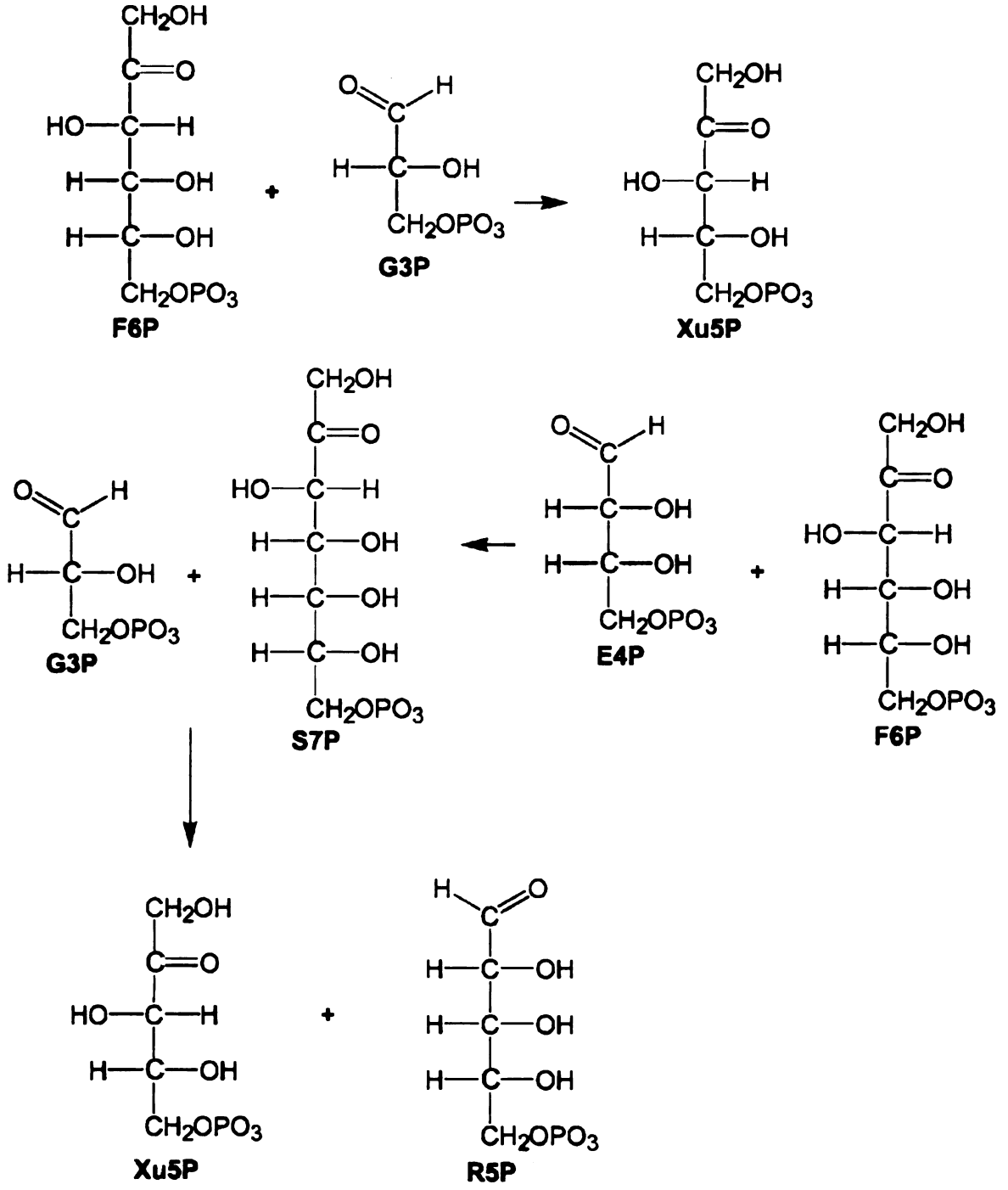

Figure 2.4: Theoretical labeling pattern of carbons for the non-oxidative portion of the PPP using 2-^{13}C glycerol as the sole carbon source. Expected ^{13}C carbons are labeled in red.

Isotopomer Content Analysis from Glycerol Carbon Sources. LeMaster and Kushlan (48) previously demonstrated the ability to specifically ^{13}C label the side chains of amino acids using *E. coli* strain DL323 with ^{13}C labeled glycerol as the carbon source. *E. coli strain* DL323 has deletions to enzymes of the citric acid cycle, preventing metabolic scrambling of carbons in precursors for amino acid side chains. Based on these results, *E. coli* strain DL323 from the *E. coli* Genetic Stock center was used to specifically ^{13}C label the ribose ring of rNMPs. The ^{1}H-^{13}C HSQC spectrum of rNMPs harvested from *E. coli* strain DL323 grown with 1,3-$^{13}C_2$ glycerol as the sole carbon source are presented in Figure 2.5. Four crosspeaks corresponding to the four ribonucleotides can be observed in each spectral region of ribose carbons except for the 4′ region. This result confirms the predicted labeling pattern where no ^{13}C labeling is observed for the 4′ atoms. Also presented is the ^{1}H-^{13}C HSQC spectrum of uniformly ^{13}C labeled adenosine monophosphate (rAMP) for comparison (Fig. 2.6). From this spectrum, the splitting of crosspeaks due to $^{1}J_{CC}$ scalar coupling can be observed. rNMPs synthesized using 2-^{13}C glycerol as the sole carbon source were also analyzed. Similar to the 1,3-$^{13}C_2$ glycerol prep, cross peaks were observed only for those predicted to be labeled. From the HSQC spectrum (Fig 2.7), cross peaks can be observed for the 1′, 2′, and 4′ spectral regions. However, no crosspeaks are detected in the 3′ and 5′ spectral regions. While

specific carbons were ^{13}C enriched using *E. coli* strain DL323, the desired alternating pattern was not obtained. To achieve the alternating ^{13}C-^{12}C pattern, additional *E. coli* strains were used.

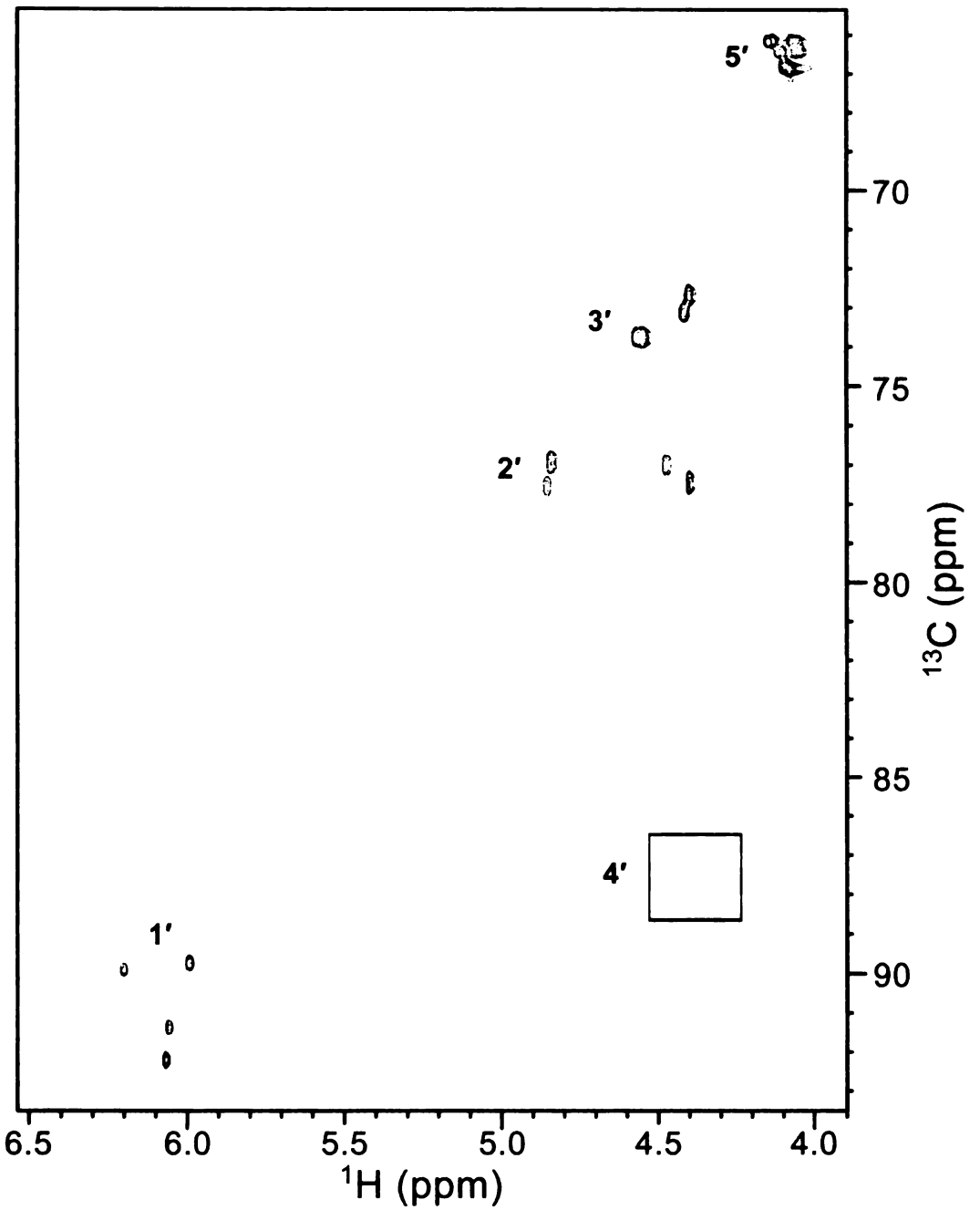

Figure 2.5: ^{1}H-^{13}C HSQC spectrum of ^{13}C rNMPs purified from *E. coli* DL323 using 1,3-$^{13}C_2$ glycerol as the carbon source.

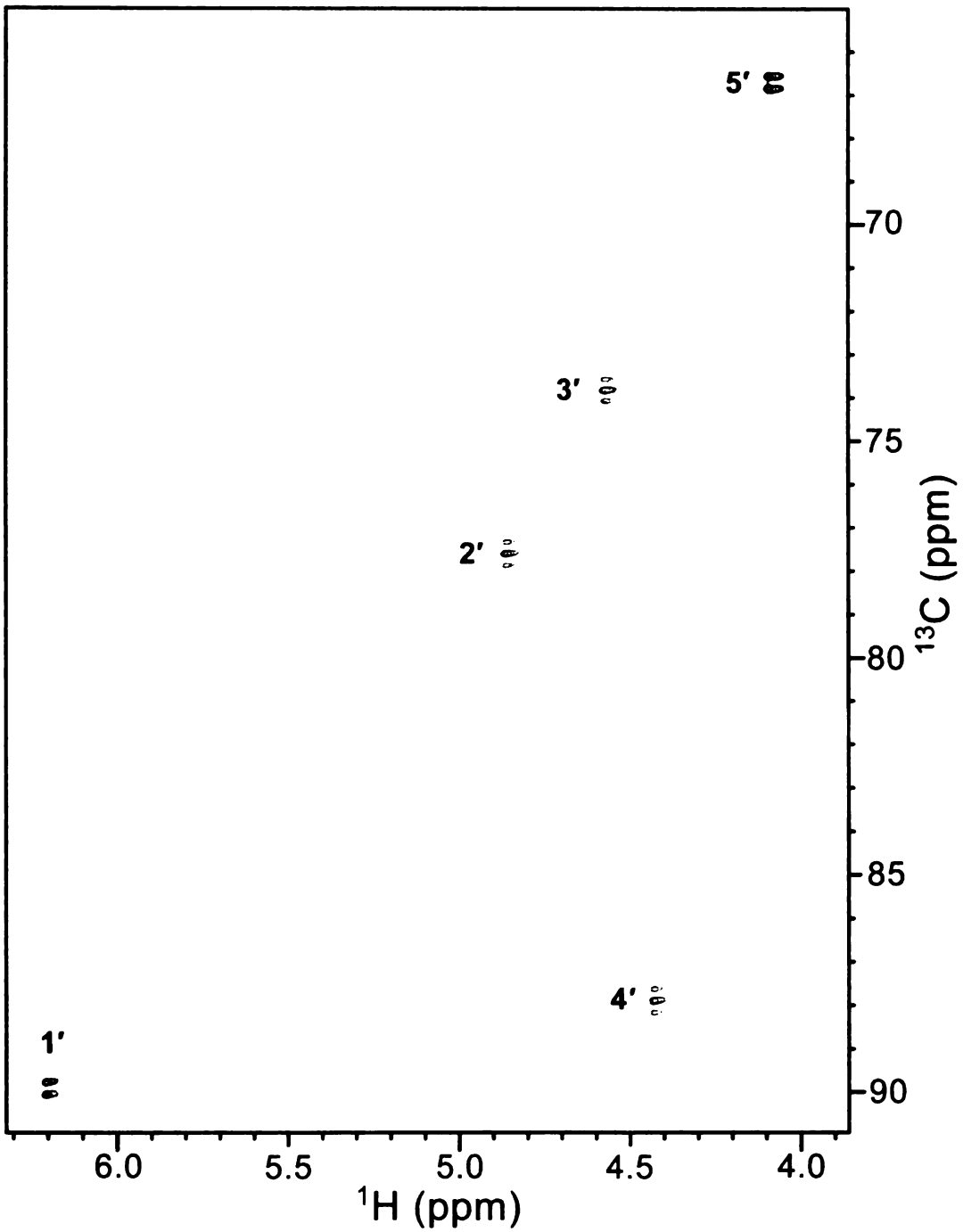

Figure 2.6: ^{1}H-^{13}C HSQC spectrum of fully labeled $^{13}C_{10}$ rAMP obtained commercially.

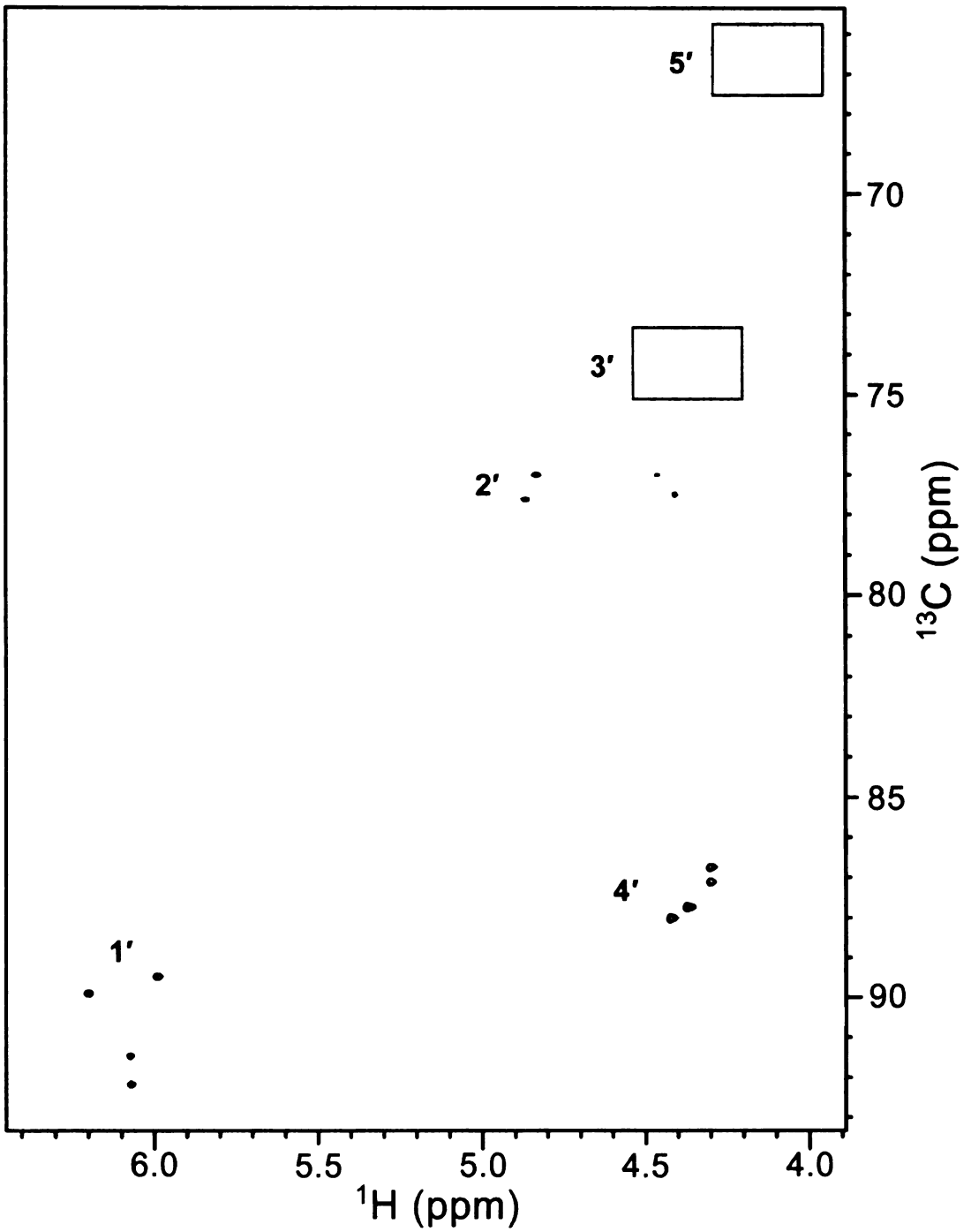

Figure 2.7: ^{1}H-^{13}C HSQC spectrum of ^{13}C rNMPs purified from *E. coli* DL323 using 2-^{13}C glycerol as the carbon source.

From the PPP, one can discern that an alternating ^{12}C-^{13}C-^{12}C labeling pattern could be obtained if R5P was biosynthetically synthesized via the non-oxidative enzymes exclusively. Deletion of the glucose-6-phosphate dehydrogenase gene should shut down the oxidative reactions and shunt R5P production exclusively to the non-oxidative portion of the PPP. The *E. coli* Stock center was queried for *E. coli* strains that were deficient in glucose-6-phosphate dehydrogenase gene, *zwf*. Out of eight possible cell lines, two cell lines were obtained, K10-15-16 and DF2001 (52). The ^{1}H-^{13}C HSQC spectrum of rNMPs harvested from *E. coli* K10-15-16 cultures shows crosspeaks for the 2′ and 4′ regions with no detectable crosspeaks for the other ribose spectral regions (Fig. 2.8). The ^{1}H-^{13}C HSQC spectrum of DF2001 is indistinguishable from the spectrum of K10-15-16 (data not shown). Hence, rNMPs with the ribose ring ^{13}C labeled in an alternating ^{12}C-^{13}C fashion can be obtained using *zwf* mutants.

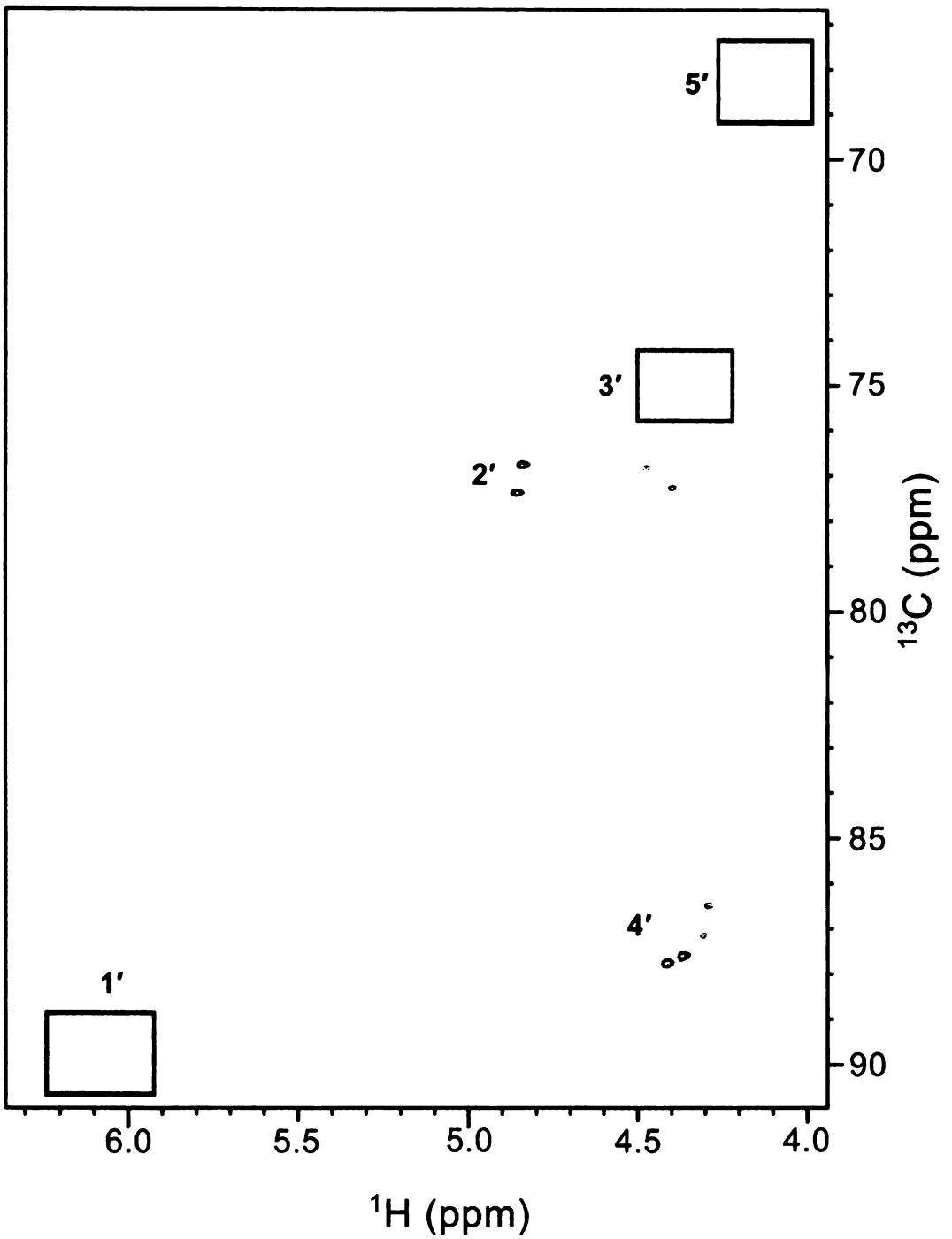

Figure 2.8: ^{1}H-^{13}C HSQC spectrum of ^{13}C rNMPs purified from *E. coli* K10-15-16 utilizing 2-^{13}C glycerol as the carbon source.

To further characterize the specific labeling pattern obtained for each cell culture protocol, the percentage of ^{13}C labeling at a given resonance was determined. This was done by comparison of one-dimensional ^{13}C decoupled and non-decoupled ^{1}H spectra and evaluation of ^{13}C scalar couplings from ^{13}C slices of HSQC spectra. The ribose protons have a narrow chemical shift range, causing data analysis of one-dimensional ^{1}H spectra for rNMP mixtures to be ambiguous due to spectral overlap. For unambiguous isotopomer content analysis, rAMP was isolated from *E. coli* strains DL323 and K10-15-16. One-dimensional ^{1}H spectra were obtained at 5°C for commercial uniformly labeled rAMP and specifically labeled rAMP using 2-^{13}C glycerol sole carbon sources for DL323 and K10-15-16 *E. coli* strains (Fig. 2.9). The effect of ^{13}C interaction can be observed in the uniformly ^{13}C labeled rAMP spectra as ribose ^{1}H singlet peaks in the decoupled spectrum are completely split into the muliplet structure in the non-decoupled spectra. It can be concluded that the C4′ atom in both *E. coli* strains DL323 and K10-15-16 non-decoupled spectra is completely ^{13}C labeled due to the absence of a singlet peak, which is consistent with the model previously mentioned for R5P obtained from the non-oxidative portion of the PPP using 2-^{13}C glycerol. Also supporting the model is the absence of multiplet structures for H3′ and H5′ peaks in the non-decoupled spectra. In the DL323 and

K10-15-16 spectra, both multiplet and singlet peaks can be observed for H1′ and H2′, which is indicative of partial ^{13}C enrichment at those sites.

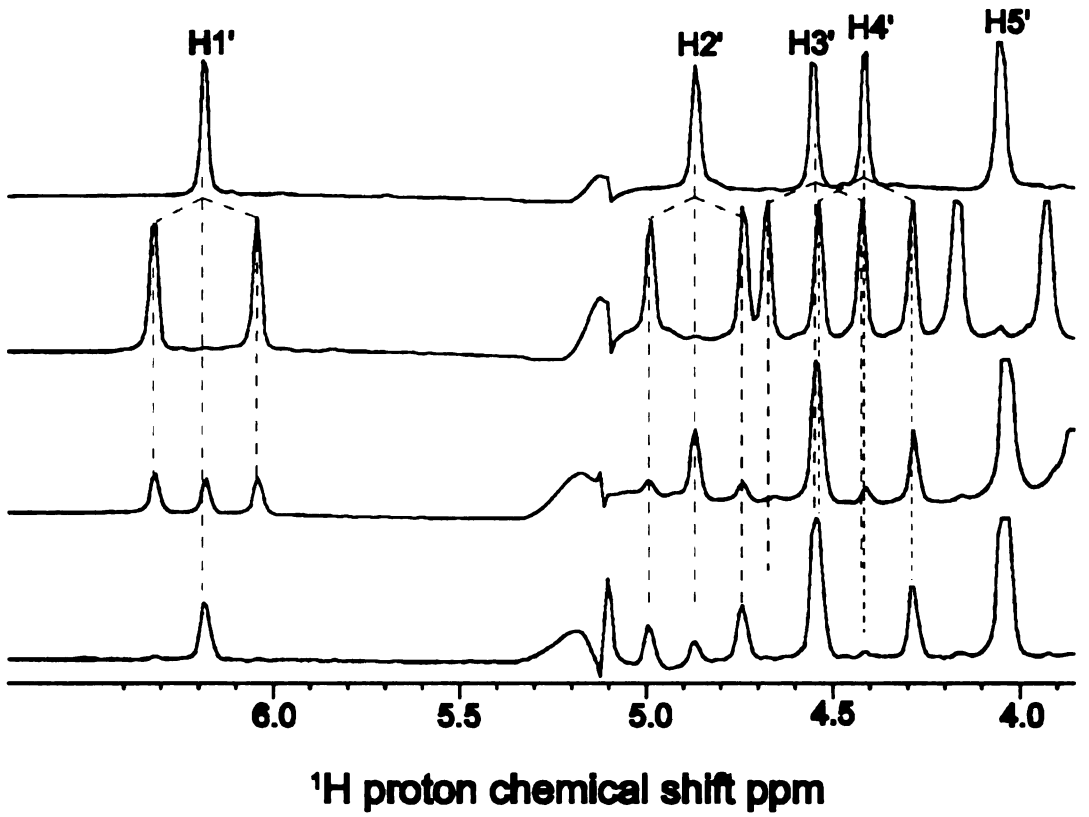

Figure 2.9: Fraction of ^{13}C label at individual sites. One-dimensional ^{1}H NMR spectra of rAMP acquired at 5 °C. The top spectrum is a ^{13}C-decoupled spectrum of uniformly labeled material shown for reference; the remaining spectra were acquired without ^{13}C decoupling. From top to bottom, uniformly labeled rAMP (decoupled); uniformly labeled rAMP (not decoupled); rAMP isolated from *E. coli* DL323; and rAMP isolated from *E. coli* K10-1516. Both bacterial strains were grown on 2 ^{13}C glycerol. Colored lines are added to help guide the eye.

While analysis of one-dimensional ^{1}H spectroscopy can ascertain the level of ^{13}C enrichment for a given site, little information can be obtained for neighboring ^{13}C-^{13}C interaction. This is vital to determine whether a ^{13}C atom is

indeed isolated from other ^{13}C neighbors. To probe neighboring ^{13}C interactions, one-dimensional ^{13}C slices from HSQC experiments were analyzed for each carbon atom of the ribose ring. One-dimensional ^{13}C slices at the C4′ show no detectable $^{1}J_{CC}$ scalar coupling (Fig 2.10). From these results, one can conclude the 4′ ^{1}H-^{13}C spin systems is essentially isolated using 2-^{13}C glycerol in DL323 and *zwf* mutants. For the DL323 prep, ^{13}C labeling can be detected for both the 1′ and 2′ resonances, whereas ^{13}C labeling is observed only for the 2′ resonance of K10-15-16. Consistent with this result is the absence of $^{1}J_{CC}$ scalar coupling for the C2′ of the K10-15-16 spectrum, unlike the DL323 spectrum. Combining the two analyses, percentages of isotopomers have been obtained for the different strains (Table 2.1). Taken together, these results demonstrate the ability to obtain 2′,4′-$^{13}C_2$ rNMPs using *E. coli* strains that exclusively use the non-oxidative portion of the PPP with 2-^{13}C glycerol as the sole carbon. For the purposes of ^{13}C NMR spin relaxation studies, ribonucleotides obtained from *zwf* strains have the most useful isotopic labeling pattern.

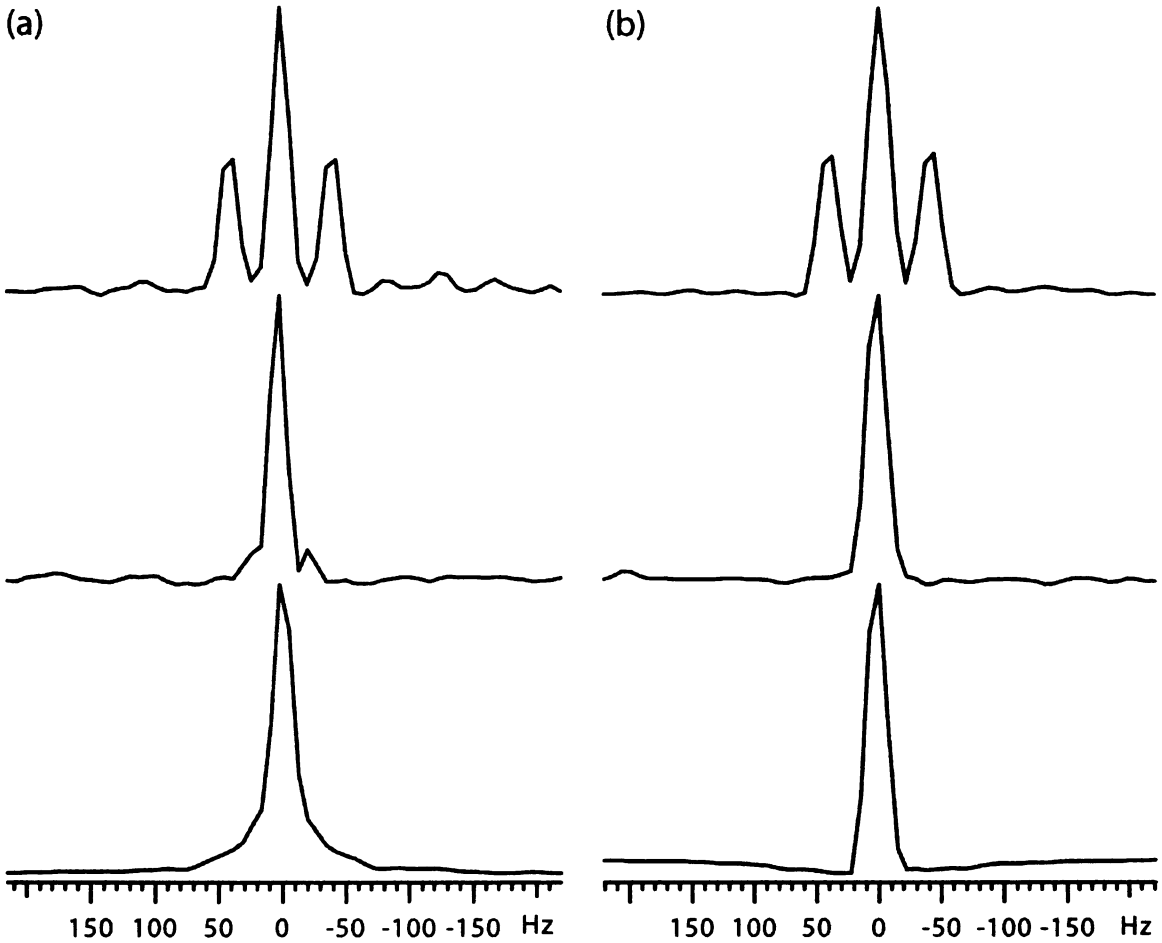

Figure 2.10: ^{13}C slices from ^{1}H-^{13}C HSQC spectra. Sections parallel to the ^{13}C frequency axis through the (a) C2′ and (b) C4′ resonance of rAMP. rAMP was obtained from (top) commercial uniformly labeled rAMP; (middle) *E. coli* strain DL323; and (bottom) *E. coli* K10-15-16. Both bacterial strains were grown with 2-^{13}C glycerol as the sole carbon source.

Table 2.1: ^{13}C isotopomer species obtained in nucleotide preparations

E. coli strain	Carbon Source	Isotopomer	Yield (%)
DL323	1,3-$^{13}C_2$ glycerol	1′,3′,5′-$^{13}C_3$ ribose	25
		2′,3′,5′-$^{13}C_3$ ribose	55
		1′,2′,3′,5′-$^{13}C_4$ ribose	10
		3′,5′-$^{13}C_2$ ribose	5
		Various $^{13}C_1$ ribose	< 5
DL323	2-^{13}C glycerol	1′,4′-$^{13}C_2$ ribose	55
		2′,4′-$^{13}C_2$ ribose	30
		1′,2′,4′-$^{13}C_3$ ribose	5
		4′-$^{13}C_1$ ribose	10
		Various $^{13}C_1$ ribose	< 5
K10-15-16	2-^{13}C glycerol	2′,4′-$^{13}C_2$ ribose	80
		4′-$^{13}C_1$ ribose	5
		1′,4′-$^{13}C_2$ ribose	5
		1′,2′,4′-$^{13}C_3$ ribose	5
		Various $^{13}C_1$ ribose	< 5

Analysis of Isotopomers from Specifically-Labeled Glucose. The above procedures can provide spectroscopically useful methods to isolate the 2′, 4′, and 5′ ^{13}C resonances. The 3′ ^{13}C resonance, however, has been predicted to undergo the greatest chemical shift change upon C3′-endo to C2′-endo interconversion (53,54), and thus may be the most sensitive spin relaxation probe of conformational exchange processes. Therefore procedures were

explored which would give rise to a fully isolated 3′ ^{1}H-^{13}C spin system. Based on previous results for ^{13}C enrichment, it was determined that R5P can be obtained from the oxidative portion of the PPP. Because the oxidative reactions remove the first carbon, ^{13}C enrichment of C3′ could potentially be obtained with glucose enriched at the fourth carbon atom. This prediction is verified by the one-dimensional ^{1}H NMR spectrum of rAMP (Fig 2.11) using wild type *E. coli* cells with 4-^{13}C glucose as the sole carbon source. In the non-decoupled spectrum of this preparation, the H3′ peak is mostly split into a doublet. Consistent with the model, no observable multiplet peaks are observed for the remaining sugar protons. This procedure provides the means to ^{13}C enrich the C3′ atom of R5P at a high percentage and excellent specificity.

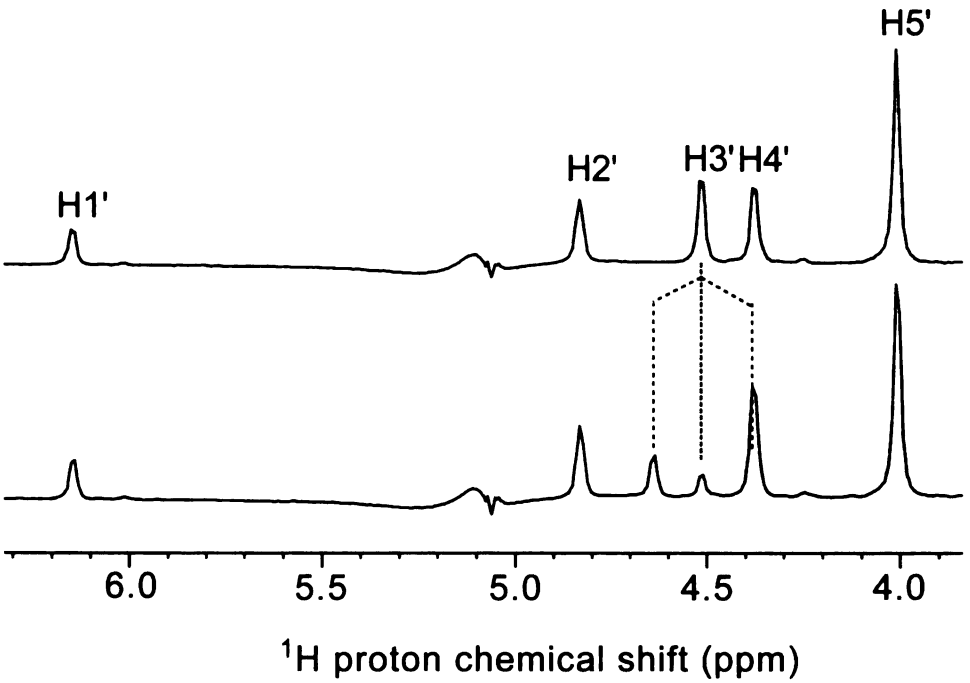

Figure 2.11: Fraction of ^{13}C label at C3′ of rAMP. ^{13}C-decoupled (top) and undecoupled (bottom) NMR spectra of rAMP prepared from wild type *E. coli* grown on 4 ^{13}C glucose. Lines were added to help guide the eye.

Measurement of ^{13}C Relaxation Rates. ^{13}C-^{13}C dipolar and scalar contributions to the relaxation mechanism have limited extensive analysis for the ribose ring of RNA molecules. An alternate-site labeling pattern has been developed that isolates ^{1}H-^{13}C spin systems within the ribose ring of ribonucleotides which can remove these contributions allowing for accurate analysis in RNA molecules. To examine the effects of ^{13}C-^{13}C interactions on the measured relaxation rate, a previous procedure measuring ^{13}C relaxation rates in side chain amino acid atoms (13) has been adapted to compare ^{13}C

relaxation rates of C2′ and C4′ atoms for specifically and uniformly labeled samples. rAMP NMR samples were solvated in 98% D_8-glycerol. The temperature dependent viscosity of glycerol allows for the control of the correlation time for global tumbling, τ_C. Acquiring the data at multiple temperatures, different τ_C values can be simulated with a single sample to analyze ^{13}C-^{13}C interactions for specifically and uniformly ^{13}C relaxation rates. Because τ_C increases with molecular size, it can be interpreted that multiple molecular weights, and thus different size molecules, were also simulated. Since the data were collected in similar fashion for both samples, any differences detected can be attributed to ^{13}C-^{13}C interactions.

Because the H2′ and H4′ peaks are well resolved from other peaks in ^{13}C-decoupled spectra (Fig. 2.9), the two-dimensional pulse sequence was reduced to a one-dimensional pulse sequence by not incrementing t_1 to frequency label ^{13}C carbons, allowing for shorter acquisition times. Table 2.2 compares the effect of varying the temperature, and thus the correlation time, on longitudinal relaxation rates in specifically labeled (2′,4′-$^{13}C_2$) rAMP, derived from *E. coli* strain K10-1516 grown on 2-^{13}C glycerol, and uniformly ^{13}C labeled rAMP. For C2′, measured R_1 values are similar at 30 and 25 °C for both specifically and uniformly labeled samples. However, the measured R_1 values are different at 20

and 15 °C, which can be attributed to ^{13}C-^{13}C interactions at higher molecular weight molecules (Fig. 2.12). This observation is in agreement with the results of Bax and coworkers (19), who showed that the contributions due to ^{13}C–^{13}C interactions are negligible for correlation times of less than 4 ns. For C4′, the measured R_1 values differ at all measured temperatures (data not shown). These results reveal the contribution of the ^{13}C-^{13}C interaction to the measured relaxation rate at C4′ and the removal of this interaction with the specific labeling scheme. Taken together, these results demonstrate the usefulness of the specific labeling scheme to measure accurate relaxation rates for ribose carbon atoms in RNA molecules.

Table 2.2: ^{13}C R_1 and $R_{1\rho}$ measurements obtained from specifically and uniformly labeled rAMP.

^{13}C R_1 Measurements (s^{-1})				
	2',4'-$^{13}C_2$		Uniform ^{13}C	
T (°C)	C2'	C4'	C2'	C4'
30	1.48 ± 0.05	1.13 ± 0.02	1.59 ± 0.07	1.29 ± 0.05
25	1.1 ± 0.1	0.90 ± 0.08	1.12 ± 0.01	1.07 ± 0.04
20	0.95 ± 0.06	0.67 ± 0.02	0.79 ± 0.02	0.84 ± 0.04
15	0.9 ± 0.2	1.9 ± 0.1	0.4 ± 0.2	0.9 ± 0.1

^{13}C $R_{1\rho}$ Measurements (s^{-1}) at $\gamma B_1/2\pi$=2980 Hz				
	2',4'-$^{13}C_2$		Uniform ^{13}C	
T (°C)	C2'	C4'	C2'	C4'
30	25 ± 1	37.0 ± 0.9	25.8 ± 0.7	47 ± 3
25	38 ± 4	53 ± 3	29 ± 4	57 ± 2
20	70 ± 10	140 ± 20	67 ± 3	120 ± 20
15	150 ± 40	nd[a]	90 ± 10	nd[a]

^{13}C $R_{1\rho}$ Measurements (s^{-1}) at $\gamma B_1/2\pi$=1550 Hz				
	2',4'-$^{13}C_2$		Uniform ^{13}C	
T (°C)	C2'	C4'	C2'	C4'
30	22 ± 2	36 ± 2	23 ± 1	38 ± 2

[a]Rates could not be measured due to interference from sidebands from the strong residual glycerol signal.

Figure 2.12: Longitudinal ^{13}C relaxation of rAMP in glycerol. R_1 curves for C2′ of (solid line) uniformly labeled and (dashed line) 2′, 4′ $^{13}C_2$ labeled rAMP at (a) 30 °C, (b) 20 °C, and (c) 15 °C.

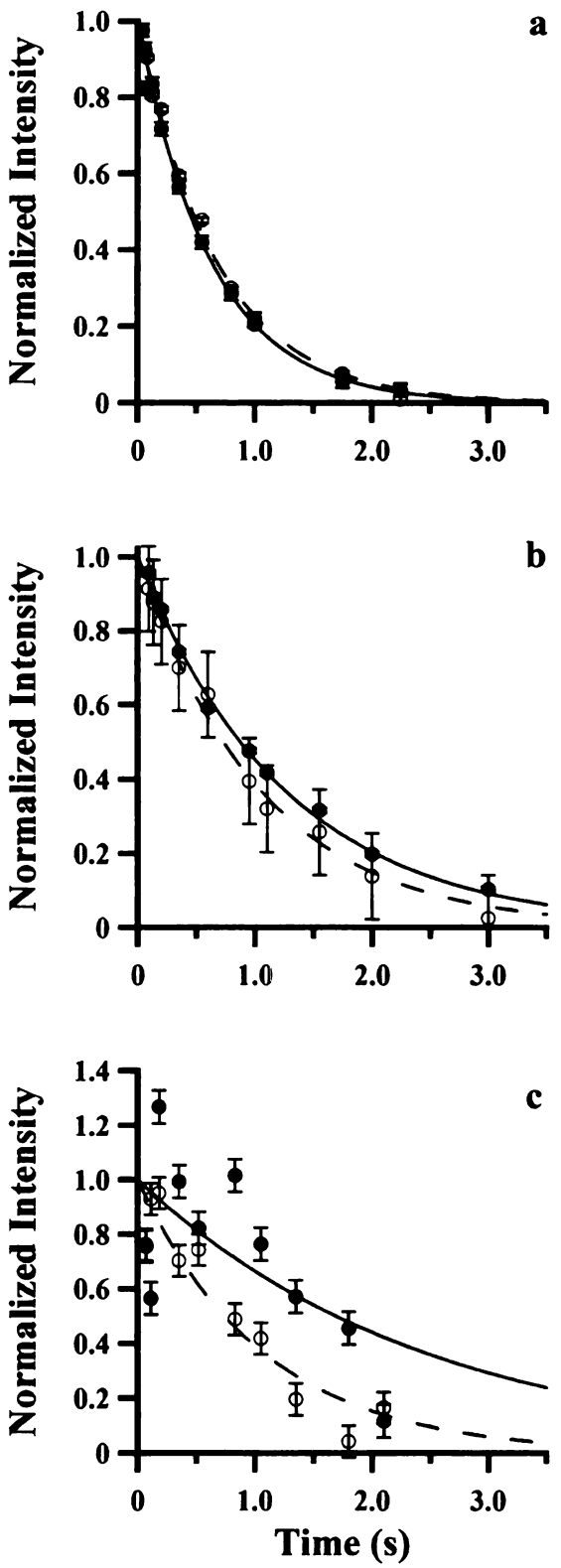
a
b
c
Normalized Intensity
Normalized Intensity
Normalized Intensity
1.0
0.8
0.6
0.4
0.2
0
1.4
1.2
0
1.0
2.0
3.0
Time (s)

For $R_{1\rho}$ values, the largest source of error arising from ^{13}C–^{13}C interaction is magnetization transfer via the Hartmann–Hahn effect during the spin-lock period (19). The Hartmann-Hahn effect can be observed for the C2′ resonance (Table 2.2). At 30 °C using a spin-lock field of almost 3 kHz, $R_{1\rho}$ values are similar between the specifically and uniformly labeled rAMP. However, as the temperature decreases, the measured relaxation rates become dissimilar (Fig. 2.13a). Measured $R_{1\rho}$ for the C4′ resonance are similar within error for both 25 and 20 °C (Fig. 2.13b). The $R_{1\rho}$ was not similar for the C4′ resonance at 30 °C (see Discussion). $R_{1\rho}$ measurements were not obtained at 15 °C due to spectral overlap arising from sidebands of the residual labeled glycerol. In the absence of exchange on the μs to ms timescale, $R_{1\rho}$ values are determined to be independent of applied γB_1 field strength (8). Thus, relaxation rates obtained at 3 kHz spin lock power should be identical to the relaxation rates obtained at a second spin lock power. To confirm this, $R_{1\rho}$ values were measured using a spin-lock field of 1.6 kHz at 30 °C. Measured $R_{1\rho}$ for C2′ and C4′ are similar for both field strengths, which is consistent with exchange models. In short, these results demonstrate the effectiveness of the specific labeling scheme to remove unwanted ^{13}C-^{13}C effects and permit accurate NMR spin relaxation analysis in RNA molecules.

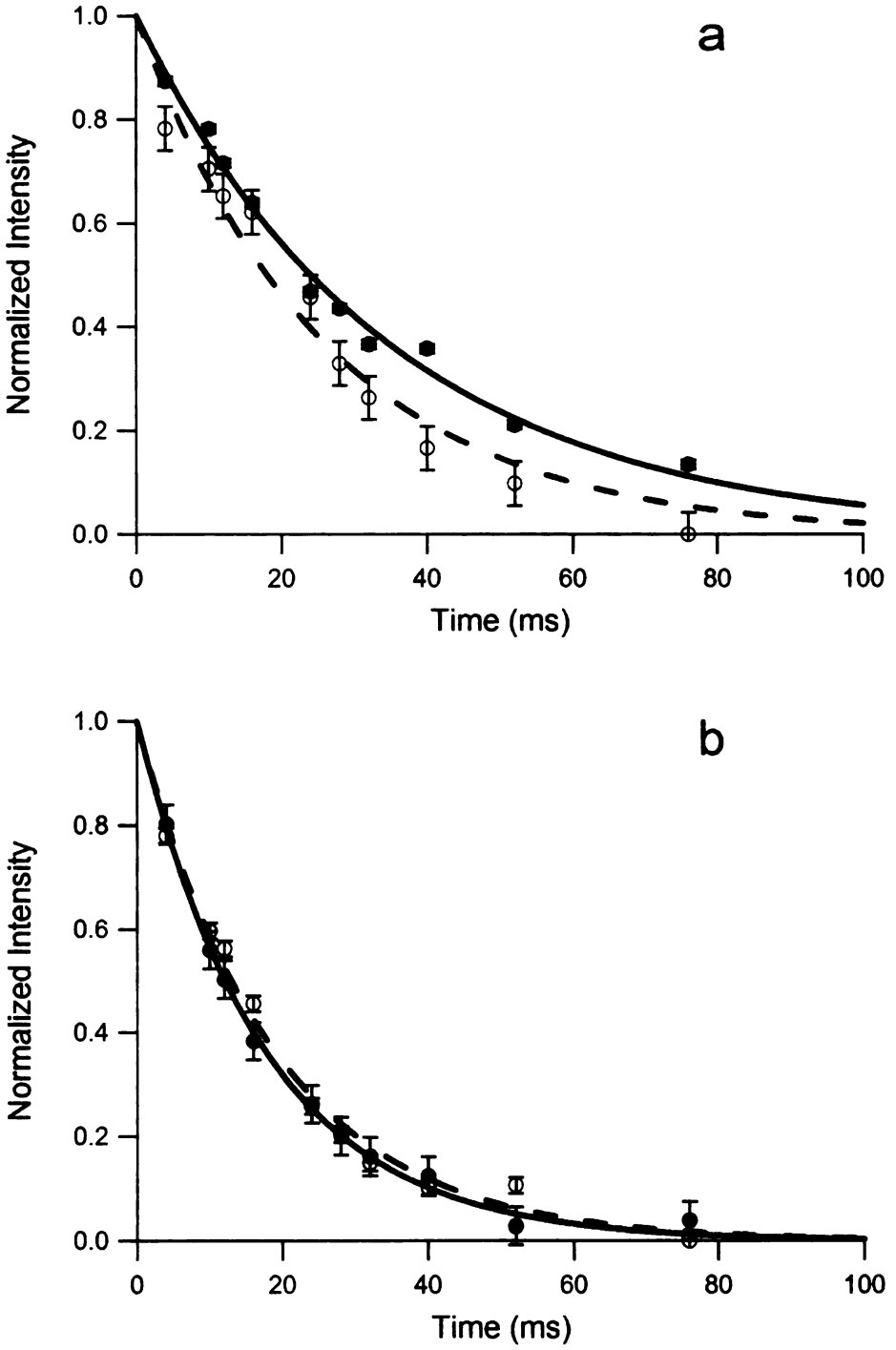

Figure 2.13: Transverse ^{13}C relaxation of rAMP in glycerol. On resonance $R_{1\rho}$ curves for (solid line) uniformly labeled and (dashed line) 2′,4′-$^{13}C_2$ labeled rAMP at 25 °C @ 2980 Hz spin-lock power for (a) C2′ and (b) C4′.

DISCUSSION

In this work, methods have been described and characterized to efficiently ^{13}C enrich specific carbons of the ribose ring of RNA molecules for ^{13}C NMR spin relaxation experiments (50). Also, quantitative analyses probing ^{13}C-^{13}C interactions for R_1 and $R_{1\rho}$ values have been compared between specifically and uniformly labeled rAMP samples.

The *E. coli* strain DL323 was designed to prevent metabolic scrambling of ^{13}C labels in the side chains of amino acids derived from the citric acid cycle intermediates (47,48). For ribonucleotides, the distribution of ^{13}C carbons within the sugar ring would be dependent on the enzymes of the PPP used for R5P production. When grown on 1,3-$^{13}C_2$ glycerol, *E. coli* strain DL323 yields a mixture of 1′,3′,5′-$^{13}C_3$ and 2′,3′,5′-$^{13}C_3$ isotopomers, with small amounts of minor species including 1′,2′,3′,5′,-$^{13}C_4$ isotopomers. Due to the lack of ^{13}C enrichment at C4′, C5′ is isolated from other ^{13}C carbons, thus removing any ^{13}C-^{13}C interactions. Unfortunately, there are still considerable ^{13}C-^{13}C interactions for C3′. When grown on 2-^{13}C glycerol, rNMPs obtained from DL323 yield a mixture of the 1′,4′-$^{13}C_2$ and 2′,4′-$^{13}C_2$ isotopomers of R5P, plus small amounts of minor species including 1′,2′,4′-$^{13}C_3$. Thus, C4′ is isolated from other ^{13}C carbons similar to C5′ using 1,3-$^{13}C_2$ glycerol as a carbon source.

Unfortunately, C2′ is not completely isolated due to interference from neighboring C1′ in a subset of isotopomers. The most likely source for ^{13}C scrambling arises due to repetitive iterations of the complete (oxidative and non-oxidative) PPP. ^{13}C scrambling could also emerge due to intermediates bleeding off the PPP into other pathways and re-entering the PPP. Finally, the level of ^{13}C incorporation at C2′ is low, which could potentially lead to problems with data analysis due to low sensitivity. Based on all these observations using *E. coli* strain DL323, other methods were explored to highly enrich C2′ in ribonucleotides.

The results obtained indicate that growth of *zwf E. coli* strains (K10-15-16 and DF2001) on specific ^{13}C glycerol synthesize essentially all of their R5P, and consequently their rNMPs, from the non-oxidative portion of the PPP. When 2-^{13}C glycerol was used as a carbon source, spectroscopically useful isolation of the 2′ ^{1}H-^{13}C and 4′ ^{1}H-^{13}C spin systems was obtained, with the desired carbons labeled at 85% and >95%, respectively. It should be noted that, in this preparation, the ratio of 2′,4′-$^{13}C_2$ R5P to 4′-^{13}C R5P is considerably higher than the 2:1 value expected. This effect can be attributed to the depletion of the intermediate erythrose-1-phosphate for use in anabolic reactions including amino acid synthesis (55). The exact source for the small amount of ^{13}C enrichment at C1′ is not clear at this time. A hypothetical reason could be due to ^{13}C scrambling in pathways not considered in this work.

The ^{13}C labeling pattern for the ribose ring using *zwf E. coli* strains is superior to the pattern obtained from *E. coli* DL323 for NMR spin relaxation studies because the alternate-site labeling pattern removes ^{13}C-^{13}C interactions as well as yields a substantially higher fraction of C2′ ^{13}C enrichment, increasing the signal-to-noise ratio, while the 1′,2′,4′-$^{13}C_3$ isotopomer is a minor contributor to the total 2′ ^{13}C atom population (≈5%). Because of this, ^{13}C-^{13}C interactions are deemed to be negligible. Therefore, the 2′,4′-$^{13}C_2$ labeling scheme obtained from 2-^{13}C glycerol preparations of *E. coli* strains K10-15-16 or DF2001 should allow for the analysis of the 2′ and 4′ ^{13}C atoms at nearly full or full occupancy, respectively, yielding a near ideal case for ^{13}C NMR spin relaxation studies of these two carbons.

Another advantage of the alternate-site labeling scheme is the collapse of ribose peak triplets (for 2′, 3′, and 4′ ^{13}C resonances) into singlets, which can help alleviate spectral overlap in multidimensional NMR spectra. This effect is of particular importance in the crowded ribose spectral region of HSQC spectra. In uniformly labeled samples, multiplet collapse is typically achieved via the use of constant-time spectroscopy (13), but at the cost of a substantial reduction in experimental sensitivity.

Based on calculations that predicted large chemical shift changes for C3′ upon a change in ribose conformations, methods were explored to reliably ^{13}C

enrich C3′. This was done with wild type *E. coli* cultures using 4-^{13}C glucose as the sole carbon source. The results show outstanding effectiveness in ^{13}C enrichment of C3′. Glucose labeled with ^{13}C at each individual carbon atom is commercially available, albeit at considerable financial expense. For example, 4-^{13}C glucose was listed at $1600/g from Cambridge Isotope Laboratories, Inc. compared to $449/g for 2-^{13}C glycerol and $699/g for 1,3-$^{13}C_2$ glycerol. Hence this route provides a robust and selective, albeit costly, method to label a desired individual ribose carbon. Even though this method costs more than specifically or uniformly labeled methods, it can be beneficial for RNA ^{13}C NMR spin relaxation studies because of the large expected chemical shift change for the C3′, due to sugar re-puckering, which will lead to a greater R_{ex} dependence in dispersion experiments (8) (see Chapter 3). This can potentially offset the need to use higher magnetic fields.

In the standard model-free analysis in biomolecules, R_1, R_2 ($R_{1\rho}$), and heteronuclear NOE values are interpreted as arising from ^{1}H–X (X = ^{13}C or ^{15}N) dipole–dipole and X chemical-shift anisotropy (CSA) relaxation mechanisms, along with possible contributions of μs-ms timescale conformational exchange to R_2 ($R_{1\rho}$) (6). In the case of ^{13}C, however, the presence of scalar and dipolar couplings between the resonance of interest and directly bonded ^{13}C atoms gives rise to additional terms in the relaxation equations that substantially

complicate the collection and/or interpretation of results (13). The alternate-site labeling scheme was developed to remove such effects. Therefore, the effects of neighboring ^{13}C atoms on measured R_1 and $R_{1\rho}$ relaxation rates in specifically and uniformly ^{13}C labeled rAMP have been examined (50).

For ^{13}C R_1 values in the presence of directly bonded ^{13}C carbons, the longitudinal relaxation rates will be affected by ^{13}C-^{13}C dipolar interactions as well as ^{1}H–^{13}C dipolar and ^{13}C CSA contributions. Boisbouvier and coworkers (19) demonstrated that ^{13}C-^{13}C dipolar relaxation can be negligible in the analysis of longitudinal relaxation rates. The τ_c for the DNA oligomer used was estimated to be 3.35 ns. However it was predicted that ^{13}C-^{13}C dipolar contributions would become more significant as the τ_c value increased, and therefore not negligible.

By adjusting the temperature, different τ_c values could be simulated ranging from 5.4 to 16.9 ns (30 °C to 15 °C) using a single NMR sample. Due to sample setup, any differences observed in the relaxation rates for the alternate-site labeling sample and uniformly labeled sample can be attributed to ^{13}C-^{13}C interactions. Such interactions were detected in both R_1 and $R_{1\rho}$ values. At higher temperatures corresponding to short correlational times, R_1 values for C2′ were similar for the alternate-site and uniformly labeled samples, while R_1 values

differed at higher temperatures. This is consistent with predictions Bax and co-workers (19) made. C4′ R_1 values are different at all temperatures. A possible reason for this could be due to the CSA for C4′. Bax and coworkers (56) measured chemical shift tensors for ribose carbons in helix-35 of 23S rRNA. From this work, the CSAs for C3′ and C4′ were determined to be greater than C1′, C2′, and C5′. Because the measured CSA of ribose C4′ is almost three times larger than ribose C2′, it can be theorized that the CSA of C4′ is not negligible at short correlation times.

For the measurement of transverse relaxation rates, two distinct measurement schemes are possible. R_2 measurements based on the Carr-Purcell-Meiboom-Gill (CPMG) pulse scheme are completely unsuitable in the presence of ^{13}C–^{13}C couplings due to oscillatory behavior arising from echo modulation (13). We did not obtain R_2 rates using CPMG pulse sequences. However, due to the removal of $^{1}J_{CC}$ scalar coupling, R_2 measurements could be reliably obtained using the ^{13}C specific labeling pattern. It should be noted that in the ^{13}C specific labeling pattern, the $^{2}J_{CC}$ scalar coupling between C2′ and C4′ is still present and, in principle, could affect R_2 measurements. However, the $^{2}J_{CC}$ coupling has been measured to 0.9 Hz in adenosine (57) as compared to 40 Hz for $^{1}J_{CC}$ (58). Due to this low value, the $^{2}J_{CC}$ scalar coupling can be neglected.

Another method to measure transverse magnetization is using a spin-locked rotating-frame ($R_{1\rho}$) pulse sequence. In this setup, the greatest source of error arises from homonuclear Hartmann–Hahn transfer to covalently bound ^{13}C carbons during the spin-lock period (13,59). This effect is negligible if magnitude of the scalar coupling is small relative to the difference in effective field strength between the two nuclei, which is the resonance offset. In uniformly ^{13}C labeled DNA, this effect is slight due to the wide separation of chemical shifts for carbons at different sites. For example, in the dodecamer studied by the Bax group (19), the closest approach is 8 ppm, between C3′ and C4′, and accurate $R_{1\rho}$ measurements could be obtained. In RNA, by contrast, the possibilities for Hartmann–Hahn transfer are substantially greater. In the lead-dependent ribozyme, the median separation between C2′ and C3′ shifts is 2.6 ppm, and the ranges of the two carbon types actually overlap (60). In rAMP, the measured chemical shift difference between the C2′ and C3′ resonances is 4 ppm, while the measured chemical shift difference between the C3′ and C4′ resonances is 12 ppm. One would presume Hartmann-Hahn transfer to be more likely between C2′ and C3′ as opposed to C3′ and C4′. ^{13}C $R_{1\rho}$ values are dissimilar among the alternate-site and uniformly C2′ at temperatures below 30 °C whereas ^{13}C $R_{1\rho}$ values are similar for C4′ at all temperatures.

$R_{1\rho}$ measurements are sensitive to motions on the μs-ms regime. In the absence of motion, $R_{1\rho}$ values are independent of RF field strength (2,33). $R_{1\rho}$ values were obtained at 30 °C at 1.5 and 3 kHz. $R_{1\rho}$ for C2′ and C4′ are similar within error at both fields measured. This result was expected because ribonucleotide monomers are not predicted to have sugar pucker conformation transitions. However, the Hartmann–Hahn effect could be particularly troublesome in the use of relaxation dispersion studies to study μs-ms timescale exchange in RNA molecules, as magnetization could vary with spin-lock strength and therefore could possibly yield an artifactual dependence of $R_{1\rho}$ relaxation rate on ω_{eff} that would be erroneously interpreted as conformational exchange. To analyze unambiguously interconversion of C3′-endo and C2′-endo conformations at the active sites of ribozymes using CPMG and $R_{1\rho}$ relaxation methods, the use of alternate-site labeling or related schemes is thus an absolute necessity (see Chapter 3).

Here, a method has been presented to use a convenient biosynthetic procedure to prepare rNMPs with favorable ^{13}C labeling patterns that isolate ^{1}H-^{13}C spin systems within the ribose ring for ^{13}C NMR spin relaxation studies. Using ^{13}C relaxation measurements for rAMP solvated in D_8-glycerol samples to simulate various correlation times, it was demonstrated that magnetic interactions from adjacent ^{13}C nuclei can be a source of error in R_1

measurements for molecules with long correlation times and in $R_{1\rho}$ measurements where coupled ^{13}C nuclei have similar effective fields. The alternate-site labeling scheme is a practical approach to removing these errors (50). The methods reported in herein will open a new window into the analysis of conformational dynamics in RNA molecules and advance efforts to understand the correlation between dynamics and function in ribozymes and other RNA systems.

ACKNOWLEDGMENTS

I would like to thank Kristine Julien for growth and isolation of rNMPs using 2-^{13}C glycerol for the DL323 strain.

REFERENCES

1. Dayie, K.T., Wagner, G. and Lefevre, J.F. (1996) Theory and practice of nuclear spin relaxation in proteins. *Annu Rev Phys Chem*, **47**, 243-282.

2. Palmer, A.G., 3rd. (2004) NMR characterization of the dynamics of biomacromolecules. *Chem Rev*, **104**, 3623-3640.

3. Palmer, A.G., 3rd. (1997) Probing molecular motion by NMR. *Curr Opin Struct Biol*, **7**, 732-737.

4. Ishima, R. and Torchia, D.A. (2000) Protein dynamics from NMR. *Nat Struct Biol*, **7**, 740-743.

5. Shajani, Z. and Varani, G. (2007) NMR studies of dynamics in RNA and DNA by ^{13}C relaxation. *Biopolymers*, **86**, 348-359.

6. Lipari, G. and Szabo, A. (1982) Model-free approach to the interpretation of nuclear magnetic resonance relaxation in macromolecules. 1. theory and range of validity. *J Am Chem Soc*, **104**, 4546-4559.

7. Lipari, G. and Szabo, A. (1982) Model-free approach to the interpretation of nuclear magnetic resonance relaxation in macromolecules. 2. analysis of experimental results. *J Am Chem Soc*, **104**, 4559-4570.

8. Palmer, A.G., 3rd, Kroenke, C.D. and Loria, J.P. (2001) Nuclear magnetic resonance methods for quantifying microsecond-to-millisecond motions in biological macromolecules. *Methods Enzymol*, **339**, 204-238.

9. Kay, L.E., Torchia, D.A. and Bax, A. (1989) Backbone dynamics of proteins as studied by ^{15}N inverse detected heteronuclear NMR spectroscopy: application to staphylococcal nuclease. *Biochemistry*, **28**, 8972-8979.

10. Zhou, H., McEvoy, M.M., Lowry, D.F., Swanson, R.V., Simon, M.I. and Dahlquist, F.W. (1996) Phosphotransfer and CheY-binding domains of the

histidine autokinase CheA are joined by a flexible linker. *Biochemistry*, **35**, 433-443.

11. Mandel, A.M., Akke, M. and Palmer, A.G., 3rd. (1995) Backbone dynamics of *Escherichia coli* ribonuclease HI: correlations with structure and function in an active enzyme. *J Mol Biol*, **246**, 144-163.

12. Mandel, A.M., Akke, M. and Palmer, A.G., 3rd. (1996) Dynamics of ribonuclease H: temperature dependence of motions on multiple time scales. *Biochemistry*, **35**, 16009-16023.

13. Yamazaki, T., Muhandiram, R. and Kay, L. (1994) NMR experiments for the measurement of carbon relaxation properties in highly enriched, uniformly ^{13}C, ^{15}N-labeled proteins: application to $^{13}C\alpha$ carbons. *J Am Chem Soc*, **116**, 8266-8278.

14. Wikstrom, M., Forsen, S. and Drakenberg, T. (1996) Backbone dynamics of a domain of protein L which binds to immunoglobulin light chains. *Eur J Biochem*, **235**, 543-548.

15. Lienin, S.F., Bremi, T., Brutscher, B., Bruschweiler, R. and Ernst, R.R. (1998) Anisotropic intramolecular backbone dynamics of ubiquitin characterized by NMR relaxation and MD computer simulation. *J Am Chem Soc*, **120**, 9870-9879.

16. Duchardt, E. and Schwalbe, H. (2005) Residue specific ribose and nucleobase dynamics of the cUUCGg RNA tetraloop motif by NMR ^{13}C relaxation. *J Biomol NMR*, **32**, 295-308.

17. Hall, K.B. and Tang, C. (1998) ^{13}C relaxation and dynamics of the purine bases in the iron responsive element RNA hairpin. *Biochemistry*, **37**, 9323-9332.

18. Shajani, Z. and Varani, G. (2005) ^{13}C NMR relaxation studies of RNA base and ribose nuclei reveal a complex pattern of motions in the RNA binding site for human U1A protein. *J Mol Biol*, **349**, 699-715.

19. Boisbouvier, J., Wu, Z., Ono, A., Kainosho, M. and Bax, A. (2003) Rotational diffusion tensor of nucleic acids from ^{13}C NMR relaxation. *J Biomol NMR*, **27**, 133-142.

20. Borer, P.N., LaPlante, S.R., Kumar, A., Zanatta, N., Martin, A., Hakkinen, A. and Levy, G.C. (1994) ^{13}C-NMR relaxation in three DNA oligonucleotide duplexes: model-free analysis of internal and overall motion. *Biochemistry*, **33**, 2441-2450.

21. Gaudin, F., Chanteloup, L., Thuong, N.T. and Lancelot, G. (1997) Selectively ^{13}C-enriched DNA: dynamics of the C1'H1' and C5'H5' or C5'H5" vectors in d(CGCAAATTTGCG)2. *Magn Reson Chem*, **35**, 561-565.

22. Millet, O., Loria, J.P., Kroenke, C.D., Pons, M. and Palmer, A.G., 3rd. (2000) The static magnetic field dependence of chemical exchange linebroadening defines the NMR chemical shift time scale. *J Am Chem Soc*, **122**, 2867-2877.

23. Loria, J.P., Rance, M. and Palmer, A.G. (1999) A relaxation-compensated Carr-Purcell-Meiboom-Gill sequence for characterizing chemical exchange by NMR spectroscopy. *J Am Chem Soc*, **121**, 2331-2332.

24. Mulder, F.A., Mittermaier, A., Hon, B., Dahlquist, F.W. and Kay, L.E. (2001) Studying excited states of proteins by NMR spectroscopy. *Nat Struct Biol*, **8**, 932-935.

25. Tollinger, M., Skrynnikov, N.R., Mulder, F.A., Forman-Kay, J.D. and Kay, L.E. (2001) Slow dynamics in folded and unfolded states of an SH3 domain. *J Am Chem Soc*, **123**, 11341-11352.

26. Cole, R. and Loria, J.P. (2002) Evidence for flexibility in the function of ribonuclease A. *Biochemistry*, **41**, 6072-6081.

27. Kovrigin, E.L., Cole, R. and Loria, J.P. (2003) Temperature dependence of the backbone dynamics of ribonuclease A in the ground state and bound to the inhibitor 5'-phosphothymidine (3'-5')pyrophosphate adenosine 3'-phosphate. *Biochemistry*, **42**, 5279-5291.

28. Korzhnev, D.M., Bezsonova, I., Evanics, F., Taulier, N., Zhou, Z., Bai, Y., Chalikian, T.V., Prosser, R.S. and Kay, L.E. (2006) Probing the transition state ensemble of a protein folding reaction by pressure-dependent NMR relaxation dispersion. *J Am Chem Soc*, **128**, 5262-5269.

29. Kim, S. and Baum, J. (2004) An on/off resonance rotating frame relaxation experiment to monitor millisecond to microsecond timescale dynamics. *J Biomol NMR*, **30**, 195-204.

30. Massi, F., Johnson, E., Wang, C., Rance, M. and Palmer, A.G., 3rd. (2004) NMR $R_{1\rho}$ rotating-frame relaxation with weak radio frequency fields. *J Am Chem Soc*, **126**, 2247-2256.

31. Massi, F., Grey, M.J. and Palmer, A.G., 3rd. (2005) Microsecond timescale backbone conformational dynamics in ubiquitin studied with NMR R1rho relaxation experiments. *Protein Sci*, **14**, 735-742.

32. Grey, M.J., Tang, Y., Alexov, E., McKnight, C.J., Raleigh, D.P. and Palmer, A.G., 3rd. (2006) Characterizing a partially folded intermediate of the villin headpiece domain under non-denaturing conditions: contribution of His41 to the pH-dependent stability of the N-terminal subdomain. *J Mol Biol*, **355**, 1078-1094.

33. Hoogstraten, C.G., Wank, J.R. and Pardi, A. (2000) Active site dynamics in the lead-dependent ribozyme. *Biochemistry*, **39**, 9951-9958.

34. Blad, H., Reiter, N.J., Abildgaard, F., Markley, J.L. and Butcher, S.E. (2005) Dynamics and metal ion binding in the U6 RNA intramolecular stem-loop as analyzed by NMR. *J Mol Biol*, **353**, 540-555.

35. Shajani, Z. and Varani, G. (2008) ^{13}C relaxation studies of the DNA target sequence for hhai methyltransferase reveal unique motional properties. *Biochemistry*, **47**, 7617-7625.

36. Maltseva, T.V., Földesi, A., Ossipov, D. and Chattopadhyaya, J. (2000) Comparative ^{13}C and ^{2}H relaxation study of microsecond dynamics of the AT tract of selectively $^{13}C/^{2}H$ double-labelled DNA duplexes. *Magn Reson Chem*, **38**, 403-414.

37. Fuson, M.M. and Prestegard, J.H. (1983) Dynamics of an interfacial methylene in dimyristoylphosphatidylcholine vesicles using carbon-13 spin relaxation. *Biochemistry*, **22**, 1311-1316.

38. Henry, G.D., Weiner, J.H. and Sykes, B.D. (1986) Backbone dynamics of a model membrane protein: ^{13}C NMR spectroscopy of alanine methyl groups in detergent-solubilized M13 coat protein. *Biochemistry*, **25**, 590-598.

39. Dellwo, M.J. and Wand, A.J. (1989) Model-independent and model-dependent analysis of the global and internal dynamics of cyclosporin A. *J Am Chem Soc*, **111**, 4571-4578.

40. Isaacs, R.J., Rayens, W.S. and Spielmann, H.P. (2002) Structural differences in the NOE-derived structure of G-T mismatched DNA relative to normal DNA are correlated with differences in ^{13}C relaxation-based internal dynamics. *J Mol Biol*, **319**, 191-207.

41. Spielmann, H.P. (1998) Dynamics in psoralen-damaged DNA by ^{1}H-detected natural abundance ^{13}C NMR spectroscopy. *Biochemistry*, **37**, 5426-5438.

42. Spielmann, H.P. (1998) Dynamics of a bis-intercalator DNA complex by ^{1}H-detected natural abundance ^{13}C NMR spectroscopy. *Biochemistry*, **37**, 16863-16876.

43. Kishore, A.I., Mayer, M.R. and Prestegard, J.H. (2005) Partial ^{13}C isotopic enrichment of nucleoside monophosphates: useful reporters for NMR structural studies. *Nucleic Acids Res*, **33**, e164.

44. Kojima, C., Ono, A., Kainosho, M. and James, T.L. (1998) DNA duplex dynamics: NMR relaxation studies of a decamer with uniformly ^{13}C-labeled purine nucleotides. *J Magn Reson*, **135**, 310-333.

45. SantaLucia, J., Jr., Shen, L.X., Cai, Z., Lewis, H. and Tinoco, I., Jr. (1995) Synthesis and NMR of RNA with selective isotopic enrichment in the bases. *Nucleic Acids Res*, **23**, 4913-4921.

46. Hatala, P.J., Kallmerten, J. and Borer, P.N. (2001) Regioselective synthesis of 1,3,5-$^{13}C_3$ and 2,4-$^{13}C_2$-labeled 2-deoxyribonolactones. *Nucleosides Nucleotides Nucleic Acids*, **20**, 1961-1973.

47. LeMaster, D.M. and Cronan, J.E., Jr. (1982) Biosynthetic production of ^{13}C-labeled amino acids with site-specific enrichment. *J Biol Chem*, **257**, 1224-1230.

48. LeMaster, D.M. and Kushlan, D.M. (1996) Dynamical mapping of *E. coli* thioredoxin via ^{13}C NMR relaxation analysis. *J Am Chem Soc*, **118**, 9255-9264.

49. Batey, R.T., Battiste, J.L. and Williamson, J.R. (1995) Preparation of isotopically enriched RNAs for heteronuclear NMR. *Methods Enzymol*, **261**, 300-322.

50. Johnson, J.E., Jr., Julien, K.R. and Hoogstraten, C.G. (2006) Alternate-site isotopic labeling of ribonucleotides for NMR studies of ribose conformational dynamics in RNA. *J Biomol NMR*, **35**, 261-274.

51. Voet, D., Voet, J. and Pratt, C.W. (2002) *Fundamentals of Biochemistry*. John Wiley & Sons, Inc., Hoboken, New Jersey, USA.

52. Fraenkel, D.G. (1968) Selection of *Escherichia coli* mutants lacking glucose-6-phosphate dehydrogenase or gluconate-6-phosphate dehydrogenase. *J Bacteriol*, **95**, 1267-1271.

53. Ebrahimi, M., Rossi, P., Rogers, C. and Harbison, G.S. (2001) Dependence of ^{13}C NMR chemical shifts on conformations of RNA nucleosides and nucleotides. *J Magn Reson*, **150**, 1-9.

54. Rossi, P. and Harbison, G.S. (2001) Calculation of ^{13}C chemical shifts in RNA nucleosides: structure-^{13}C chemical shift relationships. *J Magn Reson*, **151**, 1-8.

55. Hoogstraten, C.G. and Johnson, J.E., Jr. (2007) Metabolic Labeling: Taking advantage of bacterial pathways to prepare spectroscopically

useful isotope patterns in proteins and nucleic acids. *Concepts Magn Reson Part A*, **32A**, 35-55.

56. Bryce, D.L., Grishaev, A. and Bax, A. (2005) Measurement of ribose carbon chemical shift tensors for A-form RNA by liquid crystal NMR spectroscopy. *J Am Chem Soc*, **127**, 7387-7396.

57. Kline, P.C. and Serianni, A.S. (1990) ^{13}C-enriched ribonucleosides: synthesis and application of ^{13}C-^{1}H and ^{13}C-^{13}C spin-coupling constants to assess furanose and N-glycoside bond conformations. *J Am Chem Soc*, **112**, 7373-7381.

58. Wijmenga, S. and van Buuren, B. (1998) The use of NMR methods for conformational studies of nucleic acids. *Prog Nucl Magn Reson Spectrosc*, **32**, 287-387.

59. Hartmann, S.R. and Hahn, E.L. (1962) Nuclear double resonance in the rotating frame. *Phys Rev*, **128**, 2042.

60. Legault, P., Hoogstraten, C.G., Metlitzky, E. and Pardi, A. (1998) Order, dynamics and metal-binding in the lead-dependent ribozyme. *J Mol Biol*, **284**, 325-335.

Chapter 3

Analysis of Ribose Dynamics in the GCAA RNA Hairpin Studied by ^{13}C NMR Spin Relaxation Experiments

Portions of this chapter were derived from "Extensive backbone dynamics in the GCAA RNA tetraloop analyzed using ^{13}C NMR spin relaxation and specific isotope labeling" to be published by the Journal of the American Chemical Society (2008), written by Dr. Charles G. Hoogstraten and myself.

INTRODUCTION

Conformational dynamics play an important role in the function of enzymes. For RNA molecules, conformational dynamics play an equally important role in events such as RNA catalysis and ligand recognition (1-4). A common feature found in RNA tertiary structures are tetraloop sequences, which can be found at the capping ends of hairpin stems (5), particularly GNRA sequences where N stands for any nucleotide and R stands for either guanosine or adenine. Studies have revealed that tetraloop sequences are highly stable (6-8). In addition to stabilizing hairpin structures, GNRA tetraloop sequences have been shown to mediate tertiary RNA-RNA (9,10) and RNA-protein interactions (11,12).

NMR solution and X-ray crystal structures of GNRA RNA hairpins have been solved (13-19). The structures of GNRA RNA hairpins determined from NMR structures solved by Jucker *et al.* (14) were found to be A-form RNA with anti conformations for all glycosidic bond angles with C3′-endo sugar pucker conformations for nearly all residues. Within the tetraloop, only the ribose ring of G_5 was determined to have C3′-endo conformation while the remaining tetraloop sugar pucker conformations were determined to be in equilibrium. The GNRA tetraloop has a major change in the direction of the phosphate backbone between the first and the second loop nucleotide (G_5-N_6) forming an asymmetric loop in which the opening base stacks on the 5′ side of the helix while the remaining bases stack on the 3′ side, and G_5 and A_8 form a sheared anti-anti

base pair (Fig. 3.1a). In two of the ten structures of the NMR ensemble for the GCAA RNA hairpin (pdb code 1zih), the base of C_6 was exposed to solvent and not stacked upon A_7 (Fig. 3.1b), in contrast to A_6 of GAGA and GAAA RNA hairpins (14). This is consistent with results from molecular dynamic simulations of the GCAA RNA hairpin where the ribose ring of C_6 was observed to undergo a change in sugar conformation from C3′-endo to C2′-endo (Fig. 3.2) in a correlated fashion with base extrusion (20).

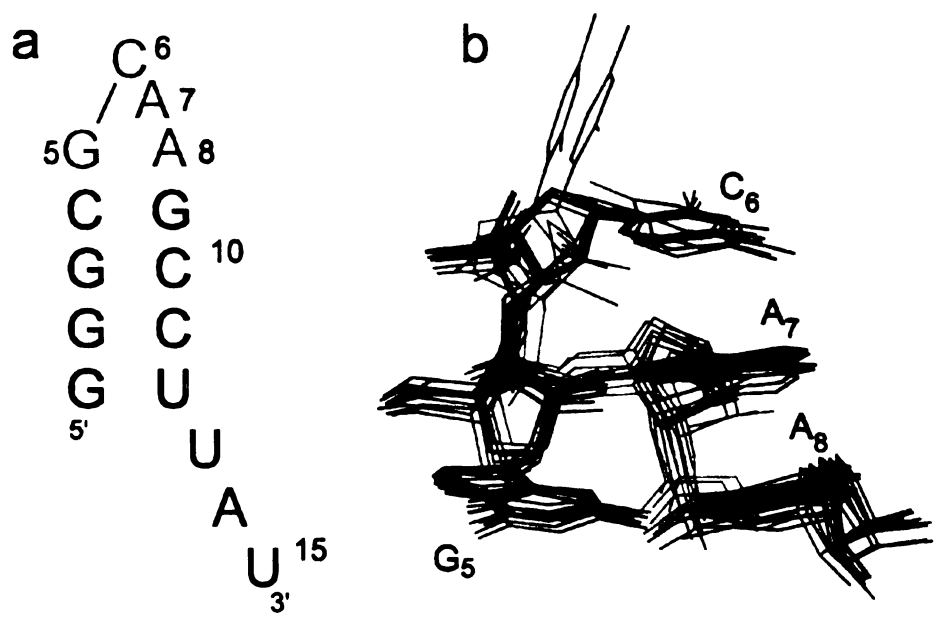

Figure 3.1: The GCAA RNA hairpin. (a) Secondary structure of the RNA construct used in these studies. Tetraloop residues are displayed in red and the unstructured 3′ tail is displayed in blue. (b) Superimposition of the ten NMR structures (pdb code 1zih) for the tetraloop residues 5-8 of the GCAA RNA hairpin (14).

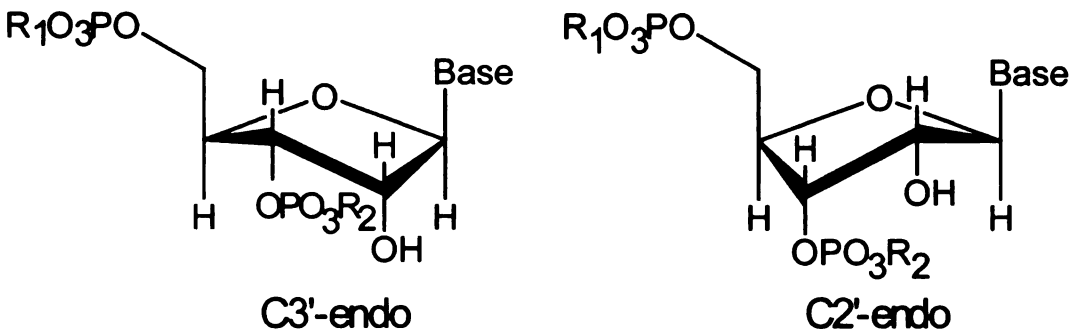

Figure 3.2: Diagram of sugar pucker conformations adopted by A-form RNA molecules.

NMR spin relaxation techniques can be used to study molecular motions on several timescales (21-30). A conformational exchange process that alters the local magnetic environment for a given nucleus will contribute to the dephasing of the transverse coherences (26). For the simplest case of a two-site exchange model of A reversibly interconverting with B, the exchange rate constant, k_{ex}, is the sum of the forward and reverse rate constants, k_1 and k_{-1}.

$$k_{ex} = k_1 + k_{-1} \qquad [3.1]$$

The populated states can be observed in the NMR spectra as two resolved resonances in the slow exchange regime or as a single population-weighted average resonance in the fast exchange regime. Determination of exchange regimes depends on the relation between k_{ex} and $\Delta\omega$, the chemical shift difference between the populated states. In the fast exchange regime, the exchange rate is much greater than the chemical shift difference. Carr-Purcell-Meiboom-Gill (CPMG) (31-33) and rotating-frame ($R_{1\rho}$) (34) transverse relaxation experiments are sensitive to motional processes that are on the μs to

ms timescale. These motional processes can contribute to the overall transverse relaxation rate as an additional term, R_{ex}:

$$R_2^{obs} = R_2^0 + R_{ex} \qquad [3.2]$$

where R_2^{obs} is the measured transverse relaxation rate and R_2^0 is the transverse relaxation rate in the absence of exchange.

CPMG experiments measure the transverse relaxation rate as a function of successive spin echo time periods, τ_{CP}, between 180° pulses. Conformational changes that affect the frequency of precession lead to imperfect refocusing of transverse magnetization during the spin-echo period. An expression for transverse relaxation rate dependence on τ_{CP} in the fast exchange regime is given by:

$$R_2(1/\tau_{CP}) = R_2(1/\tau_{CP}\rightarrow\infty) + p_A p_B(\Delta\omega)^2/k_{ex}*(1-((\tanh(k_{ex}/(4*\tau_{CP})))*4*\tau_{CP}/k_{ex})) \qquad [3.3]$$

where $R_2(1/\tau_{CP}\rightarrow\infty)$ is the transverse relaxation rate in the absence of exchange, p_A and p_B are the exchangeable populations where the sum of p_A and p_B are equal to one, $\Delta\omega$ is the chemical shift difference in radians between the populated states A and B, k_{ex} is the exchange rate constant, and $2\tau_{CP}$ is the delay time between 180° pulses.

CPMG experiments have been used to measure exchange on the slow μs to ms timescale. For short μs timescales, measurements require rapid spin echo

periods which can damage the NMR sample and/or probe from excessive heating. Also, accurate measurement of relaxation rates is limited by the evolution of heteronuclear scalar coupling during τ_{CP}, where in-phase and anti-phase magnetization interconvert. In the absence of exchange, R_2^0 is expressed as:

$$R_2^0 = \varepsilon R_2^{in} + (1 - \varepsilon) R_2^{anti} \qquad [3.4]$$

where R_2^{in} and R_2^{anti} are the transverse relaxation rate constants for in-phase and anti-phase coherences averaged over the populations of each conformational state. $0 \leq \varepsilon \leq 1$ reflects the averaging between in-phase and anti-phase coherences due to evolution under the scalar coupling during τ_{CP}. Accurate motional parameters can be determined if $\varepsilon \approx 1$, which corresponds to τ_{CP} less than $1/(4J_{XH})$. Loria *et al.* (35) have developed a relaxation compensated CPMG pulse sequence that explicitly averages in-phase and anti-phase magnetization such that $\varepsilon = 0.5$. Using this pulse sequence, τ_{CP} values as large as $2/J_{NH}$ have been used for CPMG experimentation for basic pancreatic trypsin inhibitor.

$R_{1\rho}$ experiments measure the transverse relaxation rate as a function of the effective field, ω_{eff}, under spin-locked conditions. The effective field is the vector sum of the applied ω_1 radio frequency (RF) field and the resonance offset, Ω. The effective field, ω_{eff}, in radians per second can be expressed as:

$$\omega_{eff} = (\omega_1^2 + \Omega^2)^{1/2} \quad [3.5]$$

In the fast exchange regime, the transverse relaxation rate measured as a function of ω_{eff} is:

$$R_{1\rho}(\omega_{eff}) = R_{1\rho}(\omega_{eff} \rightarrow \infty) + p_A p_B (\Delta\omega)^2 * k_{ex} / (\omega_{eff}^2 + k_{ex}^2) \quad [3.6]$$

where $R_{1\rho}(\omega_{eff} \rightarrow \infty)$ is the transverse relaxation rate in the absence of exchange and $\Delta\omega$ is the chemical shift difference in radians between p_A and p_B. During spin-locked conditions, magnetization is rotated from the z-axis to its resultant effective field at a tilt angle given by $\tan\theta = \omega_1/\Omega$ and magnetization precesses around the resultant effective field. Conformational changes which alter the resonance offset lead to a loss in transverse magnetization.

$R_{1\rho}$ experimentation also suffers from limitation of timescale measurements. Yamazaki and co-workers (36) have designed an on-resonance $R_{1\rho}$ pulse sequence for accurate measurement of transverse relaxation rates with tilt angles > 70°. To satisfy this condition, transverse relaxation rates are measured at various ω_1 field strengths with constant resonant offset. However, at low ω_1 field strengths, $R_{1\rho}$ measurements become spurious due to oscillatory behavior of the magnetization (25). Alternatively, one can use an adiabatic pulse sequence (off-resonance) to align magnetization to effective fields with tilt angles < 70° (37).

Generally, only one type of experimentation is used depending on the timescale of the conformational exchange process. While advances have been made such that individual techniques can cover broader timescales, relatively few studies have combined CPMG and $R_{1\rho}$ data for analysis (38,39). Such limitation depends on the timescale of conformational exchange. This is represented by simulated CPMG and $R_{1\rho}$ relaxation dispersion curves in figure 3.3. For exchange rates $>10^4$ s^{-1}, $R_{1\rho}$ experiments are better suited to determine exchange parameters, while CPMG experiments contribute very little to the overall curve. Conversely, CPMG experiments determine the shape of the relaxation dispersion curve while $R_{1\rho}$ experiments yield little information for exchange rates $< 10^3$ s^{-1}. Alternatively, the Palmer group has designed a $R_{1\rho}$ pulse sequence to measure transverse relaxation rates at effective fields as low as 150 Hz (40). It is feasible that exchange rates that fall in between these ranges would be best analyzed using both experimentations.

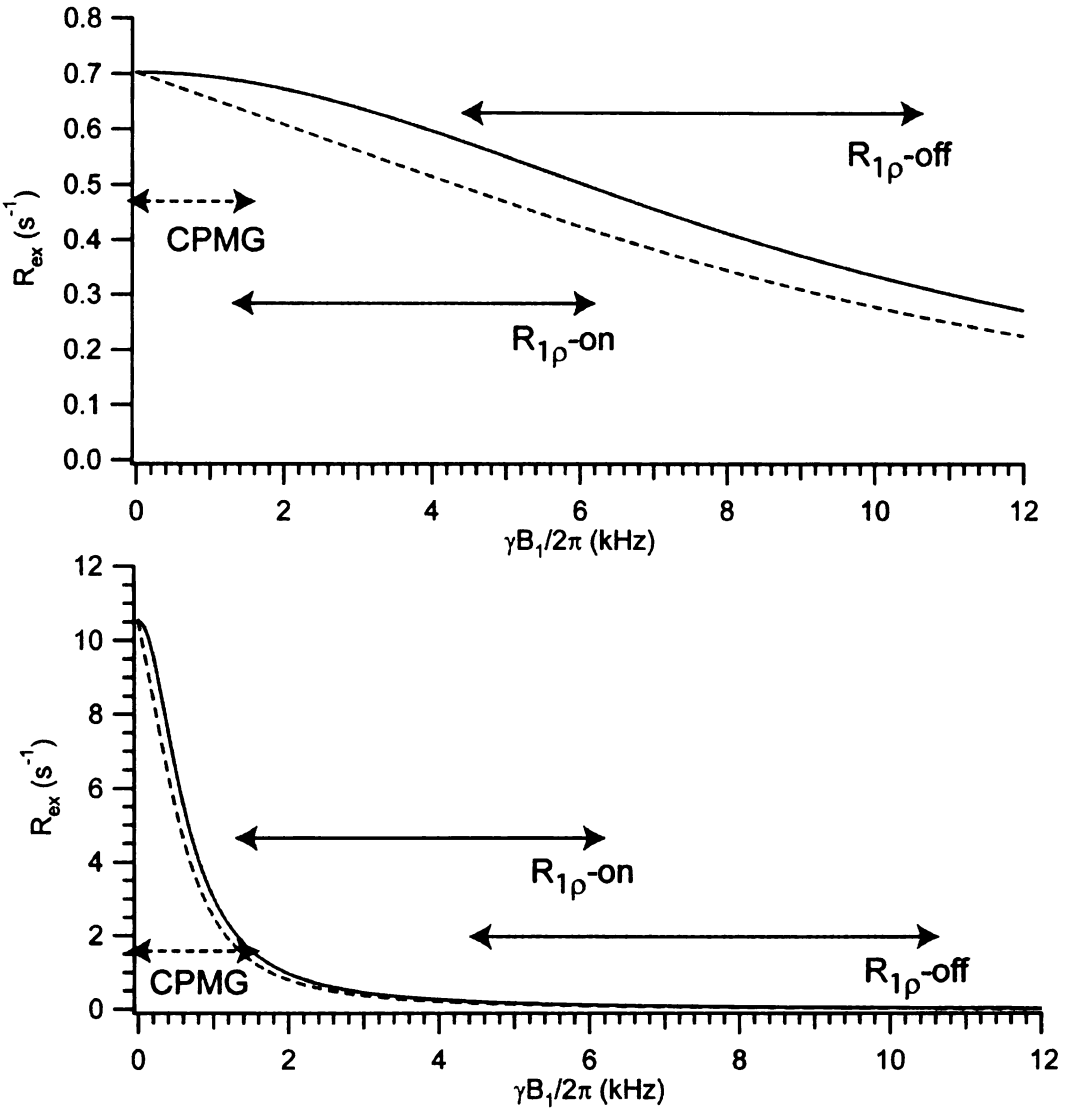

Figure 3.3: Functional forms of the dependence of exchange contributions to relaxation (R_{ex}) for $R_{1\rho}$ (solid lines) and CPMG (dashed lines) experiments on the effective γB_1 field are shown based on equations 3.3 and 3.6. Simulations are for ^{13}C nuclei at 600 MHz (150 MHz ^{13}C) and used $\Delta\omega$ = 1 ppm, p_A = 0.95, and k_{ex} = 60,000 s^{-1} (top) or 4000 s^{-1} (bottom). Approximate experimentally-accessible ranges for the three major types of relaxation dispersion experiments are shown with horizontal lines, with "on" and "off" denoting on-resonance and off-resonance $R_{1\rho}$ experiments, respectively.

As mentioned previously, conformational dynamics play an important role in the catalytic mechanism of ribozymes. A change in sugar pucker conformation was observed for the adenosine residue adjacent to the cleavage site in the active site of the hairpin ribozyme as determined from crystal structures (41). Analysis of exchange rates for this sugar pucker transition could aid in the understanding of the catalytic mechanism. While standard uniform ^{13}C enrichment renders the sugar ring of nucleotides unsuitable for NMR ^{13}C spin relaxation studies, the alternate-site labeling scheme can be used to probe sugar dynamics (see chapter 2). The tetraloop region of the GCAA RNA hairpin represents an excellent test-case for measurements of exchange rates for ribose pucker transitions. With the validation of the alternate site labeling scheme as a method to probe ribose dynamics in RNA molecules, analysis can be performed for biologically relevant RNA systems, such as the lead-dependent ribozyme or the hairpin ribozyme.

In this chapter, ribose dynamics across a broad timescale have been probed for the GCAA RNA hairpin using the alternate-site labeling scheme. Fast motions on the ps to ns timescales were analyzed by the model-free formalism of Lipari and Szabo (42-44). By analyzing combined CPMG and $R_{1\rho}$ relaxation dispersion curves at multiple field strengths, novel C2′ and C4′ ribose dynamics were observed within the tetraloop. From the similarity of measured exchange rates for C2′ and C4′ atoms, the existence of concerted residue dynamics has been proposed. Relaxation dispersion curves measured at multiple

temperatures has allowed for the determination of activation energies for ribose pucker transitions.

MATERIALS and METHODS

Preparation of Labeled ^{13}C Ribonucleotides. 2',4'-^{13}C rNTPs for the RNA GCAA hairpin were prepared as described earlier (45,46). The phosphorylation reaction was monitored by an Äkta Basic FPLC (GE Healthcare) with a Vydac 302IC4.6 Ion-Chromatography column (10 μm, 4.6mm × 250 mm) using a linear gradient from 25 mM 1:1 NaH_2PO_4:Na_2HPO_4, pH 2.8 to 125 mM 1:1 NaH_2PO_4:Na_2HPO_4, pH 2.9 over 34 min with a flow rate of 1 mL/min monitored by UV absorbance. ^{13}C rNTPs were purified from proteins using centrifugation, concentrated using a Rotovapor RE 120 (Buchi) under vacuum at 40 °C to a final volume of 1 mL, and purified using a DEAE Sephadex column with a 25 mL step gradient from 50 mM to 1M triethylamine bicarbonate, pH 7.5 at a flow rate of 2 mL/min with 4 mL fractions. ^{13}C rNTP fractions with an A_{260} above 0.1 were pooled and lyophilized repeatedly to remove excess salt. Uniformly labeled 99% ^{13}C, ^{15}N rNTPs were purchased commercially (Spectra Stable Isotopes).

Transcription of ^{13}C enriched GCAA RNA hairpin. 2',4'-$^{13}C_2$ and uniform ^{13}C rNTPs were incorporated into the fifteen nucleotide GCAA RNA hairpin by *in vitro* transcription using recombinant T7 RNA polymerase and a synthetic DNA template (47,48). Transcribed RNA was ethanol precipitated and purified using

denaturing polyacrylamide gel electrophoresis on a Bio-Rad model 491 preparative cell (49) with a flow rate of 1 mL/min with 4 mL fractions. RNA fractions corresponding to GCAA RNA hairpin as determined by gel electrophoresis were pooled, condensed as above to 1 mL, and desalted using a G-25 Sephadex column collecting 1 mL fractions. RNA was dried, exchanged into 99.9% D_2O with repeated lyophilization, and resuspended to a final concentration of 1.2 mM (2',4'-$^{13}C_2$) and 1.0 mM (uniform ^{13}C) in 280 μL 99.96% D_2O, 10 mM sodium phosphate pH 6.8, 100 mM NaCl, and 200 μM EDTA in an advanced microtube matched with D_2O (Shigemi, Inc.).

NMR Data Setup, Acquisition, and Processing. All NMR data were acquired on Varian UnityINOVA 600 MHz (^{13}C 150 MHz) or Bruker Avance 900 MHz (^{13}C 225 MHz) spectrometers. The 900 MHz spectrometer was equipped with a cryogenically cooled probe (Bruker TCI) in most cases. At 25 °C, ^{1}H-^{13}C hetereonuclear single quantum coherence (HSQC) spectra were acquired to verify chemical shift assignments previously obtained (14). The ^{1}H-^{13}C HSQC spectrum at 600 MHz was acquired with 1024 × 512 complex points in the t_2 and t_1 dimensions, respectively, with corresponding spectral widths of 6000 and 7540 Hz, and a 1 s recycle delay. The proton RF carrier was centered on the residual HDO signal, and the ^{13}C carrier frequency was set at 85 ppm to allow differential folding of the ribose and base ^{13}C resonances. The ^{1}H-^{13}C HSQC spectrum at

900 MHz was acquired with 512 × 64 complex points in the t_2 and t_1 dimensions, respectively, with corresponding spectral widths of 9920 and 15848 Hz, and 1 s recycle delay. The proton RF carrier was centered on the residual HDO signal, and the ^{13}C carrier frequency was centered at 75 ppm.

For ^{13}C relaxation experiments, all two-dimensional spectra acquired on the 600 MHz spectrometer were obtained with 1024 × 96 complex points in the t_2 and t_1 dimensions, respectively, with corresponding spectral widths of 6000 and 1800 Hz, a 2 s recycle delay, and 15 min of steady-state scans to allow for temperature equilibrium. The proton RF carrier was centered on the residual HDO signal, and the ^{13}C carrier frequency was set at 78.3 ppm. For experiments focusing on the aromatic ring, the ^{13}C carrier frequency was positioned at 138 ppm for C8 and C6 resonances and 153 ppm for C2 resonances. R_1, $R_{1\rho}$, and ^1H-^{13}C heteronuclear NOE (hNOE) data were acquired using minor variations of published pulse sequences (36). R_1 delay times ranged from 100 ms to 2000 ms collected in a random format. For $R_{1\rho}$, delay times ranged from 10 ms to 120 ms in a random format acquired at 2980 Hz spin-lock field. For saturated heteronuclear NOE experiments, protons were irradiated for 3 s with a total recycle delay of 7 s. For non-saturated heteronuclear NOE experiments, protons were not irradiated with a recycle delay of 7 s. Dispersion data were acquired using relaxation compensated CPMG

(35,50), on-resonance $R_{1\rho}$ (36), off-resonance $R_{1\rho}$ (37,51), and Hahn echo (52) pulse sequences. CPMG experiments were acquired as a function of inter-pulse spacing $2\tau_{CP}$, where τ_{CP} values ranged from 180 μs to 2500 μs, corresponding to effective spin-lock powers $\gamma B_1/2\pi$ [$\nu_{CP}=1/(4\tau_{CP})$] of ca. 1400 Hz to 80 Hz. On resonance $R_{1\rho}$ experiments were acquired as a function of the applied ω_1 RF, where $\omega_1/2\pi$ ranged from 1.5 to 6 kHz. Off resonance $R_{1\rho}$ experiments were acquired as a function of Ω at a $\omega_1/2\pi$ of 3 kHz, where $\Omega/2\pi$ ranged from 3.5 to 10 kHz. Magnetization was rotated to its effective field using adiabatic half passages of 4 ms. Hahn echo experiments were acquired with τ_{CP} values ranging from 25 to 62.5 ms. R_1, $R_{1\rho}$, ^{1}H-^{13}C hNOE, Hahn Echo, CPMG, on- and off-resonance data were acquired at 25 °C, and 35 °C. Off-resonance $R_{1\rho}$ was omitted at 15 °C. R_1 and on-resonance $R_{1\rho}$ were acquired at 20 and 30 °C.

For ^{13}C experiments acquired on the 900 MHz spectrometer, all two-dimensional spectra were obtained with 512 × 64 complex points in the t_2 and t_1 dimensions, respectively, with corresponding spectral widths of 9921 and 5656 Hz, a 1.6 s recycle delay and 256 steady-state scans. The proton RF carrier was centered on the residual HDO signal, and the ^{13}C carrier frequency was set at 77 ppm. R_1, $R_{1\rho}$, and heteronuclear NOE were acquired as described above. R_1

delay times used ranged from 0 s to 1.705 s, while $R_{1\rho}$ delay times ranged from 10 ms to 100 ms collected in a random format acquired at $\gamma B_1/2\pi$ of 1 kHz. CPMG and on-resonance $R_{1\rho}$ data were acquired as described above. On-resonance $R_{1\rho}$ experiments were acquired with a room temperature probe (Bruker TXI), and the ^{13}C RF carrier was set in the middle of the C2′ and C4′ regions, respectively. All data were acquired at 25 °C.

All NMR data were processed using FELIX 2002 (Felix NMR, Inc.). Prior to Fourier transformation in the t_2 dimension, a 20% DC offset was applied, data were zero filled, and a 3 Hz exponential line broadening function was applied. Prior to Fourier transformation in the t_1 dimension, t_1 was extended by 20% using linear prediction and a cosine-squared apodization function was applied.

Data Analysis. Resolved crosspeak intensities were integrated using FELIX 2002 and exported to Igor Pro 5.0.4 (WaveMetrics). In all experiments, one data point was acquired three times to determine error. R_1 and $R_{1\rho}^{obs}$ relaxation rates were extracted by fitting the integrated peaks to a single exponential decay. The ^1H-^{13}C hNOE was determined from the ratio of the saturated and non-saturated spectra. For dispersion curves, R_2 and $R_{1\rho}^{obs}$ rates were calculated using the equation $R_2/R_{1\rho}^{obs} = 1/T * \ln(I(T)/I_o)$, where T is the relaxation delay time, I is the measured intensity, and I_o is the measured intensity with no

relaxation delay. The I_o was acquired twice to ensure reproducibility. $R_{1\rho}$ rates were calculated from $R_{1\rho}^{obs}$ using the equation $R_{1\rho}^{obs} = R_1 \cos^2 \theta + R_{1\rho} \sin^2 \theta$, where $\theta = \tan^{-1} (\omega_1/\Omega)$ is the tilt angle of the spin lock axis from the z axis, ω_1 is the spin lock power in Hz and Ω is the offset in Hz. Errors were propagated from a single ω_{eff} or ν_{CP} repeated three times. Minimum thresholds of errors were set to 2%. k_{ex} and Φ_{ex}, where $\Phi_{ex} = p_A p_B(\Delta\omega^2)$, R_2^0, and $R_{1\rho}^0$ values were extracted by simultaneously fitting dispersion curves to CPMG and $R_{1\rho}$ equations (26) using Igor Pro 5 Global Analysis at a single field. To determine whether the timescale of exchange is in the fast, intermediate, or slow regime, a scaling factor, α, was determined using the equation (52):

$$\alpha = (B_2 + B_1) / (B_2 - B_1) * (R_{ex2} - R_{ex1}) / (R_{ex2} + R_{ex1}) \qquad [3.7]$$

where B_1 and B_2 are the magnetic field strengths in Tesla for the measured values of R_{ex1} and R_{ex2}, and $R_{ex} = p_A p_B \Delta\omega^2 / k_{ex}$.

Exchange parameters were determined from CPMG and $R_{1\rho}$ dispersion curves at 600 MHz and 900 MHz where Φ_{ex} at 900 MHz was imposed to be 2.25 times Φ_{ex} at 600 MHz. A k_{ex} was determined for each C2′ and C4′ atoms. In cases were k_{ex} values coincided in error for C2′ and C4′ atoms of a single residue, k_{ex} for that residue was refit to a single value. In cases where k_{ex}

values overlapped for several residues, multiple residues were refit to an overall k_{ex} value. F-statistic critical values (α) were calculated to justify fitting dispersion curves to motional dependent equations 3.3 and 3.6 as opposed to a horizontal line. F-values for C2′ and C4′ resonances were obtained by comparing χ^2 values obtained by fitting data sets to a horizontal line versus the dispersion equations. F-statistic critical values were obtained using the website: http://www.stattrek.com/tables/f.aspx. Confidence level was set to an α value of >0.95.

RESULTS

A method was previously reported to specifically ^{13}C label the ribose ring of ribonucleotides in an alternate-site fashion (46). Using these rNTPs, it was demonstrated that ^{13}C-^{13}C interactions were removed for R_1 and $R_{1\rho}$ measurements using the alternate-site labeling scheme when compared to uniform ^{13}C labeling. With this proof of concept, rNTPs utilizing the alternate-site labeling scheme were incorporated into a well characterized GCAA RNA hairpin to study ribose dynamics, particularly sugar re-puckering, by measuring motional timescales of C2′ and C4′ atoms.

Verification of Chemical Shifts. The ^{1}H-^{13}C HSQC at 600 MHz of the GCAA RNA was obtained to verify chemical shifts previously reported (14). Figure 3.4 shows the crosspeaks for (top) C2′ and (bottom) C4′ atoms of the GCAA RNA

hairpin. Thirteen C2′ and nine C4′ resonances were sufficiently resolved for analysis. All tetraloop resonances were resolved allowing for complete analysis of the tetraloop. From the ^{1}H-^{13}C HSQC, one can discern the severe broadening of the A_7 C2′ resonance. At 900 MHz, this resonance was so broadened that it is not observed in any spectra (data not shown). Due to this, data analysis for A_7 C2′ was only obtained at 600 MHz, while all other resonances were analyzed at both fields.

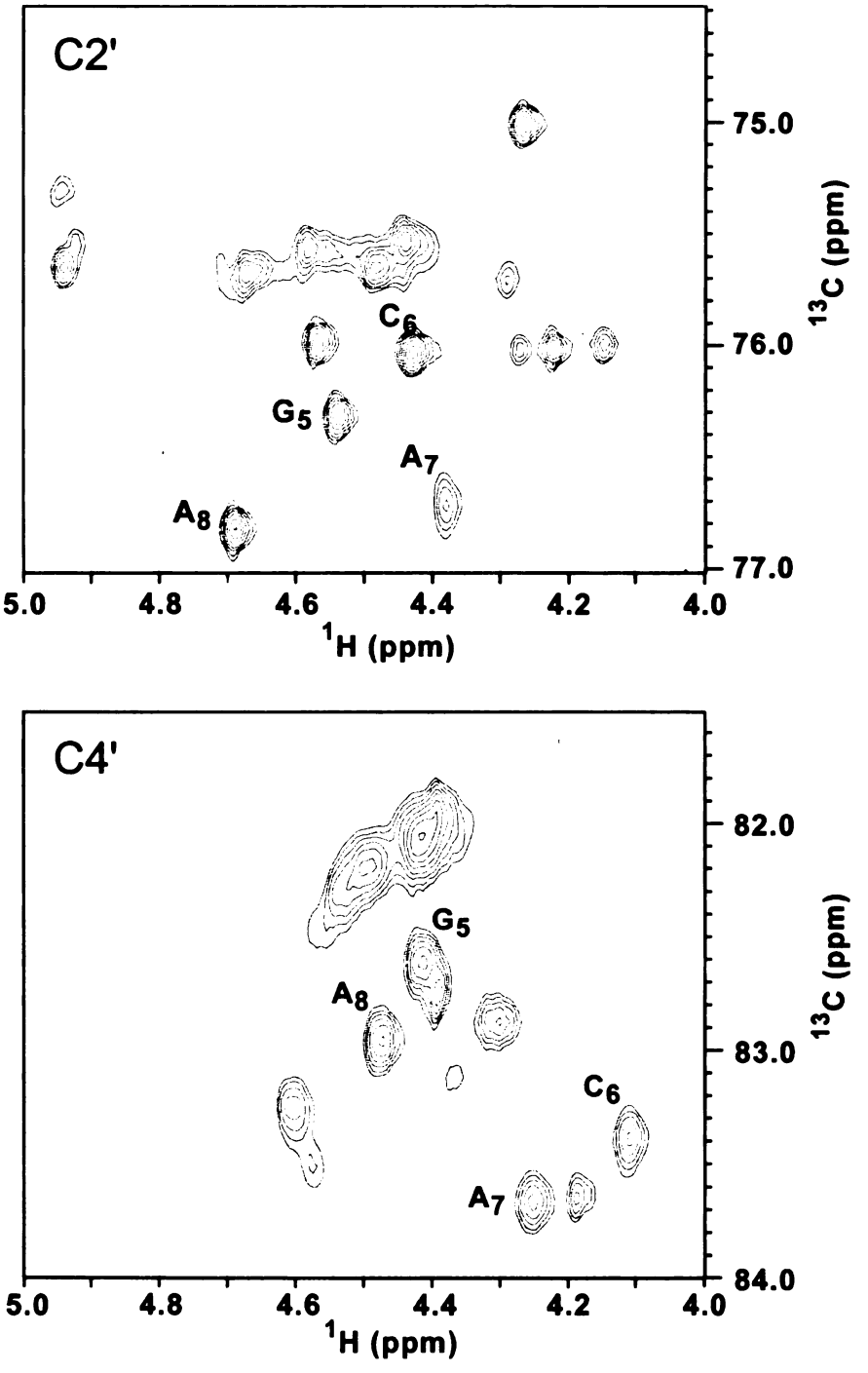

Figure 3.4: ^{1}H-^{13}C HSQC spectrum of a specifically-labeled GCAA RNA hairpin. C2′ (top) and C4′ (bottom) spectral regions are shown where tetraloop resonances are labeled.

Measurement of ^{13}C Relaxation Rates. Using modifications of published pulse sequences (36), R_1, $R_{1\rho}$, and ^1H-^{13}C hNOE measurements were acquired for C2′ and C4′ atoms of the GCAA RNA hairpin to confirm the presence of dynamics for ribose ring atoms within the tetraloop. Presented in Figure 3.5 are ^{13}C (a) R_1 and (b) $R_{1\rho}^{obs}$ curves for representative C2′ atoms for the stem, tetraloop, and 3′ tail obtained at 25 °C at 600 MHz. Shown in Table 3.1 are R_1 and offset-corrected $R_{1\rho}$ ^{13}C measurements obtained for 600 MHz data at 25 °C.

The effect of ps to ns dynamics can be revealed by an increase in R_1 values as well as a decrease in $R_{1\rho}$ values. The R_1 for U_{15} C2′ is higher (≈17%) than the average value of R_1 for helical C2's. Also, the $R_{1\rho}$ is diminished (≈18%). This is in good agreement with previous work (53,54). Because U_{15} is at the terminus in a single stranded region and presumably the least structured residue, relaxation rates obtained can be inferred as the maximum of ps to ns measurable for residues in the GCAA RNA hairpin. Dynamics on the ps to ns timescale were observed for resonances within the tetraloop. Increased R_1 values were observed for G_5 and C_6 C2's. Critical analysis of C4′ atoms is less clear due to the limited number of R_1 values.

Figure 3.5: Representative ^{13}C (a) R_1 and (b) $R_{1\rho}^{obs}$ curves obtained for (red) A_7; (black) G_9; and (blue) U_{15} at 25 °C. Curves represent non-linear least squares two-parameter fits to a single exponential.

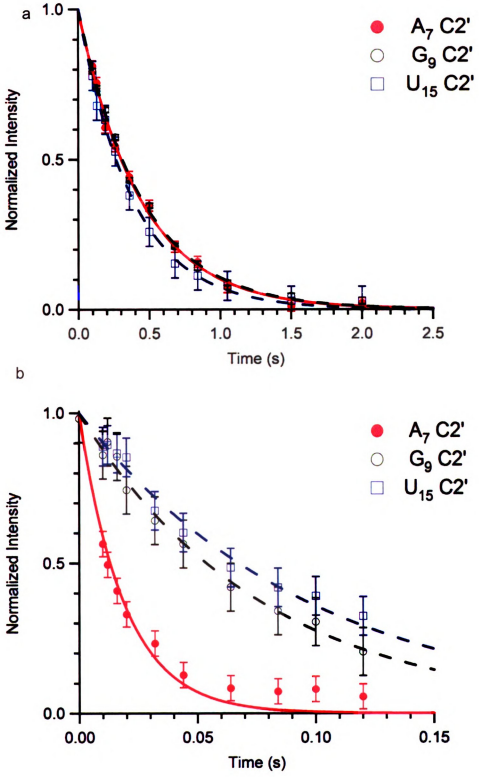
a
1.0
0.5
0.0
Normalized Intensity
0.0
0.5
1.0
1.5
2.0
2.5
Time (s)
A7 C2'
G9 C2'
U15 C2'
b
1.0
0.5
0.0
Normalized Intensity
0.00
0.05
0.10
0.15
Time (s)
A7 C2'
G9 C2'
U15 C2'

Table 3.1: R_1 and $R_{1\rho}$ ^{13}C measurement at 600 MHz for C2′ and C4′ atoms of the GCAA RNA hairpin.

R_1 Relaxation (s^{-1})				$R_{1\rho}$ Relaxation (s^{-1})			
C2′ Region		C4′ Region		C2′ Region		C4′ Region	
G_1	2.4 ± 0.1	G_1	2.12 ± 0.05	G_1	10.7 ± 0.3	G_1	13.3 ± 0.6
G_2	2.13 ± 0.05			G_2	13.2 ± 0.4		
G_3	2.27 ± 0.07			G_3	13.1 ± 0.6		
G_5	2.49 ± 0.06	G_5	2.38 ± 0.09	G_5	16.6 ± 0.7	G_5	17.6 ± 0.7
C_6	2.40 ± 0.04	C_6	2.44 ± 0.08	C_6	12.6 ± 0.4	C_6	39.3 ± 0.9
A_7	2.29 ± 0.09	A_7	2.52 ± 0.06	A_7	53 ± 4	A_7	29.1 ± 0.6
A_8	2.27 ± 0.02	A_8	2.38 ± 0.03	A_8	19.5 ± 0.6	A_8	21.5 ± 0.8
G_9	2.24 ± 0.06	G_9	2.32 ± 0.04	G_9	12.9 ± 0.6	G_9	13.4 ± 0.6
C_{10}	2.15 ± 0.03	C_{10}	2.4 ± 0.1	C_{10}	13.0 ± 0.6	C_{10}	13.2 ± 0.6
U_{12}	2.0 ± 0.1	U_{12}	2.3 ± 0.1	U_{12}	12.4 ± 0.9	U_{12}	15.8 ± 0.9
U_{13}	2.35 ± 0.08	U_{13}	2.42 ± 0.08	U_{13}	11.6 ± 0.6	U_{13}	11 ± 1
A_{14}	2.27 ± 0.05			A_{14}	13.1 ± 0.4		
U_{15}	2.6 ± 0.1			U_{15}	10.3 ± 0.5		

Tetraloop atoms are shaded in grey while 3′ single stranded atoms are shaded in blue.

Model-free Analysis. To further quantify disorder on the ps-ns timescale, the model-free formalism of Lipari & Szabo (42-44) was performed using R_1, $R_{1\rho}$, and ^1H-^{13}C hNOE measurements acquired at 600 MHz. Calculations using the model-free analysis were performed by Dr. Charles G. Hoogstraten. Using the computer program Modelfree 4.1, motional parameters were determined for atoms in the GCAA RNA hairpin using R_1, $R_{1\rho}$, and hNOE values measured at 600 MHz. Motional parameters determined were S^2, τ_e, and R_{ex}. The results of this analysis are shown in Table 3.2 and Figure 3.6 With the exception of the

terminal G_1:U_{12} base pair and the unpaired 3'-tail, the order parameter S^2, for a given type of carbon, is high and uniform, indicating a lack of structural disorder in the helix and tetraloop which is consistent with the well-structured and thermodynamically stable nature of the system (7). The resulting overall isotropic correlation time, τ_c, for overall molecular tumbling was 3.00 ns, in good agreement with a value recently reported from analysis of nucleotide aromatic ^{13}C data in a 14-nucleotide GCAA RNA hairpin construct (55). Of the total of 22 resonances analyzed, 11 could be satisfactorily fit using S^2 alone, 2 required the τ_e term in addition to the S^2 term, 6 (comprising 6 of the 8 resonances within the tetraloop) required R_{ex}, and 3 (including one resonance from the tetraloop) required all three parameters. It should be noted that relative values obtained for the two carbon types are strongly dependent on the values of the chemical shift anisotropy parameter (CSA) used (data not shown). The values of CSA used here, 26.6 ppm for C2' and 91.7 for C4', have strong experimental support for rigid A-form helices (56). Rigorous interpretation of relative S^2 values between C2' and C4' resonances would depend on careful consideration of the values and relative orientation of the C-H bond vector and the CSA tensor for various states of the ribose ring, which is beyond the scope of the present work.

Table 3.2: Model-free analysis of ps – ns motion using 600 MHz data.

Resonance[a]	S^2	τ_e, ps	R_{ex}, s^{-1}
G_2 C2′	0.808 ± 0.044	69.2 ± 19.0	2.00 ± 0.67
G_3 C2′	0.973 ± 0.023		
G_5 C2′[b]	0.903 ± 0.038	892.4 ± 291.2	3.84 ± 0.79
C_6 C2′	0.901 ± 0.028	266.0 ± 83.8	
A_7 C2′	0.984 ± 0.027		39.5 ± 4.2
A_8 C2′	0.975 ± 0.011		6.28 ± 0.64
G_9 C2′	0.960 ± 0.022		
C_{10} C2′	0.926 ± 0.014		
U_{12} C2′	0.892 ± 0.042		
A_{14} C2′	0.972 ± 0.017		
U_{15} C2′	0.709 ± 0.041	459.6 ± 108.3	
G_1 C4′	0.815 ± 0.018		
G_5 C4′	0.903 ± 0.036		3.57 ± 0.92
C_6 C4′	0.926 ± 0.030		24.9 ± 1.0
A_7 C4′	0.956 ± 0.023		14.2 ± 0.7
A_8 C4′	0.903 ± 0.014		7.47 ± 0.86
G_9 C4′	0.878 ± 0.015		
C_{10} C4′	0.875 ± 0.028		
U_{12} C4′	0.792 ± 0.049	40.3 ± 20.5	3.31 ± 1.19

(a) No satisfactory model could be fit for G_1 C2′, U_{13} C2′, and U_{13} C4′ using the combinations of S^2, τ_e, and R_{ex} tested. As these residues are at the 5′-terminus or in the 3′-unstructured tail, and thus of little relevance to the goals of the study, further detailed analysis was not attempted. (b) This residue could only be satisfactorily fit by allowing a τ_e value of ca. 30% of the isotropic correlation time, in violation of the known limits of validity of the model-free approach. Results should be interpreted with caution.

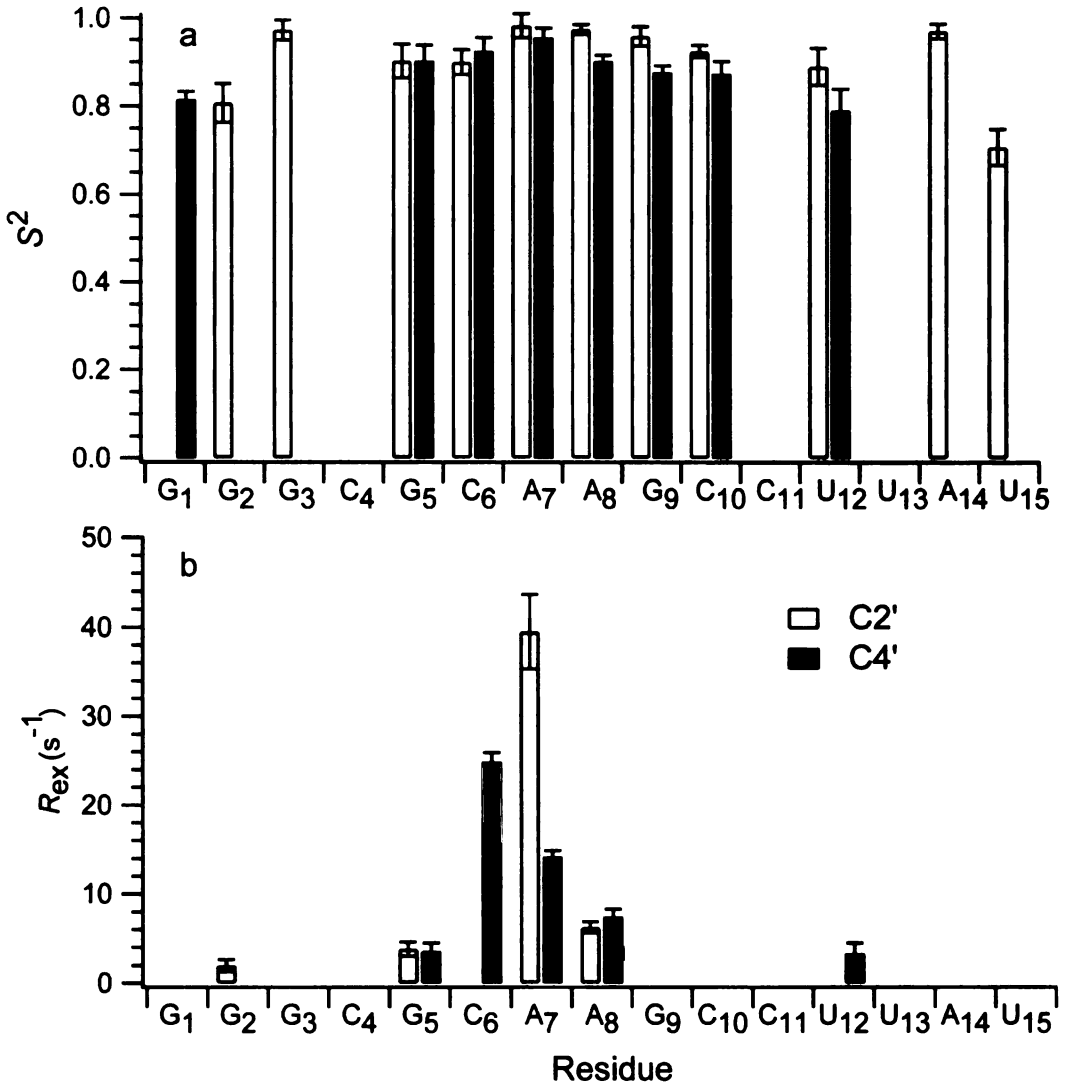

Figure 3.6: Analysis of relaxation data at 600 MHz using the model-free formalism at 25 °C where (a) generalized order parameter S^2 and (b) exchange contribution to transverse relaxation R_{ex} are shown. Open bars are C2′ atoms and shaded are C4′ atoms.

Measurement of Relaxation Dispersion Curves. Motions on the μs to ms timescales can affect the transverse relaxation as a measurable term, R_{ex}. While model-free analysis can suggest the existence of R_{ex} contributions, a more accurate determination of R_{ex} contributions is the analysis of relaxation dispersion curves. Relaxation dispersion curves are the dependence of the measured transverse relaxation rate on the effective field determined by spin-echo modulated spacing for CPMG based experiments or applied RF field and the resonance offset for $R_{1\rho}$ experiments. While relaxation dispersion curves have been utilized to investigate conformational exchange processes extensively in proteins (27-29,50,52,57,58), little analysis has been done for RNA oligomers (25,59). Because CPMG and $R_{1\rho}$ experiments are, in principle, similar and both report on transverse relaxation rates, the combination of these experiments can allow for complete analysis of effective field-dependence of relaxation rates. From these curves, one can calculate k_{ex}, the timescale of exchange within the μs – ms regime. In general, there are cases where either CMPG or $R_{1\rho}$ experiments were sufficient to obtain k_{ex} values of motion. Based on previous RNA dispersion work (25) as well as using a novel isotope labeling scheme (46), combinations of CPMG, on-, and off-resonance $R_{1\rho}$ were acquired to critically analyze ribose dynamics within the tetraloop region of the GCAA RNA hairpin.

^{13}C Hahn Echo Measurements. ^{13}C relaxation measurements were acquired using Hahn echo experiments to determine $R_{ex}(\omega_{eff} \rightarrow 0)$, which can identify resonances that are undergoing conformational exchange processes (60). Shown in Fig. 3.7 are Hahn echo R_2 measurements for (a) C2′ and (b) C4′ atoms. Increased R_2 were observed for both C2′ and C4′ atoms of A_7 and A_8, C2′ of G_5, C4′ of C_6, and a possible increase for G_5 C4′. This is in good agreement with $R_{1\rho}$ measurements obtained (Table 3.1) as well as the results of the model-free analysis (Fig 3.5b). However, no R_{ex} contribution was observed for C_6 C2′. It is not immediately obvious why no R_{ex} contribution is detected given that a significant contribution is observed for C_6 C4′ as well as R_{ex} contributions for all other tetraloop C2′ and C4′ atoms.

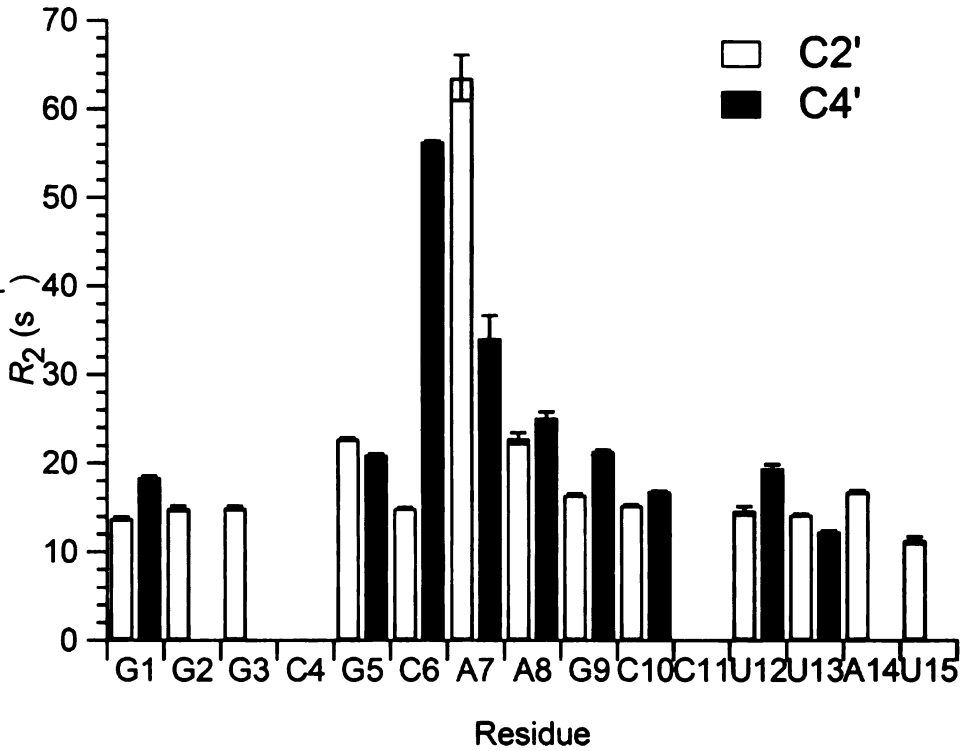

Figure 3.7: ^{13}C R_2 measurements from Hahn echo experiments. Rates are shown for C2′ (open) and C4′ (closed) atoms at 25 °C.

Measurement of μs to ms Motions. Due to the observation of increased measured transverse relaxation rates as well as R_{ex} contributions determined using the model-free analysis, relaxation dispersion curves were acquired to examine conformational exchange processes within the tetraloop in detail using relaxation-compensated CPMG (rcCPMG) and on-resonance $R_{1\rho}$ experiments acquired at two field strengths of 600 MHz (^{13}C 150 MHz) and 900 MHz (^{13}C 225 MHz) at 25 °C. Relaxation dispersion curves at 600 MHz were extended using off-resonance $R_{1\rho}$ experiments. Relaxation dispersion curves were fit to equations 3.3 and 3.6 to determine k_{ex}, R_2^0 or $R_{1\rho}^0$, and Φ_{ex}, where Φ_{ex} =

$p_A p_B(\Delta\omega)^2$. To validate the use of fast-exchange equations, an α scaling factor was determined for each residue in the tetraloop using equation 3.7. Exchange within the fast-exchange regime will have an α scaling factor of 2. α scaling factors for all ^{13}C carbons in the tetraloop that were able to be measured at both magnetic fields were calculated to be 1.7 or above. Because of this, exchange parameters could be determined from equations 3.3 and 3.6, which were derived for the fast-exchange limit, as opposed to the more general exchange equations (26,61).

In Figure 3.8, relaxation dispersion curves are shown from simultaneous fitting to equations 3.3 and 3.6, which gave a statistically significant improvement versus a description using ω_1-independent rates (cumulative probability for F-statistic > 0.99) except for G_5 C4′ (cumulative probability for F-statistic is 0.91). Statistically significant dispersive effects for G_3 and G_9 C2′ atoms were calculated, as well as for the 3′ single stranded C2′ atoms. Motional parameters determined by fitting the dispersion curves to equations 3.3 and 3.6 were either poorly defined or were not consistent with the fast-exchange regime ($k_{ex} >> \Delta\omega$).

Figure 3.8: Relaxation dispersion curves for tetraloop atoms in the GCAA RNA hairpin. CPMG (open symbols) and on- and off-resonance $R_{1\rho}$ (solid symbols) data are shown for C2′ and C4′ atoms respectively of (a,b) G_5, (c,d) C_6, (e,f) A_7, and (g,h) A_8. Upper traces represent data at 900 MHz (225 MHz ^{13}C) and lower at 600 MHz (150 MHz ^{13}C) except in the case of A_7 C2′, for which data at 900 MHz was unavailable due to fast relaxation. For C_6 C2′, a horizontal-line fit to the data is shown. Otherwise, solid lines denote simultaneous fits of all data for the corresponding atom to equations 3.3 and 3.6, dashed lines (for G_5, A_7, and A_8) denote simultaneous fits to C2′ and C4′ results for a particular residue, and dotted lines represent global fits of all data for either C_6 and A_7 (apical residues) or G_5 and A_8 (closing base pair). In many cases, dashed and/or dotted lines are not visible due to coincidence with the solid lines representing resonance-specific fits.

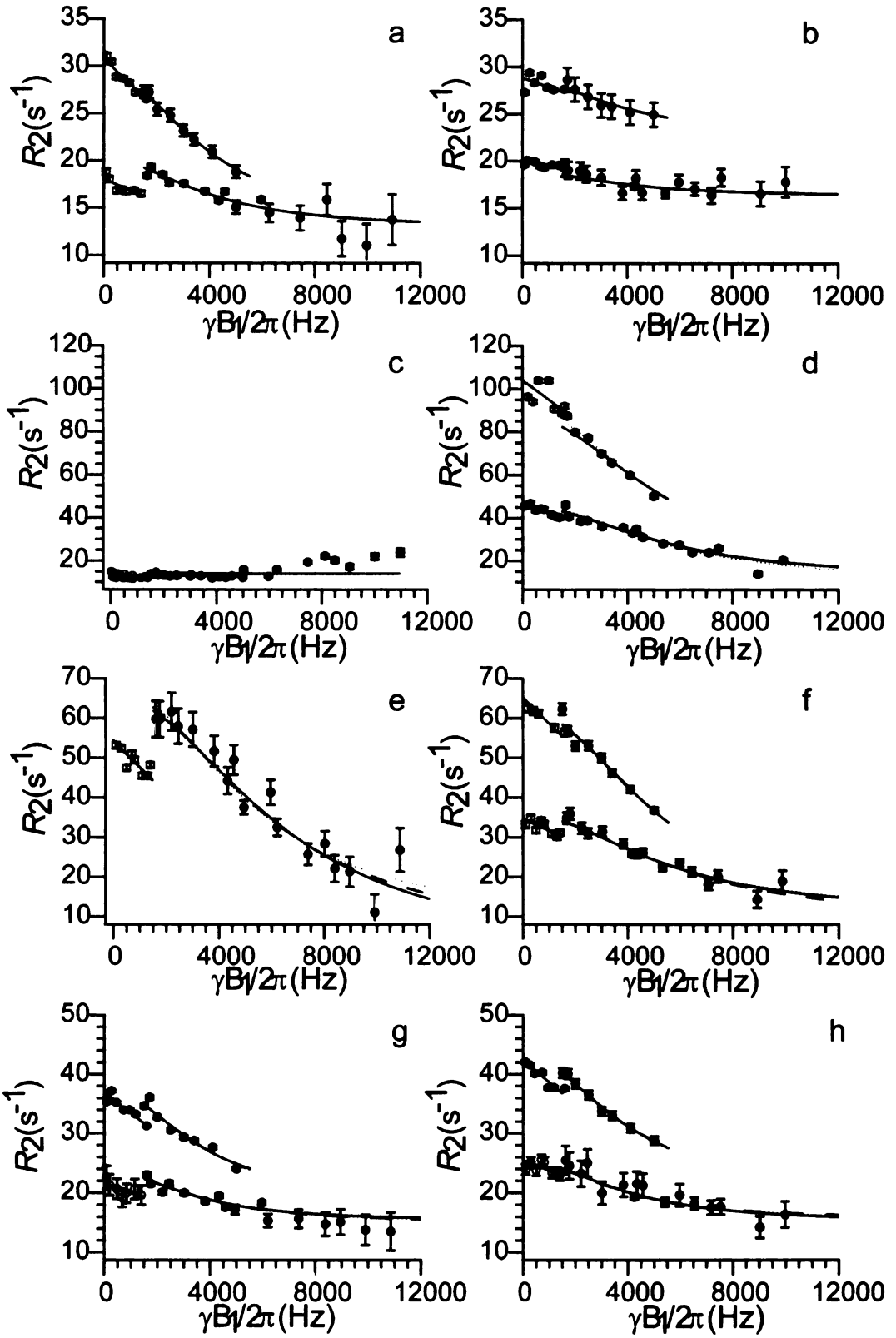
a
b
c
d
e
f
g
h
R2(s-1)
γB1/2π(Hz)
0
4000
8000
12000

Table 3.3: Motional parameters derived via fitting of relaxation dispersion data at both fields for a single atom to equations 3.3 and 3.6 at 25 °C.

Resonance	Φ_{ex}^{600}	k_{ex}, s^{-1}	$R_2^{0,600}$, s^{-1}	$R_{1\rho}^{0,600}$, s^{-1}	$R_2^{0,900}$, s^{-1}	$R_{1\rho}^{0,900}$, s^{-1}
G_5C2'	$(1.8 \pm 0.3) \times 10^5$	$(2.5 \pm 0.3) \times 10^4$	10.7 ± 0.5	12.8 ± 0.6	14.2 ± 1.9	12.8 ± 2.0
G_5C4'	$(6.4 \pm 4.7) \times 10^4$	$(2.4 \pm 1.3) \times 10^4$	17.3 ± 0.9	16.3 ± 0.9	22.9 ± 3.1	22.7 ± 3.1
C_6C4'	$(1.2 \pm 0.2) \times 10^6$	$(3.4 \pm 0.4) \times 10^4$	12.3 ± 3.3	11.5 ± 3.7	27.4 ± 9.8	11.3 ± 10.3
A_7C2'	$(2.6 \pm 0.6) \times 10^6$	$(4.0 \pm 0.6) \times 10^4$	-11.2 ± 6.6	0 ± 7.6	N/A	N/A
A_7C4'	$(8.8 \pm 1.8) \times 10^5$	$(3.5 \pm 0.4) \times 10^4$	9.3 ± 2.3	10.4 ± 2.6	8.2 ± 7.0	5.4 ± 7.6
A_8C2'	$(1.8 \pm 0.3) \times 10^5$	$(2.2 \pm 0.3) \times 10^4$	13.0 ± 0.9	15.1 ± 0.6	17.7 ± 1.5	18.7 ± 1.7
A_8C4'	$(2.6 \pm 0.6) \times 10^5$	$(2.5 \pm 0.4) \times 10^4$	15.0 ± 1.6	14.9 ± 1.1	18.9 ± 2.9	19.6 ± 3.2

Listed in Table 3.3 are parameters for the tetraloop region determined by simultaneous fitting of the relaxation dispersion curves at 600 MHz and 900 MHz, where appropriate. Φ_{ex} was only reported at 600 MHz because Φ_{ex}^{900} was imposed to be 2.25 times that of Φ_{ex}^{600}. k_{ex} values ranging from 22000 to 40000 s^{-1} were determined. Because the exchange rate constant, k_{ex}, is the sum of k_1 and k_{-1} for two states A and B, it can be postulated that k_{ex} values for atoms of the ribose ring are reporting on sugar pucker transitions, i.e., C3′-endo to C2′-endo interconversions. For A_7 C2′, non physical R_2^0 and $R_{1\rho}^0$ rates were determined. Although this atom has significant R_{ex} contribution, the data collected only at 600 MHz are not sufficient to determine accurate exchange parameters. For this reason, parameters from A_7 C2′ only should be interpreted with caution.

Furthermore, estimates for chemical shift changes for C2′ and C4′ resonances were calculated from the Φ_{ex} term. Because exchange is within the fast-exchange regime, a population weighted chemical shift average was observed. Therefore, estimates for p_A and p_B were made to determine $\Delta\omega$ from the Φ_{ex} term. Using a value of 0.5 for p_A and p_B sets a minimum value for the chemical shift difference, $\Delta\omega_{min}$, between the two populations, C3′-endo and C2′-endo. Previous work (14) has determined sugar pucker conformations for the ribose ring for residues in the GAGA RNA hairpin from $J_{H1'-H2'}/J_{H3'-H4'}$

measurements. For three out of the four tetraloop residues of GAGA RNA hairpin, sugar pucker conformations were found to be in equilibrium. Similar equilibria for sugar pucker conformations were also seen in the GCAA construct. Based on these equilibrium measurements, estimated chemical shift changes for sugar pucker transitions, $\Delta\omega_{est}$, were determined from using p_A and p_B reflective of the equilibria.

Table 3.4: Motional parameters derived via fitting of all data for a single atom to equations 3.3 and 3.6 at 25 °C.

Residue	Atom	k_{ex}, s^{-1}	$(\Delta\omega)_{min}$, ppm[a]	$(\Delta\omega)_{est}$, ppm[b]	τ_{ex} (μs)[c]
G_5	C2′	$(2.5 \pm 0.3) \times 10^4$	0.90 ± 0.08	> 1.26	41 ± 5
	C4′[d]	$(2.4 \pm 1.3) \times 10^4$	0.53 ± 0.20	> 0.75	41 ± 22
C_6	C4′	$(3.4 \pm 0.4) \times 10^4$	2.28 ± 0.24	2.63 ± 0.28	29 ± 4
A_7	C2′	$(4.0 \pm 0.6) \times 10^4$	3.42 ± 0.41	3.73 ± 0.44	25 ± 4
	C4′	$(3.5 \pm 0.5) \times 10^4$	1.98 ± 0.21	2.15 ± 0.22	29 ± 4
A_8	C2′	$(2.2 \pm 0.3) \times 10^4$	0.91 ± 0.07	1.13 ± 0.09	46 ± 6
	C4′	$(2.5 \pm 0.4) \times 10^4$	1.07 ± 0.13	1.34 ± 0.17	$40. \pm 6$

(a) Values derived from $\Phi_{ex} = p_A p_B (\Delta\omega)^2$ using $p_A = p_B = 0.5$. (b) Values derived using estimates of C3′-endo pucker populations with p_A of 0.75 for C_6, 0.70 for A_7, and 0.8 for A_8, based on NMR J-coupling analysis. For G_5, J-coupling values were consistent with a fully C3′-endo population, and a lower bound for $\Delta\omega$ was thus derived using $p_A > 0.85$. (c) The characteristic time τ_{ex} for an exchange process is the reciprocal of k_{ex} and is included here to aid physical insight. (d) Improvements in χ^2 using Equations 3.3 and 3.6 for this resonance did not reach statistical significance versus a constant relaxation rate model ($P = 0.09$ for standard F-test).

Single Exchange Process for Ribose Sugar Pucker. It has been shown previously that measurement of exchange rates that are similar within error for multiple residues can suggest a single conformational event. Due to this, a single exchange rate for multiple atoms can be determined (58). This has also been demonstrated for C8/C6 and C1′ atoms in the U6 RNA ISL (59). From Table 3.4, k_{ex} values for C2′ and C4′ atoms for a given residue were observed to be equal within error. Consequently, global fitting was used to test whether the C2′ and C4′ atoms are reporting on the same conformational event. Fitting the C2′ and C4′ atoms to a single k_{ex} value does not significantly alter motional parameters (Table 3.5 and Fig 3.8). Slight alterations of motional parameters were observed for the residue of A_7 compared to those obtained from individual atom fits. This can be attributed to limited data acquired for A_7 C2′. However, values obtained are well within error compared to individual fit. Because C2′ and C4′ atoms were fit to a single k_{ex}, it can be interpreted that these atoms are reporting on the exchange process of ribose pucker interconversion within the tetraloop region of the GCAA RNA hairpin.

From the residue fit, we also noted a clustering of k_{ex} values for multiple nucleotides. k_{ex} values of $(2.5 \pm 0.3) \times 10^4$ and $(2.3 \pm 0.2) \times 10^4$ s^{-1} were measured for G_5 and A_8, respectively, while $(3.7 \pm 0.4) \times 10^4$ s^{-1} was measured for A_7. These exchange rates suggest that motions of residues are coupled

together. Therefore, motional parameters were determined for G_5 and A_8 using a single k_{ex} value as well as for C_6 and A_7. A global k_{ex} value of $(2.4 \pm 0.2) \times 10^4$ s^{-1} was measured for G_5 and A_8; and a single k_{ex} value of $(3.3 \pm 0.2) \times 10^4$ s^{-1} was determined for C_6 and A_7 (Table 3.6 and Fig 3.8). These results hint at correlated motions for G_5 and A_8, which can be attributed to a dynamic hydrogen bond network (13,14), while correlated motions for C_6 and A_7 can be tentatively attributed to base dynamics for C_6 (14,20).

Table 3.5: Motional parameters derived via fitting C2′ and C4′ data for a single residue to equations 3.3 and 3.6 for a single k_{ex} value at 25 °C.

Resonance	Φ_{ex}^{600}	k_{ex}, s^{-1}	$R_2^{0,600}$, s^{-1}	$R_{1\rho}^{0,600}$, s^{-1}	$R_2^{0,900}$, s^{-1}	$R_{1\rho}^{0,900}$, s^{-1}
G_5C2'	$(1.8 \pm 0.3) \times 10^5$	$(2.5 \pm 0.3) \times 10^4$	10.7 ± 0.5	12.8 ± 0.6	14.1 ± 1.8	12.8 ± 2.0
G_5C4'	$(6.5 \pm 2.4) \times 10^4$		17.3 ± 0.8	16.3 ± 0.5	22.9 ± 1.9	22.7 ± 1.5
A_7C2'	$(2.3 \pm 0.4) \times 10^6$	$(3.7 \pm 0.4) \times 10^4$	-8.9 ± 4.7	3.4 ± 4.6	N/A	N/A
A_7C4'	$(9.9 \pm 1.7) \times 10^5$		7.7 ± 2.3	8.7 ± 2.3	4.7 ± 6.4	1.4 ± 6.8
A_8C2'	$(2.0 \pm 0.3) \times 10^5$	$(2.3 \pm 0.2) \times 10^4$	12.7 ± 0.9	14.8 ± 0.6	17.1 ± 1.5	17.9 ± 1.6
A_8C4'	$(2.3 \pm 0.5) \times 10^5$		15.4 ± 1.6	15.4 ± 0.9	19.8 ± 1.8	20.8 ± 1.9

Table 3.6: Motional parameters derived via fitting C2′ and C4′ resonance data for multiple residues to equations 3.3 and 3.6 for a single k_{ex} value at 25 °C.

Resonance	Φ_{ex}^{600}	k_{ex}, s^{-1}	$R_2^{0,600}$, s^{-1}	$R_{1\rho}^{0,600}$, s^{-1}	$R_2^{0,900}$, s^{-1}	$R_{1\rho}^{0,900}$, s^{-1}
G_5C2'	$(1.7 \pm 0.2) \times 10^5$	$(2.4 \pm 0.2) \times 10^4$	10.8 ± 0.5	13.0 ± 0.4	14.5 ± 1.4	13.3 ± 1.3
G_5C4'	$(6.1 \pm 2.1) \times 10^4$		17.4 ± 0.8	16.4 ± 0.4	23.1 ± 1.8	22.9 ± 1.4
A_8C2'	$(2.1 \pm 0.3) \times 10^5$		12.6 ± 0.9	14.7 ± 0.5	16.9 ± 1.4	17.6 ± 1.4
A_8C4'	$(2.4 \pm 0.5) \times 10^5$		15.2 ± 1.6	15.2 ± 0.8	19.5 ± 1.7	20.4 ± 1.7
C_6C4'	$(1.2 \pm 0.1) \times 10^6$	$(3.3 \pm 0.2) \times 10^4$	9.7 ± 1.4	9.8 ± 1.4	21.8 ± 4.9	8.3 ± 5.2
A_7C2'	$(2.0 \pm 0.2) \times 10^6$		-6.0 ± 3.8	7.4 ± 2.9	N/A	N/A
A_7C4'	$(8.3 \pm 0.9) \times 10^5$		9.9 ± 1.6	11.1 ± 1.4	9.5 ± 3.6	6.9 ± 3.5

Analysis of Base Dynamics. Timescales for sugar pucker interconversions within the tetraloop of the GCAA RNA hairpin have been determined. It is possible that these motions are correlated to the dynamic hydrogen bond network as well as base motions. To determine if aromatic base and sugar motions are coupled, analysis has been extended to the aromatic ^{13}C C8, C6, and C2 atoms in a uniformly labeled ^{13}C, ^{15}N GCAA RNA hairpin sample. This work was carried out by Jodi Boer, a graduate student doing her rotation in the Hoogstraten lab. The results from this work are presented in Figure 3.9. From molecular dynamic simulations, the aromatic ring of A_8 was observed to briefly leave the tetraloop structure (20). From the relaxation dispersion curves, no R_{ex} contributions indicative of exchange on the μs to ms timescale were observed for A_8 C8 or C2. Because similar k_{ex} values were not observed for base and ribose atoms for the tetraloop, it can be inferred that base motions are not coupled to ribose dynamics. It should be noted that relaxation dispersion curves were not obtained for C_6 C6 due to ambiguity from ^{1}H only chemical shift assignments (14).

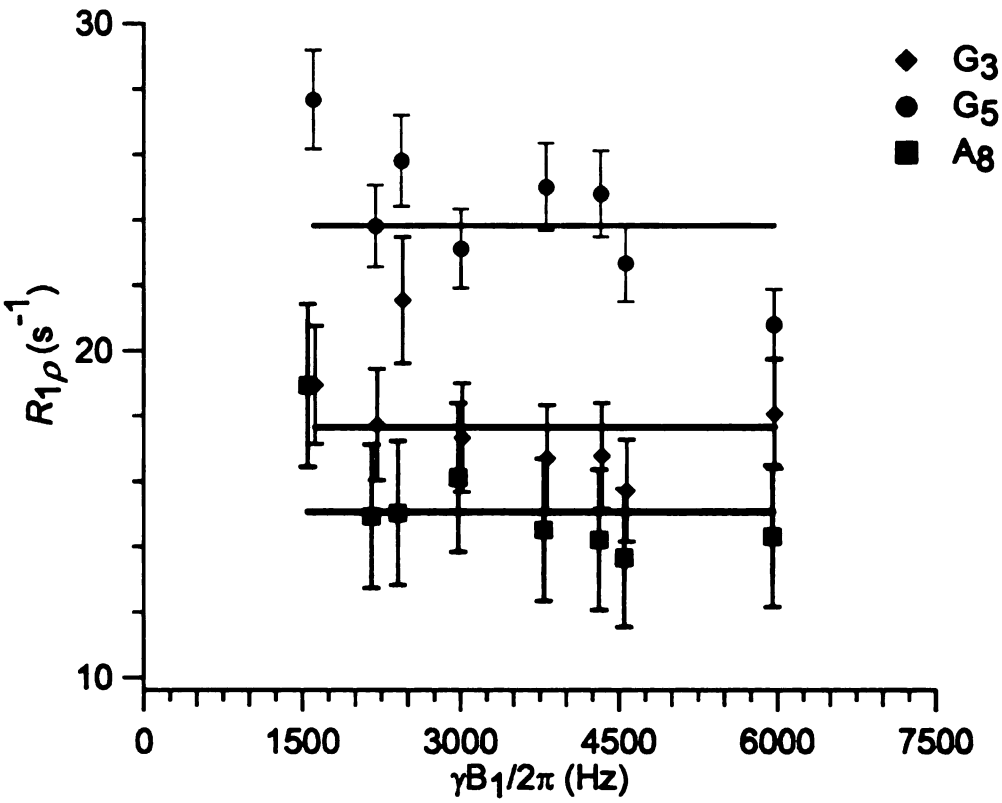

Figure 3.9: Representative relaxation dispersion curves for aromatic atoms for the GCAA RNA hairpin. On-resonance $R_{1\rho}$ (solid symbols) data are shown for C8 resonances of G_3 (black diamonds), G_5 (red circles), and A_8 (blue squares). Solid lines denote best fit to a horizontal line.

Temperature Dependence of k_{ex}. Loria and co-workers (57) have obtained relaxation dispersion curves at multiple temperatures to investigate the activation energy of μs to ms motional process in ribonuclease A. For this purpose, k_{ex} values for C2′ and C4′ atoms of the GCAA RNA hairpin tetraloop were determined from relaxation dispersion curves obtained at 15 °C, 20 °C, and 35 °C (Fig. 3.10 to 3.12; Table 3.7 to Table 3.9) to supplement those already obtained at 25 °C. At 15 °C, k_{ex} values were determined for all tetraloop atoms except C_6 C2′ that range from 11000 to 20000 s^{-1}. Unlike 25 °C, a single k_{ex} value for C2′ and C4′ atoms from a single residue fit was determined only for A_8. For G_5 and A_7, k_{ex} values for C2′ and C4′ atoms determined were not within error. At 20 °C, k_{ex} values obtained have a high degree of uncertainty due to the measurement of only on-resonance $R_{1\rho}$ data at a single magnetic field. The acquisition of CPMG data could help define the relaxation dispersion curve for better analysis as well as acquisition of dispersion curves at multiple fields. At 35 °C, a statistically significant relaxation dispersion curve was obtained for A_7 C2′ only. Even though A_7 C4′ had a cumulative probability for F-statistic of 0.2, both C2′ and C4′ atoms of A_7 were analyzed to determine a single k_{ex} value of (7.0 ± 2.3) × 10^4.

Figure 3.10: Relaxation dispersion curves in the GCAA tetraloop at 15 °C. CPMG (open symbols) and on-resonance $R_{1\rho}$ (solid symbols) data are shown for C2′ and C4′ atoms, respectively, of (a, b) G_5, (c) C_6, (d, e) A_7, and (f, g) A_8. Solid lines denote simultaneous fits of all data for the corresponding resonance to equations 3.3 and 3.6.

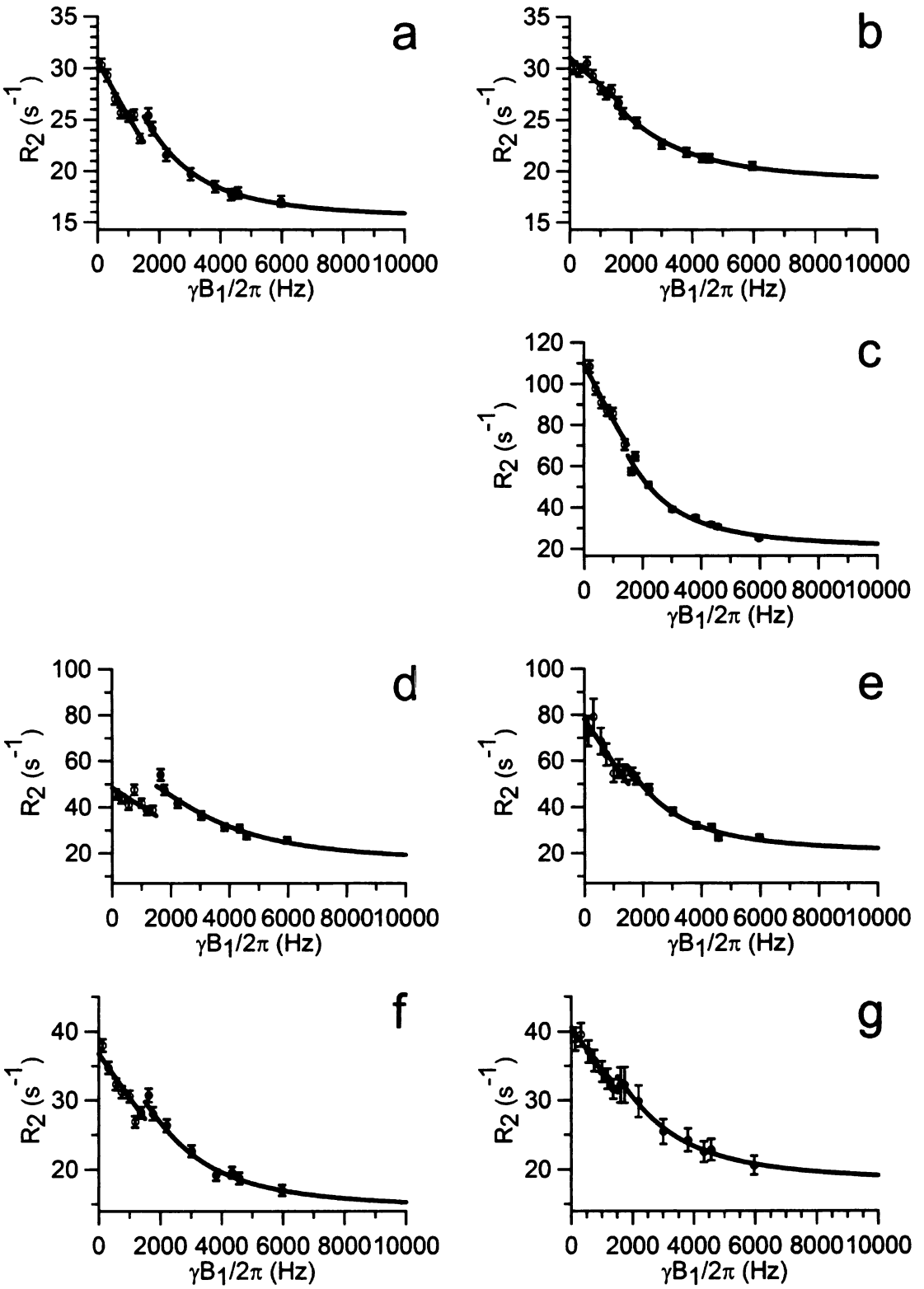
a
b
c
d
e
f
g
R2 (s-1)
γB1/2π (Hz)
0 2000 4000 6000 8000 10000

Figure 3.11: Relaxation dispersion curves in the GCAA tetraloop at 20 °C. On-resonance $R_{1\rho}$ (solid symbols) data are shown for C2′ and C4′ resonances, respectively, of (a, b) G_5, (c) C_6, (d, e) A_7, and (f, g) A_8. Solid lines denote fit of all data for the corresponding resonance to equations 3.6.

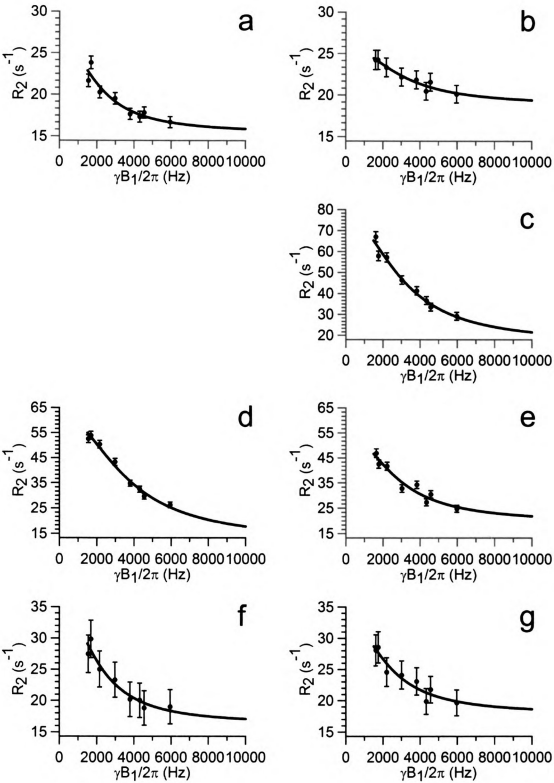
a
b
c
d
e
f
g
R2 (s-1)
γB1/2π (Hz)
0 2000 4000 6000 8000 10000

Figure 3.12: Relaxation dispersion curves in the GCAA tetraloop at 35 °C. CPMG (open symbols) and on-resonance $R_{1\rho}$ (solid symbols) data are shown for (a) C2′ and (b) C4′ atoms of A_7. Solid lines denote simultaneous fits of all data for the corresponding resonance to equations 3.3 and 3.6.

a

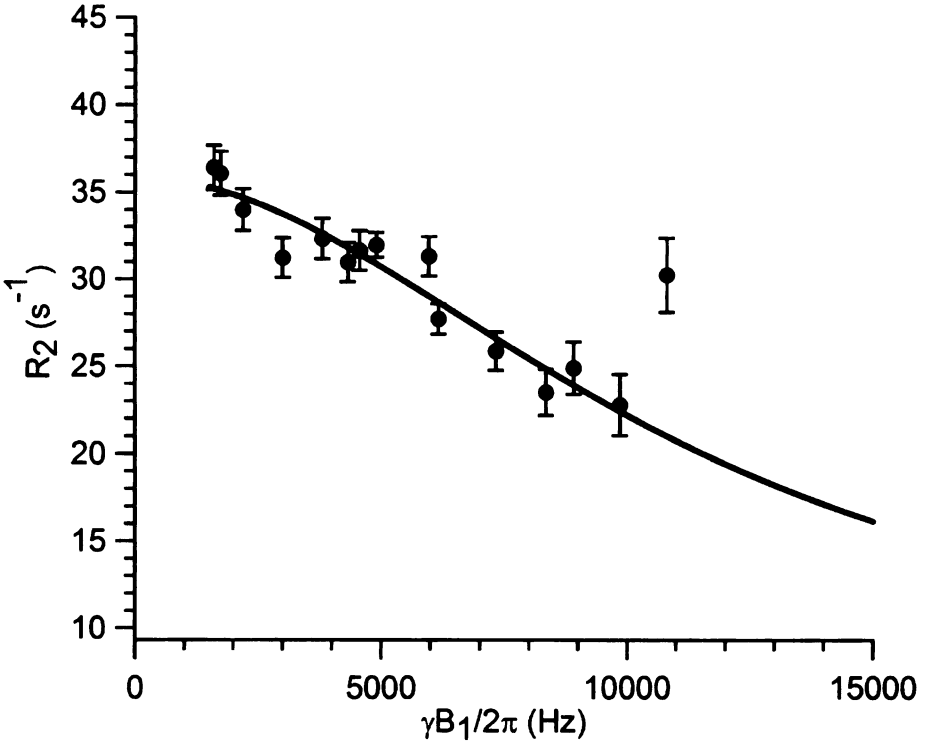
45
40
35
30
25
20
15
10
$R_2 (s^{-1})$
0
5000
10000
15000
$\gamma B_1/2\pi$ (Hz)

b

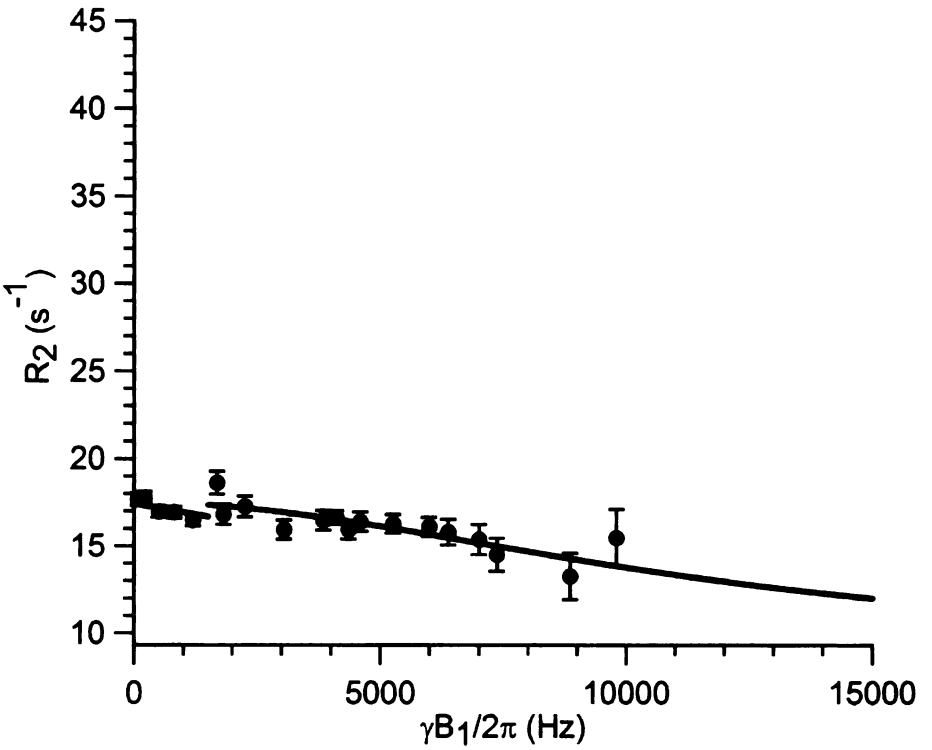
45
40
35
30
25
20
15
10
$R_2 (s^{-1})$
0
5000
10000
15000
$\gamma B_1/2\pi$ (Hz)

Table 3.7: Motional parameters derived via fitting of all data for a single atom to equations 3.3 and 3.6 at 15 °C.

Resonance	Φ_{ex}	k_{ex}, s^{-1}	R_2^0, s^{-1}	$R_{1\rho}^0$, s^{-1}
G_5 C2′	$(1.9 \pm 0.2) \times 10^5$	$(1.2 \pm 0.1) \times 10^4$	14.5 ± 0.8	15.3 ± 0.5
G_5 C4′	$(1.6 \pm 0.2) \times 10^5$	$(1.6 \pm 0.2) \times 10^4$	20.7 ± 0.7	18.9 ± 0.6
C_6 C4′	$(8.7 \pm 0.4) \times 10^5$	$(1.1 \pm 0.1) \times 10^4$	33.6 ± 2.5	19.9 ± 1.0
A_7 C2′	$(8.3 \pm 1.8) \times 10^5$	$(2.0 \pm 0.4) \times 10^4$	7.3 ± 3.4	15.4 ± 3.9
A_7 C4′	$(7.4 \pm 0.7) \times 10^5$	$(1.3 \pm 0.2) \times 10^4$	18.7 ± 3.3	19.7 ± 1.6
A_8 C2′	$(3.2 \pm 0.3) \times 10^5$	$(1.4 \pm 0.1) \times 10^4$	14.2 ± 1.2	14.2 ± 1.0
A_8 C4′	$(3.2 \pm 0.7) \times 10^5$	$(1.4 \pm 0.3) \times 10^4$	18.2 ± 2.6	18.0 ± 1.8

Table 3.8: Motional parameters derived via fitting of all data for a single atom to equation 3.6 at 20 °C.

Resonance	Φ_{ex}	k_{ex}, s^{-1}	$R_{1\rho}^0$, s^{-1}
G_5 C2′	$(1.5 \pm 0.4) \times 10^5$	$(1.3 \pm 0.6) \times 10^4$	15.4 ± 1.2
G_5 C4′	$(1.3 \pm 1.3) \times 10^5$	$(1.9 \pm 1.8) \times 10^4$	18.8 ± 3.0
C_6 C4′	$(1.2 \pm 0.2) \times 10^6$	$(1.9 \pm 0.4) \times 10^4$	16.4 ± 5.5
A_7 C2′	$(1.1 \pm 0.2) \times 10^6$	$(2.2 \pm 0.3) \times 10^4$	12.2 ± 4.2
A_7 C4′	$(6.1 \pm 1.5) \times 10^5$	$(1.7 \pm 0.5) \times 10^4$	19.4 ± 3.6
A_8 C2′	$(2.5 \pm 1.5) \times 10^5$	$(1.3 \pm 1.4) \times 10^4$	16.3 ± 4.8
A_8 C4′	$(2.3 \pm 1.6) \times 10^5$	$(1.5 \pm 1.5) \times 10^4$	17.8 ± 4.4

Table 3.9: Motional parameters derived via fitting of all data for A_7 C2′ or C4′ to equations 3.3 and 3.6 at 35 °C.

Resonance	Φ_{ex}	k_{ex}, s^{-1}	R_2^0, s^{-1}	$R_{1\rho}^0$, s^{-1}
A_7 C2′	$(2.1 \pm 1.6) \times 10^6$	$(7.0 \pm 2.4) \times 10^4$	N/A	5.3 ± 13.3
A_7 C4′	$(6.5 \pm 13.3) \times 10^5$	$(7.3 \pm 6.5) \times 10^4$	8.6 ± 10.3	8.7 ± 10.7

Activation Energy Determination. To determine activation energies for sugar pucker interconversions, the temperature dependence of k_{ex} values was analyzed. For example, relaxation dispersion curves for A_7 C4′ are plotted at all temperatures (Fig. 3.13). The figure demonstrates that R_{ex} contributions are affected by temperature. The R_{ex} contributions are determined from k_{ex}, Φ_{ex}, and R_2^{∞} terms. Interestingly, the Φ_{ex} term is not significantly different for all measured temperatures for a given atom. From this, it can be suggested that temperature changes do not significantly affect the populated states, p_A and p_B, or the chemical shift difference. k_{ex} values were plotted as a function of temperature (Fig. 3.14) as previously reported (57,58). From these plots, activation energies were determined by fitting the values of k_{ex} to the linear form of the Arrhenius equation (Table 3.10). Due to high uncertainty, interpretation of activation energies for G_5 and A_8 resonances (25% to 120% error) should be done with caution. Activation energies for the tetraloop atoms ranged from 31 to 79 kJ/mol. Activation energy values determined for G_5 and A_8 C2′ and C4′ atoms are similar within error as are C_6 and A_7 C4′ atoms. The results obtained support the theory that sugar pucker transitions can be coupled together, which are in good agreement with global fitting data obtained from relaxation dispersion curves at 25 °C.

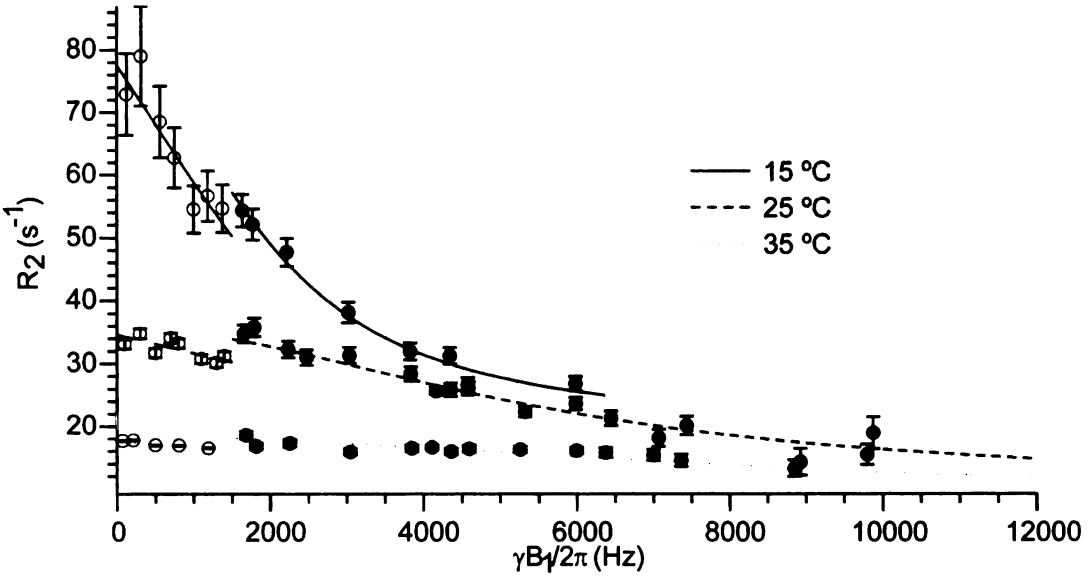

Figure 3.13: Temperature dependence of A_7 C4'. CPMG (open symbols) and $R_{1\rho}$ (solid symbols) data were acquired at 15 °C, 25 °C, and 35 °C at 600 MHz. Solid lines denote best fit to equations 3.3 and 3.6 for the individual atom A_7 C4'.

Figure 3.14: Arrhenius-type plots of the exchange rate constant k_{ex}. G_5 C2′ (black, open circles, short dash), G_5 C4′ (black, filled circle, solid line), A_8 C2′ (red, open squares, short dash), and A_8 C4′ (red, closed squares, solid line) are presented in panel a, while C_6 C4′ (red, closed circles, solid line), A_7 C2′ (black, open squares, short dash), and A_7 C4′ (black, closed squares, solid line) are presented in panel b. In all cases, k_{ex} values determined from individual resonance fits were used.

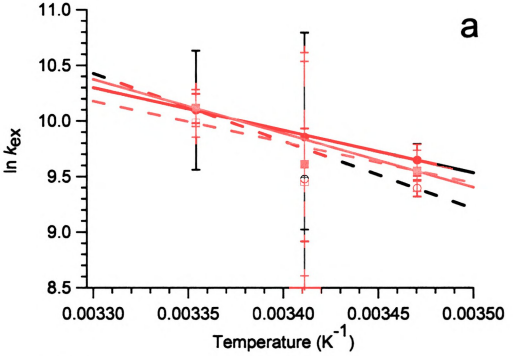
a
ln k_{ex}
11.0
10.5
10.0
9.5
9.0
8.5
0.00330
0.00335
0.00340
0.00345
0.00350
Temperature (K^{-1})

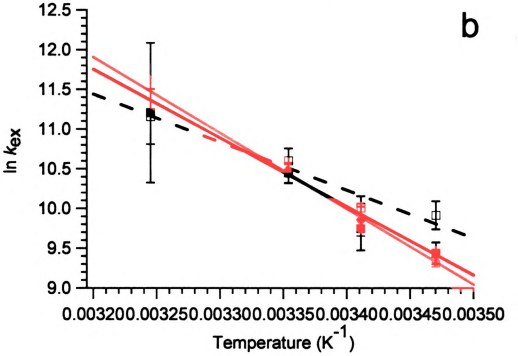
b
ln k_{ex}
12.5
12.0
11.5
11.0
10.5
10.0
9.5
9.0
0.00320
0.00325
0.00330
0.00335
0.00340
0.00345
0.00350
Temperature (K^{-1})

Table 3.10: Activation energies determined from fitting temperature dependent k_{ex} values to the linear form of the Arrhenius equation.

Resonance	E_a, kJ/mol
G_5 C2′	50 ± 11
G_5 C4′	32 ± 38
C_6 C4′	79 ± 10.
A_7 C2′	50 ± 12
A_7 C4′	72 ± 13
A_8 C2′	31 ± 11
A_8 C4′	40. ± 18

DISCUSSION

In this work, dynamics for C2′ and C4′ atoms within the tetraloop region of the GCAA RNA hairpin were analyzed using ^{13}C NMR spin relaxation experiments. This was carried out by incorporating 2′,4′-$^{13}C_2$ rNTPs into the GCAA RNA hairpin. From the model-free analysis, C2′ and C4′ atoms are highly ordered from S^2 values, with little evidence of fast internal motions on the ps to ns timescale. However, R_{ex} contributions were determined for the tetraloop atoms. Using relaxation dispersion curves, exchange rates were determined for C2′ and C4′ atoms in the tetraloop. Coupling of motion for C2′ and C4′ atoms of a residue as well as coupling of multiple residues was suggested by simultaneous fits. By analyzing the temperature dependence of k_{ex} values, activation energies for ribose ring fluctuations were determined.

The fifteen nucleotide GCAA RNA hairpin is a small, well studied molecule suitable to study ribose dynamics using the alternate-site labeling scheme to extend ^{13}C NMR analysis within the ribose ring as opposed to only the C1′ resonances. As determined earlier (see chapter 2), the use of the alternate-site labeling scheme removes ^{13}C-^{13}C interactions for the accurate measurement of relaxation rates. The removal of these interactions does not limit sensitivity of ^{13}C resonances. All NMR data were acquired without using the constant-time format. While the constant-time format can remove spectral overlap in the presence of ^{13}C-^{13}C coupling, this method is subject to sensitivity loss. RNA resonances suffer from poor chemical shift dispersion for different nucleotide atoms. As RNA oligomers increase in size, the chance for spectral overlap increases. In fact, not all the C2′ and C4′ resonances were analyzed. While the alternate-site labeling scheme does not resolve this issue, using specific residue ^{13}C NMR samples can aid analysis by removing the total number of resonances observed (see chapter 4).

R_1, $R_{1\rho}$, and ^{1}H-^{13}C hNOE data were obtained to analyze fast internal motions of the GCAA RNA hairpin using the model-free formalism of Lipari-Szabo (42-44). The results obtained reveal a relatively rigid structure on the ps – ns timescale. The overall correlation time τ_c was determined to be 3.00 ns which is in good agreement with 2.97 ns obtained previously (55). Except for atoms near the terminus and in the single-stranded 3′ tail, general order parameters S^2

are greater than 0.9, indicative of rigid nuclei. Only a few nuclei, which were located near the terminus and in the tetraloop, required an effective correlation time, τ_e,. In the tetraloop, only G_5 and C_6 C2′ atoms were analyzed requiring τ_e values of 892.4 ± 291.2 and 266.0 ± 83.8 ps, respectively. Fast internal motions using the model-free formalism of Lipari and Szabo are defined to be approximately 10% or less than the overall isotropic motion (42). The τ_e value for G_5 C2′ is almost 30% of the overall isotropic motion. While this can be interpreted as slow motion on the ns timescale, this invokes the assumption of anisotropic motion. However, G_5 did not fit to the anisotropic condition of the model-free formalism. Furthermore, Fiala and co-workers (55) determined internal motional parameters using isotropic conditions of the model-free formalism for the uniformly labeled ^{13}C GCAA RNA hairpin. This suggests that fast internal motions cannot be determined unambiguously for G_5 with the data collected. Fast internal motions for C_6 C2′ could arise from sugar pucker transitions. Nowakowski *et al.* (62) determined proton chemical shift perturbations due to sugar pucker on the ps timescale from molecular dynamic simulations of the UUCG RNA hairpin. Also, slight decreases in the general order parameter S^2 for C_6 C2′ were determined. These results suggest conformational flexibility for this atom, which is in good agreement with previous evidence of dynamics for C_6 (14,20,55).

All tetraloop resonances except C_6 C2′ required an R_{ex} term using the model-free formalism. The R_{ex} contribution from the model-free formalism is similar in magnitude to R_{ex} contributions measured from Hahn echo experiments. This result is satisfying as two technically different experiments report similar results. Relaxation dispersion curves were obtained at 25 °C using rcCPMG, on-, and off-resonance ^{13}C spin relaxation experiments at 600 MHz (^{13}C 125 MHz). Simultaneously fitting CPMG and $R_{1\rho}$ data to determine exchange parameters has seldom been done (38,39). In most cases, one type of experimentation is suitable to measure exchange parameters. However, if k_{ex} values are within intermediate μs timescales, both CPMG and $R_{1\rho}$ measurements can be effectively used to determine exchange parameters. The initial ^{13}C $R_{1\rho}$ results obtained at 600 MHz hinted at this possibility. Thus additional rcCPMG and off-resonance ^{13}C relaxation dispersion curves were obtained, as well as rcCPMG and on-resonance ^{13}C dispersion curves at 900 MHz (^{13}C 225 MHz). Motional parameters were determined by fitting relaxation dispersion curves to equations 3.3 and 3.6 from both fields simultaneously. Equations 3.3 and 3.6 are approximations from generalized exchange equations that are applicable at all timescales. To validate the use of equations 3.3 and 3.6, an α scaling factor was determined which relates the R_{ex} dependence to the static magnetic field. An α

scaling factor of 1.7 and above was calculated for all resonances except for A_7 C2′, for which no data could be obtained at the higher magnetic field. Because of this result, caution should be taken for the analysis of A_7 C2′. The A_7 C2′ resonance is severely broadened as seen from the ^{1}H-^{13}C HSQC (Fig. 3.2). Data analysis of this resonance was difficult due to data ambiguity as well as acquisition of data only at 600 MHz. These problems could arise from fitting dispersion curves using the fast-exchange equations when the general exchange equations are appropriate. To unambiguously determine the exchange regime of A_7 C2′, acquisition of relaxation dispersion curves at a second magnetic field is needed. Because this resonance was not observed at 900 MHz due to fast relaxation, acquisition of dispersion curves at lower magnetic fields could alleviate this problem and help clarify the exchange regime for A_7 C2′.

Relaxation dispersion curves were used to determine the exchange parameters Φ_{ex}, k_{ex}, and R_2^0. For the individual fit of A_7 C2′ at 25 °C, a minimum constraint of zero was imposed for $R_{1\rho}^{0,600}$. This constraint was not used when fitting k_{ex} to a single residue or global value. However, non-physical $R_2^{0,600}$ values were obtained for all determined fits for A_7 C2′. This can be attributed to inconsistencies with rcCPMG data acquisition. From Fig. 3.8, rcCPMG rates are observed to be nearly equal or greater than $R_{1\rho}$ at low effective fields at 600 MHz and 900 MHz. This is not the case for A_7 C2′ (Fig.

3.8e) where rcCPMG rates are significantly less than $R_{1\rho}$ rates. These effects could be attributed to fitting our rcCPMG data to the fast exchange equation when the general equation is more appropriate. Yet, it was demonstrated that at 25 °C, k_{ex} values for C2′ resonances were similar to C4′ of the same residue for G_5 and A_8. Also, exchange parameters for A_7 C4′ were unambiguously determined using the fast exchange equations. The source of the inconsistencies in rcCPMG data acquired for A_7 C2′ at 600 MHz is unclear at this time.

No R_{ex} dependence was observed for C_6 C2′ at 600 or 900 MHz. This result is unexpected due to the measurement of R_{ex} for all other resonances within the tetraloop. In fact, observation of substantial R_{ex} contributions for C_6 C4′ as well as relatively small R_{ex} contributions for G_5 C4′ demonstrates the sensitivity of our measurements. Also, results from two out of ten NMR solution structures solved by Jucker and co-workers (14) determined the aromatic ring of C_6 was exposed from the tetraloop region (Fig. 3.1b), along with sugar pucker equilibrium for C_6, as well as molecular simulations that observed sugar re-puckering transitions from C3′-endo to C2′-endo upon base flipping for C_6 (20). From examination of equations 3.3 and 3.6, if no chemical shift difference between A and B is observed, the R_{ex} term goes to zero. It can be tentatively

concluded that the chemical shifts of the C3'-endo and C2'-endo are the same for C_6 C2' resonance.

Evidence for correlated motions for ribose resonances in multiple residues was determined from by fitting curves to a k_{ex} value. The sugar pucker transitions in the GNRA tetraloop can be attributed to base dynamics. Hoogstraten *et al.* (25) observed exchange contributions for the terminal adenine C8 atom within the GAAA tetraloop of the lead-dependent consistent with results from Jucker *et al.* (14) that determined a heterogenous hydrogen bond network in GNRA tetraloops. However, no R_{ex} contributions were observed from on-resonance $R_{1\rho}$ curves (Fig. 3.9). A reason for this difference could be due to the sequence difference. In both sequences, the apical residue stacks upon the third base of the loop. However, the cytosine residue has been shown to flip out of the tetraloop structure for two out of ten NMR structures obtained for GCAA (14). No motions were observed for the third adenine in both sequences. This conclusion would be better supported with the observation of dispersion curves for C_6 C6 resonance. Unfortunately, no dispersion curves for this resonance were acquired due to spectral ambiguity from ^{1}H only chemical shift assignments for GCAA. The use of standard HCCH-COSY pulse sequences would correlate H5 resonances to H6 resonances, possibly clearing up spectral ambiguity. rcCPMG data could not be accurately determined due to the presence of $^2J_{CC}$ scalar coupling. To investigate μs to ms timescales using CPMG based

experiments, isolation of the aromatic carbons will be crucial. For example, Pardi and co-workers (63) have developed a method to highly enrich purine C8 atoms using ^{13}C formate in bacterial cell growths.

As well as exchange timescales, chemical shift differences can be determined from relaxation dispersion curves. Large Φ_{ex} values were determined for A_7 and C_6 atoms as opposed to G_5 and A_8 atoms. Because Φ_{ex} is proportional to the chemical shift difference, the data suggest that C_6 C4′ and A_7 C2′ and C4′ have large chemical shift differences. This can be seen from the broadening of these resonances from the HSQC (Fig 3.2). Jucker *et al.* (14) determined sugar pucker equilibrium estimates for the tetraloops studied. To better illustrate the magnitude of chemical shift change within the tetraloop ribose resonances, the tetraloop region of the 1.4 Å GUAA RNA hairpin (15) with CPK spheres sized proportional to minimum chemical shift differences is presented in Fig 3.15. Here one can see the magnitude of chemical shift changes for C_6 and A_7 atoms.

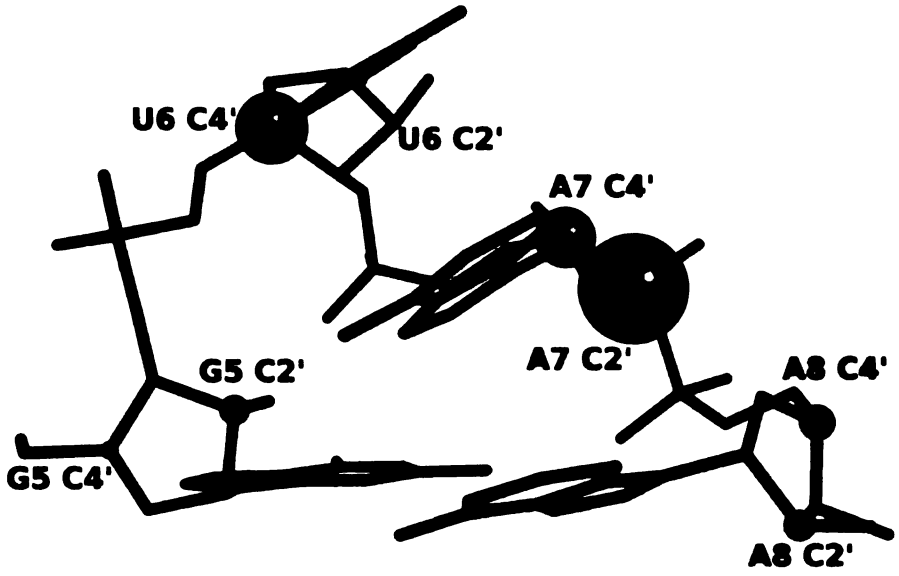

Figure 3.15: Representation of the tetraloop region of GUAA RNA hairpin determined to 1.4 Å (PDB code 1msy) by Correll and Swinger (15). CPK spheres for the C2′ and C4′ atoms are drawn proportional to $\Delta\omega_{min}$ values for the corresponding resonances.

Relaxation dispersion curves at multiple temperatures were acquired to analyze the activation energy of sugar pucker conformations within the tetraloop of the GCAA RNA hairpin. Changes in temperature are expected to change the determined k_{ex}. For the tetraloop of the GCAA RNA hairpin, temperature dependent R_{ex} contributions were observed to be proportional to k_{ex} because Φ_{ex} and R_2^0 were not significantly altered with temperature (Fig. 3.13). At 15 °C, residue level fits for G_5 and A_7 could not be obtained. For A_7, k_{ex} values for C2′ and C4′ resonances are not similar. Similar to data obtained at 25 °C, the rcCPMG measured rates for A_7 C2′ are lesser than $R_{1\rho}$. For G_5 and A_8, k_{ex}

values determined at 20 °C were poorly defined which made data analysis ambiguous, yet values for C_6 and A_7 were better defined.

It was previously demonstrated that a single k_{ex} could be obtained for both resonances in a given ribose ring which were attributed to both resonances reporting on the same conformational event of sugar pucker interconversion. If this is indeed true, calculation of similar activation energies for both resonances should be obtained. Using Arrhenius plots, activation energies for all tetraloop C2′ and C4′ atoms were calculated except C_6 C2′. C2′ and C4′ atoms of A_8 have similar activation energies which suggest these atoms are reporting on sugar pucker transitions. Likewise, C4′ resonances of C_6 and A_7 have similar activation energies which could suggest correlated motions. Activation energies measured are higher that those obtained for ^{15}N amide resonances in ribonuclease A studied by the Loria group, where measured activation energies for exchange yielded 15 kJ/mol and 31 kJ/mol (57). However, LiWang *et al.* (64) determined the lower threshold for ribose pucker activation energy is 17 kJ/mol using ribose molecules. It is possible that ribose pucker conformations within the tetraloop region are more sterically hindered. Such constraints could raise the activation energies measured.

To sum up, rigorous analysis of ribose dynamics in the tetraloop region of the GCAA RNA hairpin were presented. Fast internal motions on the ps to ns timescales were analyzed by the model-free analysis of Lipari-Szabo (42-44). Motions on the μs to ms timescale indicative of conformational exchange were

analyzed using rcCPMG, on-, and off-resonance $R_{1\rho}$ NMR spin relaxation experiments at multiple fields. This analysis was made possible using the novel alternate-site isotope labeling scheme. Motional exchange parameters for C2′ and C4′ atoms were determined from simultaneous fits of relaxation dispersion curves at multiple fields. From these results, individual fits for C2′ and C4′ atoms to a single k_{ex} value were determined. Because k_{ex} values for C2′ and C4′ atoms of a residue were determined to be similar within error, data were refit to a single k_{ex} value for a residue. Likewise, multiple residues displayed similar k_{ex} values, thus a global k_{ex} values was determined for G_5 and A_8 as well as C_6 and A_7. It can be concluded that exchange parameters are reporting on sugar pucker transitions. To ascertain thermodynamics of ribose motions within the tetraloop, activation energies for sugar pucker transitions were determined, further supporting the idea of correlated motions. The work presented here details the usefulness of the alternate-site labeling scheme to study ribose dynamics within RNA molecules. This work has laid the foundation for studies in biologically relevant molecules, such as the hairpin ribozyme, to evaluate structure/function relationships.

ACKNOWLEDGMENTS

I would like to thank Max T. Rogers NMR administrators Kermit Johnson and Dr. Daniel Holmes for assistance in programming the adiabatic pulse sequence used for the 600 MHz spectrometer. I would like to thank CTA

Biomolecular NMR Facility administrator Dr. Aizhuo Liu for assistance in setting up all pulse sequences used for the 900 MHz spectrometer. Lastly, I would like to thank Jodi Boer for acquisition of rcCPMG and on-resonance $R_{1\rho}$ dispersion curves for aromatic resonances.

REFERENCES

1. Leulliot, N. and Varani, G. (2001) Current topics in RNA-protein recognition: control of specificity and biological function through induced fit and conformational capture. *Biochemistry*, **40**, 7947-7956.

2. Treiber, D.K. and Williamson, J.R. (2001) Beyond kinetic traps in RNA folding. *Curr Opin Struct Biol*, **11**, 309-314.

3. Fedor, M.J. and Williamson, J.R. (2005) The catalytic diversity of RNAs. *Nat Rev Mol Cell Biol*, **6**, 399-412.

4. Kuimelis, R.G. and McLaughlin, L.W. (1998) Mechanisms of ribozyme-mediated RNA cleavage. *Chem Rev*, **98**, 1027-1044.

5. Varani, G. (1995) Exceptionally stable nucleic acid hairpins. *Annu Rev Biophys Biomol Struct*, **24**, 379-404.

6. Antao, V.P., Lai, S.Y. and Tinoco, I., Jr. (1991) A thermodynamic study of unusually stable RNA and DNA hairpins. *Nucleic Acids Res*, **19**, 5901-5905.

7. SantaLucia, J., Jr., Kierzek, R. and Turner, D.H. (1992) Context dependence of hydrogen bond free energy revealed by substitutions in an RNA hairpin. *Science*, **256**, 217-219.

8. Antao, V.P. and Tinoco, I., Jr. (1992) Thermodynamic parameters for loop formation in RNA and DNA hairpin tetraloops. *Nucleic Acids Res*, **20**, 819-824.

9. Uhlenbeck, O.C. (1990) Tetraloops and RNA folding. *Nature*, **346**, 613-614.

10. Murphy, F.L. and Cech, T.R. (1994) GAAA tetraloop and conserved bulge stabilize tertiary structure of a group I intron domain. *J Mol Biol*, **236**, 49-63.

11. Witherell, G.W. and Uhlenbeck, O.C. (1989) Specific RNA binding by Q beta coat protein. *Biochemistry*, **28**, 71-76.

12. Zwieb, C. (1992) Recognition of a tetranucleotide loop of signal recognition particle RNA by protein SRP19. *J Biol Chem*, **267**, 15650-15656.

13. Heus, H.A. and Pardi, A. (1991) Structural features that give rise to the unusual stability of RNA hairpins containing GNRA loops. *Science*, **253**, 191-194.

14. Jucker, F.M., Heus, H.A., Yip, P.F., Moors, E.H. and Pardi, A. (1996) A network of heterogeneous hydrogen bonds in GNRA tetraloops. *J Mol Biol*, **264**, 968-980.

15. Correll, C.C. and Swinger, K. (2003) Common and distinctive features of GNRA tetraloops based on a GUAA tetraloop structure at 1.4 Å resolution. *RNA*, **9**, 355-363.

16. Szewczak, A.A. and Moore, P.B. (1995) The sarcin/ricin loop, a modular RNA. *J Mol Biol*, **247**, 81-98.

17. Orita, M., Nishikawa, F., Shimayama, T., Taira, K., Endo, Y. and Nishikawa, S. (1993) High-resolution NMR study of a synthetic oligoribonucleotide with a tetranucleotide GAGA loop that is a substrate for the cytotoxic protein, ricin. *Nucleic Acids Res*, **21**, 5670-5678.

18. Mueller, L., Legault, P. and Pardi, A. (1995) Improved RNA structure determination by detection of NOE contacts to exchange-broadened amino protons. . *J Am Chem Soc*, **117**, 11043-11048.

19. Pley, H.W., Flaherty, K.M. and McKay, D.B. (1994) Model for an RNA tertiary interaction from the structure of an intermolecular complex between a GAAA tetraloop and an RNA helix. *Nature*, **372**, 111-113.

20. Sorin, E.J., Engelhardt, M.A., Herschlag, D. and Pande, V.S. (2002) RNA simulations: probing hairpin unfolding and the dynamics of a GNRA tetraloop. *J Mol Biol*, **317**, 493-506.

21. Palmer, A.G., 3rd. (1997) Probing molecular motion by NMR. *Curr Opin Struct Biol*, **7**, 732-737.

22. Palmer, A.G., 3rd. (2004) NMR characterization of the dynamics of biomacromolecules. *Chem Rev*, **104**, 3623-3640.

23. Akke, M. (2002) NMR methods for characterizing microsecond to millisecond dynamics in recognition and catalysis. *Curr Opin Struct Biol*, **12**, 642-647.

24. Dayie, K.T., Wagner, G. and Lefevre, J.F. (1996) Theory and practice of nuclear spin relaxation in proteins. *Annu Rev Phys Chem*, **47**, 243-282.

25. Hoogstraten, C.G., Wank, J.R. and Pardi, A. (2000) Active site dynamics in the lead-dependent ribozyme. *Biochemistry*, **39**, 9951-9958.

26. Palmer, A.G., 3rd, Kroenke, C.D. and Loria, J.P. (2001) Nuclear magnetic resonance methods for quantifying microsecond-to-millisecond motions in biological macromolecules. *Methods Enzymol*, **339**, 204-238.

27. Eisenmesser, E.Z., Bosco, D.A., Akke, M. and Kern, D. (2002) Enzyme dynamics during catalysis. *Science*, **295**, 1520-1523.

28. Korzhnev, D.M., Orekhov, V.Y., Dahlquist, F.W. and Kay, L.E. (2003) Off-resonance $R_{1\rho}$ relaxation outside of the fast exchange limit: an experimental study of a cavity mutant of T4 lysozyme. *J Biomol NMR*, **26**, 39-48.

29. Kim, S. and Baum, J. (2004) An on/off resonance rotating frame relaxation experiment to monitor millisecond to microsecond timescale dynamics. *J Biomol NMR*, **30**, 195-204.

30. Shajani, Z. and Varani, G. (2005) ^{13}C NMR relaxation studies of RNA base and ribose nuclei reveal a complex pattern of motions in the RNA binding site for human U1A protein. *J Mol Biol*, **349**, 699-715.

31. Carr, H.Y. and Purcell, E.M. (1954) Effects of diffusion on free precession in nuclear magnetic resonance experiments. *Phys Rev*, **94**, 630-638.

32. Meiboom, S. and Gill, D. (1958) Modified spin-echo method for measuring nuclear relaxation times. *Rev Sci Instrum*, **29**, 688-691.

33. Luz, Z. and Meiboom, S. (1963) Nuclear magnetic resonance study of the protolysis of trimethylammonium ion in aqueous solution - order of the reacton with respect to solvent. *J Chem Phys*, **39**, 366-370.

34. Deverell, C., Morgan, R.E. and Strange, J.H. (1970) Studies of chemical exchange by nuclear magnetic relaxation in the rotating frame. *Mol Phys*, **18**, 553-559.

35. Loria, J.P., Rance, M. and Palmer, A.G. (1999) A relaxation-compensated Carr-Purcell-Meiboom-Gill sequence for characterizing chemical exchange by NMR spectroscopy. *J Am Chem Soc*, **121**, 2331-2332.

36. Yamazaki, T., Muhandiram, R. and Kay, L. (1994) NMR experiments for the measurement of carbon relaxation properties in highly enriched, uniformly ^{13}C, ^{15}N-labeled proteins: application to $^{13}C\alpha$ carbons. *J Am Chem Soc*, **116**, 8266-8278.

37. Mulder, F.A.A., de Graaf, R.A., Kaptein, R. and Boelens, R. (1998) An off-resonance rotating frame relaxation experiment for the investigation of macromolecular dynamics using adiabatic rotations. *J Magn Reson*, **131**, 351-357.

38. Mulder, F.A., van Tilborg, P.J., Kaptein, R. and Boelens, R. (1999) Microsecond time scale dynamics in the RXR DNA-binding domain from a combination of spin-echo and off-resonance rotating frame relaxation measurements. *J Biomol NMR*, **13**, 275-288.

39. Meekhof, A.E. and Freund, S.M. (1999) Separating the contributions to ^{15}N transverse relaxation in a fibronectin type III domain. *J Biomol NMR*, **14**, 13-22.

40. Massi, F., Johnson, E., Wang, C., Rance, M. and Palmer, A.G., 3rd. (2004) NMR $R_{1\rho}$ rotating-frame relaxation with weak radio frequency fields. *J Am Chem Soc*, **126**, 2247-2256.

41. Rupert, P.B., Massey, A.P., Sigurdsson, S.T. and Ferre-D'Amare, A.R. (2002) Transition state stabilization by a catalytic RNA. *Science*, **298**, 1421-1424.

42. Lipari, G. and Szabo, A. (1982) Model-free approach to the interpretation of nuclear magnetic resonance relaxation in macromolecules. 1. theory and range of validity. *J Am Chem Soc*, **104**, 4546-4559.

43. Lipari, G. and Szabo, A. (1982) Model-free approach to the interpretation of nuclear magnetic resonance relaxation in macromolecules. 2. analysis of experimental results. *J Am Chem Soc*, **104**, 4559-4570.

44. Mandel, A.M., Akke, M. and Palmer, A.G., 3rd. (1995) Backbone dynamics of *Escherichia coli* ribonuclease HI: correlations with structure and function in an active enzyme. *J Mol Biol*, **246**, 144-163.

45. Batey, R.T., Battiste, J.L. and Williamson, J.R. (1995) Preparation of isotopically enriched RNAs for heteronuclear NMR. *Methods Enzymol*, **261**, 300-322.

46. Johnson, J.E., Jr., Julien, K.R. and Hoogstraten, C.G. (2006) Alternate-site isotopic labeling of ribonucleotides for NMR studies of ribose conformational dynamics in RNA. *J Biomol NMR*, **35**, 261-274.

47. Milligan, J.F. and Uhlenbeck, O.C. (1989) Synthesis of small RNAs using T7 RNA polymerase. *Methods Enzymol*, **180**, 51-62.

48. Milligan, J.F., Groebe, D.R., Witherell, G.W. and Uhlenbeck, O.C. (1987) Oligoribonucleotide synthesis using T7 RNA polymerase and synthetic DNA templates. *Nucleic Acids Res*, **15**, 8783-8798.

49. Cunningham, L., Kittikamron, K. and Lu, Y. (1996) Preparative-scale purification of RNA using an efficient method which combines gel electrophoresis and column chromatography. *Nucleic Acids Res*, **24**, 3647-3648.

50. Tollinger, M., Skrynnikov, N.R., Mulder, F.A., Forman-Kay, J.D. and Kay, L.E. (2001) Slow dynamics in folded and unfolded states of an SH3 domain. *J Am Chem Soc*, **123**, 11341-11352.

51. Hwang, T.L., van Zijl, P.C. and Garwood, M. (1998) Fast broadband inversion by adiabatic pulses. *J Magn Reson*, **133**, 200-203.

52. Millet, O., Loria, J.P., Kroenke, C.D., Pons, M. and Palmer, A.G., 3rd. (2000) The static magnetic field dependence of chemical exchange linebroadening defines the NMR chemical shift time scale. *J Am Chem Soc*, **122**, 2867-2877.

53. Kay, L.E., Torchia, D.A. and Bax, A. (1989) Backbone dynamics of proteins as studied by ^{15}N inverse detected heteronuclear NMR spectroscopy: application to staphylococcal nuclease. *Biochemistry*, **28**, 8972-8979.

54. Borer, P.N., LaPlante, S.R., Kumar, A., Zanatta, N., Martin, A., Hakkinen, A. and Levy, G.C. (1994) ^{13}C-NMR relaxation in three DNA oligonucleotide duplexes: model-free analysis of internal and overall motion. *Biochemistry*, **33**, 2441-2450.

55. Trantirek, L., Caha, E., Kaderavek, P. and Fiala, R. (2007) NMR ^{13}C-relaxation study of base and sugar dynamics in GCAA RNA hairpin tetraloop. *J Biomol Struct Dyn*, **25**, 243-252.

56. Bryce, D.L., Grishaev, A. and Bax, A. (2005) Measurement of ribose carbon chemical shift tensors for A-form RNA by liquid crystal NMR spectroscopy. *J Am Chem Soc*, **127**, 7387-7396.

57. Cole, R. and Loria, J.P. (2002) Evidence for flexibility in the function of ribonuclease A. *Biochemistry*, **41**, 6072-6081.

58. Mulder, F.A., Mittermaier, A., Hon, B., Dahlquist, F.W. and Kay, L.E. (2001) Studying excited states of proteins by NMR spectroscopy. *Nat Struct Biol*, **8**, 932-935.

59. Blad, H., Reiter, N.J., Abildgaard, F., Markley, J.L. and Butcher, S.E. (2005) Dynamics and metal ion binding in the U6 RNA intramolecular stem-loop as analyzed by NMR. *J Mol Biol*, **353**, 540-555.

60. Massi, F., Grey, M.J. and Palmer, A.G., 3rd. (2005) Microsecond timescale backbone conformational dynamics in ubiquitin studied with NMR R1rho relaxation experiments. *Protein Sci*, **14**, 735-742.

61. Trott, O. and Palmer, A.G., 3rd. (2002) $R_{1\rho}$ relaxation outside of the fast-exchange limit. *J Magn Reson*, **154**, 157-160.

62. Nowakowski, J., Miller, J.L., Kollman, P.A. and Tinoco, I., Jr. (1996) Time evolution of NMR proton chemical shifts of an RNA hairpin during a molecular dynamics simulation. *J Am Chem Soc*, **118**, 12812-12820.

63. Latham, M.P., Brown, D.J., McCallum, S.A. and Pardi, A. (2005) NMR methods for studying the structure and dynamics of RNA. *Chembiochem*, **6**, 1492-1505.

64. LiWang, A.C., McCready, D.E., Drobny, G.P., Reid, B.R. and Kennedy, M.A. (2003) Observation of a distinct transition in the mode of interconversion of ring pucker conformers in non-crystalline $_D$-ribose-2'-*d* from ^{2}H NMR spin-alignment. *J Biomol NMR*, **26**, 249-257.

Chapter 4

Analysis of Ribose Dynamics at the Cleavage Site of the Lead-dependent Ribozyme Using ^{13}C NMR Spin Relaxation Experiments

INTRODUCTION

The lead-dependent ribozyme, or leadzyme, is a catalytic RNA molecule that was derived from *in vitro* selection assays of yeast $tRNA^{Phe}$ (1), which was shown to undergo cleavage upon the addition of Pb^{2+} (2,3). The mechanism of the leadzyme was determined to be similar to other small, naturally occurring ribozymes in using an internal 2′ OH nucleophile, it cleaves the phosphate backbone at a specific phosphodiester bond linkage to form 2′,3′-cyclic phosphate and 5′-OH termini (4). However, the leadzyme is unique in that the 2′,3′-cyclic phosphate is further hydrolyzed to 3′-phosphate (4). As evidenced by its name, the leadzyme is specific for catalysis in the presence of Pb^{2+}. Even though Pb^{2+} is required for catalysis, the addition of divalent and trivalent metal ions including rare earth metals can enhance the catalytic rate over Pb^{2+} alone (5,6). The structure of the leadzyme (Fig 4.1, 4.2) is centered within an asymmetrical internal loop containing the cleavage site flanked by A-form helices. Within the internal loop, C_6, G_9, and G_{24} are conserved residues (7,8).

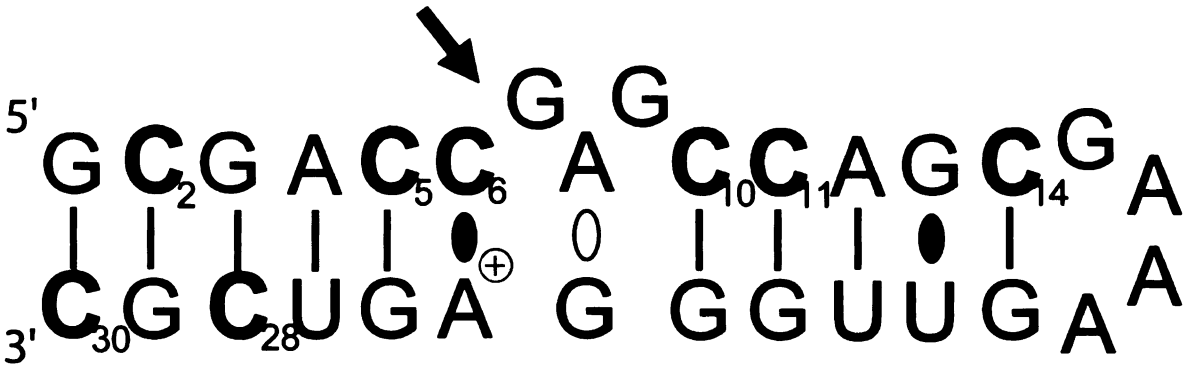

Figure 4.1: Secondary structure of the lead-dependent ribozyme used in this work. Cytidine residues are highlighted in bold; and the arrow denotes the site of phosphodiester bond cleavage. Ovals (filled and open) denote non Watson-Crick base pairs.

Kinetics studies have probed the catalytic mechanism of the leadzyme (5,7-11). Uhlenbeck and co-workers (8) have shown that the log of the cleavage rate is linear with pH in the range from 5.5 to 7.0, indicative of a basic group being involved in the rate-limiting step of catalysis, presumably Pb^{2+}-bound hydroxyl. Unfortunately, full kinetic profiles cannot be obtained for the leadzyme due to the formation of lead polyhydroxide species at high pH values.

Several structural methods including the NMR solution structure (12), X-ray crystal structures (13,14), and computer modeling (15) of the leadzyme have yielded conflicting results for the internal loop. Glycosidic torsion angles as well as sugar pucker conformations for the three guanosines within the internal loop are not consistent in the three analyses. Based on these inconsistencies, it was hypothesized that conformational changes occur for the active site to activate the

leadzyme. The use of 8-bromo-guanosine (8BrG) analogs (9) as well as locked nucleic acid (LNA) ribonucleotides (rNTPs) (10) have probed glycosidic and sugar pucker conformations, respectively. Using 8BrG analogs forces the glycosidic torsion angle into *syn* conformation through steric hinderence. The results demonstrated that G_7 and G_9 strongly prefer anti conformation while rate enhancement was observed when G_{24} was modified with 8BrG (9). Locked nucleic acids are rNTPs that restrict the sugar pucker to C3′-endo. The leadzyme with a locked nucleic residue at position 9 was shown to have a rate enhancement when the sugar pucker was restricted to C3′-endo using the LNA variant (10).

What the different structural analyses do agree on is a C3′-endo sugar pucker for C_6. Yet, in this conformation, the 2′-OH is not positioned for in-line nucleophilic attack as required for this mechanism. It was hypothesized that conformational fluctuations could participate in the catalytic mechanism of the leadzyme. In fact, comparison of residues in the asymmetric unit of the crystal structures for the leadzyme indicated that metal binding can force a sugar pucker conversion for C_6 (13,14).

As shown in previous chapters, heteronuclear NMR experiments are useful in examining conformational fluctuations. Previous NMR work by Pardi and co-workers (16,17) measured a pK_a of 6.5 for A_{25} N1 as opposed to < 3.1 for other helical adenines. Using NMR line shape analysis, an exchange lifetime of 28 ± 4 μs was determined for the protonated state of A_{25} N3 (16). Also,

Hoogstraten *et al.* (18) measured a strong R_{ex} dependence for A_{25} C2 and C8 atoms for the leadzyme from power dependent $R_{1\rho}$ measurements. For A_{25} C2 and C8 atoms, exchange lifetimes of 40 ± 1.8 μs and 47 ± 18 μs were determined, respectively. It was hypothesized that protonation of A_{25} N1 is influenced by the base of C_6 flipping out of the helix. The agreement of these experiments suggests a model whereby base pair opening is required for catalysis. Unfortunately, no dynamics could be collected for the base of C_6 due to spectral overlap.

Based on these findings, it can be suggested that the sugar pucker conformation of C_6 would be affected by the proposed base dynamics. As demonstrated in previous chapters, utilizing the alternate-site labeling scheme can probe such dynamics. In this chapter, sugar pucker transitions were examined for a cytidine-labeled leadzyme incorporating the alternate-site labeling scheme using power dependent $R_{1\rho}$ experiments. The results demonstrate active site fluctuations on the μs to ms timescale which are postulated to position the reactive nucleophile for catalytic activity.

MATERIALS and METHODS

Preparation of ^{13}C Cytidine rNTPs. Cytosine specific ^{13}C rNTPs for the lead-dependent ribozyme were prepared as described earlier (19,20). ^{13}C rCMP was

separated from other rNTPs using an Akta Basic FPLC (GE Healthcare) with a POROS PI/20 column (20 μm, 4.6 mm × 100 mm) using a linear gradient from 50 mM NH_4COOH, pH 3.0 to 500 mM NH_4COOH, pH 2.5 over 3.5 min and a flow rate of 5 mL/min collecting 10 mL fractions followed by UV absorbance. After lyophilization of pooled fractions, ^{13}C rCMP was phosphorylated to ^{13}C rCTP (19). The phosphorylation reaction was monitored using a Vydac 302IC4.6 Ion-Chromatography column (10 μm, 4.6 mm × 250 mm) with a linear gradient from 25 mM 1:1 NaH_2PO_4:Na_2HPO_4, pH 2.8 to 125 mM 1:1 NaH_2PO_4:Na_2HPO_4, pH 2.9 over 34 min and a flow rate of 1 mL/min. ^{13}C rCTP was purified from proteins using centrifugation, concentrated using a Rotovapor RE 120 (Buchi) under vacuum at 40 °C to a final volume of 1 mL, and ethanol precipitated.

Transcription of the ^{13}C Lead-dependent Ribozyme. The alternate-site labeling scheme was incorporated into the cytidines of the thirty nucleotide lead-dependent ribozyme by *in vitro* transcription using recombinant T7 RNA polymerase and a synthetic DNA template (21,22) with 2′,4′-$^{13}C_2$ rCTP and non-labeled rATP, rGTP, and rUTP. Transcribed RNA was ethanol precipitated and purified using denaturing polyacrylamide gel electrophoresis on a Bio-Rad model 491 preparative cell (23) with a flow rate of 1 mL/min with 4 mL fractions. RNA fractions corresponding to the lead-dependent ribozyme as determined by gel electrophoresis were pooled, concentrated as above to 1 mL, and desalted using Centricon-3 units (Millipore). RNA was dried, exchanged into 99.9% D_2O with

repeated lyophilization, and resuspended to a final concentration of 360 μM in 260 μL 99.96% D_2O, 10 mM sodium phosphate pH 5.5, 100 mM NaCl, and 200 μM EDTA in an advanced microtube matched with D_2O (Shigemi, Inc.). Prior to use, the NMR sample was incubated at 65 °C for 5 min and cooled on ice for 5 min.

NMR Data Setup, Acquisition, and Processing. All NMR data were acquired on a Varian UnityINOVA 600 MHz (^{13}C 150 MHz) spectrometer at 25 °C. A ^{1}H-^{13}C heteronuclear single quantum coherence (HSQC) spectrum was acquired to verify chemical shift assignments previously obtained (11). The ^{1}H-^{13}C HSQC spectrum was acquired with 1024 × 512 complex points in the t_2 and t_1 dimensions, respectively, with corresponding spectral widths of 6000 and 7540 Hz, a 1.5 s recycle delay, and 64 steady state scans. The proton radio frequency (RF) carrier was centered on the residual HDO signal and the ^{13}C carrier frequency was set at 85 ppm to allow differential folding of the ribose and base ^{13}C resonances.

For ^{13}C relaxation experiments, all two-dimensional spectra acquired on the 600 MHz spectrometer were obtained with 1024 × 128 complex points in the t_2 and t_1 dimensions, respectively, with corresponding spectral widths of 6000 and 1800 Hz, a 2 s recycle delay, and 15 min of steady state scans. The proton RF carrier was centered on the residual HDO signal, and the ^{13}C carrier

frequency was set at 78.3 ppm. R_1 data were acquired using minor variations of published pulse sequences (24). R_1 delay times ranged from 100 ms to 1050 ms collected in a random format. Dispersion curves were acquired through the use of relaxation-compensated CPMG (25,26), on-resonance $R_{1\rho}$ (24), off-resonance $R_{1\rho}$ (27,28), and Hahn echo (29) pulse sequences. The relaxation-compensated CPMG experiments were acquired as a function of inter-pulse spacing $2\tau_{CP}$, where τ_{CP} values ranged from 180 μs to 4500 μs, corresponding to effective spin-lock powers $\gamma B_1/2\pi$ [$\nu_{CP}=1/(4\tau_{CP})$] of ca. 1400 Hz to 55 Hz. On-resonance $R_{1\rho}$ experiments were acquired as a function of RF power ω_1, where $\omega_1/2\pi$ ranged from 1.5 to 6 kHz. Off-resonance $R_{1\rho}$ experiments were acquired as a function of Ω at a $\omega_1/2\pi$ of 3 kHz, where $\Omega/2\pi$ ranged from 3.5 to 9 kHz. Hahn echo experiments were acquired with a τ_{CP} value of 40 ms.

All NMR data were processed using FELIX 2002 (Felix NMR, Inc.). Prior to Fourier transformation in the t_2 dimension, a 20% DC offset was applied, data were zero filled, and a 3 Hz exponential line broadening function was applied. Prior to Fourier transformation in the t_1 dimension, t_1 was extended by 20% using linear prediction and a cosine-squared apodization function was applied.

Data Analysis. Resolved crosspeak intensities were integrated using FELIX 2002 and exported to Igor Pro 5 (Wavemetrics). In all experiments, one data

point was acquired three times to determine error. R_1 relaxation rates were extracted by fitting the integrated peaks to a single exponential decay. For dispersion curves, R_2 and $R_{1\rho}^{obs}$ rates were calculated using the equation $R_2/R_{1\rho}^{obs} = 1/T * \ln(I(T)/I_o)$, where T is the relaxation delay time, I is the measured intensity, and I_o is the measured intensity with no relaxation delay. The I_o was acquired twice to ensure reproducibility. $R_{1\rho}$ rates were calculated from $R_{1\rho}^{obs}$ using the equation $R_{1\rho}^{obs} = R_1 \cos^2\theta + R_{1\rho}\sin^2\theta$, where $\theta = \tan^{-1}(\omega_1/\Omega)$ is the tilt angle of the spin lock axis from the z axis, ω_1 is the spin lock power in Hz and Ω is the offset in Hz. Errors were propagated from a single ω_{eff} or ν_{CP} repeated three times (see chapter 3). Minimum values of errors were imposed to be 2% or greater. k_{ex}, $\Phi_{ex} = p_A p_B(\Delta\omega^2)$, R_2^0, and $R_{1\rho}^0$ values were extracted by simultaneously fitting dispersion curves to CPMG and $R_{1\rho}$ equations (30) using Igor 5.0.4.8's Global Fit. The CPMG and $R_{1\rho}$ equations used are given:

$$R_2(1/\tau_{CP}) = R_2(1/\tau_{CP}\rightarrow\infty) + p_A p_B(\Delta\omega)^2/k_{ex}*(1-((\tanh(k_{ex}/(4*\tau_{CP})))*4*\tau_{CP}/k_{ex})) \quad [4.1]$$

and

$$R_{1\rho}(\omega_{eff}) = R_{1\rho}(\omega_{eff}\rightarrow\infty) + p_A p_B(\Delta\omega)^2 * k_{ex}/(\omega_{eff}^2 + k_{ex}^2) \quad [4.2]$$

where $R_2(1/\tau_{CP}\rightarrow\infty)$ and $R_{1\rho}(\omega_{eff}\rightarrow\infty)$ are the transverse relaxation rates in the absence of exchange, respectively, p_A and p_B are the exchangeable populated states where the sum of p_A and p_B are equal to one, $\Delta\omega$ is the chemical shift difference in radians between the populated states p_A and p_B, k_{ex} is the exchange rate constant, $2\tau_{CP}$ is the delay time between 180° pulses, and the effective field, ω_{eff}, in radians per second can be expressed as:

$$\omega_{eff} = (\omega_1^2 + \Omega^2)^{1/2} \qquad [4.3]$$

F-statistic critical values (α) were calculated to justify fitting dispersion curves to exchange dependent equations as opposed to a horizontal line. F-values for C2′ and C4′ resonances were obtained by comparing χ^2 values obtained by fitting data sets to a horizontal line versus the dispersion equations. F-statistic critical values were obtained using the website: http://www.stattrek.com/tables/f.aspx. The confidence threshold was set to an α value of >0.95.

RESULTS

Hoogstraten *et al.* (18) previously analyzed dynamics of nucleotide bases within the active site of the lead-dependent ribozyme using power-dependent $R_{1\rho}$ dispersion curves. From this work, it was proposed that the base of C_6 undergoes conformational fluctuations that extrude the base from the asymmetric

internal loop. Unfortunately, spectral overlap prevented the analysis for C_6 using NMR spin relaxation techniques. To directly probe motions of C_6, ribose dynamics were analyzed for cytidine residues in the lead-dependent ribozyme using the alternate-site labeling scheme.

The ^{1}H-^{13}C HSQC for the 2′,4′-$^{13}C_2$ cytidine-only lead-dependent ribozyme was acquired to verify chemical shifts previously obtained (11) (Fig. 4.3). All eight C2′ and four C4′ resonances, including the C2′ and C4′ for the C_6 residue, were resolved for analysis. Hahn echo R_2 vales were measured to qualitatively determine resonances that have R_{ex} contributions (31) (Fig. 4.4). An increase in the R_2 value consistent with exchange on the μs to ms timescale was observed for both C2′ and C4′ resonances of C_6 as well as for C_2 C4′, but not C2′. Also, a decrease in the R_2 value was observed for C_{14} C2′ and C_{30} C2′ and C4′. This decrease is indicative of motions on the ps to ns timescale. Overall, these results suggest motions on multiple timescales for sugar carbons in the leadzyme. Relaxation dispersion curves were obtained to analyze ribose pucker transitions for C_6 in detail.

Figure 4.2: ^{1}H-^{13}C HSQC spectra of the cytidine-only specifically-labeled lead-dependent ribozyme corresponding to C2′ (top) and C4′ (bottom) resonances. Both C_6 resonances are labeled. The * denotes the resonance of C_{30} C2′.

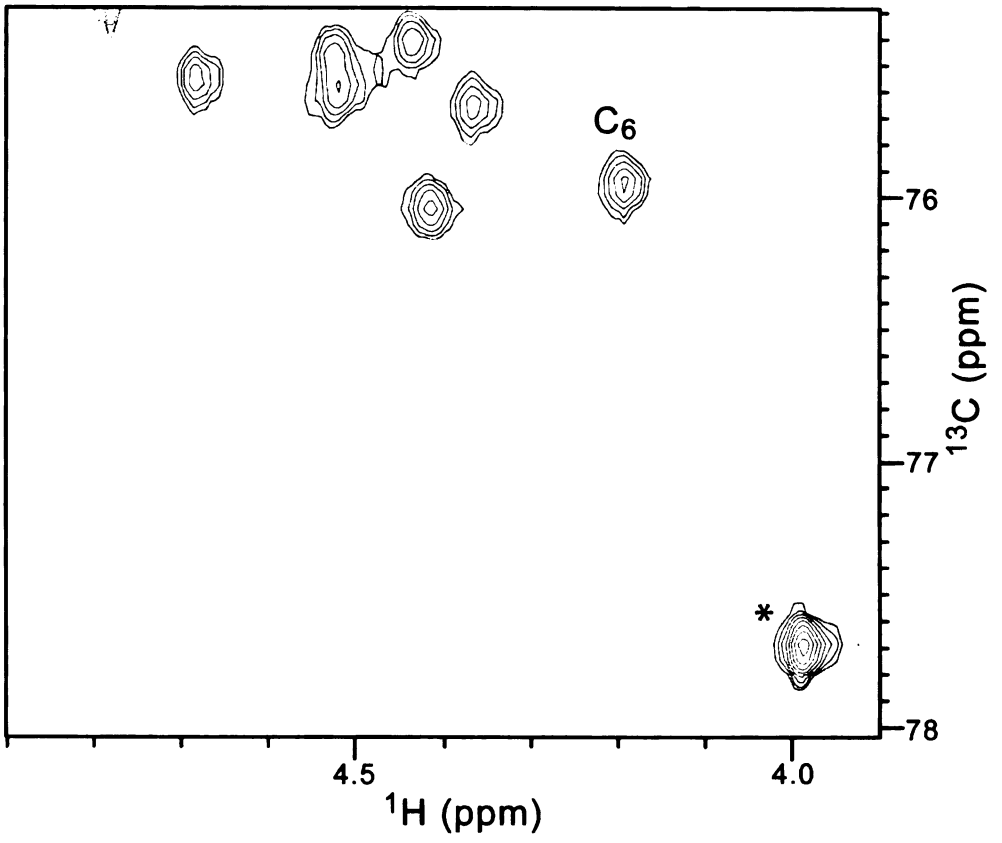
C6
*
76
77
78
13C (ppm)
4.5
4.0
1H (ppm)

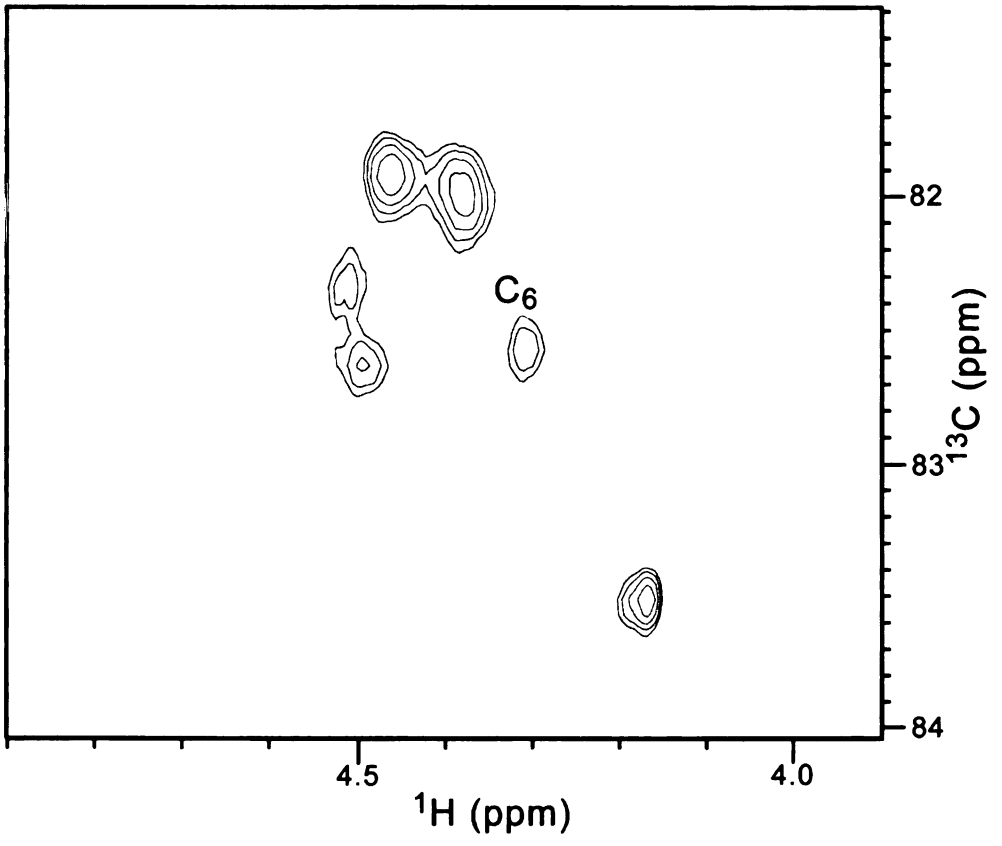
C6
82
83
84
13C (ppm)
4.5
4.0
1H (ppm)

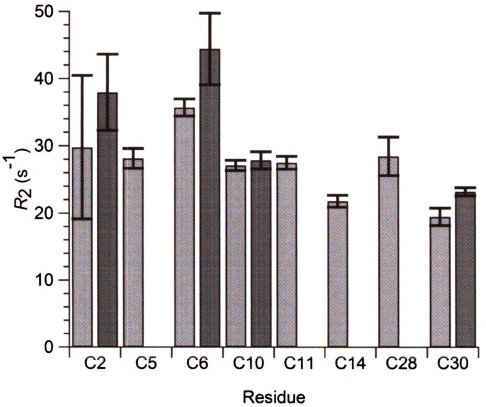

Figure 4.3: ^{13}C R_2 measurements from Hahn echo experiments for cytidine C2′ (grey) and (b) C4′ (black) resonances at 25 °C.

Analysis of μs-ms Motions. Relaxation dispersion curves were acquired for C2′ and C4′ atoms of cytidine residues in the lead-dependent ribozyme. Inconsistencies were observed for rcCPMG data points for C6 C2′ (Fig. 4.5a). Due to these inconsistencies, rcCPMG data points were deemed unreliable and motional parameters were determined from $R_{1\rho}$ data points only. Motional parameters were extracted from statistically significant fits to equation 4.2 for C_6 and C_{30} C2′ atoms. In Figure 4.4a, relaxation dispersion curves obtained for C_6

C2′ $R_{1\rho}$ data are presented. Also shown are the rcCPMG and $R_{1\rho}$ data for C_6 C4′. Motional parameters could not be obtained for C4′ due to the large errors. In Table 4.1, motional parameters determined from relaxation dispersion curves are presented. For C_6 C2′, the k_{ex} was determined to be $(1.1 \pm 0.4) \times 10^4$ s^{-1}, which corresponds to an exchange lifetime, τ_{ex}, of 93 ± 36 μs. This value is larger than the τ_{ex} values previously reported for A_{25} atoms around 40 to 50 μs (16,18).

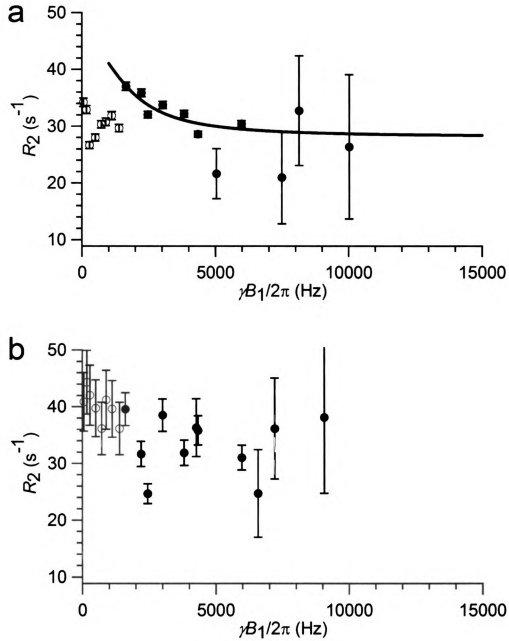

Fig. 4.4: CPMG (open circles) and $R_{1\rho}$ (closed circles) data for C_6 (a) C2′ and (b) C4′ of the lead-dependent ribozyme. Solid line represents fit to equation 4.2 for $R_{1\rho}$ data.

Table 4.1: Motional parameters derived via fitting C_6 and C_{30} C2′ $R_{1\rho}$ data to equation 4.2 at 25 °C.

	C_6 C2′	C_{30} C2′
Φ_{ex}	1.8e5 ± 0.2e5	1.5e5 ± 0.2e5
k_{ex}	1.1e4 ± 0.4e4	2.5e4 ± 0.3e4
$R_{1\rho}^0$	28.2 ± 0.9	14.9 ± 0.5
$\Delta\omega_{min}$ (ppm)	0.91 ± 0.05	0.81 ± 0.07
τ_{ex} (μs)	93 ± 36	41 ± 5

DISCUSSION

In this work, sugar pucker transitions in the lead-dependent ribozyme were analyzed using ^{13}C NMR spin relaxation experiments. Base dynamics of the leadzyme were previously studied using on-resonance $R_{1\rho}$ dispersion data (18). R_{ex} contributions were observed for several residues found within the tetraloop and in the asymmetric internal loop covering a range of exchange lifetimes. Interestingly, A_{25} C2 and C8 nuclei showed evidence of R_{ex} contributions that were attributed to proposed C_6 base fluctuations (18). It was postulated that this motion could be coupled to a sugar pucker interconversion from C3′-endo to C2′-endo (12,14) that would position the 2′-nucleophile for catalytic attack on the scissile phosphate.

For analysis of ribose dynamics, the leadzyme was transcribed using 2′,4′-$^{13}C_2$ rCTPs and commercial non-labeled rATPs, rGTPs, and rUTPs. Because

only cytidine residues are ^{13}C enriched with the alternate-site labeling scheme and there are only eight cytidines in the leadzyme, spectral overlap is decreased. Near complete resolution for the C2′ resonances was achieved. Only C_{14} and C_{28} were slightly overlapped; however, they were resolved well enough to allow for data analysis. Only four resonances were resolved for the C4′ resonances. Fortunately, both C_6 ^{13}C resonances were completely resolved allowing analysis of the critical nucleotide at the cleavage site.

Hahn echo experiments were acquired to verify μs-ms motions for the ribose ring. Hahn spin-echo experiments measure R_2 values at low effective fields. An increase in R_2 for both C2′ and C4′ atoms of C_6 were observed (Fig. 4.4). An increase in the R_2 was also observed for C_2 C4′ which is adjacent to the terminal residues. Because terminal residues are normally frayed, it can be presumed that dynamics for C_2 is due to terminal fraying. A decrease in the measured R_2 was observed for C_{14} C2′ and both C_{30} resonances, indicative of ps to ns motions. Both residues are located at the end of the helix. To further probe these motions, analysis using the model-free formalism (32-34) would be best suited.

Conformational change has been hypothesized to position the 2′-OH of C_6 to attack the scissile phosphate. Functional studies demonstrated that conformational flexibility for C_6 is required for catalysis. Cedegren and co-

workers (7) observed decreases in the observed catalytic rate when mutations stabilized the base pairing of site 6 to site 25. For example, when C_6 was involved in a Watson-Crick base pair at site 25 with a guanosine, catalysis is reduced by 50% (7). However, the catalytic rate was enhanced when modifications were utilized that disrupted stable base-pair formation for site 6. In fact, an increased catalytic rate over wild type was observed for an abasic residue of A_{25} (7).

Interpretation of data for C_{30} is complex due to the existence of motions on multiple timescales. Motional parameters were extracted from the relaxation dispersion curve of C_6 C2′ fitted to equation 4.2. Motions in the ribose ring have been attributed to ribose puckering transitions (see chapter 3). An exchange rate of $(1.1 \pm 0.4) \times 10^4\ s^{-1}$ was calculated for C_6 C2′. This corresponds to an exchange lifetime of almost 95 μs, which is longer than the exchange lifetimes for A_{25} C2 (40 μs) and C8 (47 μs) aromatic carbons (18). It should be noted that rcCPMG measured R_2 data were not included in the analysis. To rigorously analyze exchange for cytidine residues, acquisition of relaxation dispersion curves at a second field could aid in the interpretation of dynamics for C_6, particularly at 900 MHz. Though motional parameters were obtained from using $R_{1\rho}$ data acquired at only one magnetic field, this initial result is promising

because it demonstrates that the ribose ring of C_6 is dynamic consistent with the assumption that fluctuations at this site are needed to activate the leadzyme.

A statistically significant relaxation dispersion curve was not observed for C_6 C4′ (α = 0.48) which can be attributed to the large error bars on these data points. However, an increased R_2 was observed from Hahn echo experiments. It is possible that there is an exchange contribution present, yet the R_{ex} contribution is too small to accurately determine. Sugar pucker interconversions have been shown to be coupled to both C2′ and C4′ atoms of a given residue (see chapter 3). Acquisition of relaxation data at higher magnetic fields can increase R_{ex} contributions, which could clarify ambiguities.

The τ_{ex} value obtained for the ribose C_6 C2′ is longer than aromatic C2 and C8 for A_{25} previously obtained (18). One reason that these values are not similar could be additional constraints affecting sugar pucker interconversion. In the GCAA RNA hairpin, correlated motions for C_6 and A_7 residues and G_5 and A_8 residues (see chapter 3) were observed. This could also be occurring in the lead-dependent ribozyme. Dr. Minako Sumita of the Hoogstraten lab is investigating ribose dynamics for guanosine residues in a guanosine ^{13}C specifically labeled leadzyme NMR sample. Based on previous work by Julien *et al.* (10), the restriction of G_9 to C3′-endo conformation using a guanosine LNA greatly increased the observed catalytic rate. The measurement of ribose sugar

pucker interconversion for the guanosine residues could elucidate a pattern of concerted motions that helps position the 2′-OH of C_6 for proper orientation. These results coupled with C_6 dispersion data taken at multiple fields can yield insight into the active site of the leadzyme.

In this chapter, preliminary dynamics for sugar carbons of the lead-dependent ribozyme enriched with ^{13}C cytidine residues using the alternate-site labeling scheme were examined via NMR spin relaxation techniques. As evidenced from increased R_2 values from Hahn spin-echo measurements, an exchange lifetime of 93 μs was measured for C_6 C2′, which is longer than values reported for base carbons of A_{25}. While intra-residue correlated motions were not observed, these preliminary results suggest conformational flexibility for the ribose ring of C_6 which could aid in the catalytic mechanism of the lead-dependent ribozyme. For detailed analysis of the active site in the lead-dependent ribozyme, acquisition of relaxation dispersion curves at higher magnetic fields will be critical to aid in the understanding the catalytic mechanism.

REFERENCES

1. Pan, T. and Uhlenbeck, O.C. (1992) *In vitro* selection of RNAs that undergo autolytic cleavage with Pb^{2+}. *Biochemistry*, **31**, 3887-3895.

2. Brown, R.S., Dewan, J.C. and Klug, A. (1985) Crystallographic and biochemical investigation of the lead(II)-catalyzed hydrolysis of yeast phenylalanine tRNA. *Biochemistry*, **24**, 4785-4801.

3. Krzyzosiak, W.J., Marciniec, T., Wiewiorowski, M., Romby, P., Ebel, J.P. and Giege, R. (1988) Characterization of the lead(II)-induced cleavages in tRNAs in solution and effect of the Y-base removal in yeast tRNAPhe. *Biochemistry*, **27**, 5771-5777.

4. Pan, T. and Uhlenbeck, O.C. (1992) A small metalloribozyme with a two-step mechanism. *Nature*, **358**, 560-563.

5. Ohmichi, T. and Sugimoto, N. (1997) Role of Nd^{3+} and Pb^{2+} on the RNA cleavage reaction by a small ribozyme. *Biochemistry*, **36**, 3514-3521.

6. Sugimoto, N. and Ohmichi, T. (1996) Site-specific cleavage reaction catalyzed by leadzyme is enhanced by combined effect of lead and rare earth ions. *FEBS Lett*, **393**, 97-100.

7. Chartrand, P., Usman, N. and Cedergren, R. (1997) Effect of structural modifications on the activity of the leadzyme. *Biochemistry*, **36**, 3145-3150.

8. Pan, T., Dichtl, B. and Uhlenbeck, O.C. (1994) Properties of an in vitro selected Pb^{2+} cleavage motif. *Biochemistry*, **33**, 9561-9565.

9. Yajima, R., Proctor, D.J., Kierzek, R., Kierzek, E. and Bevilacqua, P.C. (2007) A conformationally restricted guanosine analog reveals the catalytic relevance of three structures of an RNA enzyme. *Chem Biol*, **14**, 23-30.

10. Julien, K.R., Sumita, M., Chen, P.H., Laird-Offringa, I.A. and Hoogstraten, C.G. (2008) Conformationally restricted nucleotides as a probe of structure-function relationships in RNA. *RNA*, **14**, 1632-1643.

11. Legault, P., Hoogstraten, C.G., Metlitzky, E. and Pardi, A. (1998) Order, dynamics and metal-binding in the lead-dependent ribozyme. *J Mol Biol*, **284**, 325-335.

12. Hoogstraten, C.G., Legault, P. and Pardi, A. (1998) NMR solution structure of the lead-dependent ribozyme: evidence for dynamics in RNA catalysis. *J Mol Biol*, **284**, 337-350.

13. Wedekind, J.E. and McKay, D.B. (1999) Crystal structure of a lead-dependent ribozyme revealing metal binding sites relevant to catalysis. *Nat Struct Biol*, **6**, 261-268.

14. Wedekind, J.E. and McKay, D.B. (2003) Crystal structure of the leadzyme at 1.8 A resolution: metal ion binding and the implications for catalytic mechanism and allo site ion regulation. *Biochemistry*, **42**, 9554-9563.

15. Lemieux, S., Chartrand, P., Cedergren, R. and Major, F. (1998) Modeling active RNA structures using the intersection of conformational space: application to the lead-activated ribozyme. *RNA* **4**, 739-749.

16. Legault, P. and Pardi, A. (1997) Unusual dynamics and pK_a shift at the active site of a lead-dependent ribozyme. *J Am Chem Soc*, **119**, 6621-6628.

17. Legault, P. and Pardi, A. (1994) *In situ* probing of adenine protonation in RNA by ^{13}C NMR. *J Am Chem Soc*, **116**, 8390-8391.

18. Hoogstraten, C.G., Wank, J.R. and Pardi, A. (2000) Active site dynamics in the lead-dependent ribozyme. *Biochemistry*, **39**, 9951-9958.

19. Batey, R.T., Battiste, J.L. and Williamson, J.R. (1995) Preparation of isotopically enriched RNAs for heteronuclear NMR. *Methods Enzymol*, **261**, 300-322.

20. Johnson, J.E., Jr., Julien, K.R. and Hoogstraten, C.G. (2006) Alternate-site isotopic labeling of ribonucleotides for NMR studies of ribose conformational dynamics in RNA. *J Biomol NMR*, **35**, 261-274.

21. Milligan, J.F. and Uhlenbeck, O.C. (1989) Synthesis of small RNAs using T7 RNA polymerase. *Methods Enzymol*, **180**, 51-62.

22. Milligan, J.F., Groebe, D.R., Witherell, G.W. and Uhlenbeck, O.C. (1987) Oligoribonucleotide synthesis using T7 RNA polymerase and synthetic DNA templates. *Nucleic Acids Res*, **15**, 8783-8798.

23. Cunningham, L., Kittikamron, K. and Lu, Y. (1996) Preparative-scale purification of RNA using an efficient method which combines gel electrophoresis and column chromatography. *Nucleic Acids Res*, **24**, 3647-3648.

24. Yamazaki, T., Muhandiram, R. and Kay, L. (1994) NMR experiments for the measurement of carbon relaxation properties in highly enriched, uniformly ^{13}C, ^{15}N-labeled proteins: application to $^{13}C\alpha$ carbons. *J Am Chem Soc*, **116**, 8266-8278.

25. Loria, J.P., Rance, M. and Palmer, A.G. (1999) A relaxation-compensated Carr-Purcell-Meiboom-Gill sequence for characterizing chemical exchange by NMR spectroscopy. *J Am Chem Soc*, **121**, 2331-2332.

26. Tollinger, M., Skrynnikov, N.R., Mulder, F.A., Forman-Kay, J.D. and Kay, L.E. (2001) Slow dynamics in folded and unfolded states of an SH3 domain. *J Am Chem Soc*, **123**, 11341-11352.

27. Mulder, F.A.A., de Graaf, R.A., Kaptein, R. and Boelens, R. (1998) An off-resonance rotating frame relaxation experiment for the investigation of macromolecular dynamics using adiabatic rotations. *J Magn Reson*, **131**, 351-357.

28. Hwang, T.L., van Zijl, P.C. and Garwood, M. (1998) Fast broadband inversion by adiabatic pulses. *J Magn Reson*, **133**, 200-203.

29. Millet, O., Loria, J.P., Kroenke, C.D., Pons, M. and Palmer, A.G., 3rd. (2000) The static magnetic field dependence of chemical exchange

linebroadening defines the NMR chemical shift time scale. *J Am Chem Soc*, **122**, 2867-2877.

30. Palmer, A.G., 3rd, Kroenke, C.D. and Loria, J.P. (2001) Nuclear magnetic resonance methods for quantifying microsecond-to-millisecond motions in biological macromolecules. *Methods Enzymol*, **339**, 204-238.

31. Massi, F., Grey, M.J. and Palmer, A.G., 3rd. (2005) Microsecond timescale backbone conformational dynamics in ubiquitin studied with NMR R1rho relaxation experiments. *Protein Sci*, **14**, 735-742.

32. Lipari, G. and Szabo, A. (1982) Model-free approach to the interpretation of nuclear magnetic resonance relaxation in macromolecules. 1. theory and range of validity. *J Am Chem Soc*, **104**, 4546-4559.

33. Lipari, G. and Szabo, A. (1982) Model-free approach to the interpretation of nuclear magnetic resonance relaxation in macromolecules. 2. analysis of experimental results. *J Am Chem Soc*, **104**, 4559-4570.

34. Mandel, A.M., Akke, M. and Palmer, A.G., 3rd. (1995) Backbone dynamics of *Escherichia coli* ribonuclease HI: correlations with structure and function in an active enzyme. *J Mol Biol*, **246**, 144-163.

Chapter 5

Assignment of ^{1}H, ^{13}C, and ^{15}N Resonances of Domain A of the Hairpin Ribozyme

INTRODUCTION

The hairpin ribozyme is a catalytic RNA that is derived from the minus strand of the tobacco ringspot virus satellite RNA (1). *In vivo*, the function of the ribozyme is to generate monomeric genomes from the rolling circle replication of the viroid genome for packaging (2). The hairpin ribozyme is similar to other small endonucleolytic ribozymes in that the cleavage reaction produces 2′,3′-cyclic phosphate and 5′-OH termini ends (3). Unlike other small ribozymes, such as the hammerhead and Hepatitis delta virus, the equilibrium favors ligation of the products rather than cleavage (4). An interesting characteristic of the hairpin ribozyme is that metal ions are required for folding, but do not directly participate in the chemical reaction. Catalysis for the hairpin ribozyme has been shown to occur in the presence of Mg^{2+} as well as non-ligand exchangeable $Co(III)[NH_3]_6^{3+}$ (5,6). Because of this, it has been theorized that nucleotide aromatic groups play an important role in the catalytic mechanism.

In vivo, the hairpin ribozyme uses a four-way helical junction to stabilize the tertiary structure (Fig. 5.1) (4). However, a reduced structure known as the minimal form that comprises the helix-loop-helix domains A and B that are linked together by a hinge is capable of catalysis (7), as are constructs in which the domains have been isolated and function *in trans*. (8). The scissile phosphate is located within the internal loop of domain A. For catalysis to occur, the two domains must interact with each other. This process is commonly referred to as docking. The domains for the hairpin ribozyme have been characterized from NMR solution structures of isolated domains A (9) and B (10), and from X-ray

crystal structures of the docked hairpin ribozyme complex (11-14), as well as functional studies (4-7,15-24).

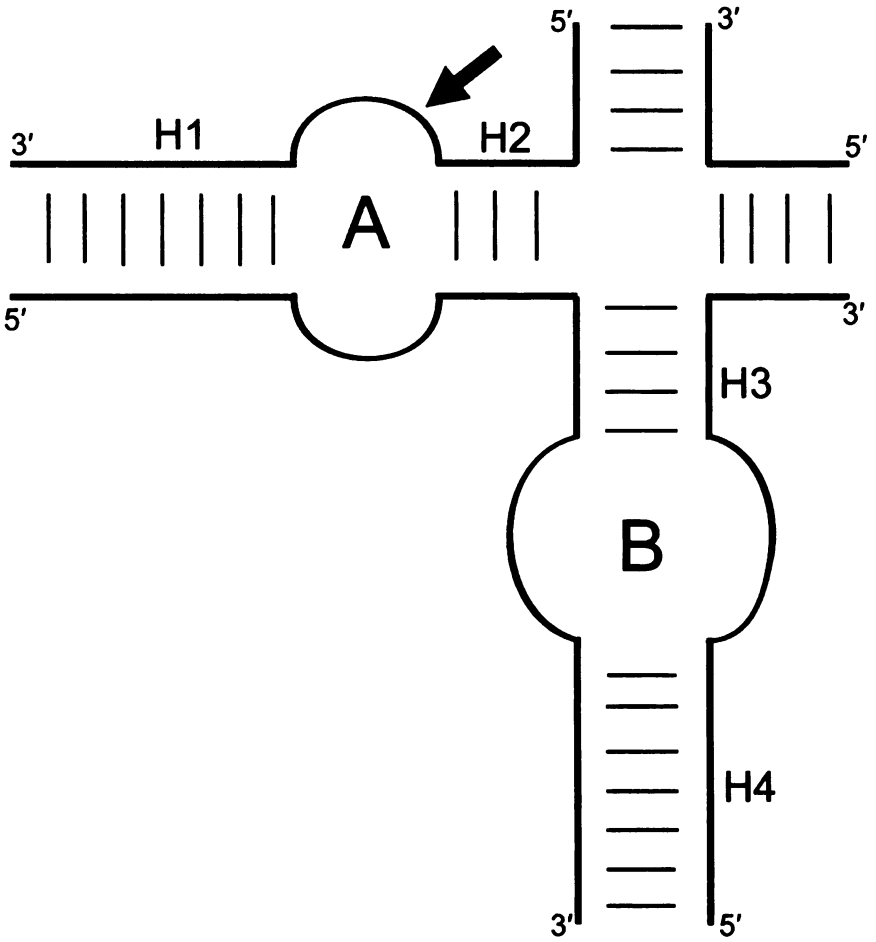

Figure 5.1: Diagram of the hairpin ribozyme utilizing a four-way junction. The internal loops are labeled, and the arrow denotes the site of cleavage.

In the NMR solution structure of the isolated domain A, an A-form RNA structure with anti χ glycosidic angles for all residues was found with a C3′-endo sugar pucker for all stem residues (9). In the NMR structure, the residue 5′ of the cleavage site was cytidine as opposed to adenosine in our sequence (Fig. 5.2). Within the internal loop, C3′-endo sugar pucker conformations were determined

for A_9, A_{10}, and C_{-1}, C2'-endo sugar pucker for G_8 and G_{+1}, and an equilibrium between the two forms for A_7, U_{+2}, and C_{+3} (see figure 5.2 for numbering). This cytidine base pairs with A_{10}, which is protonated due to a shift in the pK_a to 6.2, similar to results seen in the lead-dependent ribozyme (25,26). Also, G_{+1} was shown to form a non Watson-Crick base pair with A_9.

Conformational changes have been implicated in the catalytic mechanism for the hairpin ribozyme. From X-ray crystal structures, Ferre-D'Amare and co-workers (11) observed the extrusion of G_{+1} from the domain to base pair with C_{25} in the internal loop of domain B upon docking, which is hypothesized to be strengthened by base stacking with A_{38}. Comparison of the docked active site precursor, transition state mimic, and product structures of the hairpin ribozyme demonstrates a rigid active site (12) where changes were observed for the scissile phosphate and sugar moiety of A_{-1}, including a switch of pucker conformation from C3'-endo to C2'-endo. Investigation of ribose and base dynamics could help elucidate the role that conformational flexibility of active site nucleotides contributes to the overall catalytic mechanism of the hairpin ribozyme.

Mutational studies have been important in highlighting residues that are critical for the catalytic mechanism of the hairpin ribozyme, particularly within the active site (27-30). For instance, Burke and co-workers (30) investigated binding

and cleavage assays using single base substitutions of A_{-1} and U_{+2}. While it was determined that U_{+2} is not required for catalysis, the data suggested that U_{+2} is involved in tertiary contacts that can properly align the active site. From NMR analysis, the U_{+2} sugar pucker conformation was determined to be in equilibrium and the residue was modeled to be bulged from the internal loop with evidence of conformational flexibility on the ms timescale (9). Burke and co-workers (21) used time resolved fluorescence resonance energy transfer experiments to probe how U_{+2} mutations affect docking. Although cleavage rates decreased significantly, nucleotide substitutions did not drastically affect formation of the docked complex, including a $U_{+2}C$ modification which could form a Watson-Crick base pair with G_8. From X-ray crystal structures, U_{+2} was determined to have cross-strand interaction with G_8 (11,13,14). What still remains unknown is how mutations within the internal loop prohibit catalysis, but allow for global conformational changes such as docking. It is possible that the mutations that alter the internal loop architecture can quench key dynamics that are required for catalysis and not affect docking, a hypothesis which can be clarified by comparing dynamics between wild type and mutant sequences. One possible mutant sequence to test is $U_{+2}C/C_{+3}U$ domain A (Fig. 5.2). Burke and co-workers (31) demonstrated that $U_{+2}C/C_{+3}U$ sequences inactivate G_8 ribozyme strands in ligation assays, which could partially be rescued with the

introduction of a G_8U mutation. Unlike the $U_{+2}C$ mutant, the double mutant was shown to inhibit formation of the docked complex, which again could partially be restored with G_8U. Taken together, these results suggest that the role of U_{+2} is to properly align G_8 in the active site such that catalysis can occur efficiently. With the $U_{+2}C/C_{+3}U$ mutant sequence, internal loop dynamics may be decreased such that key interactions cannot be made.

Several groups have measured ^{13}C nucleotide base dynamics of RNA molecules (32-36). In previous chapters, methods and results were described that detailed the investigation of conformational exchange for ribose atoms in RNA molecules using NMR spin relaxation experiments. These methods can aid in understanding the catalytic mechanism of the hairpin ribozyme, particularly by investigating conformational exchange within the active site. Even though the NMR solution structure has been determined and chemical shift assignments for that sequence have been reported, the sequence used in this thesis is different (Fig. 5.2). Thus, chemical shift assignments for the wild type and mutant sequences are needed for detailed analyses using NMR spin relaxation experiments.

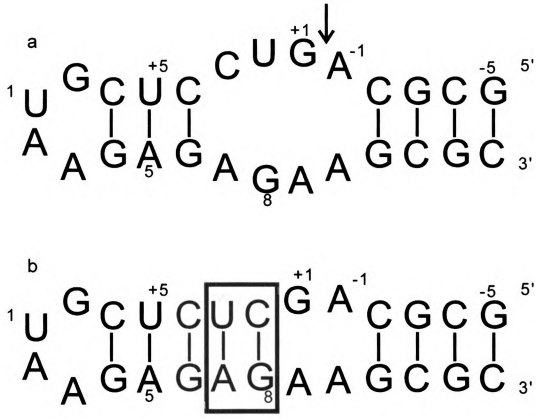

Figure 5.2: Secondary structure of the (a) wild type and (b) $U_{+2}C/C_{+3}U$ mutant domain A. The numbering scheme is similar to the hinge form of the hairpin ribozyme in which the structure is constructed from separate strands. Arrow denotes the site of catalysis. For the mutant sequence, the box denotes the residues that were transposed which could result in Watson-Crick base pairs.

Standard methods employing multidimensional spectroscopy of RNA molecules focus on two assignment strategies (37-40). The strategy of through-bond correlation uses scalar coupling between covalently bound nuclei to identify spin pairs, while through-space correlations of spin pairs are determined based on distances. The use of standard uniform isotope labeling can greatly aid in the determination of chemical shifts. Specific heteronuclear experiments have been designed to take advantage of heteronuclear spin pairs in RNA molecules. For

example, H1′ and H2′ ribose spin pairs can be identified using an HCCH-COSY pulse sequence. The H1′ region of the spectrum from this pulse sequence has less resonance overlap as compared to a ^{1}H-^{1}H NOESY spectrum of the same region. Even though correlated spectroscopy can identify spin pairs for a given nucleotide, NOE based experiments are vital to determine sequential nucleotide assignments. By combining the results obtained using both strategies, the complete assignment of a RNA molecule can be determined.

In this work, partial ^{1}H, ^{13}C, and ^{15}N chemical shift assignments have been determined for the wild type and $U_{+2}C/C_{+3}U$ mutant domain A of the hairpin ribozyme. These assignments were obtained from exchangeable and non-exchangeable spectroscopy experiments. Comparing exchangeable spectroscopy, new imino proton peaks and amino proton peaks were detected for the mutant $U_{+2}C/C_{+3}U$ indicating a tightening of the internal loop. While two-dimensional experiments were acquired, the acquisition of three-dimensional data as well as RNA-specific triple resonance experiments will allow for the complete determination of chemical shifts for detailed analysis of active site dynamics of domain A of the hairpin ribozyme.

MATERIALS and METHODS

Transcription of the ^{13}C, ^{15}N Domain A of the Hairpin Ribozyme. Uniformly ^{13}C, ^{15}N labeled ribonucleotides (Spectra Isotopes) were incorporated into the

twenty-six nucleotide domain A of the wild type and mutant $U_{+2}C/C_{+3}U$ hairpin ribozyme by *in vitro* transcription using recombinant T7 RNA polymerase and a synthetic DNA template (41,42). For the wild type sequence, transcribed RNA was purified from an ethanol precipitate of the previous reaction using denaturing polyacrylamide gel electrophoresis on a Bio-Rad model 491 preparative cell with a flow rate of 1 mL/min and 4 mL fractions. Fractions corresponding to domain A of the hairpin ribozyme as determined by gel electrophoresis were pooled, concentrated using a Rotovapor RE 120 (Buchi) under vacuum at 40 °C to a final volume of 1 mL, desalted using a G-25 Sephadex column collecting 1 mL fractions, pooled again and dried. For exchangeable proton spectroscopy, wild type domain A was resuspended to a final concentration of 1 mM in 270 μL 90%/10% H_2O/D_2O, 10 mM sodium phosphate pH 6.4, 150 mM NaCl, and 100 μM EDTA in an advanced NMR microtube matched with D_2O (Shigemi). For non-exchangeable proton spectroscopy, wild type domain A was resuspended in 99.96% D_2O after repeated lyophilization and resuspension with 99.9% D_2O to a final concentration of 1 mM as mentioned above.

For the mutant $U_{+2}C/C_{+3}U$, Patrick Ochieng, a graduate student in the lab, transcribed domain A and purified RNA using gel filtration chromatography on an Akta Basic FPLC (GE Healthcare) using a HiLoad 26/60 Superdex 75 column (34 μm, 26 mm × 60 mm) (43) monitored at A_{260} with an isocratic flow rate of 3 mL/min of 10 mM sodium phosphate pH 6.4, 100 mM NaCl collecting 5

mL fractions. Fractions corresponding to mutant domain A of the hairpin ribozyme were pooled and exchanged with H_2O with Amicon Ultra-4 centrifugal filter units, 3000 MWCO (Millipore). Mutant domain A was resuspended to a final concentration of 0.8 mM in 250 μL 90%/10% H_2O/D_2O, 10 mM sodium phosphate pH 6.4, 150 mM NaCl, and 100 μM EDTA in an advanced NMR microtube matched with D_2O (Shigemi). Prior to use, both NMR samples were heated to 65 °C for 5 min before cooling on ice for 5 min.

NMR Data Acquisition and Processing. All NMR data were acquired on a Varian UnityINOVA 600 MHz or Bruker Avance 900 MHz spectrometer. The 900 MHz spectrometer was equipped with a cryogenically cooled probe (Bruker TCI).

Exchangeable proton spectra were acquired at 5 and 15 °C. In all cases, the proton RF carrier was placed on the HDO residual peak. One-dimensional imino-optimized spectroscopy was performed using a 1-1 echo pulse sequence with 16388 complex points in the t_1 dimension, a spectral width of 15003.8 Hz, a 3 s recycle delay, and 80 steady state scans. ^{1}H-^{15}N heteronuclear single quantum coherence (HSQC) spectra were acquired with 1024 × 256 complex points in the t_2 and t_1 dimensions, respectively, with corresponding spectral widths of 13197 and 6078.76 Hz, a 1.5 s recycle delay and 128 steady-state scans. The ^{15}N carrier frequency was set at 118 ppm as determined from indirect referencing to internal reference standard 10 mM of sodium 2,2 dimethyl-2-silapentane-5-sulfonate (DSS). ^{1}H-^{1}H ^{15}N-edited homonuclear nuclear

Overhauser spectroscopy (NOESY-HSQC) spectra were acquired with 1024 × 128 complex points in the t_2 and t_1 dimensions, respectively, with corresponding spectral widths of 11995.8 and 11995.8 Hz, a 1 s recycle delay, 256 steady-state scans, and mixing times of 150 ms and 300 ms.

All non-exchangeable proton spectra were acquired at 25 °C for the wild type domain A. The proton RF carrier was placed on the HDO residual peak. Unless otherwise noted, the ^{13}C carrier was positioned at 111 ppm based on indirect referencing to internal reference standard DSS.

^{1}H-^{13}C HSQC spectrum was acquired with 1024 × 256 complex points in the t_2 and t_1 dimensions, respectively, with corresponding spectral widths of 6000.15 and 7540 Hz, and a 2 s recycle delay. ^{13}C carrier frequency was set at 85 ppm, as determined from indirect referencing to internal reference standard DSS (10 mM), to allow folding of the aromatic ^{13}C resonances. ^{1}H-^{13}C HSQC spectrum at 900 MHz was acquired with 512 × 256 complex points in the t_2 and t_1 dimensions, respectively, with corresponding spectral widths of 9920.64 and 15847.86 Hz, a 1.5 s recycle delay, and 256 steady-state scans. ^{1}H-^{1}H HCCH-correlated spectroscopy (COSY) sub-spectra were acquired with 1024 × 256 complex points in the t_2 and t_1 dimensions, respectively, with corresponding spectral widths of 2999.18 and 2399.18 Hz, a 2 s recycle delay, and 256 steady-state scans. ^{1}H-^{1}H HCCH-total correlated spectroscopy (TOCSY) sub-spectra

were acquired with 512 × 256 complex points in the t_2 and t_1 dimensions, respectively, with corresponding spectral widths of 2999.18 and 2999.18 Hz, a 2 s recycle delay, and 384 steady-state scans. For carbon correlation, a 10 ms DIPSI-3 mixing period was used. ^{1}H-^{1}H homonuclear ^{13}C-edited nuclear Overhauser spectroscopy (NOESY-HSQC) sub-spectra were acquired with 1024 × 256 complex points in the t_2 and t_1 dimensions, respectively, with corresponding spectral widths of 5997.9 and 5997.9 Hz, a 2 s recycle delay, 256 steady-state scans and mixing times of 150 ms and 300 ms. At 900 MHz, ^{1}H-^{1}H homonuclear NOESY spectrum was acquired with 1024 × 200 complex points in the t_2 and t_1 dimensions, respectively, with corresponding spectral widths of 9920.64 and 9920.64 Hz, a 1.5 s recycle delay, 256 steady-state scans and a mixing period of 150 ms.

All two-dimensional exchangeable spectra in H_2O were processed using Varian VNMR 6.1. Prior to Fourier transformation, 3 Hz exponential line broadening function was applied for the t_2 dimension and a Gaussian window function was applied for the t_1 dimension. All other experiments were processed using FELIX 2002 (Accelrys). Prior to Fourier transformation in the t_2 dimension, a 20% DC offset was applied, data was zero filled, and a 3 Hz exponential line broadening function was utilized. Prior to Fourier transformation in the t_1 dimension, a cosine-squared apodization function was applied.

RESULTS

One-Dimensional Spectroscopy. RNA molecules have different types of exchangeable protons including those on imino (-NH) groups of guanosines and uridines, and amino ($-NH_2$) protons for cytidines, guanosines, and adenosines. These protons are not observed in ^1H NMR unless they are protected from fast exchange with solvent, primarily through base pairing (37). The observation of these exchangeable protons can provide information about secondary structure of the RNA molecule. Figure 5.3 shows imino proton resonances detected at 15 °C for (top) mutant $U_{+2}C/C_{+3}U$ and (bottom) wild type domain A of the hairpin ribozyme. Guanosine imino protons usually resonate between 10 and 13 ppm while uridine imino protons typically resonate between 12 and 15 ppm. From the wild type imino proton spectrum, six guanosine imino protons and one uridine imino proton were detected, which is in good agreement with the predicted secondary structure. Guanosine imino protons detected upfield at 10 ppm have been observed from sheared G:A base pairs (37). The guanosine imino proton of G_{+7} was observed in both sequences at 10.5 ppm. From the wild type sequence, the lone uridine imino proton for U_{+5} was detected at 14.16 ppm whereas two uridine imino protons were detected in the mutant sequence, one at 14.2 (U_{+5}) and another at 13.96 ppm (U_{+3}). From 12 to 13 ppm, five distinct guanosine imino protons were detected in the wild type sequence. Several additional imino protons were detected in the mutant sequence. Interestingly,

four guanosine imino protons have similar chemical shifts in both the wild type and mutant sequence in this chemical shift range. These peaks can be attributed to base-paired guanosine imino protons of G_{-3}, G_4, G_{11}, and G_{13}. For the mutant sequence, an additional guanosine imino proton was detected at 12.36 ppm, which can be attributed to G_8 located in the internal loop. This imino proton was not observed in the wild type spectrum. Also, the guanosine imino proton detected at 12.62 ppm in the wild type spectrum was shifted to 12.76 in the mutant spectrum. This guanosine imino proton was tentatively attributed to G_6. In the mutant spectra, an imino proton peak was detected at 12.49 ppm. The identity of this peak is unknown (see discussion). No imino proton peaks were detected for G_{+1} in either spectrum. G_{+1} imino proton would resonate upfield similar to G_{+7} due to non Watson-Crick base pairing with A_9. These results strongly suggest a properly folded RNA molecule with good agreement with predicted RNA secondary structure. Based on overlap of chemical shift assignments in both spectra and the addition of new peaks in the mutant spectrum, these results display consistent secondary structure predictions with variations localized near the internal loop.

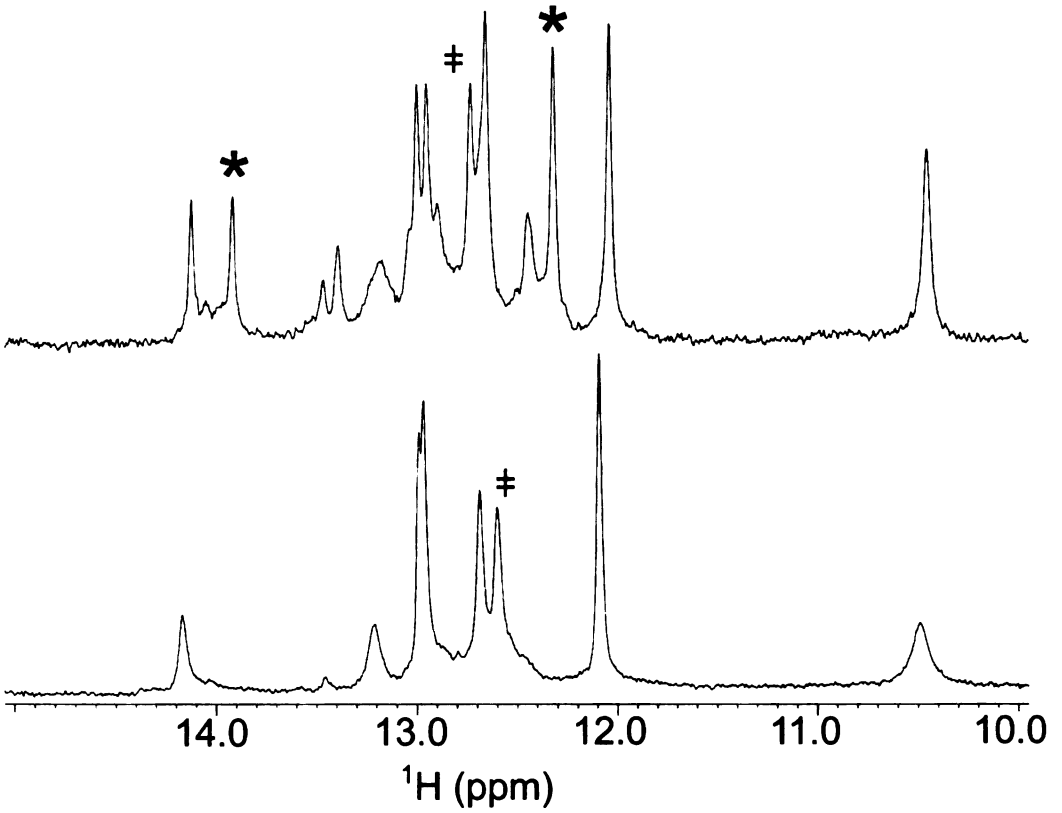

Figure 5.3: One-dimensional comparison of the imino proton region for the (top) mutant $U_{+2}C/C_{+3}U$ and (bottom) wild type isolated domain A at 15 °C. For the mutant spectrum, * represents new peaks not observed in the wild type spectrum. ‡ represents a downfield shift for G_6 H1 in the mutant spectrum.

Two-dimensional Exchangeable Spectroscopy. For the imino proton region, the ^{1}H-^{15}N HSQC spectra acquired at 15 °C confirms the ^{1}H assignments from one-dimensional spectroscopy of the wild type and mutant $U_{+2}C/C_{+3}U$ sequences (Fig. 5.4). In addition, ^{15}N chemical shifts were correlated to ^{1}H chemical shifts.

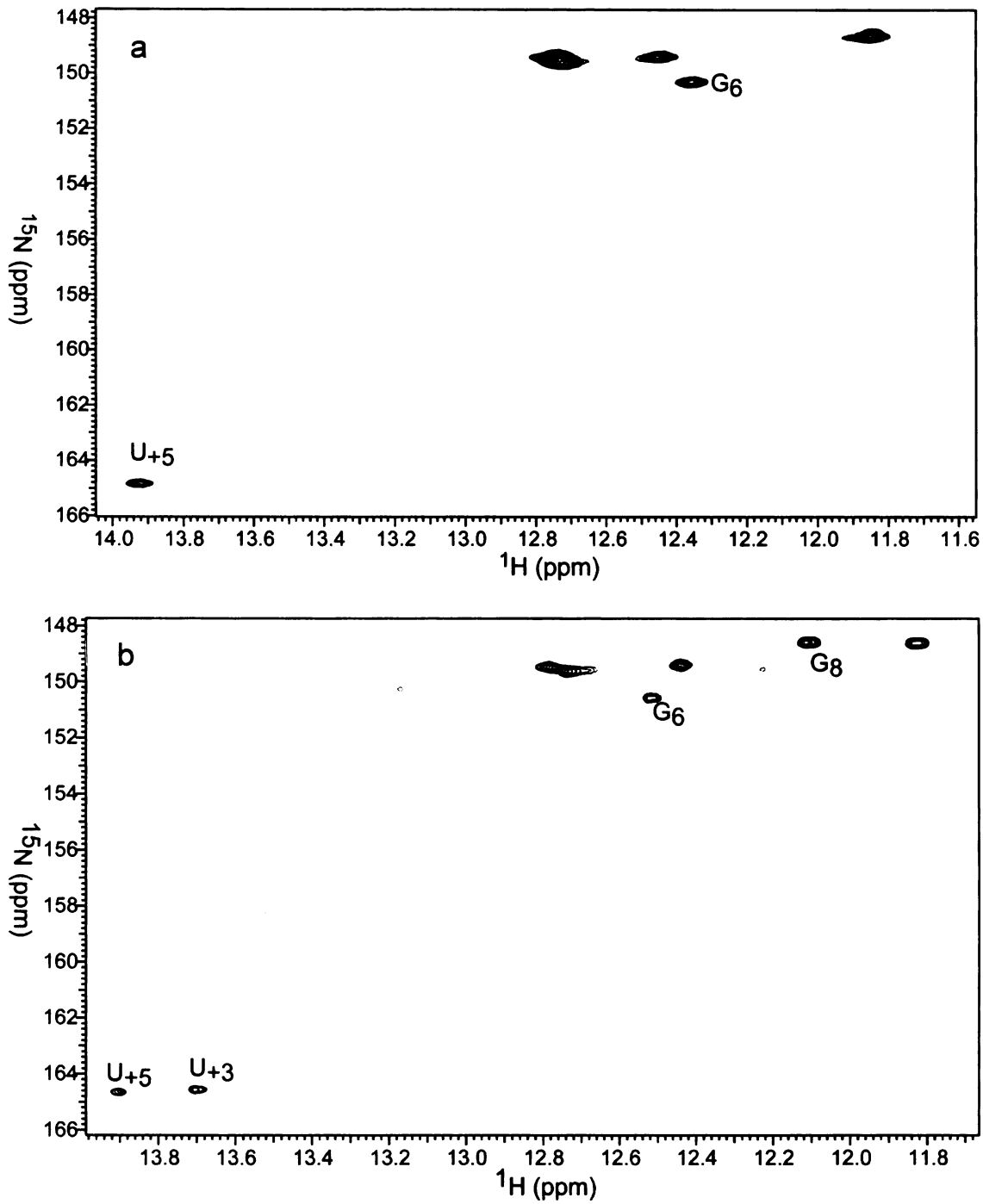

Figure 5.4: ^{1}H-^{15}N HSQC spectra of the imino proton region for (a) wild type and (b) mutant $U_{+2}C/C_{+3}U$ domain A of the hairpin ribozyme at 15 °C. Labeled crosspeaks were determined from one- and two-dimensional spectra.

Analyzing exchangeable amino protons is less straightforward than imino protons due to resonance overlap with aromatic protons. The use of two-dimensional spectroscopy can reduce resonance overlap and identify amino ^{1}H chemical shifts. Two dimensional ^{1}H-^{15}N HSQC spectra for the amino proton region at 15 °C are shown in Figure 5.5 for the wild type and mutant $U_{+2}C/C_{+3}U$ sequences. Resonances are observed in two distinct chemical shift ranges. These ranges correspond to the hydrogen-bond proton (downfield) and non-hydrogen bond proton (upfield) of the amino NH_2 for cytidines base paired with guanosines. Both protons correlate to the same ^{15}N nuclei. For the wild type sequence, five amino proton pairs are detected while seven amino proton pairs are detected for the mutant sequence, which is in good agreement with predicted Watson-Crick base pairs for domain A. Unlike imino proton resonances, ^{1}H and ^{15}N amino proton chemical shifts are dissimilar for wild type and mutant sequences. In the mutant spectrum, a feature derived from an additional cytidine amino group was observed. Because amino proton chemical shifts are dissimilar between the wild type and mutant spectra, tentative residue assignments could not be made.

Amino protons from purine residues are less commonly observed due to intermediate exchange which results in severely broadened resonances. Temperature and pH changes could allow for detection in some cases. Lowering the temperature to 5 °C did not result in the detection of purine amino protons

(data not shown). It is possible pH changes could result in the detection of purine amino protons; however, pH changes were not examined in this work.

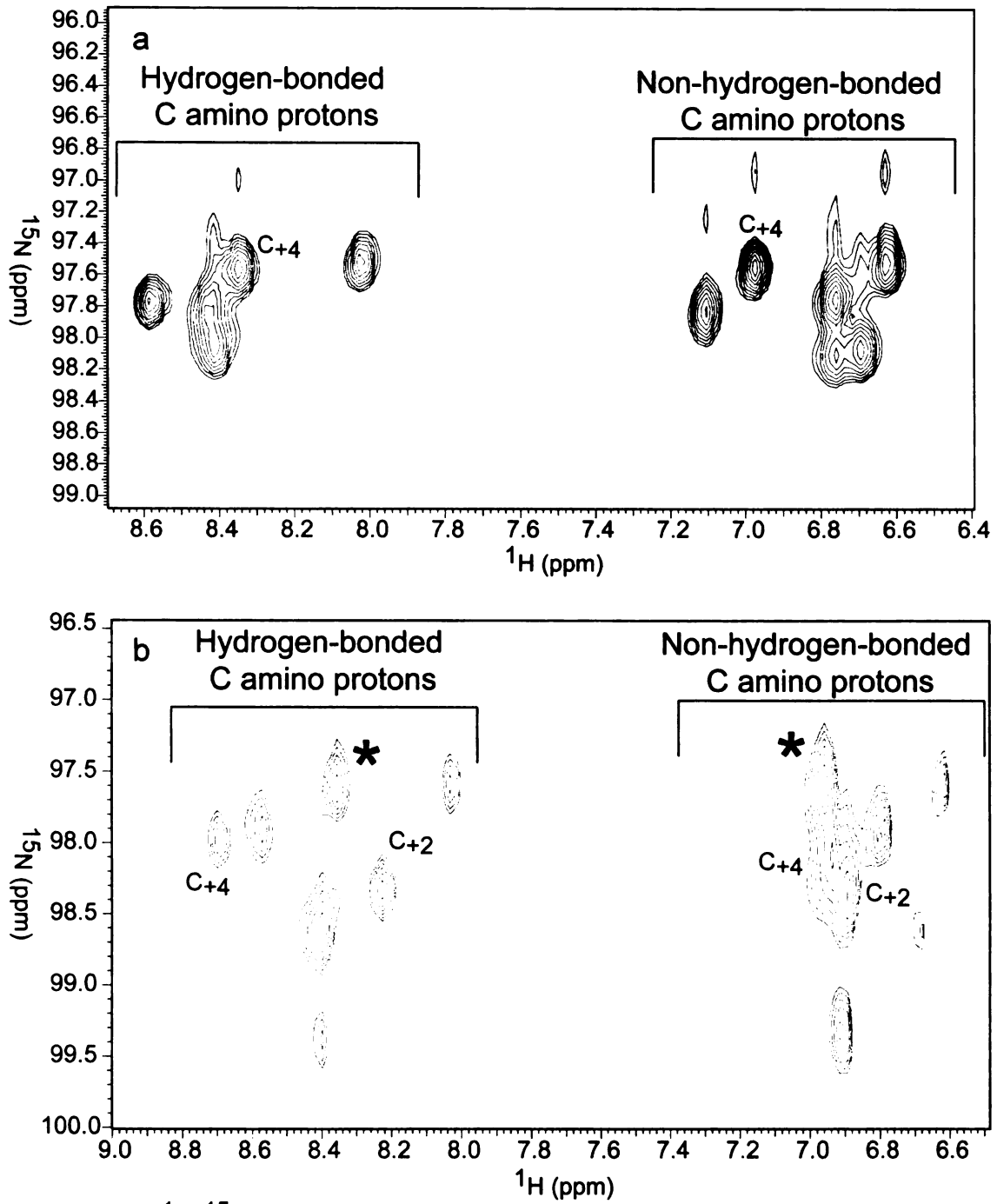

Figure 5.5: ^{1}H-^{15}N HSQC spectra of the amino proton region for (a) wild type and (b) mutant $U_{+2}C/C_{+3}U$ domain A of the hairpin ribozyme at 15 °C. For the mutant spectrum, * denotes crosspeaks from a non-predicted cytidine residue.

To identify Watson-Crick G:C base pairs, ^{1}H-^{1}H ^{15}N-edited NOESY sub-spectra were acquired (Fig. 5.6 and 5.7). From these spectra, amino protons of cytidine NH_2 groups were identified which confirmed the identification of spin pairs determined from ^{1}H-^{15}N HSQC experiments. G:C base pairs were identified from guanosine imino proton to cytosine amino proton crosspeaks. Two NOE correlations were observed for each imino proton resonance. These NOEs, again, confirm amino proton assignments for cytidine residues. With the tentative identification of G_6 and G_8 chemical shifts, imino to amino proton correlations allowed the identification of C_{+4} and C_{+2}, respectively. Also, the unknown guanosine imino proton at 12.49 ppm was observed to correlate with unknown cytidine amino protons. This was not observed in the wild type spectrum. The identity of this G:C base pair is unclear.

NOESY experiments can also identify A:U base pairs. Uridine imino protons in A-form RNA have been shown to exhibit strong NOEs to H2 of base paired adenines. A single NOE was observed for each uridine imino proton to the base paired adenosine H2 in the wild type and mutant spectra. These crosspeaks can be attributed to H2 of A_5 and A_7 for U_{+5} and U_{+3}, respectively.

The inter-residue distance for imino protons in base pairs is $\approx$ 4 Å. For NOESY experiments, this can give rise to weak NOEs at longer mixing times. From these NOEs, a NOESY walk would aid in the sequential assignment of

Watson-Crick base paired regions, particularly G_{-5}, G_{-3}, G_4, G_{11}, and G_{13}. With these assignments, the remaining cytidine resonances could be identified. No imino to imino proton NOEs were observed for spectra acquired with 150 and 300 ms mixing periods at 15 °C. Even at 5 °C, imino to imino proton NOEs were not observed at 300 ms mixing times (data not shown). Because imino to imino proton crosspeaks were not observed, complete imino proton sequential assignments were not obtained for the wild type or mutant domain A. However, partial assignments have been made and are listed in Tables 5.1 and 5.2.

Taken together, all ^{1}H and ^{15}N chemical shifts for guanosine and uridine imino protons as well as cytidine amino protons have been determined, which are consistent with a properly folded RNA molecule and agree well with predicted secondary structures for the wild type and mutant sequences of domain A. Preliminary residue assignments were determined for helix cytidine amino protons, uridine and guanosine imino protons including G_8.

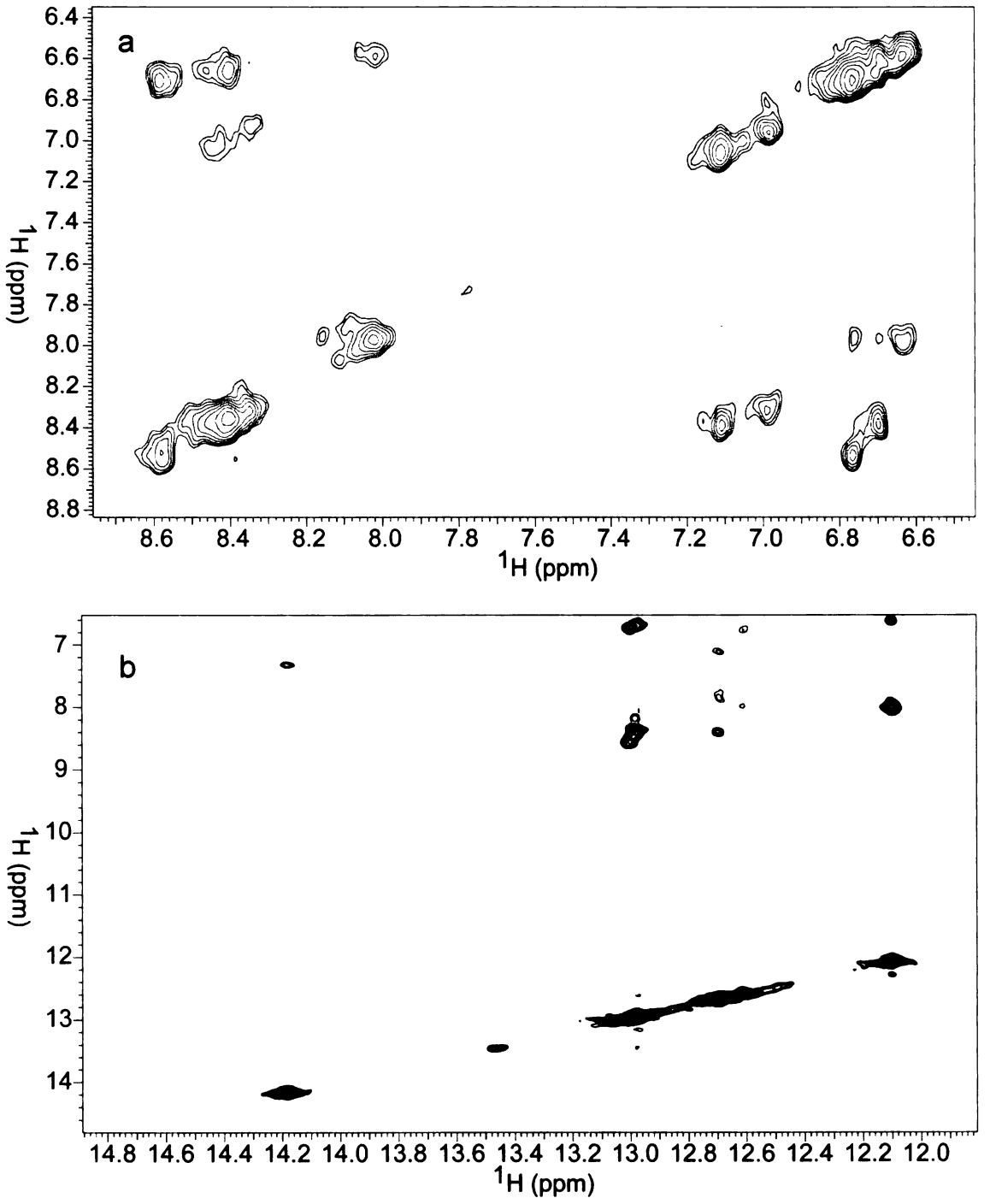

Figure 5.6: ^{1}H-^{1}H NOESY-HSQC sub-spectra of the wild type hairpin domain A at 15 °C. Shown are the (a) amino to amino proton and (b) amino to imino proton regions at 150 ms mixing time.

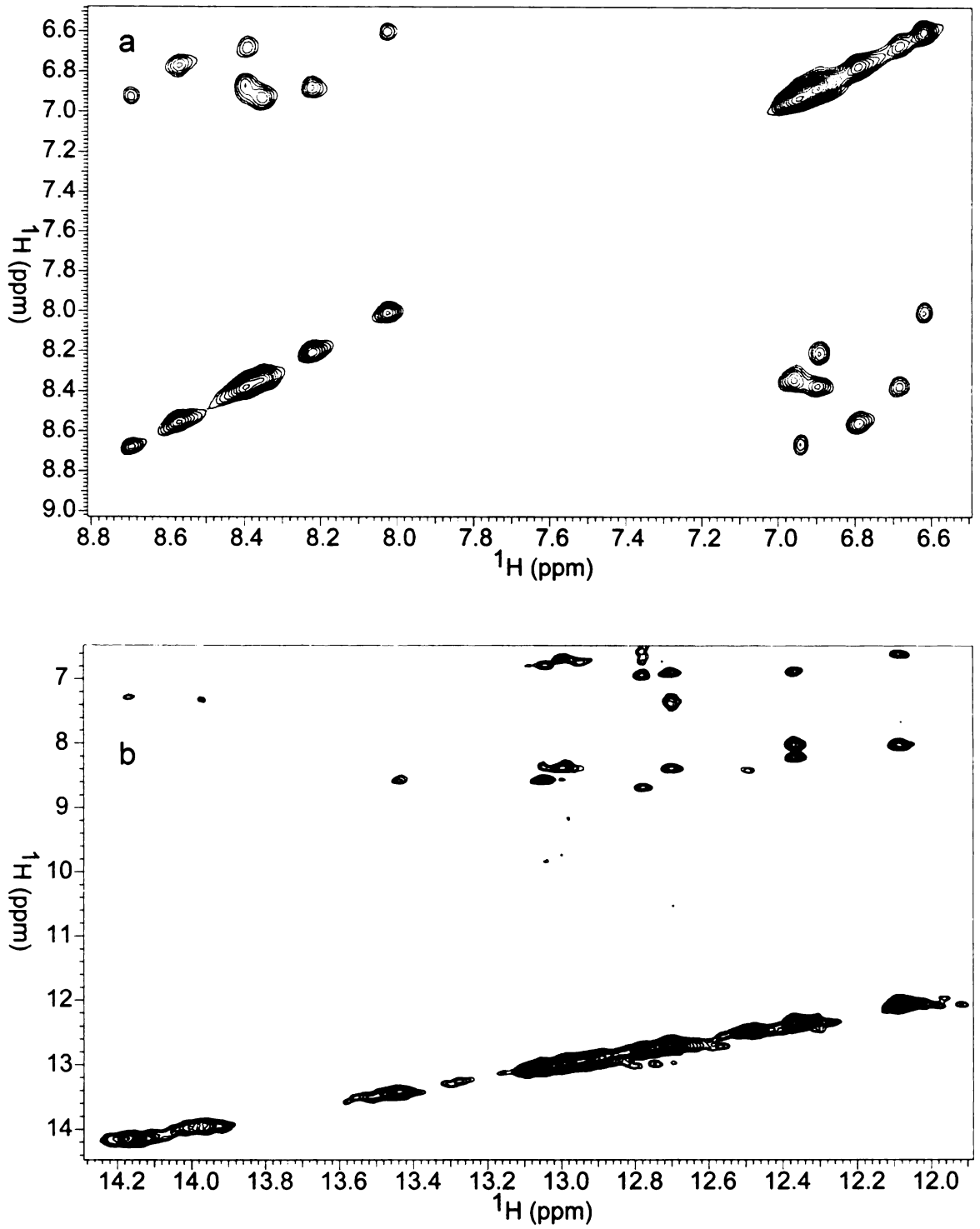

Figure 5.7: ^{1}H-^{1}H NOESY sub-spectra of the mutant $U_{+2}C/C_{+3}U$ hairpin domain A at 15 °C. Shown are the (a) amino to amino proton and (b) amino to imino proton regions at 150 ms mixing time.

Table 5.1: Wild type domain A ^{1}H and ^{15}N chemical shifts.

Imino proton assignment	^{1}H chemical shift (ppm)[a]	^{15}N chemical shift (ppm)
G_{+7}	10.50	146.14
GX1	12.11	147.61
G_{+6}	12.62	147.61
GX2	12.70	147.46
GX3	12.98	147.68
GX4	13.00	147.47
U_{+5}	14.19	162.93

Amino proton assignment	^{1}H chemical shift (ppm)[b]	^{15}N chemical shift (ppm)
CX1	8.03, 6.63	97.52
C_{+4}	8.35, 6.97	97.58
CX2	8.42, 6.69	98.04
CX3	8.43, 7.10	97.87
CX4	8.59, 6.76	97.77

Resonances are ordered based on [a]imino proton or [b]amino proton chemical shifts. X denotes unknown assignment of resonance.

Table 5.2: Mutant $U_{+2}C/C_{+3}U$ domain A ^{1}H and ^{15}N chemical shifts.

Imino proton assignment	^{1}H chemical shift (ppm)[a]	^{15}N chemical shift (ppm)
G_{+7}	10.51	146.18
GX1	12.08	146.69
G_{8}	12.36	146.65
GX2	12.49	147.62
GX3	12.70	147.48
G_{6}	12.76	148.64
GX4	13.00	147.69
GX5	13.04	147.55
U_{+3}	13.96	162.65
U_{+5}	14.16	162.74

Amino proton assignment	^{1}H chemical shift (ppm)[b]	^{15}N chemical shift (ppm)
CX1	8.03, 6.62	97.59
C_{+2}	8.23, 6.89	98.35
CX2	8.36, 6.81	97.65
CX3	8.40, 6.91	99.41
CX4	8.40, 6.68	98.64
CX5	8.57, 6.79	97.91
C_{+4}	8.70, 6.94	98.02

Resonances are ordered based on [a]imino proton or [b]amino proton ^{1}H chemical shift. X denotes unknown assignment of resonance.

Two-Dimensional Spectroscopy of Non-exchangeable Resonances. To identify ^{1}H-^{13}C proton spin systems and obtain ^{1}H and ^{13}C assignments, non-exchangeable experiments have been utilized for the wild type sequence. Mutant $U_{+2}C/C_{+3}U$ ^{1}H and ^{13}C assignments would be compared to wild type chemical shifts. It is possible that ^{1}H and ^{13}C chemical shifts would be roughly similar between both sequences, as was the case for imino proton resonance chemical shifts. With this approach, mutant chemical shifts could be easily identified with noticeable chemical shift changes limited to resonances in the internal loop.

^{1}H-^{13}C spin pairs were identified from a ^{1}H-^{13}C HSQC experiment at 25 °C acquired at 600 MHz (Fig. 5.8) for the wild type sequence. For the ribose atoms, significant overlap is observed for H2′/C2′, H3′/C3′, H4′/C4′, H5′/C5′, and H5″/C5″ crosspeaks while the H1′/C1′ crosspeaks are well dispersed. From the latter region, twenty-three resonances have been identified out of a total of twenty-six. For the aromatic atoms of cytidine and uridine, all twenty H5/C5 and H6/C6 crosspeaks have been identified. Thirteen out of sixteen crosspeaks were detected for purine H8/C8 atoms. Although the regions of purine H8/C6 and pyrimidine H6/C6 resonances overlap, they could be differentiated based on multiplet structures. Because ^{13}C labeled C6 are coupled to ^{13}C labled C5, the H6/C6 crosspeak is observed as a doublet in the ^{13}C dimension. Moderate

overlap was observed for adenine H2/C2 resonances. Similar results were obtained for a ^{1}H-^{13}C HSQC acquired at 900 MHz (data not shown).

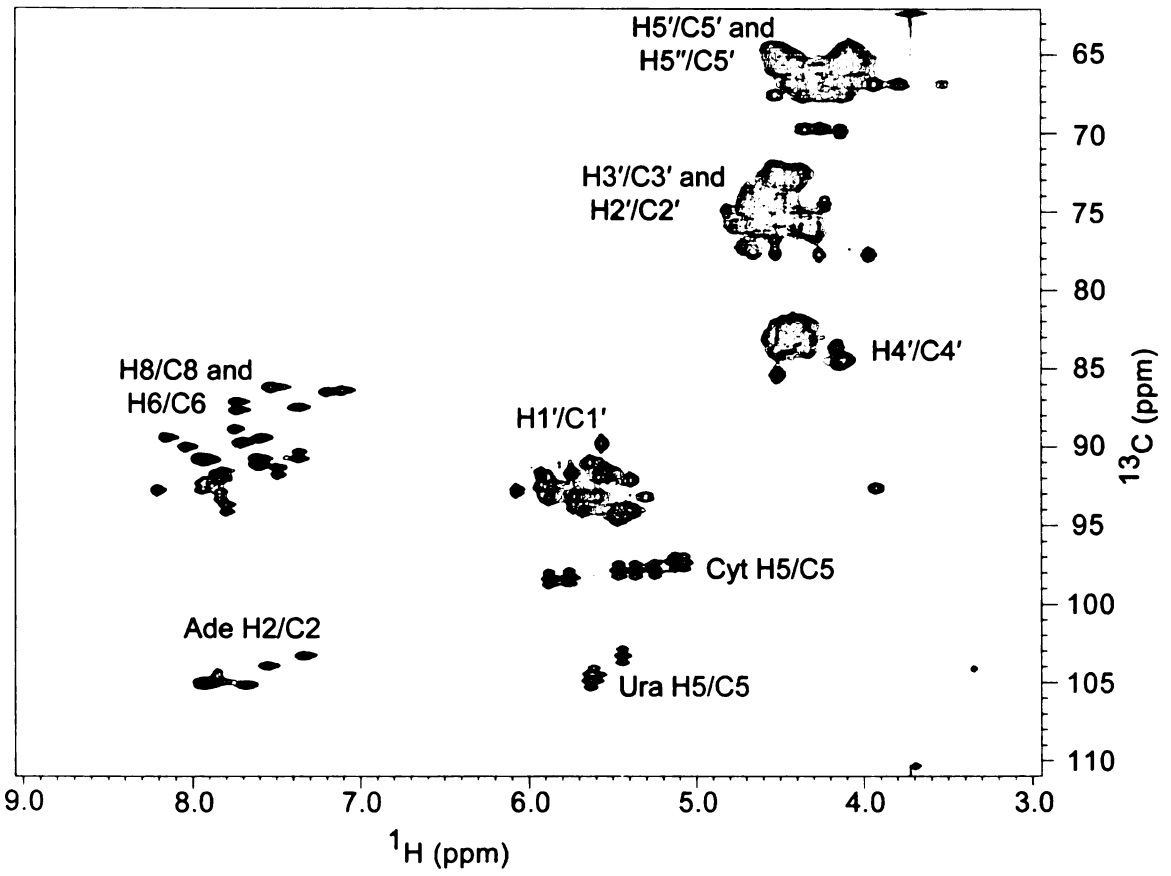

Figure 5.8: ^{1}H-^{13}C HSQC spectrum of the non-exchangeable resonances of the wild type domain A of the hairpin ribozyme at 25 °C acquired at 600 MHz. Spectral regions are labeled.

Considerable overlap for the H2′/C2′, H3′/C3′, H4′/C4′, H5′/C5′, and H5″/C5″ spin pairs prevents accurate obtainment of chemical shift assignments from these data. However, the use of sophisticated RNA correlation experiments can alleviate ambiguity by the detection of crosspeaks from multiple spin

systems, particularly correlations to well dispersed spin systems. HCCH-COSY experiments were used to correlate covalently bound ^{1}H-^{13}C spin pairs. Briefly, the HCCH-COSY pulse sequence transfers proton magnetization to adjacent protons through one-bond ^{13}C-^{13}C coupling. The ^{1}H-^{1}H HCCH-COSY sub-spectrum that shows correlation of H1′ and H2′ proton chemical shifts is presented in Figure 5.9a. Nineteen H1′-H2′ resolved crosspeaks out of twenty-six were observed. Two H1′ protons with 5.57 ppm chemical shifts that were resolved in the HSQC based on ^{13}C chemical shifts were correlated to a single H2′ proton. This was also observed at 5.59 ppm. Because a two-dimensional sub-spectrum was acquired, the acquisition of three-dimensional spectrum could clarify which H1′ correlates to H2′. Correlations among other ribose protons could not be differentiated due to their similar chemical shifts. The ^{1}H-^{1}H HCCH-COSY sub-spectrum that shows correlation of H5 and H6 chemical shifts is shown in Figure 5.9b. Ten crosspeaks are observed consistent with the total number of pyrimidine residues.

Figure 5.9: ^{1}H-^{1}H HCCH-COSY sub-spectra of the wild type domain A at 25 °C at 600 MHz. Shown are the (a) ribose H1′-H2′ correlations and (b) pyrimidine H5-H6 correlations.

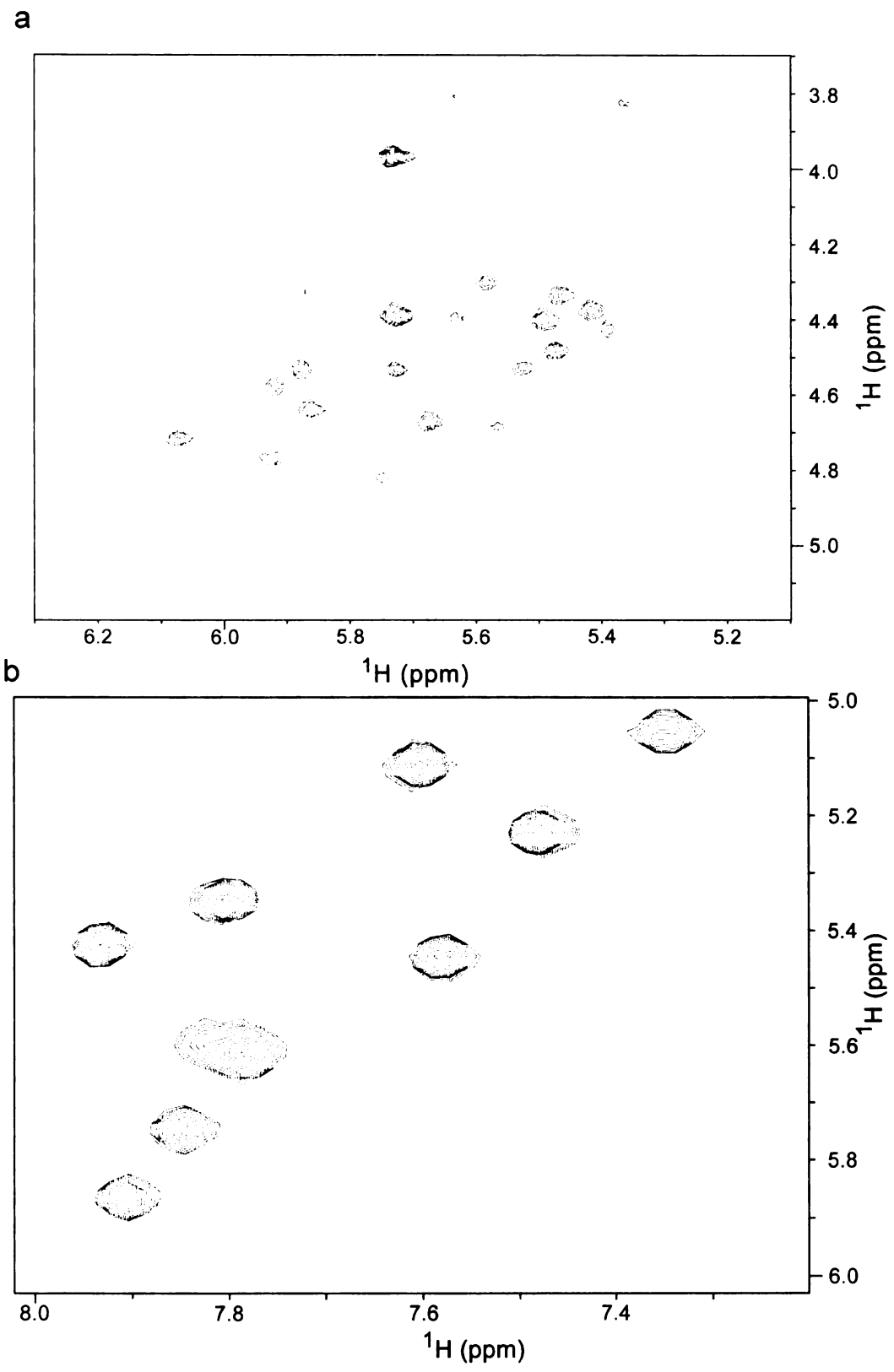
a
3.8
4.0
4.2
4.4
4.6
4.8
5.0
^{1}H (ppm)
6.2
6.0
5.8
5.6
5.4
5.2
^{1}H (ppm)
b
5.0
5.2
5.4
5.6
5.8
6.0
^{1}H (ppm)
8.0
7.8
7.6
7.4
^{1}H (ppm)

To complete accurate chemical shift assignments for ribose protons, HCCH-TOCSY experiments were employed. HCCH-TOSCY experiments are similar to HCCH-COSY experiments. However, the HCCH-TOCSY pulse sequence employs a mixing period where magnetization can be transferred through several ^{13}C-^{13}C couplings, thus connecting all ^{1}H-^{13}C pairs within a single spin system. Combining HCCH-COSY H1′-H2′ correlations with HCCH-TOCSY H3′, H4′, and H5′ correlations to H1′, the entire ribose ^{1}H-^{13}C spin system can be assigned. From the ^{1}H-^{1}H HCCH-TOCSY sub-spectrum presented in Figure 5.10, additional crosspeaks are observed when compared to the ^{1}H-^{1}H HCCH-COSY sub-spectrum of the same region. These additional crosspeaks can be attributed to correlations to H3′, H4′, and H5′ to H1′.

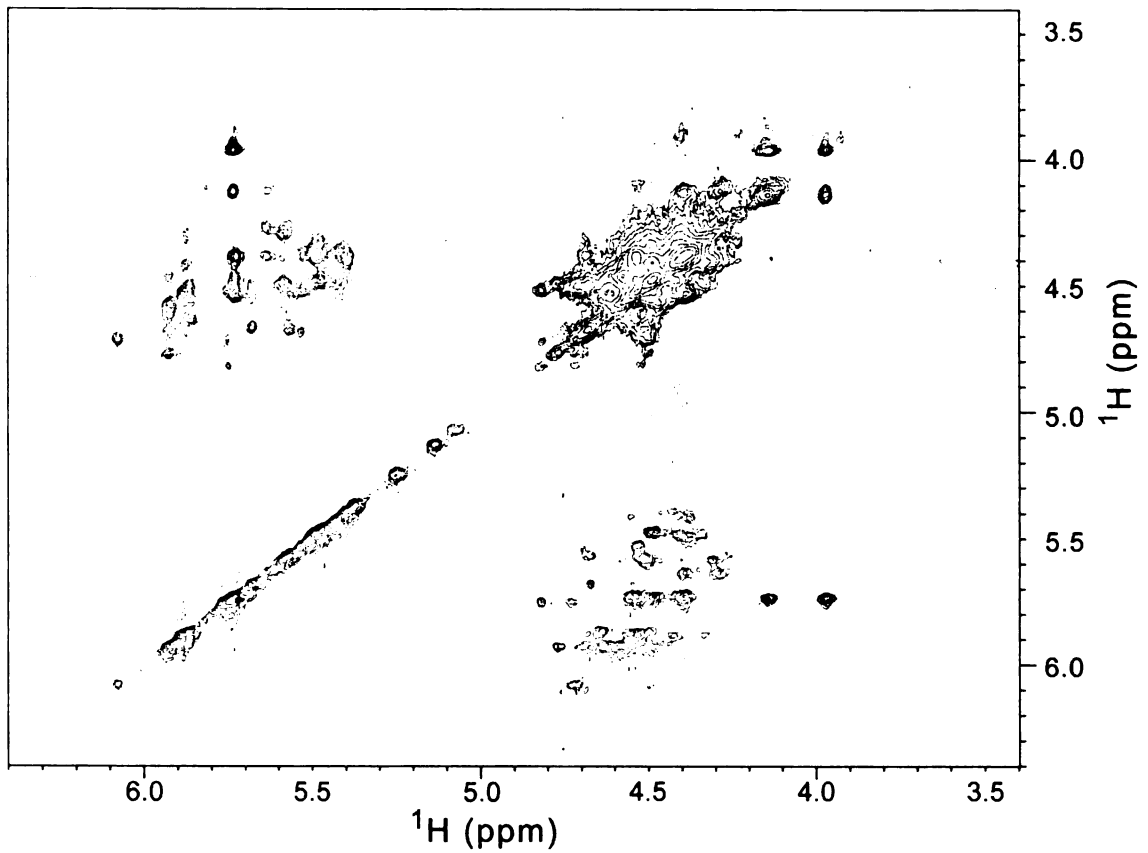

Figure 5.10: ^{1}H-^{1}H HCCH-TOCSY sub-spectra of the wild type domain A at 25 °C at 600 MHz.

The ribose and aromatic ^{1}H and ^{13}C chemical shift were obtained using correlated spectroscopy identifying intra-residue correlations. This approach, however, does not correlate ribose and aromatic chemical shifts to adjacent residues. NOE based experiments can be used to correlate intra-residue sugar and base protons, as well as inter-residue correlations. Both correlations can be used to obtain sequential assignment of residues. Sequential assignments can be made through H8/H6 to H2′ correlations which give rise to strong NOEs although significant overlap limits the usefulness of acquired data. Sequential

assignments can also be obtained from H8/H6 to H1′ correlations. Because H1′ chemical shifts are more dispersed than H2′, assignment can be less ambiguous. In A-form RNA, the distance between H8/H6 and H1′ are close enough to detect NOEs (≈ 5 Å).

^{1}H-^{1}H ^{13}C-edited NOESY-HSQC sub-spectra were acquired for the ribose and aromatic regions. From the ribose optimized ^{1}H-^{1}H NOESY-HSQC sub-spectra shown in figure 5.11a, correlations among ribose atoms were determined from strong NOEs, consistent with HCCH-COSY and HCCH-TOCSY sub-spectra. Correlations can also be observed among intra-residue H2′ to H8/H6 from weak NOEs. This is probably due to the optimization of the pulse sequence which attenuates aromatic proton signals. Intra- and inter-residue correlations for H1′ to H8/H6 could not be unambiguously determined due to overlap even with a 300 ms mixing period (data not shown). To complement the ribose NOESY, aromatic ^{1}H-^{1}H ^{13}C-edited NOESY-HSQC sub-spectra were acquired (Fig. 5.11b). Consistent with the ribose NOESY, inter-residue correlations were observed for H2′ to H8/H6. A few weak NOEs were observed for H1′ to H8/H6 correlations. Other NOEs may be present yet overlapped with more intense H5 to H6 crosspeaks.

Figure 5.11: ^{1}H-^{1}H ^{13}C-edited NOESY-HSQC sub-spectra of the wild type hairpin loop A at 25 °C at 600 MHz. Shown are the (a) ribose and (b) aromatic spectra using a 300 ms mixing time.

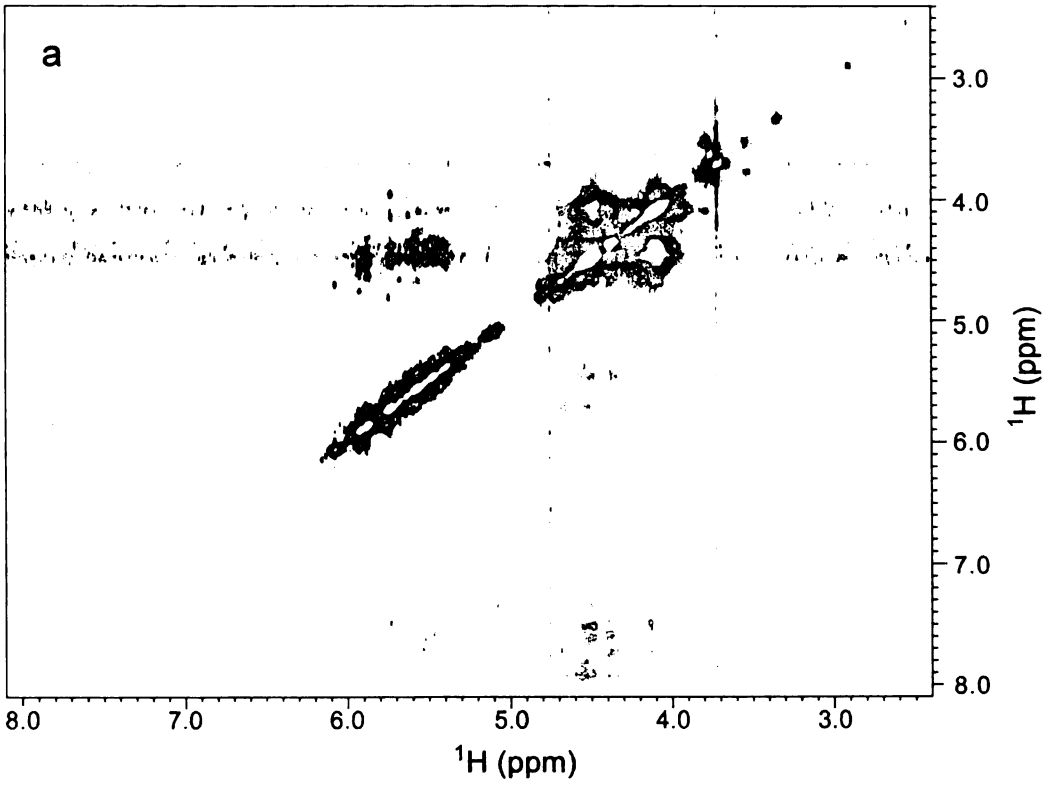
a
3.0
4.0
5.0
6.0
7.0
8.0
^{1}H (ppm)
8.0
7.0
6.0
5.0
4.0
3.0
^{1}H (ppm)

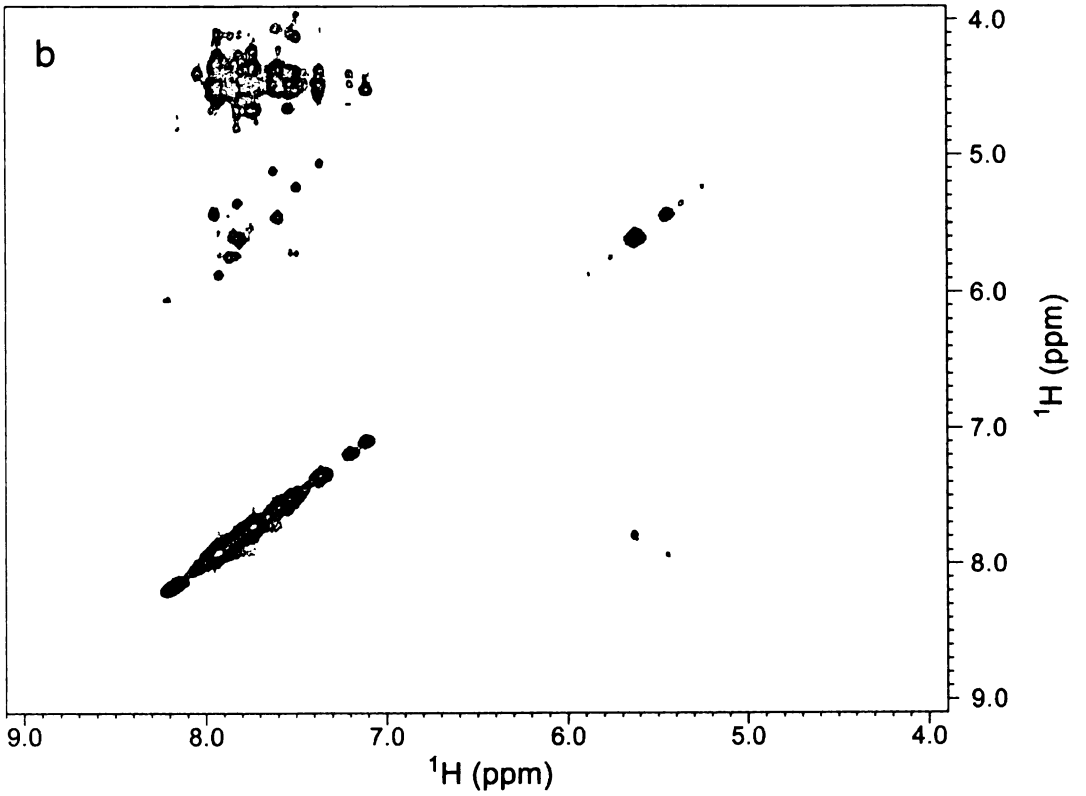
b
4.0
5.0
6.0
7.0
8.0
9.0
^{1}H (ppm)
9.0
8.0
7.0
6.0
5.0
4.0
^{1}H (ppm)

For NOE based experiments, signal intensities can be enhanced at higher magnetic field strengths. The aromatic to sugar region of a two-dimensional ^{1}H-^{1}H NOESY spectrum acquired at 900 MHz with a 150 ms mixing period is presented in Figure 5.12. Additional crosspeaks were observed compared to 600 MHz. These crosspeaks can be attributed to H1′ to H8/H6 correlations intra- and inter-residue correlations. Unfortunately, significant overlap with H5 to H6 prevents unambiguous assignments. While using a longer mixing period could enhance magnetization transfer for increased S/N, three-dimensional acquisition would be more useful due to H1′ and H5 separation.

All results were acquired as two-dimensional ^{1}H-^{1}H sub-spectra. With the acquisition of three-dimensional spectra, overlapped resonances can be resolved with ^{13}C chemical shifts. Combining the information of ribose spin systems with intra-residue H1′ to H8/H6 correlations, the entire nucleotide ^{1}H-^{13}C spin systems can be identified. The inter-residue H1′ to H8/H6 correlation can identify residue assignments. At this point, three-dimensional experiments have been acquired for HCCH-COSY, HCCH-TOCSY, and NOESY experiments, but have not been processed for detailed analysis.

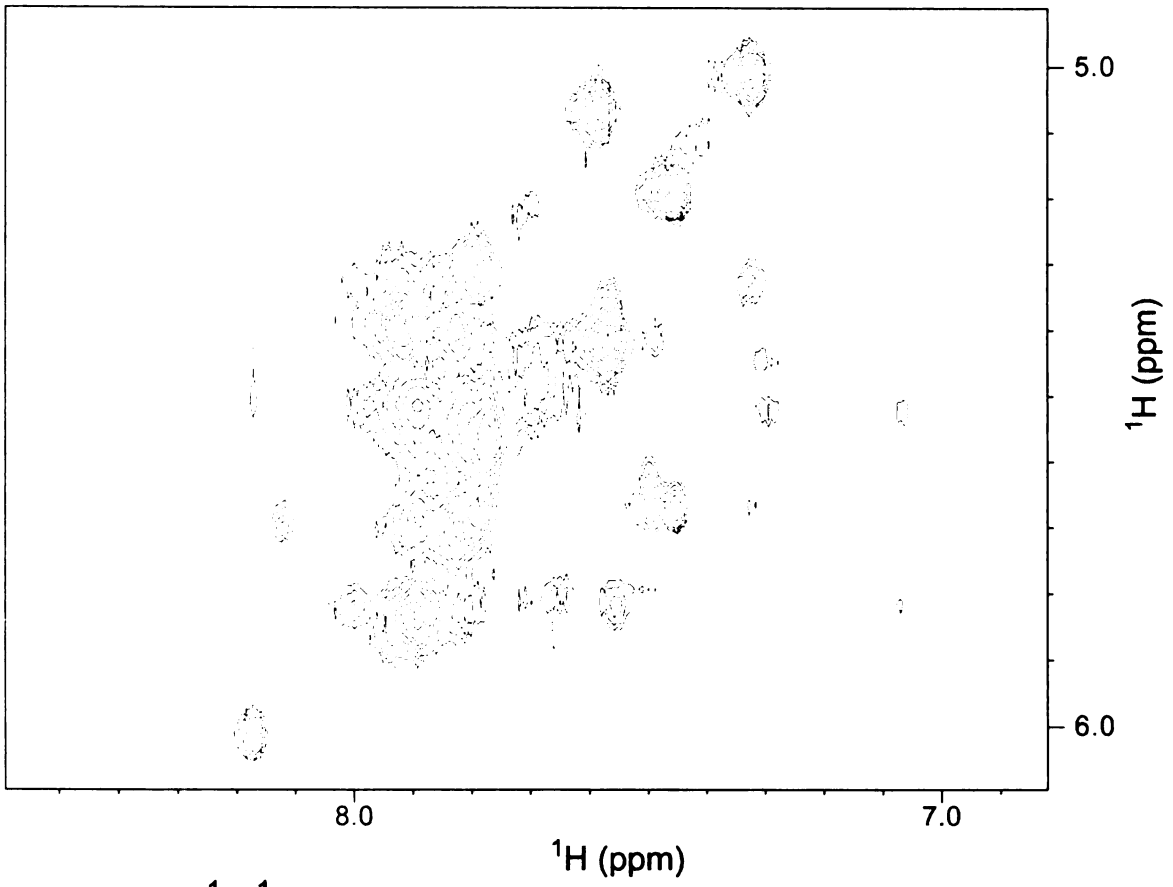

Figure 5.12: ^{1}H-^{1}H NOESY spectrum of the wild type hairpin loop A at 25 °C with a 150 ms mixing time at 900 MHz.

Table 5.3: Ribose ^{1}H and ^{13}C chemical shifts for wild type domain A.

	H1′ ^{1}H (ppm)[a]	C1′ ^{13}C (ppm)	H2′ ^{1}H (ppm)
1	5.30	93.19	4.42
2	5.39	92.12	4.57
3	5.39	94.17	4.38
4	5.42	93.87	4.34
5	5.47	94.66	4.48
6	5.47	93.97	4.40
7	5.49	94.36	4.53
8	5.53	91.82	4.68
9	5.57	89.77	4.30[a]
10	5.57	91.53	
11	5.59	91.92	4.39[a]
12	5.59	93.19	
13	5.63	91.04	4.67
14	5.68	94.07	4.39
15	5.73	93.19	4.53
16	5.73	93.87	3.97
17	5.75	91.73	4.81
18	5.82	91.14	4.63
19	5.87	92.61	4.63
20	5.88	93.29	4.53
21	5.92	91.82	4.57
22	5.93	92.51	4.77
23	6.07	92.80	4.71

[a]Resonances are ordered based on H1′ chemical shift

Table 5.4: Aromatic ^{1}H and ^{13}C chemical shifts for wild type domain A.

	H5 ^{1}H (ppm)[a]	C5 ^{13}C (ppm)	H6 ^{1}H (ppm)	C6 ^{13}C (ppm)
1	5.05	97.29	7.36	140.56
2	5.11	97.29	7.61	140.95
3	5.23	97.78	7.47	141.63
4	5.35	97.88	7.81	141.82
5	5.42	103.35	7.92	142.61
6	5.44	97.88	7.57	141.04
7	5.60	104.52	7.83	143.19
8	5.62	104.91	7.79	143.97
9	5.76	98.27	7.85	141.92
10	5.87	98.37	7.90	142.41

	H8 ^{1}H (ppm)[b]	C8 ^{13}C (ppm)		H2 ^{1}H (ppm)[c]	C2 ^{13}C (ppm)
1	7.11	136.45	1	7.33	153.25
2	7.20	136.55	2	7.56	153.93
3	7.36	137.53	3	7.69	155.20
4	7.53	136.26	4	7.92	155.01
5	7.59	139.38			
6	7.71	139.77			
7	7.73	137.72			
8	7.74	137.14			
9	7.75	138.90			
10	7.93	140.95			
11	8.04	139.97			
12	8.15	139.48			
13	8.21	142.80			

Resonances are ordered based on [a]H5, [b]H8, [c]H2 ^{1}H chemical shift

DISCUSSION

Partial ^{1}H, ^{13}C, and ^{15}N chemical shift assignments were determined for the isolated domain A of the hairpin ribozyme. These assignments were made possible by assignment strategies using standard through-space and through-bond correlated spectroscopy experiments for uniformly enriched nucleic acids.

Due to ambiguity from spectral overlap in two-dimensional sub-spectra, only partial chemical shift assignments were documented for wild type and mutant $U_{+2}C/C_{+3}U$ domain A.

From one-dimensional exchangeable spectroscopy, imino proton and amino proton peaks were observed. The observation of imino and amino proton peaks is indicative of folded RNA oligomer. The quantity of guanosine and uridine imino proton peaks from wild type and mutant sequences, which can be attributed to involvement in Watson-Crick base pairs, is consistent with predicted secondary structures. One- and two-dimensional exchangeable data exhibited high similarity between both sequences of domain A used. Consistent with predicted secondary structure, imino proton peaks for G_8-NH and U_{+3}-NH were observed in the mutant $U_{+2}C/C_{+3}U$ sequence. Also, G_6-NH was determined to be shifted downfield in the mutant sequence at 12.76 compared to 12.62 in the wild type sequence. This is plausible because G_6 is adjacent to the internal loop in the wild type sequence and sandwiched by A:U base pairs in the mutant sequence. This shift can be attributed to additional base stacking interactions. However, no base pairing was observed for G_{+1}. Because G_{+1} would form a non Watson-Crick base pair, the G_{+1}-NH chemical shift can be expected to resonate near 10 ppm, similar to G_{+7}. No additional peaks besides G_{+7} were observed between 10 to 11 ppm in the mutant sequence.

The proposed role of U_{+2} is to position G_8 properly in the active site. From wild type one- and two-dimensional spectra, no imino proton interactions were observed for G_8. However, an intense imino proton peak was observed in the $U_{+2}C/C_{+3}U$ mutant spectra for G_8 as well as a second uridine imino proton not present in the wild type spectra, U_{+3}. Interestingly, the $U_{+2}C/C_{+3}U$ mutant not only abolishes chemistry, it also disrupts proper formation of the docked complex. Docking and catalysis can be restored with a G_8U substitution, suggesting flexibility at site +2 in the internal loop of the wild type sequence. In fact, an abasic residue at site +2 only leads to ≈10 fold decrease in catalysis while nucleotide substitutions (G, C, and A) lead to more significant decreases in the catalytic rate (21). Because the $U_{+2}C/C_{+3}U$ mutant has been shown to not form a docked complex, this can be interpreted as quenched dynamics for G_{+1}. While the $U_{+2}C$ severely reduced the cleavage rate constant, efficient docking still occurred. Differences observed between wild type and mutant samples from exchangeable data in this work indicate changes were localized to the active site. It is possible that the $U_{+2}C/C_{+3}U$ mutant sequence restricts the flexibility of G_{+1}, particularly limiting its ability to form a cross domain base pair with C_{25}. Comparison of C8 dynamics of G_{+1} using ^{13}C NMR spin relaxation techniques

between the wild type and $U_{+2}C/C_{+3}U$ samples could discern quenched dynamics for the $U_{+2}C/C_{+3}U$ mutant.

Tentative sequential assignments have been made for wild type and mutant $U_{+2}C/C_{+3}U$ domain A. Unambiguous sequential assignments could not be obtained due to absence of imino to imino proton NOEs from ^{1}H-^{1}H ^{15}N-edited NOESY-HSQC sub-spectra. Several methods were attempted to observe imino to imino proton NOEs including increasing the mixing period to 300 ms, reducing the temperature to 5 °C to limit exchange, moving the proton irradiation frequency to 12.5 ppm to maximize enhancement for imino proton resonances, and the acquisition of a ^{1}H-^{1}H NOESY spectrum at 900 MHz. All methods produced results similar to Figures 5.6 and 5.7. It is not clear why imino to imino proton NOEs were not observed for wild type and mutant domain A spectra. It is possible that imino to imino proton NOEs could be more easily observed from ^{1}H-^{1}H NOESY spectra as opposed to ^{1}H-^{1}H ^{15}N-edited NOESY-HSQC sub-spectra. The removal of ^{15}N-editing would decrease the pulse sequence length, thus increasing the signal to noise ratio of observed crosspeaks.

Using correlated spectroscopy, proton intra-residue correlations for H1′ and H2′ were determined. To clear up ambiguities, such as H3′, H4′, H5′ (H5″) correlations to H1′ and H2′ assignments, the use of three-dimensional data acquisition can remove spectral overlap within the ribose region. To determine intra- and inter-residue correlations, ^{1}H-^{1}H ^{13}C-edited NOESY-HSQC sub-

spectra were acquired. While intra-residue proton to proton as well as aromatic H5 to H6 NOEs were easily observed, H1′ to H8/H6 were not easily detected. The detection of these NOEs would aid in the sequential assignment of domain A. Proper identification of aromatic and sugar resonances is crucial for detailed analysis of dynamics of domain A using NMR spin relaxation experiments. Acquisition of a three-dimensional ^{1}H-^{1}H ^{13}C-edited NOESY-HSQC sub-spectrum at 300 ms using 600 MHz and/or 900 MHz could help remove spectral overlap with aromatic H5 resonances.

A complementary strategy that can be employed is using residue specific triple resonance experiments that correlate exchangeable and non-exchangeable protons. Pardi and co-workers (44,45) have developed residue specific pulse sequences for guanosine, cytdine, and uridine residues that correlate exchangeable and non-exchangeable protons. The combined results from these experiments as well as other correlated spectroscopy could greatly refine the assignment process. Unfortunately, no information was obtained implementing modified versions of these pulse sequences (46) (data not shown).

In this chapter, partial ^{1}H, ^{13}C, and ^{15}N chemical shift assignments were determined for wild type and mutant $U_{+2}C/C_{+3}U$ sequences of the isolated domain A of the hairpin ribozyme. From exchangeable spectroscopy, imino and amino ^{1}H-^{15}N spin pairs were identified, which led to preliminary residue assignments. New imino and amino proton peaks were detected for the mutant $U_{+2}C/C_{+3}U$ domain A compared to the wild type domain A. These new peaks

were localized to the internal loop. These results support the proposed model that reduced mutant activity may be linked to decreased flexibility of internal loop residues.

^{1}H-^{13}C spin pairs were identified from spectroscopy of non-exchangeable resonances. To obtain complete sugar intra-residue spin systems, three-dimensional HCCH-TOCSY spectra would aid in unambiguous assignment. While sequential assignments could not be obtained, three-dimensional ^{13}C-edited NOESY-HSQC spectra will be critical. With the obtainment of complete chemical shifts, active site dynamics for the isolated domain A of the hairpin ribozyme can be investigated. Comparing dynamics in wild type and mutant sequences, the role of key residues in the catalytic mechanism can be better characterized.

ACKNOWLEDGEMENTS

I would like to thank Patrick Ochieng for the transcription and purification of mutant $U_{+2}C/C_{+3}U$ mutant used in this work.

REFERENCES

1. Hampel, A. and Tritz, R. (1989) RNA catalytic properties of the minimum (-)sTRSV sequence. *Biochemistry*, **28**, 4929-4933.

2. Prody, G.A., Bakos, J.T., Buzayan, J.M., Schneider, I.R. and Bruening, G. (1986) Autolytic processing of dimeric plant virus satellite RNA. *Science*, **231**, 1577-1580.

3. Buzayan, J.M., Gerlach, W.L., Bruening, G., Keese, P. and Gould, A.R. (1986) Nucleotide sequence of satellite tobacco ringspot virus RNA and its relationship to multimeric forms. *Virology*, **151**, 186-199.

4. Fedor, M.J. (2000) Structure and function of the hairpin ribozyme. *J Mol Biol*, **297**, 269-291.

5. Nesbitt, S., Hegg, L.A. and Fedor, M.J. (1997) An unusual pH-independent and metal-ion-independent mechanism for hairpin ribozyme catalysis. *Chem Biol*, **4**, 619-630.

6. Nesbitt, S.M., Erlacher, H.A. and Fedor, M.J. (1999) The internal equilibrium of the hairpin ribozyme: temperature, ion and pH effects. *J Mol Biol*, **286**, 1009-1024.

7. Hampel, K.J., Walter, N.G. and Burke, J.M. (1998) The solvent-protected core of the hairpin ribozyme-substrate complex. *Biochemistry*, **37**, 14672-14682.

8. Butcher, S.E., Heckman, J.E. and Burke, J.M. (1995) Reconstitution of hairpin ribozyme activity following separation of functional domains. *J Biol Chem*, **270**, 29648-29651.

9. Cai, Z. and Tinoco, I., Jr. (1996) Solution structure of loop A from the hairpin ribozyme from tobacco ringspot virus satellite. *Biochemistry*, **35**, 6026-6036.

10. Butcher, S.E., Allain, F.H. and Feigon, J. (1999) Solution structure of the loop B domain from the hairpin ribozyme. *Nat Struct Biol*, **6**, 212-216.

11. Rupert, P.B. and Ferre-D'Amare, A.R. (2001) Crystal structure of a hairpin ribozyme-inhibitor complex with implications for catalysis. *Nature*, **410**, 780-786.

12. Rupert, P.B., Massey, A.P., Sigurdsson, S.T. and Ferre-D'Amare, A.R. (2002) Transition state stabilization by a catalytic RNA. *Science*, **298**, 1421-1424.

13. Salter, J., Krucinska, J., Alam, S., Grum-Tokars, V. and Wedekind, J.E. (2006) Water in the active site of an all-RNA hairpin ribozyme and effects of Gua8 base variants on the geometry of phosphoryl transfer. *Biochemistry*, **45**, 686-700.

14. Torelli, A.T., Krucinska, J. and Wedekind, J.E. (2007) A comparison of vanadate to a 2'-5' linkage at the active site of a small ribozyme suggests a role for water in transition-state stabilization. *RNA*, **13**, 1052-1070.

15. Ryder, S.P. and Strobel, S.A. (1999) Nucleotide analog interference mapping of the hairpin ribozyme: implications for secondary and tertiary structure formation. *J Mol Biol*, **291**, 295-311.

16. Berzal-Herranz, A., Joseph, S., Chowrira, B.M., Butcher, S.E. and Burke, J.M. (1993) Essential nucleotide sequences and secondary structure elements of the hairpin ribozyme. *EMBO J*, **12**, 2567-2573.

17. Butcher, S.E. and Burke, J.M. (1994) Structure-mapping of the hairpin ribozyme. Magnesium-dependent folding and evidence for tertiary interactions within the ribozyme-substrate complex. *J Mol Biol*, **244**, 52-63.

18. Butcher, S.E. and Burke, J.M. (1994) A photo-cross-linkable tertiary structure motif found in functionally distinct RNA molecules is essential for catalytic function of the hairpin ribozyme. *Biochemistry*, **33**, 992-999.

19. Walter, F., Murchie, A.I., Duckett, D.R. and Lilley, D.M. (1998) Global structure of four-way RNA junctions studied using fluorescence resonance energy transfer. *RNA*, **4**, 719-728.

20. Walter, F., Murchie, A.I., Thomson, J.B. and Lilley, D.M. (1998) Structure and activity of the hairpin ribozyme in its natural junction conformation: effect of metal ions. *Biochemistry*, **37**, 14195-14203.

21. Walter, N.G., Chan, P.A., Hampel, K.J., Millar, D.P. and Burke, J.M. (2001) A base change in the catalytic core of the hairpin ribozyme perturbs function but not domain docking. *Biochemistry*, **40**, 2580-2587.

22. Walter, N.G., Hampel, K.J., Brown, K.M. and Burke, J.M. (1998) Tertiary structure formation in the hairpin ribozyme monitored by fluorescence resonance energy transfer. *EMBO J*, **17**, 2378-2391.

23. Zhuang, X., Kim, H., Pereira, M.J., Babcock, H.P., Walter, N.G. and Chu, S. (2002) Correlating structural dynamics and function in single ribozyme molecules. *Science*, **296**, 1473-1476.

24. Hegg, L.A. and Fedor, M.J. (1995) Kinetics and thermodynamics of intermolecular catalysis by hairpin ribozymes. *Biochemistry*, **34**, 15813-15828.

25. Hoogstraten, C.G., Legault, P. and Pardi, A. (1998) NMR solution structure of the lead-dependent ribozyme: evidence for dynamics in RNA catalysis. *J Mol Biol*, **284**, 337-350.

26. Legault, P. and Pardi, A. (1997) Unusual dynamics and pK_a shift at the active site of a lead-dependent ribozyme. *J Am Chem Soc*, **119**, 6621-6628.

27. Shippy, R., Siwkowski, A. and Hampel, A. (1998) Mutational analysis of loops 1 and 5 of the hairpin ribozyme. *Biochemistry*, **37**, 564-570.

28. Komatsu, Y., Kumagai, I. and Ohtsuka, E. (1999) Investigation of the recognition of an important uridine in an internal loop of a hairpin ribozyme prepared using post-synthetically modified oligonucleotides. *Nucleic Acids Res*, **27**, 4314-4323.

29. Perez-Ruiz, M., Barroso-DelJesus, A. and Berzal-Herranz, A. (1999) Specificity of the hairpin ribozyme. Sequence requirements surrounding the cleavage site. *J Biol Chem*, **274**, 29376-29380.

30. Chowrira, B.M., Berzal-Herranz, A. and Burke, J.M. (1991) Novel guanosine requirement for catalysis by the hairpin ribozyme. *Nature*, **354**, 320-322.

31. Sargueil, B., Hampel, K.J., Lambert, D. and Burke, J.M. (2003) In vitro selection of second site revertants analysis of the hairpin ribozyme active site. *J Biol Chem*, **278**, 52783-52791.

32. Hoogstraten, C.G., Wank, J.R. and Pardi, A. (2000) Active site dynamics in the lead-dependent ribozyme. *Biochemistry*, **39**, 9951-9958.

33. Blad, H., Reiter, N.J., Abildgaard, F., Markley, J.L. and Butcher, S.E. (2005) Dynamics and metal ion binding in the U6 RNA intramolecular stem-loop as analyzed by NMR. *J Mol Biol*, **353**, 540-555.

34. Shajani, Z. and Varani, G. (2005) ^{13}C NMR relaxation studies of RNA base and ribose nuclei reveal a complex pattern of motions in the RNA binding site for human U1A protein. *J Mol Biol*, **349**, 699-715.

35. Trantirek, L., Caha, E., Kaderavek, P. and Fiala, R. (2007) NMR ^{13}C-relaxation study of base and sugar dynamics in GCAA RNA hairpin tetraloop. *J Biomol Struct Dyn*, **25**, 243-252.

36. Shajani, Z., Drobny, G. and Varani, G. (2007) Binding of U1A protein changes RNA dynamics as observed by ^{13}C NMR relaxation studies. *Biochemistry*, **46**, 5875-5883.

37. Flinders, J. and Dieckmann, T. (2006) NMR spectroscopy of ribonucleic acids. *Prog Nucl Magn Reson Spectrosc*, **48**, 137-159.

38. Cromsigt, J., van Buuren, B., Schleucher, J. and Wijmenga, S. (2001) Resonance assignment and structure determination for RNA. *Methods Enzymol*, **338**, 371-399.

39. Nikonowicz, E.P. and Pardi, A. (1993) An efficient procedure for assignment of the proton, carbon and nitrogen resonances in $^{13}C/^{15}N$ labeled nucleic acids. *J Mol Biol*, **232**, 1141-1156.

40. Wijmenga, S. and van Buuren, B. (1998) The use of NMR methods for conformational studies of nucleic acids. *Prog Nucl Magn Reson Spectrosc*, **32**, 287-387.

41. Milligan, J.F., Groebe, D.R., Witherell, G.W. and Uhlenbeck, O.C. (1987) Oligoribonucleotide synthesis using T7 RNA polymerase and synthetic DNA templates. *Nucleic Acids Res*, **15**, 8783-8798.

42. Milligan, J.F. and Uhlenbeck, O.C. (1989) Synthesis of small RNAs using T7 RNA polymerase. *Methods Enzymol*, **180**, 51-62.

43. Kim, I., McKenna, S.A., Viani Puglisi, E. and Puglisi, J.D. (2007) Rapid purification of RNAs using fast performance liquid chromatography (FPLC). *RNA*, **13**, 289-294.

44. Simorre, J.P., Zimmermann, G.R., Pardi, A., Farmer, B.T., 2nd and Mueller, L. (1995) Triple resonance HNCCCH experiments for correlating exchangeable and nonexchangeable cytidine and uridine base protons in RNA. *J Biomol NMR*, **6**, 427-432.

45. Simorre, J.P., Zimmermann, G.R., Mueller, L. and Pardi, A. (1996) Correlation of the guanosine exchangeable and nonexchangeable base protons in ^{13}C-/^{15}N-labeled RNA with an HNC-TOCSY-CH experiment. *J Biomol NMR*, **7**, 153-156.

46. Lukavsky, P.J. and Puglisi, J.D. (2001) RNAPack: an integrated NMR approach to RNA structure determination. *Methods*, **25**, 316-332.

Chapter 6

Conclusions and Future Work

CONCLUSIONS

This thesis was motivated by an interest in investigating dynamics in RNA molecules by use of NMR spin relaxation techniques. NMR spectroscopy is a versatile tool which can detect motions across a broad range of molecular motion timescales (1). While investigations of molecular motions have been extensively probed in proteins, dynamics in RNA molecules have been less studied. Motions in RNA molecules have mostly been limited to the nucleotide base C8 and C6 atoms (2-5), and little information has been obtained for the ribose atoms. Studies of ribose dynamics have been hampered because of difficulties in acquiring reliable data due to the coupling among ^{13}C atoms of the ribose ring when using uniform isotope labeling schemes (6). Other methods, such as natural abundance acquisition (7,8) or chemical synthesis (9) have their limitations as well. Because the ribose ring of RNA molecules has may play an important role in the catalytic mechanism (10), a method is needed to accurately extend dynamic studies throughout sugar molecule. With the combined analysis of base and ribose carbons of RNA molecules, the role of dynamics can be defined for RNA molecules during RNA folding or catalysis.

In chapter two, a method was outlined to make use of the pentose phosphate pathway of *E. coli* cells to obtain ribonucleotides that have an alternating ^{13}C-^{12}C pattern for the ribose ring, thereby isolating ^{13}C atoms for NMR dynamic studies. This pattern was obtained using *E. coli* strains (*zwf*) deficient in the oxidative portion of the pentose phosphate pathway. Other methods were identified to effectively isolate other carbons, including C3′. These

results along with previous techniques provide a method to specifically label all ^{13}C atoms in ribonucleotides such that NMR dynamic studies are suitable.

The utility of the alternate-site labeling scheme for relaxation studies was validated by comparing R_1 and $R_{1\rho}$ measurements for specifically (2',4'-$^{13}C_2$) and uniformly labeled rAMP. Consistent with previous work (11), it was shown, from R_1 measurements, that ^{13}C-^{13}C dipolar interactions can be neglected at short correlation times, but these interactions become more significant at longer correlation times consistent with previous results. While ^{13}C-^{13}C dipolar interactions are negligible for R_2 measurements, ^{13}C-^{13}C scalar interactions limit data analysis of transverse relaxation. This was demonstrated by the removal of Hartmann-Hahn ^{13}C-^{13}C interaction from $R_{1\rho}$ measurements. The specific labeling scheme removes ^{13}C-^{13}C dipolar and scalar coupling, greatly simplifying the determination of relaxation parameters from ^{1}H-^{13}C spin systems. From these results, it is clear that the alternate-site labeling scheme can be used in RNA molecules to study ribose dynamics on multiple timescales.

In chapter three, dynamics were studied in the GCAA RNA hairpin via the alternate-site labeling scheme. Previous NMR studies and molecular simulations reported sugar conversion for C_6 from C3'-endo to C2'-endo in conjunction with C_6 base flipping out of the ground state structure, as well as a heterogeneous hydrogen bond model for the tetraloop (12,13). With the specific labeling

scheme, ribose dynamics were investigated on multiple timescales, particularly on the μs to ms timescale.

Motions on the ps to ns timescale were investigated using the Model-free approach pioneered by Lipari-Szabo (14,15) from ^{13}C R_1, $R_{1\rho}$, and heteronuclear NOE values at 600 MHz. The GCAA RNA hairpin was found to be a rigid molecule on this timescale with internal order parameters, S^2, of at least 0.9 for non-terminal atoms. Some atoms were determined to have internal, effective correlation times indicative of fast motions on the ps to ns timescale. Interestingly, all tetraloop atoms except C_6 C2′ exhibited an R_{ex} contribution, indicative of μs to ms motions. To accurately ascertain the R_{ex} contribution, relaxation dispersion curves were analyzed.

Motional parameters were determined from fits to relaxation dispersion curves obtained at multiple field strengths. With the combined approach of CPMG, on-, and off resonance $R_{1\rho}$ measurements, as well as multiple fields, the complete dispersion profiles for nearly all atoms in the GCAA RNA tetraloop hairpin were determined, particularly the tetraloop atoms. Exchange lifetimes were determined for C2′ and C4′ atoms of all tetraloop atoms except C_6 C2′. For G_5, A_7, A_8, the C2′ and C4′ exchange lifetimes were determined to be similar within error. The C2′ and C4′ atoms of a given residue could be fit to a single τ_{ex}, which implies that atoms of a residue are reporting on a single conformational event. This motional event was proposed to be sugar pucker transitions, where

previous results determined the sugar puckers of the GCAA RNA tetraloop to be in equilibrium (12). Also, exchange lifetimes clustered into two groups across the tetraloop, which suggested two different motional timescales. The C_6 and A_7 atoms were fit to a single τ_{ex} while G_5 and A_8 were fit to another τ_{ex}. This suggests that the motions of C_6 and A_7 are coupled and G_5 and A_8 are coupled. It is plausible that the C_6 and A_7 motions are reporting on the base flipping motion of C_6, while the G_5 and A_8 are reporting on the dynamic hydrogen bond network. These results demonstrate the usefulness in measuring conformational changes for RNA molecules using NMR experiments, whereas other methods would not be able to detect such motions.

Relaxation dispersion curves were obtained at multiple temperatures to ascertain the temperature dependence of the exchange rate constant for C2′ and C4′ in the tetraloop. The activation energy of sugar pucker transitions was determined from Arrhenius plots. While the data are somewhat ambiguous due to large error bars, the fitted activation energy values suggest that sugar pucker transitions require ≈30 kJ/mol. Not surprisingly, the activation energies for G_5 and A_8 atoms were clustered within a narrow range, while the activation energies of C_6 and A_7 C4′ were reported to be similar within error. These results depict the first analysis of ribose dynamics for C2′ and C4′ of RNA molecules. Taken along with nucleotide base dynamics, a complete assessment of motions within

RNA molecules can be obtained yielding a wealth of information, such as correlated motions.

In chapter four, the alternate-site labeling scheme was incorporated into cytidine residues of the lead-dependent ribozyme. Preliminary results suggest an R_{ex} contribution for C_6 C2', which is the nucleophile in the catalytic mechanism. An exchange lifetime of 93 ± 36 μs was determined, suggesting possible motional correlation to the protonation/deprotonation of A_{25} N1, which forms a non Watson-Crick base pair with C_6.

In chapter five, preliminary ^{1}H, ^{13}C, and ^{15}N chemical shifts are reported for wild type and $U_{+2}C/C_{+3}U$ mutant isolated domain A of the hairpin ribozyme. From comparison of exchangeable spectroscopy data between the wild type and mutant domain A, additional peaks were observed in the mutant sequence. These peaks were attributed to the residues in the internal loop. Because the $U_{+2}C/C_{+3}U$ mutant is not able to form a docked structure, and the $U_{+2}C$ single mutant does form a stable docked structure, it is plausible that the $U_{+2}C/C_{+3}U$ mutant reduces or quenches dynamics.

FUTURE WORK

While this thesis has documented methods and analyses in RNA molecules, many questions still remain. Several of these issues have been listed below:

Further Characterization of the GCAA RNA Hairpin. The usefulness of the specific labeling scheme was demonstrated to obtain motional parameters for C2′ and C4′ of the ribose ring of the tetraloop region. It was concluded that C2′ and C4′ report on the same motion of sugar pucker interconversion. To further examine sugar pucker transitions, motional parameters can be obtained for C3′ atoms of the tetraloop residues to further probe ribose dynamics. This can be done by obtaining ribonucleotides from wild type *E. coli* cells with 4-^{13}C glucose as the sole carbon source. These ribonucleotides can then be incorporated into any RNA oligomer of choice, i.e. the GCAA RNA hairpin.

Concerted motions for the ribose ring were determined, even among multiple residues. However, concerted base and ribose motions were not detected. In the GCAA RNA hairpin, C_6 was predicted to de-stack from the tetraloop structure. However, dynamics for C_6 C6 were not observed which was due in part from the unambiguous ^{1}H only assignments for the GCAA RNA hairpin. Using ^{1}H-^{1}H HCCH-COSY sub-spectra, H5 and H6 correlations can be used to clarify H6/C6 spin system for accurate acquisition of relaxation dispersion data.

Investigation of Dynamics for the Lead-dependent Ribozyme. Preliminary data have been presented that suggest exchange contributions for C2′ of C_6 in the lead-dependent ribozyme. To further characterize this motion, the acquisition of CPMG and $R_{1\rho}$ measurements at higher fields, particularly 900 MHz, could aid

in the analysis of leadzyme dynamics. As shown previously, acquisition at higher magnetic fields increases the R_{ex} contribution, aiding in the analysis of small R_{ex} contributions. Also, to investigate base motions, a uniformly labeled ^{13}C cytidine-only leadzyme NMR sample could unambiguously detect aromatic C_6 C6 motions.

Investigation of Dynamics for the Hairpin Ribozyme. Preliminary ^{1}H, ^{13}C, and ^{15}N chemical shifts were obtained for wild type and mutant $U_{+2}C/C_{+3}U$ hairpin ribozymes. To complete the chemical shift assignments, three-dimensional HCCH-TOCSY and NOESY will be essential. Three dimensional datasets have been acquired at both 600 and 900 MHz. Processing and analysis of these datasets would greatly improve the effectiveness of chemical shift assignment.

With the unambiguous assignment of ^{1}H and ^{13}C resonances for wild type and $U_{+2}C/C_{+3}U$ mutant sequences, active site dynamics can be investigated on multiple timescales using R_1, $R_{1\rho}$, and heteronuclear NOE measurements as well as relaxation dispersion curves at multiple field strengths for base and ribose atoms using uniform and specific labeling schemes, respectively, particularly A_{-1}, G_{+1}, U_{+2}, and G_8. These experiments may reveal never-before-seen dynamics within the active site that NMR spectroscopy is uniquely suited to measure.

With the ground state dynamics defined, active site perturbations due to docking can be probed using labeled domain A with unlabeled domain B in the presence and absence of $Co(III)[NH_3]_6^{3+}$. To prevent cleavage, a $G_8A/A_{38}U$ mutant will be used which has been shown to dock but does not cleave on the timescale of NMR experiments (personal communication). These experiments have the unique ability to probe timescale of docking perturbations.

To conclude, the work detailed in this thesis has probed ribose dynamics in RNA molecules. The methods documented herein in conjunction with other studies can aid in the understanding the catalytic mechanism of ribozymes.

REFERENCES

1. Palmer, A.G., 3rd. (2004) NMR characterization of the dynamics of biomacromolecules. *Chem Rev*, **104**, 3623-3640.

2. Hoogstraten, C.G., Wank, J.R. and Pardi, A. (2000) Active site dynamics in the lead-dependent ribozyme. *Biochemistry*, **39**, 9951-9958.

3. Blad, H., Reiter, N.J., Abildgaard, F., Markley, J.L. and Butcher, S.E. (2005) Dynamics and metal ion binding in the U6 RNA intramolecular stem-loop as analyzed by NMR. *J Mol Biol*, **353**, 540-555.

4. Shajani, Z. and Varani, G. (2005) ^{13}C NMR relaxation studies of RNA base and ribose nuclei reveal a complex pattern of motions in the RNA binding site for human U1A protein. *J Mol Biol*, **349**, 699-715.

5. Shajani, Z. and Varani, G. (2008) ^{13}C relaxation studies of the DNA target sequence for hhai methyltransferase reveal unique motional properties. *Biochemistry*, **47**, 7617-7625.

6. Shajani, Z. and Varani, G. (2007) NMR studies of dynamics in RNA and DNA by ^{13}C relaxation. *Biopolymers*, **86**, 348-359.

7. Borer, P.N., LaPlante, S.R., Kumar, A., Zanatta, N., Martin, A., Hakkinen, A. and Levy, G.C. (1994) ^{13}C-NMR relaxation in three DNA oligonucleotide duplexes: model-free analysis of internal and overall motion. *Biochemistry*, **33**, 2441-2450.

8. Spielmann, H.P. (1998) Dynamics of a bis-intercalator DNA complex by ^{1}H-detected natural abundance ^{13}C NMR spectroscopy. *Biochemistry*, **37**, 16863-16876.

9. SantaLucia, J., Jr., Shen, L.X., Cai, Z., Lewis, H. and Tinoco, I., Jr. (1995) Synthesis and NMR of RNA with selective isotopic enrichment in the bases. *Nucleic Acids Res*, **23**, 4913-4921.

10. Rupert, P.B., Massey, A.P., Sigurdsson, S.T. and Ferre-D'Amare, A.R. (2002) Transition state stabilization by a catalytic RNA. *Science*, **298**, 1421-1424.

11. Boisbouvier, J., Wu, Z., Ono, A., Kainosho, M. and Bax, A. (2003) Rotational diffusion tensor of nucleic acids from ^{13}C NMR relaxation. *J Biomol NMR*, **27**, 133-142.

12. Jucker, F.M., Heus, H.A., Yip, P.F., Moors, E.H. and Pardi, A. (1996) A network of heterogeneous hydrogen bonds in GNRA tetraloops. *J Mol Biol*, **264**, 968-980.

13. Sorin, E.J., Engelhardt, M.A., Herschlag, D. and Pande, V.S. (2002) RNA simulations: probing hairpin unfolding and the dynamics of a GNRA tetraloop. *J Mol Biol*, **317**, 493-506.

14. Lipari, G. and Szabo, A. (1982) Model-free approach to the interpretation of nuclear magnetic resonance relaxation in macromolecules. 1. theory and range of validity. *J Am Chem Soc*, **104**, 4546-4559.

15. Lipari, G. and Szabo, A. (1982) Model-free approach to the interpretation of nuclear magnetic resonance relaxation in macromolecules. 2. analysis of experimental results. *J Am Chem Soc*, **104**, 4559-4570.